

Jordan Journal of Mechanical and Industrial Engineering (JJMIE)

JJMIE is a high-quality scientific journal devoted to fields of Mechanical and Industrial Engineering. It is published by The Hashemite University in corporation with the Jordanian Scientific Research Support Fund.

EDITORIAL BOARD

Editor-in-Chief

Prof. **Nabil Anagreh**

Editorial board

Prof. **Mohammad Ahmad Hamdan**
The University of Jordan

Prof. **Ibrahim A. Rawabdeh**
The University of Jordan

Prof. **Amin Al Robaidi**
Al Balqa Applied University

Prof. **Naser Al-Huniti**
The University of Jordan

Prof. **Suhil Kiwan**
The Jordan University of Science and Technology

Prof. **Mahmoud Abu-Zaid**
Mutah University

Assistant Editor

Dr. Khalid Al-Widyan
Hashemite University

THE INTERNATIONAL ADVISORY BOARD

Abu-Qudais, Mohammad
Jordan University of Science & Technology, Jordan

Abu-Mulaweh, Hosni
Purdue University at Fort Wayne, USA

Afaneh Abdul-Hafiz
Robert Bosch Corporation, USA

Afonso, Maria Dina
Institute Superior Tecnico, Portugal

Badiru, Adedji B.
The University of Tennessee, USA

Bejan, Adrian
Duke University, USA

Chalhoub, Nabil G.
Wayne State University, USA

Cho, Kyu-Kab
Pusan National University, South Korea

Dincer, Ibrahim
University of Ontario Institute of Technology,
Canada

Douglas, Roy
Queen's University, U. K

El Bassam, Nasir
International Research Center for Renewable
Energy, Germany

Haik, Yousef
United Arab Emirates University, UAE

Jaber, Jamal
Al- Balqa Applied University, Jordan

Jubran, Bassam
Ryerson University, Canada

Kakac, Sadik
University of Miami, USA

Khalil, Essam-Eddin
Cairo University, Egypt

Mutoh, Yoshiharu
Nagaoka University of Technology, Japan

Pant, Durbin
Iowa State University, USA

Riffat, Saffa
The University of Nottingham, U. K

Saghir, Ziad
Ryerson University, Canada

Sarkar, MD. Abdur Rashid
Bangladesh University of Engineering &
Technology, Bangladesh

Siginer, Dennis
Wichita State University, USA

Sopian, Kamaruzzaman
University Kebangsaan Malaysia, Malaysia

Tzou, Gow-Yi
Yung-Ta Institute of Technology and Commerce,
Taiwan

EDITORIAL BOARD SUPPORT TEAM

Language Editor

Dr. Qusai Al-Debyan

Publishing Layout

Eng. Mohannad Oqdeh

SUBMISSION ADDRESS:

Prof. **Nabil Anagreh**, Editor-in-Chief
Jordan Journal of Mechanical & Industrial Engineering,
Hashemite University,
PO Box 330127, Zarqa, 13133, Jordan
E-mail: jjmie@hu.edu.jo



Hashemite Kingdom of Jordan



Hashemite University

Jordan Journal of
Mechanical and Industrial Engineering

JJMIIE

An International Peer-Reviewed Scientific Journal
Financed by Scientific Research Support Fund

<http://jjmie.hu.edu.jo/>

ISSN 1995-6665

Jordan Journal of Mechanical and Industrial Engineering (JJMIE)

JJMIE is a high-quality scientific journal devoted to fields of Mechanical and Industrial Engineering. It is published by The Jordanian Ministry of Higher Education and Scientific Research in corporation with the Hashemite University.

Introduction: The Editorial Board is very committed to build the Journal as one of the leading international journals in mechanical and industrial engineering sciences in the next few years. With the support of the Ministry of Higher Education and Scientific Research and Jordanian Universities, it is expected that a heavy resource to be channeled into the Journal to establish its international reputation. The Journal's reputation will be enhanced from arrangements with several organizers of international conferences in publishing selected best papers of the conference proceedings.

Aims and Scope: *Jordan Journal of Mechanical and Industrial Engineering (JJMIE)* is a refereed international journal to be of interest and use to all those concerned with research in various fields of, or closely related to, mechanical and industrial engineering disciplines. *Jordan Journal of Mechanical and Industrial Engineering* aims to provide a highly readable and valuable addition to the literature which will serve as an indispensable reference tool for years to come. The coverage of the journal includes all new theoretical and experimental findings in the fields of mechanical and industrial engineering or any closely related fields (Materials, Manufacturing, Management, Design, Thermal and Fluid, Energy, Control, Mechatronics, and Biomedical). The journal also encourages the submission of critical review articles covering advances in recent research of such fields as well as technical notes.

Guide for Authors

Manuscript Submission:

High-quality submissions to this new journal are welcome now and manuscripts may be either submitted online or email.

Online: For online and email submission upload one copy of the full paper including graphics and all figures at the online submission site, accessed via <http://jjmie.hu.edu.jo>. The manuscript must be written in MS Word 2010 Format. All correspondence, including notification of the Editor's decision and requests for revision, takes place by e-mail and via the Author's homepage, removing the need for a hard-copy paper trail.

Submission address and contact:

Prof. Nabil Anagreh
Editor-in-Chief
Jordan Journal of Mechanical & Industrial Engineering,
Hashemite University,
PO Box 330127, Zarqa, 13115, Jordan
E-mail: jjmie@hu.edu.jo

Types of contributions: Original research papers and Technical reports

Corresponding author: Clearly indicate who is responsible for correspondence at all stages of refereeing and publication, including post-publication. Ensure that telephone and fax numbers (with country and area code) are provided in addition to the e-mail address and the complete postal address. Full postal addresses must be given for all co-authors.

Original material: Submission of an article implies that the work described has not been published previously (except in the form of an abstract or as part of a published lecture or academic thesis), that it is not under consideration for publication elsewhere, that its publication is approved by all authors and that, if accepted, it will not be published elsewhere in the same form, in English or in any other language, without the written consent of the Publisher. Authors found to be deliberately contravening the submission guidelines on originality and exclusivity shall not be considered for future publication in this journal.

Withdrawing: If the author chooses to withdraw his article after it has been assessed, he shall reimburse JJMIE with the cost of reviewing the paper.

Manuscript Preparation:

General: Editors reserve the right to adjust style to certain standards of uniformity. Original manuscripts are discarded after publication unless the Publisher is asked to return original material after use. Please use MS Word 2010 for the text of your manuscript.

Structure: Follow this order when typing manuscripts: Title, Authors, Authors title, Affiliations, Abstract, Keywords, Introduction, Main text, Conclusions, Acknowledgements, Appendix, References, Figure Captions, Figures and then Tables. Please supply figures imported into the text AND also separately as original graphics files. Collate acknowledgements in a separate section at the end of the article and do not include them on the title page, as a footnote to the title or otherwise.

Text Layout: Use 1.5 line spacing and wide (3 cm) margins. Ensure that each new paragraph is clearly indicated. Present tables and figure legends on separate pages at the end of the manuscript. If possible, consult a recent issue of the journal to become familiar with layout and conventions. All footnotes (except for table and corresponding author footnotes) should be identified with superscript Arabic numbers. To conserve space, authors are requested to mark the less important parts of the paper (such as records of experimental results) for printing in smaller type. For long papers (more than 4000 words) sections which could be deleted without destroying either the sense or the continuity of the paper should be indicated as a guide for the editor. Nomenclature should conform to that most frequently used in the scientific field concerned. Number all pages consecutively; use 12 or 10 pt font size and standard fonts.

Corresponding author: Clearly indicate who is responsible for correspondence at all stages of refereeing and publication, including post-publication. The corresponding author should be identified with an asterisk and footnote. Ensure that telephone and fax numbers (with country and area code) are provided in addition to the e-mail address and the complete postal address. Full postal addresses must be given for all co-authors. Please consult a recent journal paper for style if possible.

Abstract: A self-contained abstract outlining in a single paragraph the aims, scope and conclusions of the paper must be supplied.

Keywords: Immediately after the abstract, provide a maximum of six keywords (avoid, for example, 'and', 'of'). Be sparing with abbreviations: only abbreviations firmly established in the field may be eligible.

Symbols: All Greek letters and unusual symbols should be identified by name in the margin, the first time they are used.

Units: Follow internationally accepted rules and conventions: use the international system of units (SI). If other quantities are mentioned, give their equivalent in SI.

Maths: Number consecutively any equations that have to be displayed separately from the text (if referred to explicitly in the text).

References: All publications cited in the text should be presented in a list of references following the text of the manuscript.

Text: Indicate references by number(s) in square brackets in line with the text. The actual authors can be referred to, but the reference number(s) must always be given.

List: Number the references (numbers in square brackets) in the list in the order in which they appear in the text.

Examples:

Reference to a journal publication:

[1] M.S. Mohsen, B.A. Akash, "Evaluation of domestic solar water heating system in Jordan using analytic hierarchy process". Energy Conversion & Management, Vol. 38 (1997) No. 9, 1815-1822.

Reference to a book:

[2] Strunk Jr W, White EB. The elements of style. 3rd ed. New York: Macmillan; 1979.

Reference to a conference proceeding:

[3] B. Akash, S. Odeh, S. Nijmeh, "Modeling of solar-assisted double-tube evaporator heat pump system under local climate conditions". 5th Jordanian International Mechanical Engineering Conference, Amman, Jordan, 2004.

Reference to a chapter in an edited book:

[4] Mettam GR, Adams LB. How to prepare an electronic version of your article. In: Jones BS, Smith RZ, editors. Introduction to the electronic age, New York: E-Publishing Inc; 1999, p. 281-304

Free Online Color : If, together with your accepted article, you submit usable color and black/white figures then the journal will ensure that these figures will appear in color on the journal website electronic version.

Tables: Tables should be numbered consecutively and given suitable captions and each table should begin on a new page. No vertical rules should be used. Tables should not unnecessarily duplicate results presented elsewhere in the manuscript (for example, in graphs). Footnotes to tables should be typed below the table and should be referred to by superscript lowercase letters.

Notification: Authors will be notified of the acceptance of their paper by the editor. The Publisher will also send a notification of receipt of the paper in production.

Copyright: All authors must sign the Transfer of Copyright agreement before the article can be published. This transfer agreement enables Jordan Journal of Mechanical and Industrial Engineering to protect the copyrighted material for the authors, but does not relinquish the authors' proprietary rights. The copyright transfer covers the exclusive rights to reproduce and distribute the article, including reprints, photographic reproductions, microfilm or any other reproductions of similar nature and translations.

Proof Reading: One set of page proofs in MS Word 2010 format will be sent by e-mail to the corresponding author, to be checked for typesetting/editing. The corrections should be returned within **48 hours**. No changes in, or additions to, the accepted (and subsequently edited) manuscript will be allowed at this stage. Proofreading is solely the author's responsibility. Any queries should be answered in full. Please correct factual errors only, or errors introduced by typesetting. Please note that once your paper has been proofed we publish the identical paper online as in print.

Author Benefits:

No page charges: Publication in this journal is free of charge.

Free offprints: One journal issues of which the article appears will be supplied free of charge to the corresponding author and additional offprint for each co-author. Corresponding authors will be given the choice to buy extra offprints before printing of the article.

PAGES	PAPERS
257 - 264	Synthesis and Characterization of Aluminum Composites Materials Reinforced with TiC Nano- Particles. <i>Malek Ali, Samer Falih.</i>
265 – 274	The Effects of Content and Surface Modification of Filler on the Mechanical Properties of Selective Laser Sintered Polyamide12 Composites. <i>Alkhair A. Mousa</i>
275– 288	Dynamic Response of Beam with Multi-Attached Oscillators and Moving Mass: Fractional Calculus Approach. <i>Ibrahim M. Abu-Alshaikh, Anas N. Al-Rabadi, and Hashem S. Alkhaldi</i>
289– 296	Nonlinear Dynamic Modeling of Double Helical Gear System <i>Chang Qinglin, Hou Li , Sun Zhijun, Wang Wei, You Yunxia</i>
297 – 303	Automobile Longitudinal Axis Detection Method Based on Image Segmentation and Preliminary Results <i>Peijiang Chen and Yongjun Min .</i>
305 – 312	Performance Comparison of Adaptive Neural Networks and Adaptive Neuro-Fuzzy Inference System in Brain Cancer Classification <i>Bassam Al-Naami , Mohammed Abu Mallouh, Eman Abdel Hafez</i>
313 – 321	Fabrication and Characterization of Copper-Red Mud Particulate Composites Prepared by Powder Metallurgy Technique <i>N. Vijaya Sai</i>
323 – 331	Multi-Objective Optimization of Process Parameters for Electrochemical Machining of 6061Al/ 10%Wt Al₂O₃/ 5%Wt SiC Composite using Hybrid Fuzzy-Artificial Bee Colony Algorithm <i>Ayyappan Solaiyappan , Kalaimathi Mani , Venkatachalam Gopalan</i>
333 – 342	PSO-Based Neural Network Prediction and its Utilization in GMAW Process <i>Pathiyasseril Sreeraj, Thangavel Kannan, Subhasis Maji</i>

Synthesis and Characterization of Aluminum Composites Materials Reinforced with TiC Nano- Particles

Malek Ali ^{a *}, Samer Falih ^b

^aDepartment of Mechanical Engineering, Faculty of Engineering, University of Tabuk, Saudi Arabia.

^bSchool of Materials & Mineral Resources Engineering, USM, 14300 Penang, Malaysia.

Received 30 Jul 2014

Accepted 29 Sep 2014

Abstract

In this paper, aluminum matrix composites are successfully synthesized by reinforcing various TiC Nano-particles (273.196 nm, 194.732nm, and 149.071 nm). The green compacts of Al-TiC composites were sintered for 3 h at 500, 550, and 600°C. Hardness test and wear test were carried out on the Al-TiC composites. Powders of (Al, and TiC), and composites of (Al-TiC) were characterized using scanning electron microscopy, and X-ray diffraction techniques. Different weight ratios (5%wt, 15%wt, and 25%wt TiC) and different particles size of TiC were used to study the microstructure, and mechanical properties. The results obtained reveal that the densities of sintered composites show a marginal increase with the decrease in the particle size. Al-25wt % TiC composites (particle size 149.07 nm) with 600°C sintering temperature exhibited highest hardness (63.7 HV). Al-25wt % TiC composites with TiC particle size 273.196 nm exhibit the lowest wear rate (0.043 mm³/s).

© 2014 Jordan Journal of Mechanical and Industrial Engineering. All rights reserved

Keywords: : Aluminum Matrix, Composites, Various Average Particles, TiC.

1. Introduction

TiC reinforced Metal Matrix Composites (MMCs) are increasingly being used in the automobile, aircraft, cutting tools, and space industries. Worldwide attention has been focused on the processing and fabrication of MMCs because of both favourable manufacturing costs and performance [1]. MMCs offer outstanding properties such as high strength-to-weight ratio, high torsion stiffness, good corrosion resistance and versatility to the designer. Two major processing techniques that have been found suitable for these composites are powder metallurgy and solidification processing [2]. As investigated by Yang *et al.* [3], hard TiC particles help to improve the soft matrix in terms of hardness and wear resistance the improvement depends on the amount and uniformity of distribution of particles of TiC, and the strength of the particle-matrix boundary and the mechanical properties of the matrix. The Al-TiC composites occupy a unique position in the family of metal matrix composites due to their excellent wear/stiffness, strength-to-weight ratio with good mechanical properties. The most common applications of these composites are in commercial aerospace, space technology, automobile, general industrial and engineering structures. Typical examples are found in helicopter blade, automotive piston, engine block, cylinder liners,

motorcycle brake disk, and valve engines [4-7]. Powder metallurgy technique is a promising technique for fabricating the composites of Al reinforced with a hard ceramic phase. TiC particle-reinforced MMCs have been developed by many researchers because of the thermodynamically stability of TiC and the hardness and low density which it imparts to the composite [8, 9]. The Al-TiC composite system has been studied by a number of researchers and has been found to possess good strength and stiffness. It has been reported that the TiC reinforced Al matrix composites exhibit higher stiffness and ductility than TiB₂ reinforced composites. This may be attributed to the stronger interfacial bonding in the Al-TiC system due to the increased tendency for nucleation of solid on the particle surfaces [8-10]. Solay and Mohan studied the effect of varying weight percent of particulate TiC (ranges from 1% to 10%) reinforcement with elemental 6061 Aluminum alloy on mechanical properties (hardness and tensile strength) of specimens processed through powder metallurgy, compaction pressure from 125 MPa to 175 MPa, the density, hardness and tensile strength value increases[12]. Kennedy and Wyatt reported that the interfacial bond strength in Al-TiC MMCs varies significantly with manufacturing method (flux-assisted casting method, powder metallurgy followed by hot isostatic pressing (PM-HIP), extruding mixed powders at slow (PM-EXTS) and fast (PM-EXTF) ram speeds.

* Corresponding author. e-mail: mali@ut.edu.sa.

Conventional mechanical testing (elastic modulus, tensile, and extrusion) was performed on composite materials. Tong and Ghosh evaluated the room and elevated temperature mechanical behavior (tensile properties) of Al/TiC, high-strength Al-Si/TiC and the elevated temperature-resistant Al-Fe(-V-Si)/TiC composites [13]. Zhang *et al.* studied in situ process-Reaction synthesis used to fabricate Al/TiC composites, the phase constitute, microstructure and mechanical property of the Al/TiC composite [14]. Therefore, in the present paper, Al-TiC composites and examined the effects of sintering temperature, ratio and particles size of TiC on microstructure, density, hardness, and wear behaviour in detail.

2. Experimental Procedure

The aluminum powder used was of 99.9% purity (purchased from Fluka) and average particle size of less than 47.5 μm . Different average particle sizes (273.196 nm, 194.732 nm, 149.071 nm) of TiC (99.9% purity, purchased from Fluka) were prepared by ball milling. Mixtures Al powder with different average particle sizes and different compositions (5%, 15%, 25%wt TiC) were prepared. Mixtures were subjected to normal mixing for 2 h at the speed of 20 rpm then compacted into pellets by 750 MPa applied for 3 min. 0.5g of the powder mixture was pressed into 1 pellet in a steel mold of 10mm internal diameter. Zinc stearate was used as a mould wall lubricant. The green compacts of Al-TiC composites were sintered by tube furnace under protective argon gas atmosphere for 3 h at 500, 550, and 600°C. SEM technique was used for microstructure examination of the raw powders, and Al-TiC composites. The hardness test of the sample was done by using micro hardness Vickers, the micro-Vickers hardness was measured at 5 points from the along the surface of the samples. Dry sliding wear tests were performed by a pin-on-disc apparatus. Sliding velocity was 150 rpm with abrasive paper under a constant load. The abrasive paper was replaced with a new one after every test. Each test was repeated three times and the average value was taken.

2.1. Characterization

Aluminum and titanium carbide powders were used as a raw material. Morphology and physical characteristics of the powder were identified with scanning electron microscopy (SEM) and X-ray diffraction (XRD) techniques.

2.2. SEM Images Analyses

Morphology and microstructure of the initial (as received) powder particles used are given in Figures 1 (a) and (b).

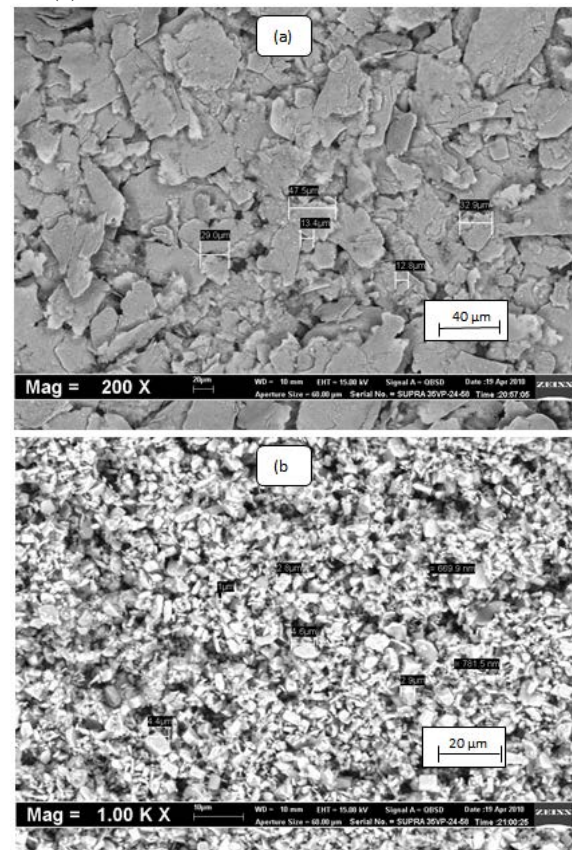


Figure 1. SEM images for (a) as received Al powder (b) received TiC powder

From SEM image in Figure 1, the size distribution of aluminium particles mostly lies in the range of 29.0-47.5 μm with some fine particles in the range of 12.8-13.4 μm . It also shows that the Al particle is in a flaky shape. The particle size distribution of as received TiC powder exhibits that most (~75%) of the particles are in the range of 781.5 nm to 2.9 μm . Some TiC particles are agglomerated due to their fineness and are in the range of 4.4 to 4.6 μm . The image shows that the TiC particle is in an angular shape with sharp edges. The titanium carbide powder was milled for different duration (5h, 10h, and 15h). SEM images of the TiC powders after different milling time (5, 10 and 15h) are shown in Figure 2. (a, b and c), respectively.

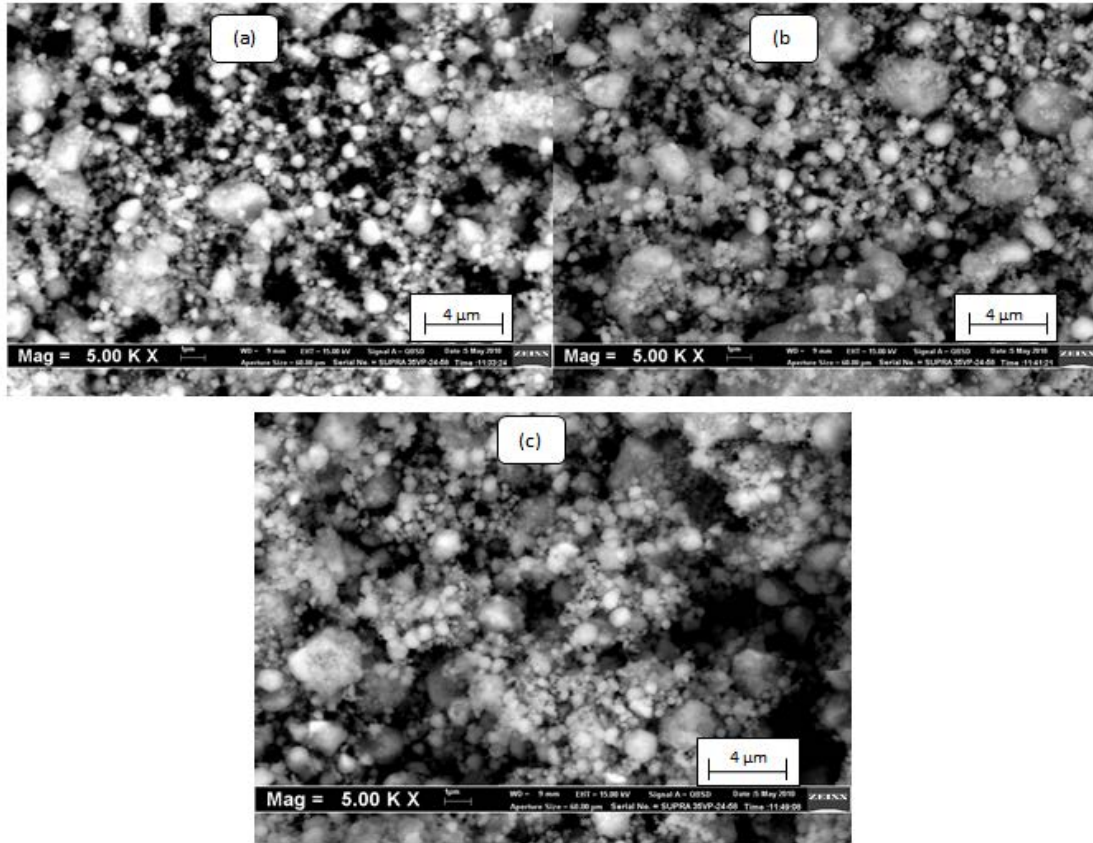


Figure 2. SEM images for TiC after milling for (a) 5 h, (b) 10 h and (c) 15 h

Figure 2 clearly reveals that large particles are in fact agglomerates of much smaller particles especially after 5 to 15 h milling time due to during the milling process; the particles are deformed, cold welded and fractured due to high energy collision [15]. Those events may change particle shape and also decrease particle size and form layered structure [16- 18]. In addition, the aluminum is generally a ductile material and it shows a highly non-linear stress-strain relationship up to the maximum strength with lower Young modulus.

3. Results and Discussion

3.1. X-Ray Diffraction and Rietveld Refinement Analyses

The aluminum and titanium carbide as received powders were characterized by X-ray diffraction. The identification of the phase of Al and TiC powders were

done through the matching of diffraction patterns of powders with the International Center for Diffraction Data (ICDD). In the XRD patterns of aluminum and titanium carbide clearly a few main peaks of these powders are visible, as shown in Figure 3(a) diffraction patterns relative to Al powder exhibited peaks at 38.5° , 45.8° , 65.1° , 68° and 82.5° corresponding, respectively to the (111), (200), (220), (311) and (222) reflections of F.C.C, and as shown in Figure 3(b) diffraction patterns relative to TiC powder exhibit peaks at 48.5° , 54.8° , 65° , 78.2° and 82.4° corresponding, respectively to the (111), (200), (220), (311) and (222). The peaks in these patterns gave a good match with the references patterns (ICDD No. 3828). Figures 3 (a) and (b) show the diffraction pattern of Al and TiC powders respectively. From Figures 3 (a) and (b), all the starting powders were pure and so no impurities in these starting powders were visible.

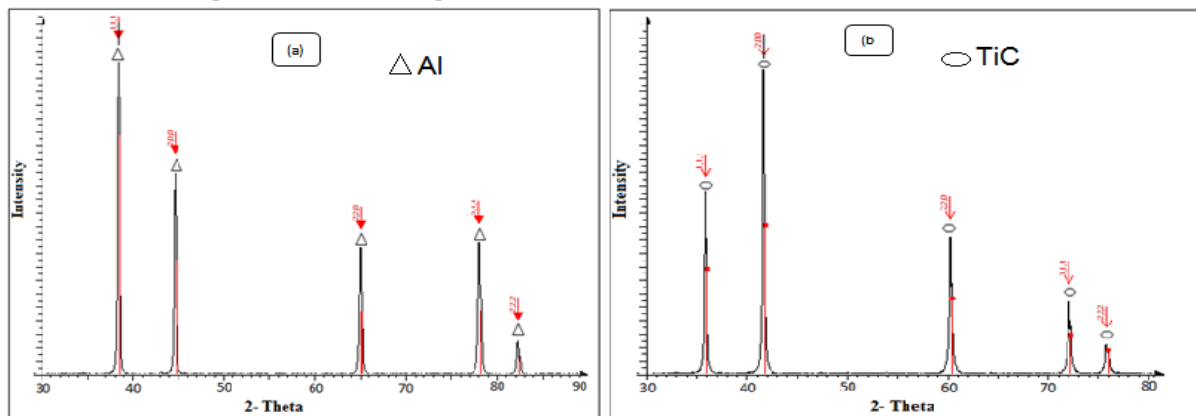


Figure 3. XRD pattern of as received (a) Al powder (b) TiC powder

The titanium carbide powder after milling for different duration (5h, 10h, and 15h) was characterized by XRD in order to study the effect of milling time on the particle size. The XRD patterns of TiC powder with different milling time are plotted in one graph, as shown in Figure 4.

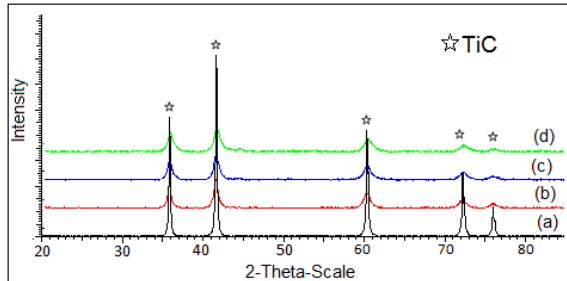


Figure 4. XRD patterns for TiC powder after milling for: (a) 0 h, (b) 5 h, (c) 10 h, and (d) 15 h

It is apparent that with increasing the milling time, the diffraction peaks for TiC powder become broader and their relative intensity decreases. During the milling process, particles underwent collision between balls and between balls to walls, so the particle size decreases for longer milling time. Average crystallite size for TiC before and

after milling for 5h, 10h and 15h were 47.3, 17.4, 15.8 and 12.4 nm, respectively and average particles sizes of TiC 273.196 nm, 194.732nm, and 149.071 nm. The crystallite size and average particles of TiC decreased with increasing milling time due to large and continuous number of dislocations resulting from heavy deformation caused by high energy mechanical milling. The average crystallite size of TiC was estimated by using the Scherrer formula, $D = k / B \cos \theta$, where D is the average crystallite size, k is the CuK α wave length, B is the diffraction peak width at half-maximum intensity and θ is the Bragg diffraction angle.

Basically, after the composites were sintered under argon atmosphere for 3 h, they were characterized with the X-ray diffraction technique. This process is to check the phases in the composition of the final product, as well as to check the stability of the raw materials used in the sample. This analysis was necessary in order to confirm that there was no formation of undesirable substance such as Al_4C_3 , Al_2O_3 , etc. The XRD patterns of Al based composites reinforced with 5, 15, and 25 wt% of TiC are shown in Figure 5 (a), (b), and (c), respectively.

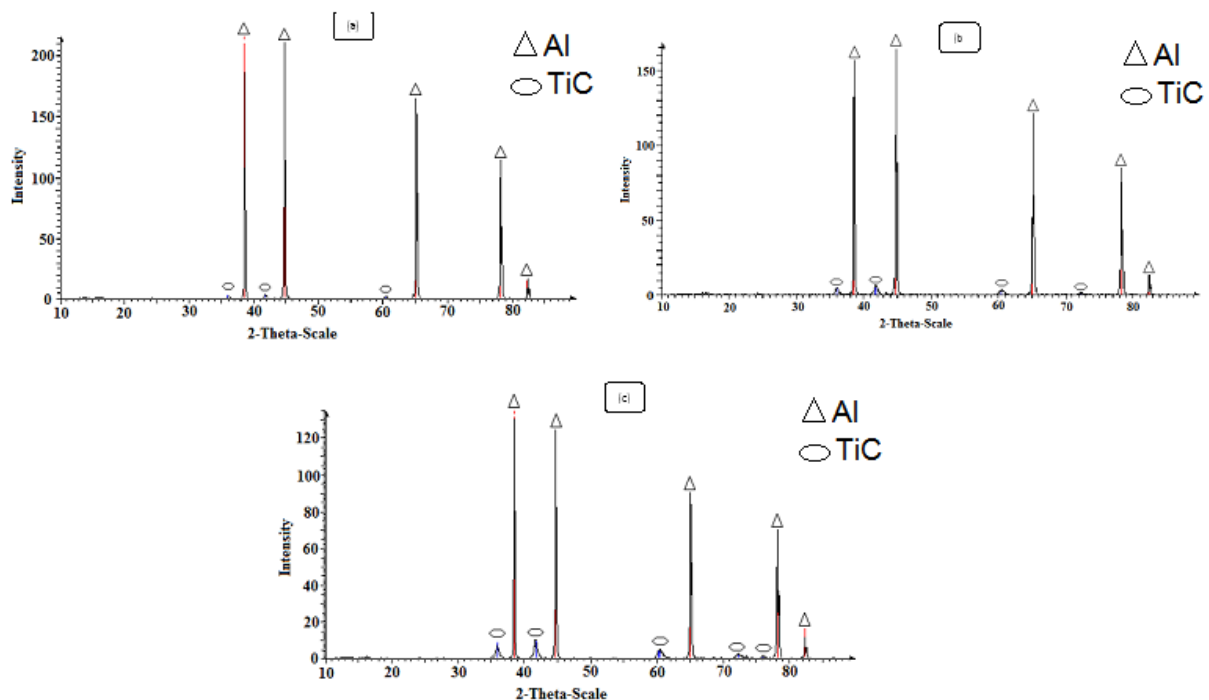


Figure 5. XRD patterns of (a) Al-5% wt TiC, (b) Al-10% wt TiC, (c) Al-25% wt TiC

Based on the XRD result, it is shown that the aluminum-titanium carbide powders do not have reaction with each other after sintering, and these two powders maintain their own intensities (no new phase formation). Furthermore, no peaks from the Al_4C_3 phase, which is often formed as an undesirable reaction product in Al-TiC composites, and no peaks from oxides, such as Al_2O_3 , could be seen. All the samples show the presence of TiC peaks along with Al peaks. It is clearly observed that the intensity of TiC peaks has increased with increase in TiC content from 5% to 25%.

3.2. SEM Images Analyses

The distribution of the reinforcement (TiC) particles in the aluminum matrix has been observed by scanning electron microscopy (SEM). Figure 6 (a), (b), and (c) show the SEM micrograph of aluminum composites reinforced with 5, 15, and 25 wt% of TiC with particle size 149.071 nm.

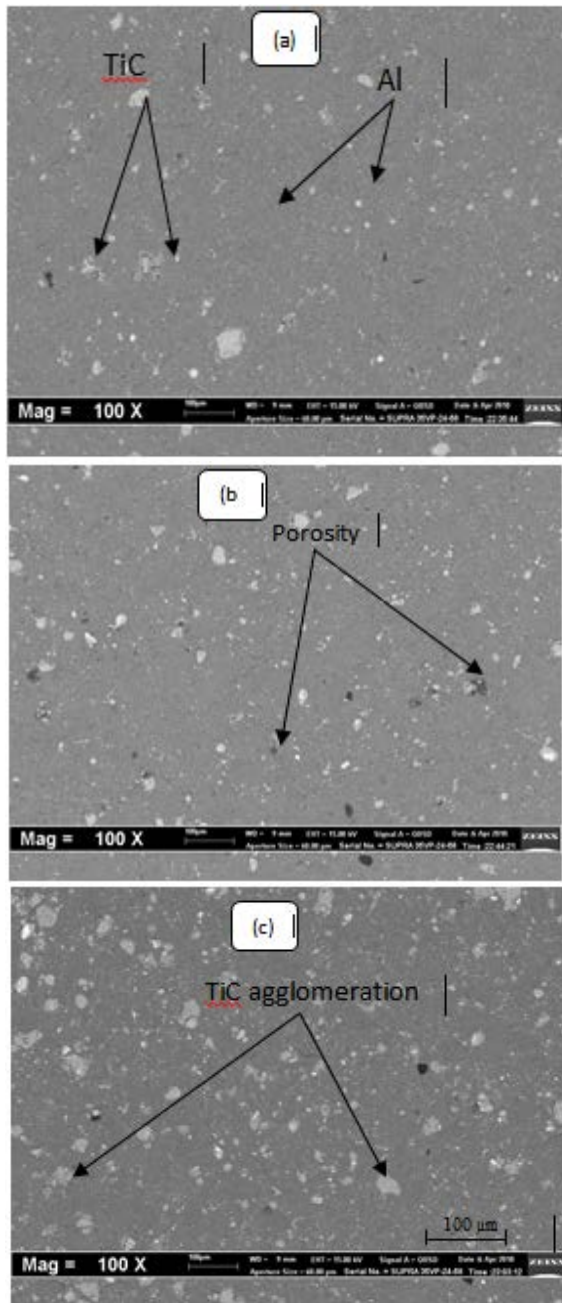


Figure 6. SEM images of the composites after 600°C sintering temperature (a) Al-5% wt TiC, (b) Al-15% wt TiC, and (c) Al-25% wt TiC

As shown in Figure 6, the small particles are distributed homogeneously between the big particle (agglomeration of many small particles together) and the particle size of the small particles is uniform. However, some pores can be observed. The formation of pores is mainly due to the non-uniformity of the initial powder particles. Also, it is clear from Figures 6 (a, b and c) that the reinforcement particles of the composites are embedded in the aluminum matrix. A small agglomeration of TiC particles in the aluminum matrix has been noticed and this is mainly due to non-homogeneity involved in the mixing and blending process carried out before sintering. The microstructure evaluation also shows that, for a given series of composites, the size of the TiC particles in the composites increases as the TiC content increases.

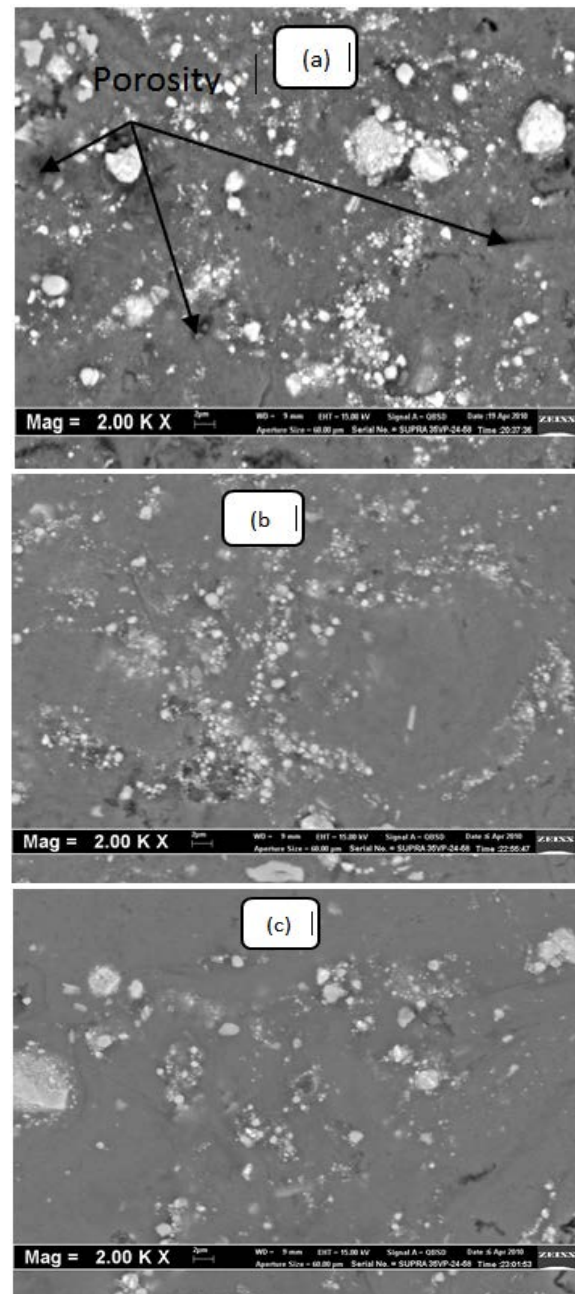


Figure 7. SEM images of the Al-25wt% TiC composite at different sintering temperatures

Figure 7 shows the SEM images of aluminum matrix composite reinforced with 25wt. % of TiC (particle size 149.071 nm) at different sintering temperatures.

From Figures 7 (a, b, and c), it is observed that the sintered surfaces were porous and the composite has small grains of TiC when it is sintered at 500°C. With the increase in sintering temperature, the number of pores decreased and the rate of grain growth apparently increased. Moreover, significant grain growth was observed and the pores were almost eliminated at 550°C. Also the microstructural study revealed that TiC clusters and TiC-free regions were formed after consolidation at the high sintering temperature (600°C). It seems that the aluminum matrix was locally moved during the consolidation to fill the voids (Kamrani *et al.*). Kamrani *et al.* suggested that the diffusion of the matrix into the interparticle pores is responsible for this observation.

Similarly, it is suggestible that the high diffusivity of the aluminum matrix close to the melting point caused inter-particle pore diffusion, causing the TiC clusters and TiC-free areas [19].

3.3. Effect the Particle Size of TiC on Density, Hardness, and Wear

The average particle size of TiC with different milling time was estimated by using the following formulas [20, 21]:

$$\text{Particle size} = \frac{6}{\text{Density} \times S.S.A}$$

Average particle size = \sum Particle size / Number of calculation for Particles size

The effect of the particle size on the density of the Al-25wt.% TiC composite is shown in the Figure 8.

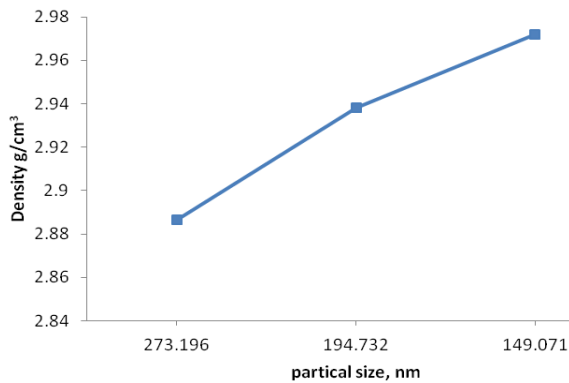


Figure 8. Effect of particle size of TiC on the density of Al-25wt.% TiC composites

The density of Al-TiC composites was determined according to Archimedes' principle.

The result indicates that the density of Al-TiC composites which were reinforced with TiC (149.071 nm) achieves the highest value of density. Meanwhile, composites, which were reinforced with TiC (273.196 nm), have the lowest density. The results obtained reveal that the densities of sintered composites show a marginal increase with the decrease in the particle size. On the other hand, the coarser particles lead to bigger voids which decreasing the density [20]. The volume of voids is affected by the relative particle size and weight fraction of TiC. The size of TiC particle was found to have influence in determining the hardness of the composites. The smaller the reinforcement particle size, the higher the hardness would be. Figure 9 illustrates the relationship between hardness and particle size.

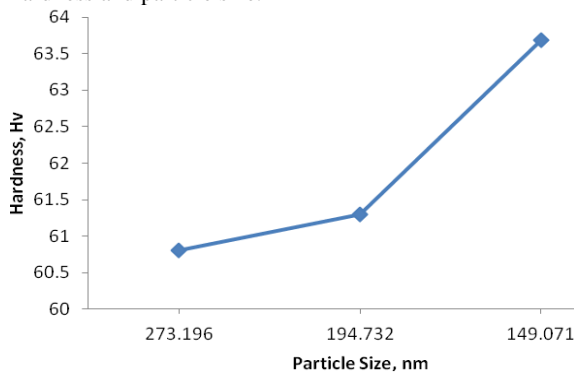


Figure 9. Effect of particle size of TiC on the hardness of Al-25wt.% TiC composites

The result indicates that the hardness increases with decreasing the particle size. At 15 h of milling time (149.071 nm), the microhardness achieves the highest value of 63.7 HV. Meanwhile, composites which were reinforced with TiC milled for 5 h (273.196 nm) have the lowest hardness value of 60.8 HV. Small reinforcement particles permit larger contact area with aluminum particles. On the other hand, large reinforcement particles have small area of contact and prevent the diffusion process from progressing [23]. The TiC particles act as barriers to dislocation flow in aluminum matrix. Composites reinforced with smaller TiC particles have a higher number of barrier per unit area compared to composites reinforced with larger particles at the same weight percentage [22, 24]. The particle size of the reinforcement is one of the intrinsic factors that could have an effect on the wear resistance besides other mechanical properties of particulate reinforced AMCs. Figure 10 shows the effect of particle size of TiC on the wear rate.

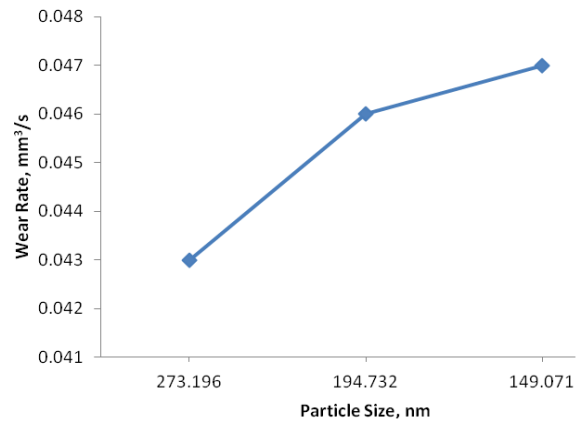


Figure 10. Effect of particle size of TiC on the wear rate of Al-25wt.% TiC

The wear resistance of metal matrix composites is known for improving considerably with increasing the size of reinforcing particles. Figure 10 shows that the composites with 5 h milling (particle size 273.196 nm) exhibit the lowest wear rate (0.043 mm³/s). Meanwhile, composites which were reinforced with TiC milled for 15 h (particle size 149.071 nm) have the highest wear rate value (0.046 mm³/s). During the friction process bigger TiC particles on the friction surface are impressed deeper to the tested surface and are not easily releasable from the surface, and simultaneously they reinforce the composite surface. On the other hand, smaller TiC particles on the friction surface are easily released from the surface of composite and become constituent of mobile friction layer, which abrade the friction surface of tested samples. This result is in agreement with those reported earlier [25]. The larger size of reinforcing particles can offer protection to the matrix during sliding. Once the reinforcing particles fracture or loosen from the matrix, they can be removed easily from the matrix, resulting in a certain amount of material loss. In order to investigate the wear mechanism, the surfaces of the worn composites were examined under SEM. Figures 11 (a- c) show typical worn surfaces of the Al-5, 15, and 25 wt.% TiC composites, respectively. The worn surface of the composites (Figures 11 (a- c)) shows a small plough groove and a little dimple. The abraded surfaces of the composites also show scratches on the

worn surface, and there is little evidence of particulate fracture, even in composites with the highest weight fraction. The reason for this is explained as follows: when the surface of the composite initially comes in contact with abrasive paper, adhesive contact occurs; the TiC abrasive particles with sharp edges then cause microploughing and grooving in the surface of aluminum matrix; therefore, materials, in the form of chips, are removed from the grooves, thereby exposing TiC particles; thus, the increase in the weight fraction of TiC particles appears to reduce the severity of grooving and plastic deformation; this is because the hard particulate phase is well bonded by Al-based matrix and strong enough to withstand abrasive wear induced by the counter wear ring at applied load [4, 24].

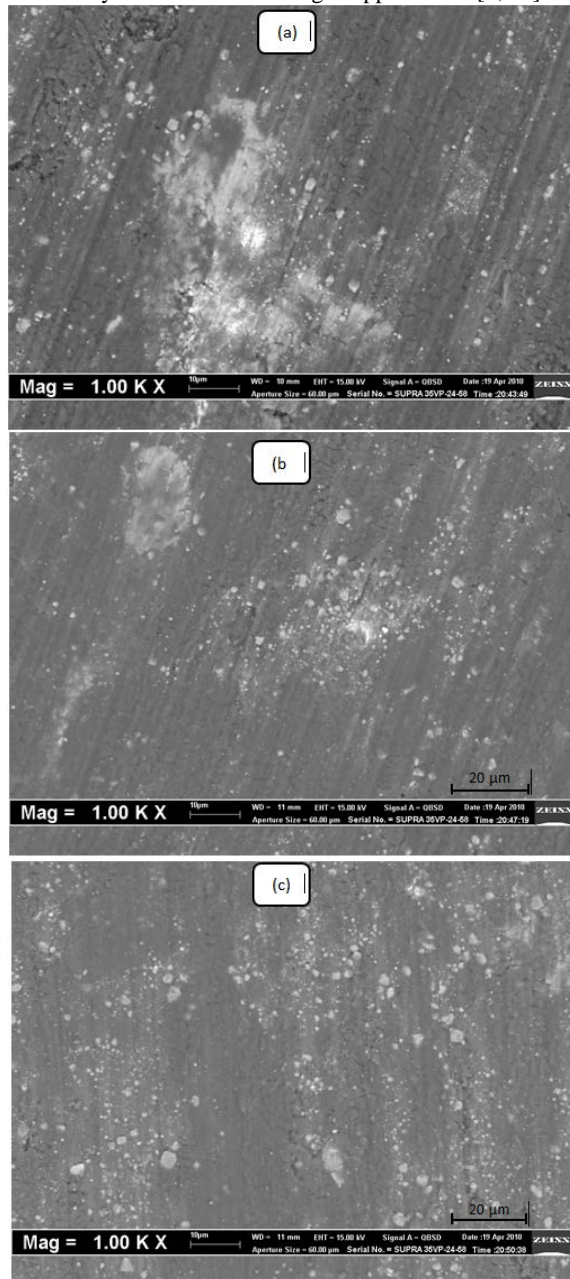


Figure 11. SEM images show worn surface of Al-TiC, (a) Al-5wt% TiC, (b) Al-15wt% TiC, (c) Al-25wt% TiC

4. Conclusions

In summary, we have obtained the Al-TiC composites by various average particles sizes of TiC Nano-particles, different weight ratios of TiC, and different sintering temperature. In general, the aluminum is ductile material and shows a highly non-linear stress-strain relationship up to the maximum strength with lower Young modulus. The crystallite size and average particles of TiC decreased with increasing milling time due to large numbers of dislocations resulting from heavy deformation caused by high energy mechanical milling. The coarser reinforcement particles, bigger voids formed leading to a lower density. Composites reinforced with smaller TiC particles have higher number of barrier per unit area compared to composites reinforced with larger particles at the same weight percentage. With the increase in sintering temperature, the number of pores decreased and the rate of grain growth apparently increased. The results obtained reveal that the densities of sintered composites increase with the decrease in the particle size. Al-25wt. % TiC composites (particle size of TiC =149.07 nm) with 600°C sintering temperature exhibited highest hardness (63.7 HV). Al-25wt. % TiC composites with 273.196 nm TiC particle size exhibit the lowest wear rate (0.043 mm³/s).

Acknowledgement

The authors would like to acknowledge the financial support this work received from the Deanship of Scientific Research (DSR), University of Tabuk, Tabuk, Saudi Arabia, under grant No. S-1435-0018.

References

- [1] K. Ramesh and R. Sagar, "Fabrication of Metal Matrix Composite Automotive Parts". *Journal of Advanced Manufacturing Technology*, Vol. 15 (1999) 114-118.
- [2] R. S. Rana, R. Purohit and S. Das, "Review of recent Studies in Al matrix composites". *International Journal of Scientific & Engineering Research*, Vol. 3 (2012) 1-15.
- [3] Q. Yang, T. Senda, and A. Ohmori, "Effect of Carbide Grain Size on Microstructure and Sliding Wear Behavior of HVOF-sprayed WC-12% Co Coatings". *Wear*, Vol. 254, (2003), 23-34.
- [4] R. J. Mustafa, "Abrasive Wear of Continuous Fibre Reinforced Al And Al-Alloy Metal Matrix Composites". *Jordan Journal of Mechanical and Industrial Engineering*, Vol. 4 (2010) No. 2, 246 - 255.
- [5] W. Khraisat and W. Abu Jadayil, "Strengthening Aluminum Scrap by Alloying with Iron", *Jordan Journal of Mechanical and Industrial Engineering*, Vol. 4 (2010) No. 3, 372 - 377.
- [6] T. Nukami, "The Growth of TiC Particles in an Al Matrix", *Journal of Materials Science Letters*, Vol. 17 (1998) 267-269.
- [7] A. Karantzalis, A. Lekatou, E. Georgatis, V. Poulas, and H. Mavros, "Microstructural Observations in a Cast Al-Si-Cu/TiC Composite", *Journal of Materials Engineering and Performance* Vol. 10 (2009) 1-16.
- [8] Humphreys F., A. Basu, and M. Djazeb, "The Microstructure and Strength of Particulate Metal Matrix Composites", *Proceeding on the 12th Riso International Symposium on Material Science*, 1991, 51-66.
- [9] A. Kennedy. and A. Karantzie, "The Incorporation of Ceramic Particles in Molten Al and the Relationship to

- Contact Angle Data", *Material Science and Engineering A*, 264, (1999), 122-129.
- [10] A. Kennedy and S. Wyatt, "Characterizing Particle-Matrix Interfacial Bonding in Particulate Al-TiC MMCs Produced by Different Methods Composite Part A", *Applied Science and Manufacturing*, Vol. 32 (2001), (3-4), 555-559.
- [11] A. Albiter, A. Contreras, E. Bedolla, and R. Perez, "Structural and Chemical Characterization of Precipitates in Al-2024/TiC Composites Composite Part A", *Applied Science and Manufacturing*, Vol. 34 (2003) No. 1, 17-24.
- [12] S. Solay and B. Mohan, "Enhanced Hardness Property in the Development of Al-TiC Composites through P/M Techniques", *Advanced Materials Research*, Vol. 548 (2012), 243- 249.
- [13] X. Tong, and A. Ghosh, Fabrication of in Situ TiC Reinforced Aluminum Matrix Composites, *Journal of Materials Science* Vol. 36 (2001) No. 16, 4059-4069.
- [14] E. Zhang, X. Zeng, and S. Zeng, Li Qingchun, Microstructure and Property of Al/TiC Composites Prepared by Reaction Synthesis, *Transactions of Nonferrous Metal Society of China* Vol. 16 (1996) No. 1, 114-119.
- [15] A. Canakci, T. Varol, and C. Nazik, Effects of amount of methanol on characteristics of mechanically alloyed Al-Al₂O₃ composite powders". *Materials Technology* Vol. 27(2012) NO 4, 320-327.
- [16] C. Suryanarayana, "Mechanical Alloying and Milling". *Progress in Materials Science*, Vol. 46 (2001) No. 1-2, 1-184.
- [17] L. Dong-hua, L. Yong, Z. Da-peng, and W. Yan, "Effect of Ball Milling Time on Microstructures and Mechanical Properties of Mechanically-Alloyed Iron-Based Materials". *Transactions of Nonferrous Metal Society of China* Vol. 20 (2010) No. 5, 831-838.
- [18] J. Lee, S. Ko, and C. Won, "Sintering Behavior of Al₂O₃-TiC Composite Powder Prepared by SHS Process". *Materials Research Bulletin*, Vol. 36 (2001) 989-996.
- [19] S. Kamrani, R. Riede, S. Reihani, and A. Kleebe, "Effect of Reinforcement Volume Fraction on the Mechanical Properties of Al-SiC Nanocomposites Produced by Mechanical Alloying and Consolidation". *Journal of Composite Materials*, Vol. 44 (2009) 1-14.
- [20] L. Kong, J. Ma, W. Zhu, and O. Tan, "Phase Formation and Thermal Stability of (Zr_{1-x}-Ti_x) O₂ Solid Solution Via a High-Energy Ball Milling Process". *Journal of Alloys and Compounds*, Vol. 335(2002) 290-296.
- [21] A. Godymchuk, E. Arzamastseva, D. Kuznetsov, and S. Milyaeva, "Dispersion of ZrO₂ and Y₂O₃ Nanopowders in Physiological Suspensions". *Journal of Physics* Vol. 304 (2011) No. 1, 12-43.
- [22] K. Ahmad, S. Jamaludin, L. Hussain, and Z. Ahmad, "The Influence of Alumina Particle Size on Sintered Density and Hardness of Discontinuous Reinforced Aluminum Metal Matrix Composite". *Universiti Teknologi Malaysia Institutional Repository*, Vol. 42 (2005) 49-57.
- [23] K. Al-Rubaie, "Abrasive Wear of Al-SiC Composites". *Materialwissenschaft und Werkstofftechnik*, Vol. 31(2000) No. 4, 300-311.
- [24] J. Shamsul, A. Ashiqin, S. Rizam, M. Fitri, and K. Azmi, "The Effect of Milling Time on Microstructure and Hardness of the Aluminum Silicon Carbide (Al-10 wt % SiCp) Composite, ICOSM, 205-207 (2007).
- [25] S. Tjong and K. Lau, "Tribological Behaviour of SiC Particle-Reinforced Copper Matrix Composites". *Materials Letters*, Vol. 43 (2000) No 5-6, 274-280.

The Effects of Content and Surface Modification of Filler on the Mechanical Properties of Selective Laser Sintered Polyamide12 Composites

Alkhair A. Mousa *

Technology Collage of Engineering, Department of Mechanical Engineering, Houn-Libya

Received 3 Sep 2014

Accepted 25 Oct 2014

Abstract

In selective laser sintering, the mechanical properties of the sintered part are largely influenced by many factors such as powder material, processing parameters, fabrication position and orientation. The present paper investigates the influence of content and surface modification of glass beads on the mechanical properties. The aim is particularly to better understand the effect of coupling agents on the mechanical properties of laser sintered parts. The specific material of interest is Polyamide 12 filled with two types of A-glass beads. The production of test specimens is carried out on a DTM Sinterstation 2000 Machine. Quasi-static mechanical tests are used to examine the mechanical properties of selective laser sintered specimens. The results show that adding glass beads (coated/ un-coated) to Polyamide 12 improves the tensile strength and elastic modulus but reduces the impact strength and ductility of the sintered parts.

© 2014 Jordan Journal of Mechanical and Industrial Engineering. All rights reserved

Keywords: : *Selective Laser Sintering, Polyamide 12, Coupling Agents, Glass Beads.*

1. Introduction

Although the use of fillers in plastics industry has been known for several decades, there is still an enormous interest in all the fields of the development of composite materials with enhanced properties. Mineral fillers are added to the polymers in commercial production primarily for reasons related to cost reduction and properties improvement. Improving the existing materials and developing new materials for use in Selective Laser Sintering (SLS) are continually being pursued in the industrial and academic domains [1].

The use of polymeric materials in the SLS process offers some advantages over metallic and ceramic materials, which are related to the low processing temperature, melting flow control and high corrosion resistance. However, the variety of commercial polymeric materials available for SLS process is restricted, and this reduces the options available during material selection for manufacturing particular parts. The use of available non-commercially polymers and mixtures of polymers can increase the range of properties of SLS parts [2].

Thermoplastics, such as polycarbonate and polyamide, have been developed as SLS materials for different applications. However, these materials cannot completely meet the needs of different functional end use parts. In recent years, the modification and improvement of

physical properties of pure polyamide by adding inorganic fillers (such as clays, talc, silica, glass bead, wollastonite and kaolin, etc.) have received close attention.

Glass beads-filled polyamide composites have become attractive due to their low cost and widespread applications in automobile, aerospace and electrical industries. The modification of the surface of glass beads is essential to improving surface wetting and adhesion between the filler and matrix. This may be improved by chemically incorporating specific interaction sites onto the glass beads surface or coating it with reactive surfactants or coupling agents [3].

In this study, glass beads (GB), by weight ratios wt%, were added to Polyamide12 (PA 12, PA2200). The influence of the addition of glass beads on the mechanical properties of the specimens produced under predetermined processing parameters was examined.

2. Previous work on the relationship between part properties, fillers and process parameters in SLS

Numerous attempts have been made to study the effect of powder material and process parameters on mechanical properties of SLS parts. The influence of fabrication parameters on the properties of SLS parts has been investigated by Gibson and Shi [4] who showed that the mechanical properties vary when different powders are used if similar process parameters are selected. They

* Corresponding author. e-mail: alkhair_brno@yahoo.com.

concluded that, besides powder material properties, fabrication parameters, orientation and building position also influence the mechanical properties. Wong *et al.* [5] studied the SLS of blended powder from PA12 and organically modified rectorite (OREC). Compared with pure PA12, the results of this investigation showed that the laser power needed for sintering greatly decreased and the mechanical properties of the sintered samples considerably improved with the addition of OREC (0-5 wt%). Experimental investigations into the production of particulate silicon carbide (SiC) polyamide matrix composites using the selective laser sintering process have been conducted by Gill *et al.* [6]. Their investigation revealed that the optimum energy density for producing samples of maximum strength was independent of the initial powder blend composition. For SLS applications, Mozzoli *et al.* [7] developed and characterized a new aluminium-filled polyamide powder from a rheological perspective. They reported that the new material allowed SLS manufacturing of models with considerably high dimensional accuracy, strength and resistance to mechanical stresses. A study of mechanical anisotropy due to build orientation and the end-of-vector effects in the laser sintering process was presented by Ajoku *et al.* [8]. The results of the tests showed that the build orientation of the samples had an effect on the mechanical properties obtained. They concluded that the orientation of a part in the laser sintering machine is the primary variable which affects its mechanical properties and the end-of-vector effect is a secondary factor, which is more prominent in parts with small x dimensions. A paper investigating the mechanical properties of parts produced via SLS has been published by Caulfield *et al.* [9]. They investigated the influence of several process parameters on the physical and mechanical properties of polyamide 12 parts. They generally showed that the mechanical properties of parts are highly dependent on process parameters and part orientations. Experimental investigations have been made by Jain *et al.* [10] to understand the effect of the delay time on part strength in selective laser sintering. They successfully developed an algorithm and implemented it to predict part orientation for the improved part strength by considering delay time. They concluded that comparatively higher strength can be achieved by orienting the part so that the maximum area on all layers falls within the optimum delay time range. Another experimental investigation was carried out by Jain *et al.* [11] to study the feasibility of processing blended powder of polyamide (PA) and organically modified nanoclay using SLS process. The authors found that the addition of clay did not improve the mechanical properties of the laser sintered polyamide; rather, it resulted in decreased mechanical properties. Goodridge *et al.* [12] have presented initial research into the reinforcement of laser sintered polyamides with carbon nanofibres (CNF). They investigated the effects of CNF addition on the processing parameters and mechanical properties of laser sintered parts and demonstrated that CNF can increase the strength of a base polyamide 12 laser sintering polymer prepared using a melt-mixing technique. They reached the conclusion that the nanofibres were well-dispersed within the polymer matrix and increased the storage modulus compared to the base material. Improvements to the

production of the nanocomposite starting powder were required to use these materials effectively with laser sintering.

However, none of the abovementioned studies considered the mechanical properties of laser sintered PA 12 parts by investigating the relationship between surface pre-treated filler and, in particular, the effect of coupling agents on the mechanical properties of selective laser sintered glass bead-filled polyamide 12 composites. Currently, to the best of our knowledge, no such studies have been conducted on PA 12/GB composites processed using the SLS technique. The present paper is the first attempt to address this issue by experimentally analyzing the influence of coupling agents on the mechanical properties of sintered components in polyamide 12 composites.

3. Coupling Agents

The adhesion between polymeric materials and particulate fillers is usually weak due to the poor compatibility of the polymer with the mineral surface. To improve the compatibility, adhesion promoters are commonly required. The most widely used of these are the silane coupling agents with the general structure $(RO)_3SiY$, where RO is an alkoxy group and Y is an organo-functional group [13], as shown in Figure 1:

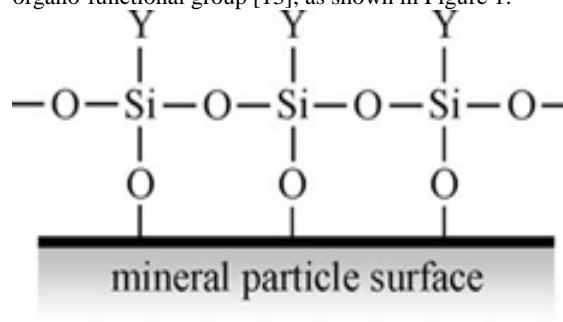


Figure 1. Idealistic view of a silane-treated surface [13]

Silane is a molecule containing a central silicon atom bonded to two types of groups: Alkoxy groups and organo-functional groups. These two types exhibit different reactivity and allow sequential reactions. In the crosslinking process, the first step is generally the grafting of the silane the polymer backbone via condensation of silanols. Silane coupling agent will act in this case as a link between an inorganic substrate and an organic material to bond, or couple, the two dissimilar materials together. Figure 2 shows a simplified picture of the coupling mechanism [14]:

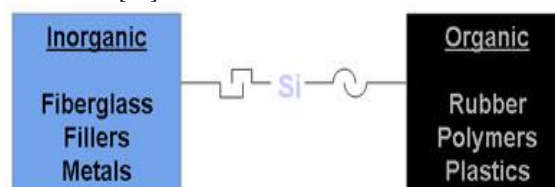


Figure 2. Silane coupling mechanism [14]

The main role of the coupling agents is to promote adhesion which will result in developing the mechanical properties, such as tensile and flexural strength, fracture toughness, tensile modulus, etc. [15].

4. Experimental Procedures

4.1. Materials and Processing

Polyamide 12 powder, used in this study, was a commercial fine polyamide (PA 2200) supplied by EOS GmbH with average grain size of 60 μm . The density, according to DIN EN ISO 60 (2000-01) was 0.435 to 0.445 $\text{g}\cdot\text{cm}^{-3}$.

Two A-glass beads (Spheriglass: 3000CP00 no surface modification and 3000CP03 surface modified with a silane coupling agents) with mean diameter of 35 μm were selected as filler, Figure (3). The glass beads, small solid spherical particles with a density of 2.5 $\text{g}\cdot\text{cm}^{-3}$, were supplied by Potters Industrial Inc/Omya UK Ltd.

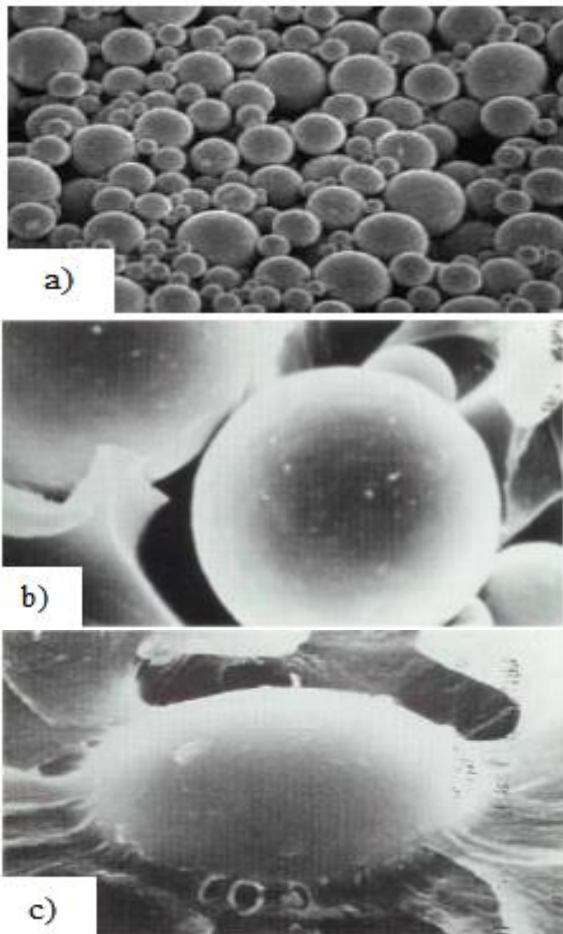


Figure 3. Spheriglass, A Glass: a) Solid Glass Spheres; b) Uncoated; c) with coating [16]

4.2. Specimens Preparation

In specimens preparation process, pure PA12 was compounded with (GB) with 10, 20, 30 and 40wt% ratios, using a rotating drum mixer (type BS125) for 30 min to produce the composites.

Selective laser sintering process was performed, under predetermined processing parameters, using a SLS machine to manufacture the specimens of PA12/GB composites with: fill laser power of 10W; laser beam speed of 914mm/s; scan spacing of 0.15mm; layer thickness of 0.10mm; beam diameter of 0.40mm and

powder bed temperature of 176 $^{\circ}\text{C}$. The energy density, regarded as the relative applied laser energy per unit area, can be calculated as follows [9]:

$$ED = \frac{LP}{BS \times SCSP} \quad (1)$$

Therefore, the corresponding laser energy density is 0.073 J/mm^2 . Table 1 summarises the optimum process parameters used in manufacturing of test specimens from the PA12/GB composites.

Table 1. Optimized processing parameters used in manufacturing of test specimens

PA12/GB [wt/wt%]	90/10	80/20	70/30	60/40
Laser power; LP [W]	10			
Energy density; ED [J/mm^2]	0.073			
Beam Speed; BS [mm/s]	914			
Powder bed temperature; T_b [$^{\circ}\text{C}$]	176			
Scan Spacing; SCSP [mm]	0.15			

4.3. Equipment and Methodology

In the testing step, the tensile, flexural and Izod impact specimens according to BS EN ISO 527, 178 and 180/1A standards were produced using SLS machine. In order to maintain consistency in this study, all specimens were built flat, laid parallel to the direction of the movement of the roller, and at fixed places in the middle of the build area as shown in Figure 4.

The tensile, flexural and fracture toughness tests were carried out using Testometric materials testing machine. The impact test was carried out at room temperature using pendulum impact test machine type W&T AVERY LTD.

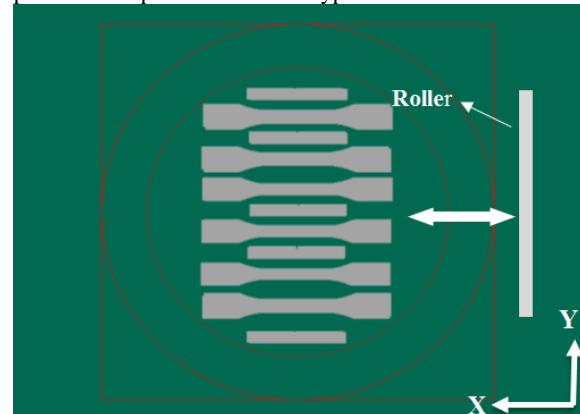


Figure 4. Orientation of the specimens in the build platform (Top view)

The tensile strength, elastic modulus, elongation at break, impact strength, flexural strength and fracture toughness were recorded and obtained. For the morphological observations a Scanning Electron Microscope (SEM) type (ZEISS XB 1540 workstation) was used to observe the morphology of scan surfaces and the fracture cross-section of tensile bars.

5. Results and Discussion

5.1. Density Measurements of Sintered Density Specimens

The density of selective laser sintered components has an important influence on the mechanical properties and a nearly full relative density is one of the most important properties required for functional parts. Therefore, the density prediction of SLS parts provides suitable guidelines in the selection of appropriate process parameters as seen in Figure 5.

The density of the sintered specimens from the PA12/GB composites was predicted by building density specimens. These density specimens were small square prisms with the intended dimensions of 20mm x 20mm x 5mm. Once the density specimens were built, their dimensions were determined manually by measuring with a digital caliper and they were weighed. The average density of the sintered specimens was 0.92 g/cm³ obtained from six measurements as shown in Table 2.

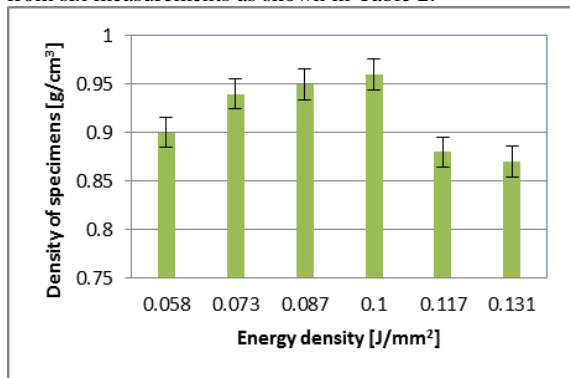


Figure 5. Influence of energy density on the density of sintered density specimens

Table 2. Measured data of the sintered density specimens

Energy density [J/mm ²]	<i>l</i> [mm]	<i>w</i> [mm]	<i>h</i> [mm]	<i>m</i> [g]	<i>V</i> [mm ³]	<i>P</i> [g/cm ³]
0.058	20.64	20.64	5.74	2.2	2445.3	0.90
0.073	20.46	20.46	5.56	2.2	2327.5	0.94
0.087	20.24	20.24	5.40	2.1	2212.1	0.95
0.100	20.04	20.04	5.17	2.0	2076.3	0.96
0.117	20.40	20.40	5.48	2.0	2280.5	0.88
0.131	20.43	20.43	5.75	2.1	2400.0	0.87

5.2. Dimensional Measurement of Sintered Test Specimens

The dimensions of the sintered specimens in PA12/GB composites were measured using a digital vernier caliper and listed in Table 3. It is shown that the specimens have a good dimensional accuracy and there were no obvious differences between both systems.

As depicted in Figure 6, the average values were within the intended dimensions. However, it is not difficult to conclude that the dimensional accuracy is material- and machine-dependent; also it is well known that the isotropic behaviour of glass spheres provides uniform shrinkage which is an important factor in the reduction of the dimensional inaccuracy.

Table 3. Measured dimensions of sintered tensile test specimens (PA12/CP03 system)

Energy density [J/mm ²]	0.073				
PA12/CP03 [w%/wt%]	100/0	90/10	80/20	70/30	60/40
Thickness of specimen [mm]	3.990	3.978	3.864	3.934	3.872
Width of specimen [mm]	10.011	10.052	10.352	10.168	10.331
Length of specimen [mm]	150.015	149.754	150.206	150.112	150.177
Average cross-sectional area [mm ²]	39.944	39.987	40.000	40.000	40.002

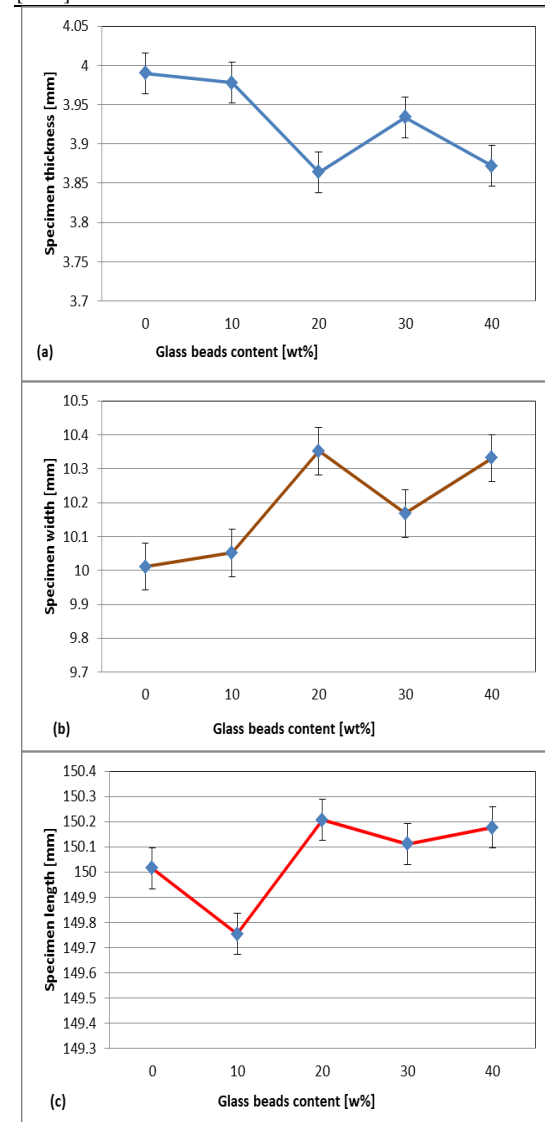


Figure 6. Variation of specimen dimensions with filler ratio: (a) thickness; (b) width; (c) length

5.3. Mechanical Properties

The mechanical properties of the composites (PA12/CP00 and PA12/CP03 systems) were investigated as a function of content and surface modification of glass beads using selective laser sintered test specimens. Optimized process parameters and scale factors for compensation of the shrinkage were applied to all fabricated test specimens.

Tensile Strength

The tensile specimens had a nominal thickness of 4mm, width of 10mm and other dimensions were determined with reference to BS EN ISO 527-2 Type 1A, shown in Figure 7. The as-sintered specimens were tested under ambient conditions and at a crosshead speed of 5 mm/min.

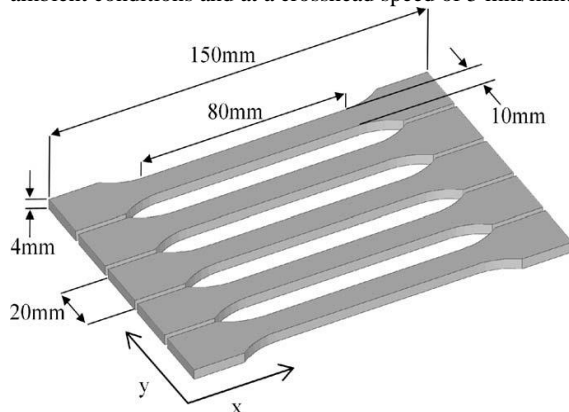


Figure 7. Shape and dimensions of the tensile test specimens

The value of average tensile strength was obtained from six tests. Figure 8 displays the variation of tensile strength of the PA12 composite with glass beads content for both systems.

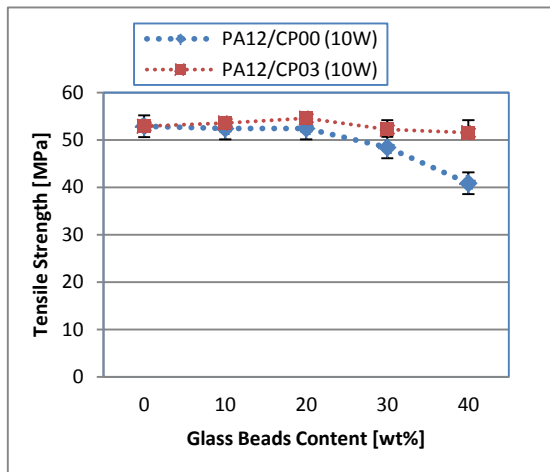


Figure 8. Variation in tensile strength of the composites.

Initially, it is clear that the tensile strength increases with the increase in the glass beads ratio, namely: from 53 MPa at 10 wt% to 55 MPa at 20 wt%. Above 20 wt% the addition of increasing amounts of glass beads led to decrease in the tensile strength. The reduction in the strength may be attributed to the reduction in the adhesion strength between the matrix (PA12) and the aggregate (glass beads) due to less polyamide and increasing structural microporosity. Compared to PA12/CP00 system, the better interfacial adhesion gives higher composite

strength in case of surface modified glass beads, PA12/CP03 system.

Elastic Modulus

Modulus of elasticity is the stiffness of material at the elastic stage of tensile test. It markedly improved by adding rigid particles to the polymer matrix since the rigidity of inorganic fillers is generally higher than that of the polymers.

From Figure 9, it can be seen that increasing the ratio of glass beads from 10 to 40 wt% led to a remarkable increase in the elastic modulus from approximately 1974.4 to 3399.6 MPa.

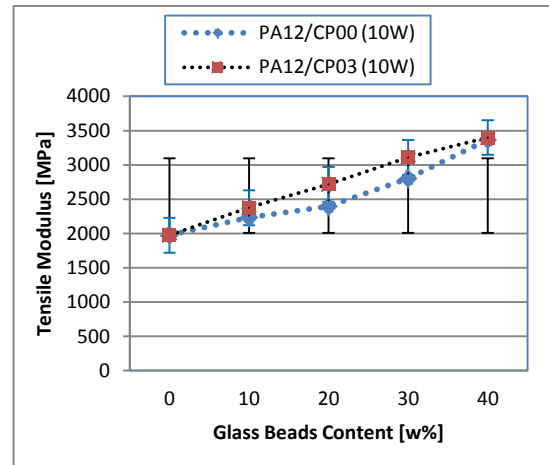


Figure 9. Variation of modulus of elasticity

The changes of the adhesion parameters in the composites as a consequence of the glass beads surface modification are expected to reflect in the changes of the composite mechanical properties. However, there were no obvious differences in the elastic modulus between the PA12/CP00 and PA12/CP03 laser sintered specimens. It is seen that the elastic modulus is independent of the interfacial adhesion between PA12 and GB. However, since elastic modulus is measured at a relatively low deformation, there is insufficient dilation to cause interface separation. Thus, it is easy to understand that the adhesion strength does not noticeably affect the elastic modulus [17].

Elongation at break

As it can be seen from Figure 10 the measured elongation at break with 10 wt% glass beads was 4.18% then decreased to 0.18% at glass beads ratio of 40 wt%. The decrease of elongation at break with the presence of glass beads is generally explained by the immobilisation of the macromolecular chains by the glass beads which increase the brittleness of the PA12 matrix.

In the same way, the lowering of the elongation at break of the composites may be also associated with weak GB/PA12 adhesion. Even though there was a proper interfacial adhesion between GB and PA12, this adhesion appeared unable to withstand the deformations and elongations at rupture of glass beads filled composites failing it catastrophically. Additionally, from the trend in variation in the elongation at break of the PA12/GB composites, it is clear that, as the content of GB increases, the elongation at break decreases considerably.

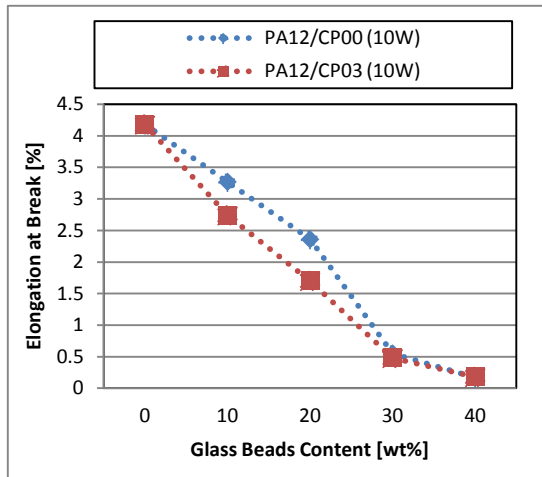


Figure 10. Variation of elongation at break

Flexural Strength and Modulus

Figure 11 shows the variation of the flexural strength and modulus with glass beads content. Flexural strength and modulus were obtained through a three-point bending test. The results from the experiments show that flexural strength increased gradually, whilst the flexural modulus values increased steadily as the glass beads loading increased from 10 to 40 wt%.

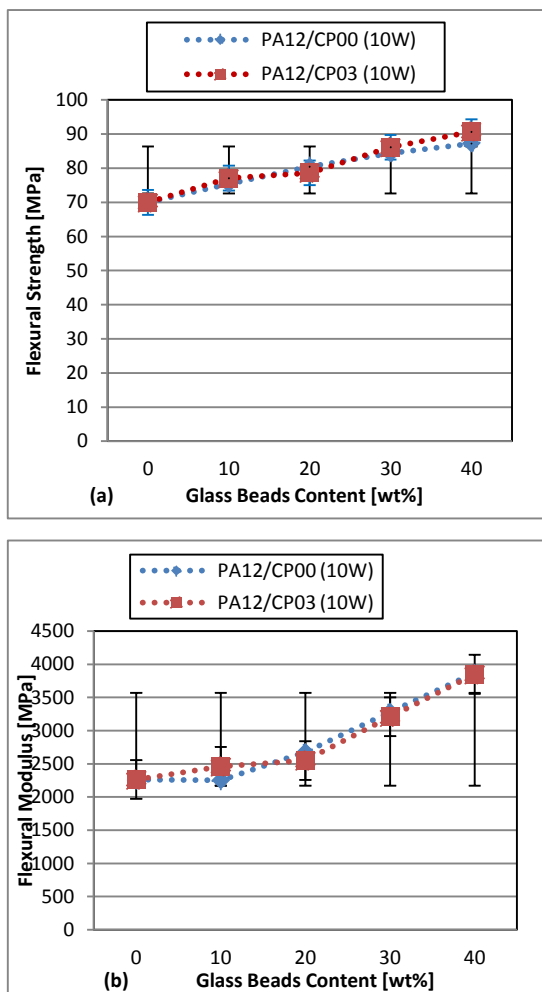


Figure 11. Variation of flexural strength (a) and flexural modulus (b)

However, the flexural strength and flexural modulus values of the PA12/CP03 system were slightly higher than those of the PA12/CP00 system, where, as generally believed, the coupling agent would soften the PA12 matrix around the glass beads which have a smooth spherical surface and should not initiate fine cracks in the matrix around them.

Impact Strength

The impact strength of notched specimens was measured at ambient temperature by the notched Izod test. Izod impact tests were carried out on 80mm x 10mm x 4mm rectangular bars with a single-edge of 45° V-shaped notch (tip radius 0.25 mm, depth 1.5 mm).

The impact strength of different PA12/GB composites with different filler content is shown in Figure 12. It becomes apparent that the impact strength increased to some extent with increased glass beads ratio, particularly at 10 wt%. With loading up to 20 %wt, the significant drop in impact strength was readily apparent. The explanation of this observation is that: for lower contents, glass beads are well- dispersed in the PA12 matrix, the impact energy is more uniformly distributed and the effect is higher impact strength. For higher contents, the decrease in impact strength may be related to the tendency to form glass bead agglomerates, resulting in a poor dispersion of the fillers on the PA12 matrix. Furthermore, the degradation in impact properties can be attributed to the immobilisation of the macromolecular chains by the glass beads which limits their ability to deform freely and reduces the ductility of the composites [18].

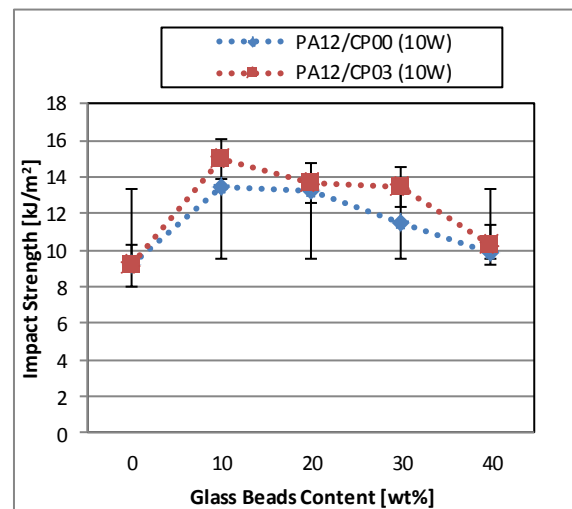


Figure 12. Variation of impact strength

From the impact experiment, it was found that the strengths of both composites decreased monotonically from 14.40 to 9.84 kJm^{-2} with increasing GB weight ratio regardless to surface modification. Table 4 represents the experimental results of mechanical properties of sintered PA12/GB composites.

Table 4. Experimentally obtained mechanical properties of SLS specimens

PA12/ CP00 ratios [wt%]	100/0	90/10	80/20	70/30	60/40
Laser power [W]	10				
Properties; Composite Material: PA12/CP00					
Tensile strength [MPa]	52.89	52.39	52.40	48.40	40.85
Tensile modulus [MPa]	1974.4	2233.8	2395.7	2800.9	3366.5
Ultimate elongation [%]	4.18	3.27	2.36	0.55	0.17
Flexural strength [MPa]	69.97	75.43	80.41	84.38	87.20
Flexural modulus [MPa]	2262.91	2252.98	2675.18	3280.86	3870.03
Impact strength [kJ/m ²]	9.14	13.97	13.18	11.46	9.84
Properties; Composite Material: PA12/CP03					
Tensile strength [MPa]	52.89	53.59	54.61	52.23	51.54
Tensile modulus [MPa]	1974.4	2377.2	2716.5	3110.0	3399.6
Ultimate elongation [%]	4.18	2.74	1.70	0.48	0.18
Flexural strength [MPa]	69.97	77.07	78.61	86.14	90.70
Flexural modulus [MPa]	2262.91	2460.51	2549.98	3208.68	3849.12
Impact strength [kJ/m ²]	9.14	14.40	13.65	13.41	10.29

6. Fracture Toughness

To determine the fracture toughness of the glass beads-filled polyamide12 composites under quasi-static load there are two approaches: the stress intensity approach and the energy approach. The first approach yields fracture toughness (K_{Ic}); the second provides a critical energy release rate (G_c). The fracture toughness specimens were produced using a DTM Sinterstation 2000 machine under the same conditions applied to other test specimens. The length (L), thickness (B) and width (W) of the specimens were 80mm, 10mm and 4mm, respectively (BS ISO 17281), shown in Figure 13. The single edge V- shaped notches of 45°, with a tip radius of 0.25mm and different depths were introduced using the SLS machine.

Single- Edge- Notched Three- Point Bending Fracture Toughness Tests

It is well known that the toughness tests could also be performed on the composites at slower rate than impact conditions by drawing out the notched rectangular bar specimens. For this purpose, five sets from which five replicate specimens of each were produced and tested at room temperature on a Testometric materials testing machine AX at a cross-head speed of 1 mm/min using a span of 64 mm.

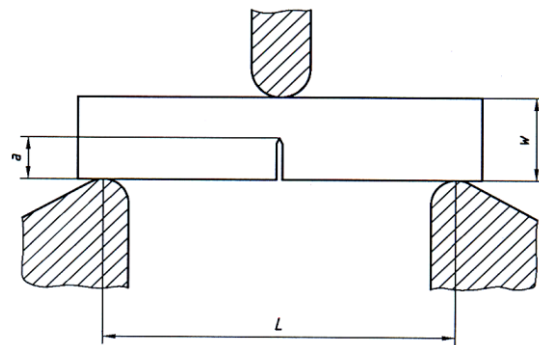


Figure 13. Specimen configuration and dimensions for fracture toughness measurements [19]

Single-edge-notched (SEN) type specimens were prepared for the determination of the critical stress intensity factor (K_{Ic}) in the three-point bending (3PB) test. The obtained load-displacement curves allowed for making statements about the behavior of the composites. An example for the resulting load-displacement curves of the glass beads-filled polyamide composites is given in Figure 14. Looking at the effect of the notch depth on the stress-strain curves of the specimen, it is clear that as the depth increased, the stress and the strain decreased.

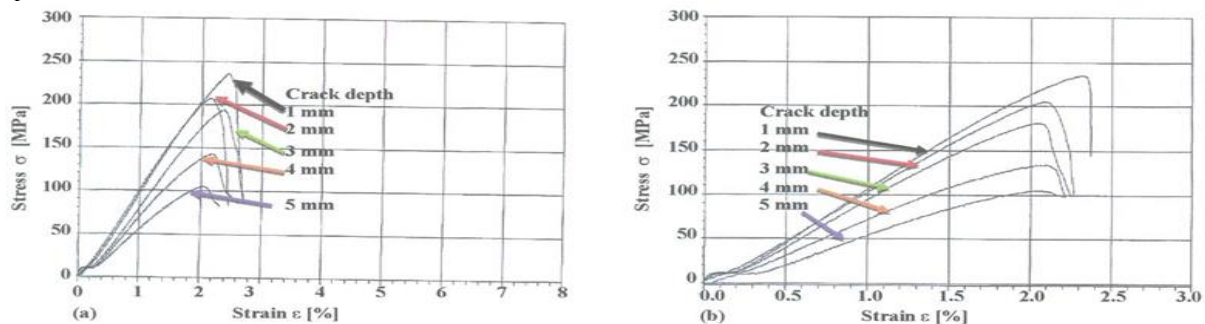


Figure 14: Stress-strain curves for composites containing 20 wt% of glass beads (a) CP00/PA12; (b) CP03/PA12

Correlation between Fracture Toughness and Glass Beads Content

The fracture toughness was studied as a function of glass beads loading. It was found that the toughness reached a maximum at 10 wt% of glass beads and then decreased with more glass beads added.

The dependency of plain strain fracture toughness, i.e., the critical stress intensity factor (K_{IC}) of glass bead-filled polyamide 12 is given in Figure 15. The most distinctive feature in this figure is that the fracture toughness of the both composite systems did not show any significant increase with increasing glass beads content. In fact, it decreased with the increase in glass beads content. In other words, the addition of glass beads led to composites with brittle behavior.

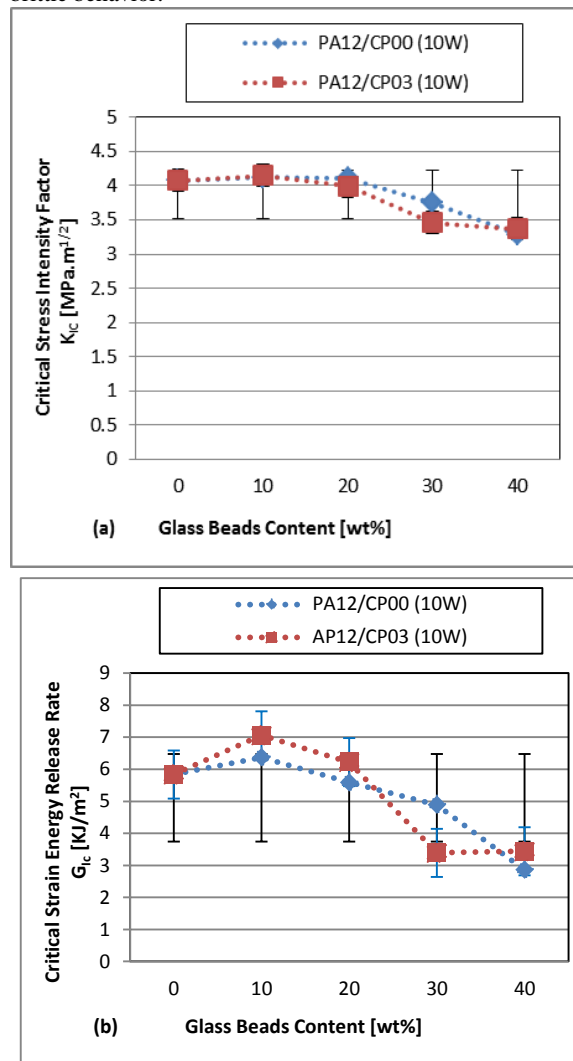


Figure 15. Dependency of fracture toughness of polyamide 12 composites on glass beads content (a) K_{IC} ; (b) G_{IC}

From the abovementioned figure, it can be observed that the influence of the surface treatment on fracture toughness is insignificant; therefore, a small amount of energy can be damped via de-bonding. Besides, a crack

can propagate through an interface easily because of a weak interface adhesion.

7. Morphological Observations

The effect of the coupling agent on the interfacial adhesion is often evaluated from the micrographs of fractured surfaces. The morphological study included the intrinsic microstructures of the blends of the fractured surfaces after tensile tests. The SEM micrographs of the PA12/ GB composites processed using the optimal parameter sets are shown in Figures 16; 17 and 18.

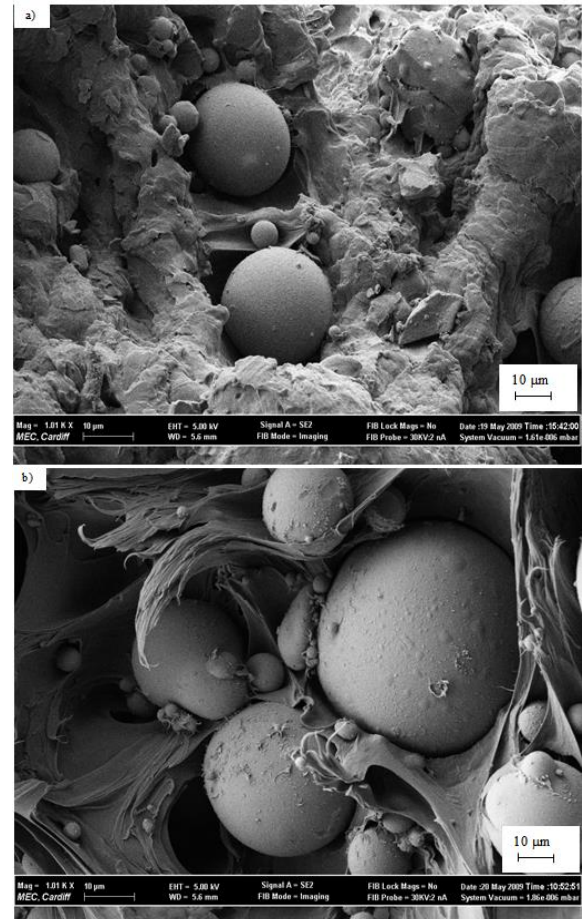


Figure 16. SEM micrographs of tensile fracture surfaces: PA12/CP00 composite containing 20 wt% of glass beads; ED= 0.073 J/mm²

For PA12/CP00 system (20 wt% at ED= 0.073 J/cm²), it can be seen from Figure 16(a) and (b) that the connection between the GB and PA12 was not perfect; many glass beads have been pulled out and that PA12 was stretched during breakage, resulting in a rough spongy surface.

The de-bonded glass particles surrounded by the void created due to deformation of the PA12/GB composite. However, the tensile fracture cross-section of the untreated GB in the composite after de-bonding was relatively smooth and this specifies that the interfacial adhesion was poor between PA12 and GB.

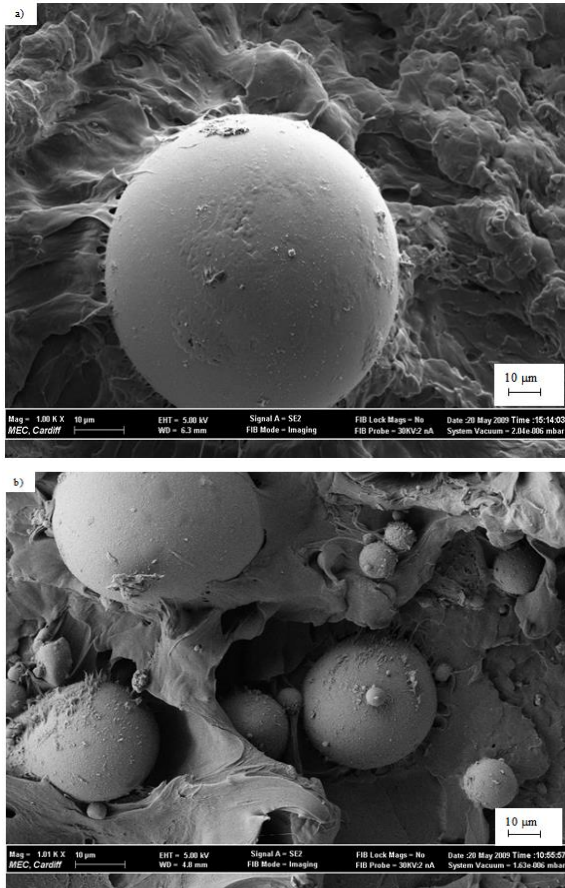


Figure 17. SEM micrographs of tensile fracture surfaces: PA12/CP03 composites containing 20 wt% of glass beads; ED= 0.073 J/mm²

Figure 17 depicts SEM micrographs taken of the tensile fracture cross-sections of the PA12/CP03 system (20 wt% at ED= 0.073 J/cm²). In this case, the treated beads appear to remain solidly anchored and strongly adhered to the matrix and their surface become relatively rough. Hence, the bonding between the glass beads and the matrix was strengthened. These results indicate that the silane agent coated on the surface of glass beads enhanced the interaction between the PA12 and GB, and improved the adhesion, Figure 17(a) and (b).

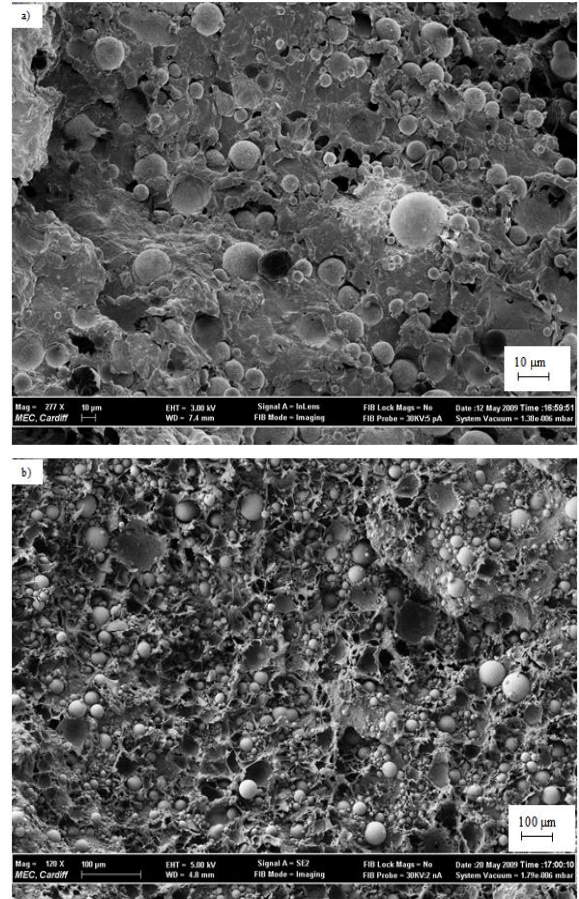


Figure 18. SEM micrographs of tensile fracture surfaces: a) PA12/CP00 and b) PA12/CP03 composites containing 40 wt% of glass beads each; ED= 0.073 J/mm²

The fractured surfaces of Figure 18(a) and (b) represent a kind of median situation for each type of glass bead; they do not provide a completely accurate description of the composite. In fact, it is possible to find in untreated glass beads-polyamide 12 composites a significant proportion of glass bead particles that have not separated from the matrix, see Figure 18(a). Conversely, in surface treated glass bead composites, a significant number of de-bonded particles have been observed, see Figure 18(b).

8. Conclusions

In the present work, an attempt has been made to study the effects of content and surface modification of glass beads on the mechanical properties of SLS parts fabricated from polyamide 12 composites. Under predetermined processing parameters, several mechanical properties, such as tensile strength, elasticity modulus, elongation at break, flexural strength and modulus, impact strength, fracture toughness and microstructural properties of PA12/GB composites, were investigated. The following results can be drawn from the experimental results:

- The strength of PA12/GB composites is generally affected by PA12/GB interface adhesion and glass beads content. Initially, it increased with the increase in the glass beads ratio from 53MPa at 10 wt% to 55 MPa at 20 wt%; then decreased above 20 wt%.
- Regardless of the surface modification, elastic modulus increased considerably from 2000 to 3400 MPa as the glass beads content increased.
- In both systems, the elongation at break decreased steadily as the glass beads content increased, namely from 2.74% at 10 wt% to 0.18% at glass beads ratio of 40 wt%.
- There was a significant increment in the flexural properties with an increase in the beads loading. The flexural strength increased gradually (77 to 91 MPa), whilst the flexural modulus values increased steadily (2500 to 3800 MPa) as the glass beads ratio increased (10 to 40wt%).
- The impact strengths of both composites decreased monotonically (14 to 10 kJm⁻²) with increasing GB weight ratio regardless of the surface modification. The significant drop in impact strength was readily apparent with loading up to 20 % wt.
- The fracture toughness of PA12/GB composites was observed to peak slightly at low glass beads content and then decreased with more beads added. Regardless of the surface modification, increasing notch depth leads to a decrease in the fracture toughness.
- SEM micrographs of fracture surfaces showed that PA12 was pulled away from uncoated GB as the test specimen was stretched whereas it was strongly adhered to the surface modified GB.

Important Note

This research received no specific grant from any funding agency in the public, commercial, or not-for-profit sectors.

References

[1] I. Švab, V. Musil, M. Leskovic: "The Adhesion Phenomena in Polypropylene/ Wollastonite Composites". *Acta Chim. Slov.* Vol. 52 (2005) 264–271.

[2] G. V. Salmoria, J. L. Leite, R. A. Paggi, A. Lago, A. T. N. Pires: "Selective laser sintering of PA12/HDPE blends: Effect of components on elastic/plastic behaviour". *Polymer Testing*, Vol. 27 (2008) No. 6, 654-659.

[3] H. Unal: "Morphology and mechanical properties of composites based on polyamide 6 and mineral additives". *Materials and Design*, Vol. 25 (2004) 483 – 487.

[4] I. Gibson, D. Shi: "Material properties and fabrication parameters in selective laser sintering process". *Rapid Prototyping Journal*, Vol. 3 (1997) No. 4, 129 – 136.

[5] Y. Wang, Y. Shi, S. Huang: "Selective laser sintering of polyamide-rectorite composite". *Proceedings of the Institution of Mechanical Engineers, Part L: Journal of Materials Design and Applications* January, Vol. 1 (2005) No. 219, 11-15.

[6] T. J. Gill, K. K. B Hon: "Experimental investigation into the selective laser sintering of silicon carbide polyamide composites". *Proceedings of the Institution of Mechanical Engineers, Part B: Journal of Engineering Manufacture* October 1, (2004) No. 218, 1249-1256

[7] A. Mazzoli, G. Moriconi, M. G. Pauro: "Characterization of an aluminum filled polyamide powder for applications in selective laser sintering". *Materials & Design*, Vol. 28 (2007) No. 3, 993-1000.

[8] U. Ajoku, N. Saleh, N. Hopkinson, R. Hague, P. Erasenthiran: "Investigating mechanical anisotropy and end-of-vector effect in laser-sintered nylon parts". *Proceedings of the Institution of Mechanical Engineers, Part B: Journal of Engineering Manufacture* July 1, (2006) 220, 1077-1086.

[9] B. Caulfield, P. E. McHugh, S. Lohfeld: "Dependence of mechanical properties of polyamide components on build parameters in the SLS process". *Journal of Materials Processing Technology*, Vol. 182. (2007) No. 1-3, 477-488

[10] P. K. Jain, P. M. Pandey, P. V. M. Rao: "Effect of delay time on part strength in selective laser sintering". *Advanced Manufacturing Technology*, Vol. 43 (2009) No. 1-2, 117-126

[11] P. K. Jain, P. M. Pandey, P. Rao: "Selective laser sintering of clay reinforced polyamide". *Polymer Composites*, Vol. 31 (2010) No. 4, 732–743.

[12] R. D. Goodridge, M. L. Shofner, R. J. M. Hague, M. McClelland, M. R. Schlea, R. B. Johnson, C. J. Tuck: "Processing of a Polyamide-12/carbon nanofibre composite by laser sintering". *Polymer Testing*, Vol. 30 (2010) No. 1, 94-100

[13] A. C. Miller, J. C. Berg: "Effect of silane coupling agent adsorbate structure on adhesion performance with a polymeric matrix". *Composites Part A: Applied Science and Manufacturing*, Vol. 34 (2003) No. 4, 327-332

[14] <http://www.specialchem4polymers.com/> SpecialChem, [Accessed 12. Feb. 2014].

[15] S. Shokoohi, A. Arefazar, R. Khosrokhavar: "Silane Coupling Agents in Polymer based Reinforced Composites; a review". *Journal of Reinforced Plastics and Composites* Vol. 27 (2008) No. 5, 473-485

[16] <http://www.potterseurope.org/> [Accessed 10. Oct. 2014].

[17] S. Y. Fu, X. Q. Feng, B. Lauke, Y. W. Mai: "Effects of particle size, particle/matrix interface adhesion and particle loading on mechanical properties of particulate– polymer composites". *Composites Part B: Engineering*, Vol. 39 (2008) No. 6, 933-961.

[18] P. Mareri, S. Bastide, N. Binda, A. Crespy: "Mechanical behaviour of Polypropylene Composites Containing Fine Mineral Filler: Effect of Filler Surface Treatment". *Composites Science and Technology*, Vol. 58 (1998) No. 5, 747-752

[19] British Standards Institution: BS ISO 17281: "Plastics — Determination of fracture toughness (G_{IC} and K_{IC})" At moderately high loading rates (1 m/s). London: British Standards Institute, 2002.

Dynamic Response of Beam with Multi-Attached Oscillators and Moving Mass: Fractional Calculus Approach

Ibrahim M. Abu-Alshaikh^a, Anas N. Al-Rabadi^b, and Hashem S. Alkhalidi^{a*}

^aMechanical Engineering Department, The University of Jordan, Amman-11942-Jordan

^bComputer Engineering Department, The University of Jordan, Amman-11942-Jordan

Received 21 Jan 2014

Accepted 22 Sep 2014

Abstract

This paper presents the dynamic response of Bernoulli-Euler homogeneous isotropic fractionally-damped simply-supported beam. The beam is appendaged to single-degree-of-freedom (SDOF) fractionally-damped N-oscillators and subjected to a moving load with a uniform velocity. The damping characteristics of the beam and oscillators are formally described in terms of fractional derivative of an arbitrary order. In the analysis, the initial conditions are assumed to be homogeneous, and the Laplace transform is combined with the used decomposition method to find the solution of the handled problem. Subsequently, curves are plotted to show the vibration of the utilized beam under different sets of parameters including different orders of fractional derivatives for both of the beam and oscillators. The numerical results obtained in this paper show that the dynamic response decreases as the number of absorbers attached to the beam increases, as both the damping-ratios of absorbers and beam increase the dynamic response decreases, and there are some critical values of fractional derivatives which are different from unity at which the beam has less dynamic response than that obtained for the full-order derivatives model. In addition, the obtained results show very good agreement with special case studies that were previously published in literature.

© 2014 Jordan Journal of Mechanical and Industrial Engineering. All rights reserved

Keywords: : Absorbers, Fractional Calculus, Fractional Damping, Fractional Derivative, Moving Load, Simply-Supported Beam Vibration.

1. Introduction

1.1. Fractional Calculus Approach

Fractional calculus is a branch of mathematical analysis that studies the possibility of taking real number powers or complex number powers of the differentiation operator [35, 42, 66]. The motivation behind this extension to the differential operator is that the semi-group of powers D^ν will form a continuous semi-group with parameter ν , inside which the original discrete semi-group of D^n for integer n can be recovered as a subgroup. Continuous semi-groups are prevalent in mathematics, and have an interesting theory, where an important point is that the fractional derivative at a point x is a local property only when ν is an integer; in non-integer cases we cannot say that the fractional derivative at x of a function f depends only on the graph of f very near x , in the way that integer-power derivatives do. Therefore, it is expected that the theory involves a sort of boundary conditions, involving information on the function further out, and thus the fractional derivative requires some peripheral information. In calculus-based formulation, fractional calculus is based

on the definition of the fractional derivative which can be defined by the following convolution integral as [66]:

$$D^\nu f(x) = \frac{d^\nu f(x)}{dx^\nu} = \frac{1}{\Gamma(-\nu)} \int_0^x \frac{1}{(x-\zeta)^{\nu+1}} f(\zeta) d\zeta, \quad (1)$$

Where $\Gamma(\cdot)$ is the gamma function [11, 55]. From this equation, fractional derivatives can be defined accordingly. Due to its generality, fractional calculus has found numerous applications in various fields in science and engineering [12, 16, 17, 20, 22-27, 33, 35, 37-38, 41-42, 52, 56, 59-60, 63, 67, 68, 70-71, 75-77, 86, 90]. For example, since quantum computing and mechanics have been increasingly considered as important synthesis and analysis parts in modern computational systems [7-9], the effects and uses of fractional derivatives within quantum mechanics have been investigated [24-25, 33, 62, 67]. Also, fractional calculus has found important implementations in electronics applications and in designing filters [77]. A fractal time series is taken as the solution of differential equation of a fractional order, or a

* Corresponding author. e-mail: h.alkhalidi@ju.edu.jo.

response of a fractional system, or a fractional filter driven with a white noise in the domain of stochastic processes [44]. A general approach for approximating ideal filters that are based on fractional calculus from the point of view of systems of fractional order was introduced [45]. The analysis of signals generated by fractional-order process, and applications of such model in a wide range of physical, mechanical and biological systems were discussed in [77].

The fractional derivatives of order β or γ , may be defined in many ways [65]. Among these are the two most frequently encountered: the Riemann-Liouville and Caputo fractional derivatives of order β , which are defined, respectively, by the following convolution integrals:

$$\frac{\partial^\beta w(x,t)}{\partial t^\beta} = \frac{1}{\Gamma(k-\beta)} \frac{\partial^k}{\partial t^k} \int_0^t \frac{w(x,u)}{(t-u)^{\beta+1-k}} du \quad (2a)$$

$$\frac{\partial^\beta w(x,t)}{\partial t^\beta} = \frac{1}{\Gamma(k-\beta)} \int_0^t \frac{1}{(t-u)^{\beta+1-k}} \frac{\partial^k w(x,u)}{\partial u^k} du \quad (2b)$$

where k is a positive integer such that $(k-1 \leq \beta < k)$. The solutions of fractional Langevin equation of two different orders which are known as the fractional Ornstein-Uhlenbeck processes, based on Weyl and Riemann-Liouville fractional derivatives were obtained [54].

Many physical problems were adequately described by the differential equations of fractional order. The list of these problems is long and the areas of applications are broad. Among these applications are polymeric damping, fluid mechanics, and the theory of viscoelasticity [16, 41, 56, 67, 68, 76]. However, as noted from literature, a clear physical interpretation of the fractional derivative has been elusive. Good examples are: (1) in the diffusion process; fractional differential equations have been employed to describe an anomalous diffusion regime including both sub-diffusion and super-diffusion [27], (2) many linear viscoelastic damping materials exhibit a macroscopic constitutive behavior which has been the subject of many investigations involving fractional order derivative [20], and (3) tests on (Aerstop CN20) are performed with different values of amplitudes and always the theoretical relaxation and creep functions overlap the experimental data leading to the conclusion that the fractional model is able to fully capture the visco-elastic behavior and that may be widely used, since these tests are performed on polymers that have different chemical physical properties [65]. However, in the fractional model of viscoelastic material over extended ranges of time and frequency, the deformation work corresponds to springs and losses to dashpots have both energy types (stored and dissipated) at any point of the material [33, 38]. Transverse vibration of homogeneous beams whose damping behavior is described by a fractional derivative of arbitrary orders was an important subject of matter [12, 52, 70]. The solution in the closed form to a class of SDOF fractional oscillators subjected to an impulse response is investigated [48]. Relationship between fractional oscillator processes and the corresponding fractional Brownian motion processes is well established in research. However, the increment process of fractional Brownian motion can be described by a random function with long-range dependence fractional

Gaussian noise model [46]. Power-laws-type data may further, in earthquake and wind engineering applications, be governed by stochastically differential equations of fractional order [50].

1.2. Beam Response

Dynamic response characteristics of beams resulting from the passage of different moving load systems, and with the existence of dampers and oscillators, have been of continuing engineering interest for the recent several decades [1-2, 4, 13, 15, 18, 28-29, 31-32, 36, 62, 69, 72-73, 80-83, 85]. Some of the applications of this problem are the vibrations occur in bridges, aircraft carriers, and railroad tracks due to moving vehicles, and vibrations occur in piping systems due to fluid flow. One of the main objectives of studying such problems is to minimize or to suppress the dynamic response characteristics or vibration levels of beams when subjected to different load systems. The simplest and most economical way to achieve this objective is by having different lumped appendages attached to the beam at different points. The problem of beams subjected to different moving load systems has been studied extensively in the literature [74, 85, 88]. For example, the text in [30] contained a variety of problems related to the moving loads on structures. The problem that deals with inherent randomness due to material properties, force, support and speed can be found in [79, 87]. Extensions to rotating beams and Timoshenko beams can be found in [14, 39, 89]. The vibration response of beams on elastic foundation due to a moving force can be found in [57, 82]. The response of a simply supported beam subjected to a moving mass using an approximation based on modal analysis is presented in [58]. The problem of an elastic system subjected to a moving oscillator is studied in [65, 84]. The associated problem of beams loaded with different appendages is also studied by different authors with emphasis on natural frequencies and mode shapes of beams with different boundary conditions [10, 19, 21, 34, 40, 43, 47, 49, 51, 61, 90]. In these references, numerical and analytical solutions are adopted. For example, [61] used Green functions formulation to analyze the free vibration of a linear undamped beam subjected to grounded and one-degree of freedom oscillator appendages at different discrete points. They compared their results with the approximate solution obtained by the Galarkin's method. In [34], an approximation which is based on the general eigenvalue problem of the fundamental frequency and the first mode shape to which point masses and springs are attached has been obtained. Based on the dynamic Green functions, the work in [40] used modal analysis to investigate the effects of added masses on vibration characteristics of a simply supported beam subjected to a harmonic point force. In [10], it has been investigated the effect of added masses and/or springs on beam vibrations subjected to a harmonic force. An approach was proposed which is based on frequency equation formulation to determine the eigenvalues of an arbitrarily supported beam carrying any combination of lumped attachments [19, 90]. In [43], a formulation was proposed of the problem to control a bridge subjected to moving loads using a tuned mass damper. The tuned mass damper is a single mass-spring dashpot system. In [21], the analysis of a

Timoshenko beam with tuned mass dampers under moving load excitation was done. The technique used is based on the first mode of the Timoshenko beam.

In this paper, a homogeneous isotropic Euler beam with different appendages attached at different points subjected to a uniformly moving load system is investigated. The solution to the vibration displacement response presented in this paper is based on decomposing the generalized displacements of the beam and oscillators into infinite components. Then the generalized displacements are recursively solved by in the Laplace transform domain. Case studies for different velocity parameters, the inertia effect of the load moving system, the effect of the attached appendages, and the fractional derivative orders, are discussed.

The remainder of this paper is organized as follows: Section 2 presents the required mathematical formulation of the handled problem. Section 3 introduces three important case studies that illustrate the corresponding optimization of fractional-order derivatives and number of fractionally-damped oscillators on suppressing the beam dynamic response. Conclusions and future work are presented in Section 4.

2. Formulation of the Problem

Transverse vibration of Bernoulli-Euler homogeneous isotropic fractionally-damped simply supported beam is investigated. The beam is assumed to be subjected to a moving load (from left to right) with a constant velocity (v). Moreover, the beam is assumed to be of finite length (L) and undisturbed before the load is applied, i.e., originally at rest. Furthermore, N -rigid body single-degree-of-freedom (SDOF) fractionally-damped oscillators of order γ , with masses \hat{M}_i , stiffnesses \hat{K}_i , damping constants \hat{C}_i at locations d_i are attached to the beam ($i=1,2,\dots,N$), as shown in Figure 1. The governing equation of the beam under investigation, whose damping characteristics are described by a fractional derivative of order β , can be written as:

$$EI \frac{\partial^4 w(x,t)}{\partial x^4} + C \frac{\partial^\beta w(x,t)}{\partial t^\beta} + \mu \frac{\partial^2 w(x,t)}{\partial t^2} + \tag{3a}$$

$$\sum_{i=1}^N \hat{M}_i \hat{z}_i(t) \delta(x-d_i) = P(x,t), \quad x \in (0,L), \quad t > 0,$$

$$\text{BC's: } w(0,t) = 0, \quad w(L,t) = 0, \tag{3b}$$

$$w_{xx}(0,t) = 0, \quad w_{xx}(L,t) = 0,$$

$$\text{IC's: } w(x,0) = 0, \quad \frac{dw(x,0)}{dt} = 0. \tag{3c}$$

The equations corresponding to the N -oscillators appended to the beam are given as:

$$u_i(t) = w(d_i, t) - \hat{z}_i(t), \quad t > 0, \tag{4a}$$

$$\hat{M}_i \hat{z}_i(t) = \hat{K}_i u_i(t) + \hat{C}_i \frac{d^\gamma u_i(t)}{dt^\gamma}, \quad t > 0, \tag{4b}$$

$$\hat{z}_i(0) = 0, \quad \frac{d\hat{z}_i(0)}{dt} = 0 \tag{4c}$$

where $\{ E, I, \mu, C \}$ are the modulus of elasticity, moment of inertia of cross-sectional area, mass per unit

length, and the coefficient of external damping of the beam, respectively. It is assumed that $\{ E, I, \mu, C \}$ are constants. Furthermore, $P(x,t)$ is the applied moving load, $w(x,t)$ is the transverse deflection of the beam at point x and time t , $u_i(t)$ is the total displacement of the i^{th} oscillator, and $\hat{z}_i(t)$ denotes the transverse displacement of the masses \hat{M}_i for the i^{th} SDOF oscillator.

In modal form, the transverse deflection of the beam is written as [30]:

$$w(x,t) = \sum_{n=1}^{\infty} Y_n(t) X_n(x) \tag{5}$$

where $Y_n(t)$ is the generalized displacement or the modal response of the beam, $X_n(x)$ are the normal modes of the undamped free vibration of the simply supported beam written as [1]:

$$X_n(x) = \sin(\kappa_n x), \tag{6}$$

where $(\kappa_n = \frac{n\pi}{L})$ is the frequency parameter associated

with the simply-supported beam. Equation (6) should satisfy the following differential equation:

$$EI \frac{\partial^4 X_n(x)}{\partial x^4} Y_n(t) + \mu \frac{\partial^2 Y_n(t)}{\partial t^2} X_n(x) = 0 \tag{7}$$

Substituting Eq. (5) into Eqs. (3a) and (4b) leads to the following system of ordinary differential equations:

$$EI \sum_{n=1}^{\infty} Y_n(t) \frac{d^4 X_n(x)}{dx^4} + C \sum_{n=1}^{\infty} \frac{d^\beta Y_n(t)}{dt^\beta} X_n(x) + \tag{8}$$

$$\mu \sum_{n=1}^{\infty} \frac{d^2 Y_n(t)}{dt^2} X_n(x) + \sum_{i=1}^N \hat{M}_i \hat{z}_i(t) \delta(x-d_i) = P(x,t)$$

$$\hat{M}_i \hat{z}_i(t) = \sum_{r=1}^{\infty} \hat{K}_r Y_r(t) X_r(d_i) + \sum_{r=1}^{\infty} \frac{d^\gamma Y_r(t)}{dt^\gamma} \hat{C}_r X_r(d_i) - \tag{9}$$

$$\left(\hat{K}_i \hat{z}_i(t) + \hat{C}_i \frac{d^\gamma \hat{z}_i(t)}{dt^\gamma} \right).$$

Multiplying Eq. (8) by $X_m(x)$ and integrating over the domain ($0 \leq x \leq L$) yields:

$$\sum_{n=1}^{\infty} \int_0^L EI Y_n(t) \frac{d^4 X_n(x)}{dx^4} X_m(x) dx + \tag{10}$$

$$\sum_{n=1}^{\infty} \int_0^L \frac{d^\beta Y_n(t)}{dt^\beta} C X_n(x) X_m(x) dx +$$

$$\sum_{n=1}^{\infty} \int_0^L \frac{d^2 Y_n(t)}{dt^2} \mu X_n(x) X_m(x) dx +$$

$$\sum_{i=1}^N \int_0^L \hat{M}_i \hat{z}_i(t) X_m(x) \delta(x-d_i) dx = \int_0^L X_m(x) P(x,t) dx.$$

The dynamic response of the beam represented by Eq. (3a) is analyzed after projecting the 4th order partial derivative into a complete orthogonal basis. For the present problem, the eigenfunctions of the linear operator representing the simply supported beam with no appendages given in Eq. (6) can be used. These eigenfunctions satisfy the following orthogonality conditions:

$$\int_0^L \mu X_n(x) X_m(x) dx = \frac{\mu L}{2} \delta_{nm}, \quad (11a)$$

$$\int_0^L (EI X_n''(x))'' X_m(x) dx = \frac{EI n^4 \pi^4}{2L^3} \delta_{nm} \quad (11b)$$

for $n, m = 1, 2, 3, \dots$

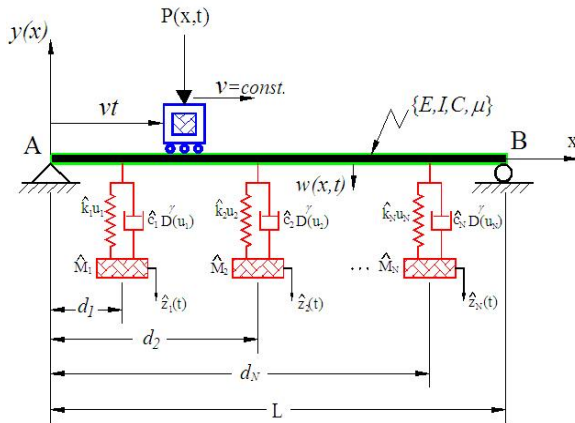


Figure 1. The model of simply-supported beam subjected to a moving load with single-degree-of-freedom appended N-oscillators.

By considering these orthogonality conditions, the differential equation of the n^{th} mode of the generalized beam-displacement (Eq. (10)) which is the modal response can be expressed as:

$$\sum_{n=1}^{\infty} Y_n(t) \frac{EI n^4 \pi^4}{2L^3} \delta_{nm} + \sum_{n=1}^{\infty} \frac{d^\beta Y_n(t)}{dt^\beta} \frac{CL}{2} \delta_{nm} + \sum_{n=1}^{\infty} \frac{d^2 Y_n(t)}{dt^2} \frac{\mu L}{2} \delta_{nm} + \sum_{i=1}^N \hat{M}_i \hat{z}_i(t) X_m(d_i) = Q_n(t). \quad (12)$$

Substituting Eq. (6) into (12) and (9), and noting that ($m = n$), leads to the following coupled ordinary differential equations:

$$\frac{d^2 Y_n(t)}{dt^2} + 2\omega_n \zeta_n \frac{d^\beta Y_n(t)}{dt^\beta} + \omega_n^2 Y_n(t) = \eta_1 \left(Q_n(t) - \sum_{i=1}^N \hat{M}_i \hat{z}_i(t) \sin(\kappa_n d_i) \right) \quad (13a)$$

$$\hat{z}_i(t) = - \left(\hat{\omega}_i^2 \hat{z}_i(t) + 2\hat{\omega}_i \hat{\zeta}_i \frac{d^\gamma \hat{z}_i(t)}{dt^\gamma} \right) + \sum_{r=1}^{\infty} \sin(\Omega_r d_i / v) \left[\hat{\omega}_i^2 Y_r(t) + 2\hat{\omega}_i \hat{\zeta}_i \frac{d^\gamma Y_r(t)}{dt^\gamma} \right] \quad (13b)$$

where:

$$\omega_n = \kappa_n^2 \sqrt{EI / \mu} \quad (14)$$

$$\zeta_n = C / 2\mu\omega_n \quad (15)$$

$$\hat{\zeta}_i = \frac{\hat{C}_i}{2\hat{M}_i \omega_i}, \quad (16)$$

$$Q_n(t) = \int_0^L X_n(x) P(x,t) dx \quad (17)$$

$$\hat{\omega}_i = \sqrt{\frac{\hat{K}_i}{\hat{M}_i}}, \quad (18)$$

are the undamped natural circular frequency (ω_n), beam damping ratio (ζ_n), i^{th} oscillators damping ratio ($\hat{\zeta}_i$), the generalized load ($Q_n(t)$) and the natural frequency of the i^{th} oscillator ($\hat{\omega}_i$), respectively, and ($\eta_1 = \frac{2}{\mu L}$).

In Eqs. (8) and (17), the load $P(x,t)$, which moves over the beam from left to right, is written as:

$$P(x,t) = P_0 \delta[x - f(t)] \quad (19)$$

Where P_0 is the intensity of the applied moving load and $f(t) = vt$ is a function describing the motion of the force at time t , with v being the constant speed of the moving load. Hence, Eq. (19) becomes:

$$P(x,t) = P_0 \delta(x - vt) \quad (20)$$

Substituting the last relation into Eq. (17) yields:

$$Q_n(t) = P_0 \int_0^L X_n(x) \delta(x - vt) dx = P_0 X_n(vt) = P_0 \sin(\kappa_n vt) \quad (21)$$

Substituting Eq. (21) into the coupled system in Eqs. (13) yields:

$$\frac{d^2 Y_n(t)}{dt^2} + 2\omega_n \zeta_n \frac{d^\beta Y_n(t)}{dt^\beta} + \omega_n^2 Y_n(t) = \eta_1 \left(P_0 \sin(\Omega_n t) - \sum_{i=1}^N \hat{M}_i \hat{z}_i(t) \sin(\Omega_n d_i / v) \right) \quad (22a)$$

$$\hat{z}_i(t) = - \left(\hat{\omega}_i^2 \hat{z}_i(t) + 2\hat{\omega}_i \hat{\zeta}_i \frac{d^\gamma \hat{z}_i(t)}{dt^\gamma} \right) + \sum_{r=1}^{\infty} \sin(\Omega_r d_i / v) \left[\hat{\omega}_i^2 Y_r(t) + 2\hat{\omega}_i \hat{\zeta}_i \frac{d^\gamma Y_r(t)}{dt^\gamma} \right] \quad (22b)$$

where Ω_n is the load frequency defined as:

$$\Omega_n = \frac{n\pi v}{L} \quad (23)$$

To find the solution of the system in Eqs. (22), associated with the boundary and initial conditions given in Eqs. (3b-3c) and (4c), $Y_n(t)$ and $\hat{z}_i(t)$ can be decomposed into infinite series of the form:

$$Y_n(t) = \sum_{k=0}^{\infty} Y_n^k(t) = Y_n^0(t) + Y_n^1(t) + Y_n^2(t) + \dots, \quad (24a)$$

$$\hat{z}_i(t) = \sum_{k=0}^{\infty} \hat{z}_i^k(t) = \hat{z}_i^0(t) + \hat{z}_i^1(t) + \hat{z}_i^2(t) + \dots, \quad (24b)$$

where $Y_n^k(t)$ and $\hat{z}_i^k(t)$ for ($k = 0, 1, 2, \dots$) are the components of $Y_n(t)$ and $\hat{z}_i(t)$, respectively. It should be mentioned that the solutions of Eqs. (22) for the cases of ($\beta = \gamma = 1$), i.e., full-order derivatives, are extensively

studied in the literature [72-73]. The components of $Y_n(t)$ can be recursively determined by substituting Eqs. (24) into Eqs. (22) as:

$$\frac{d^2 Y_n^0(t)}{dt^2} + \omega_n^2 Y_n^0(t) = P_0 \eta_1 \sin(\Omega_n t), \tag{25a}$$

$$\frac{d^2 \hat{z}_i^0(t)}{dt^2} = \sum_{r=1}^{\infty} \sin(\Omega_r d_i / v) \left[\hat{\omega}_i^2 Y_r^0(t) + 2\hat{\omega}_i \hat{\zeta}_i \frac{d^\gamma Y_r^0(t)}{dt^\gamma} \right] \tag{25b}$$

$$\begin{aligned} \frac{d^2 Y_n^{k+1}(t)}{dt^2} + \omega_n^2 Y_n^{k+1}(t) = \\ -2\omega_n \zeta_n \frac{d^\beta Y_n^k(t)}{dt^\beta} - \eta_1 \sum_{i=1}^N \hat{M}_i \frac{d^2 \hat{z}_i^k(t)}{dt^2} \sin(\Omega_n d_i / v) \end{aligned} \tag{25c}$$

$$\frac{d^2 \hat{z}_i^{k+1}(t)}{dt^2} = - \left(\hat{\omega}_i^2 \hat{z}_i^k(t) + 2\hat{\omega}_i \hat{\zeta}_i \frac{d^\gamma \hat{z}_i^k(t)}{dt^\gamma} \right) + \tag{25d}$$

$$\sum_{r=1}^{\infty} \sin(\Omega_r d_i / v) \left[\hat{\omega}_i^2 Y_r^{k+1}(t) + 2\hat{\omega}_i \hat{\zeta}_i \frac{d^\gamma Y_r^{k+1}(t)}{dt^\gamma} \right]$$

for $k \geq 0$. Using the Laplace transform for the Caputo fractional derivative defined in Eq. (2b) as [65]:

$$\ell \left(\frac{d^\beta Y_n^k(t)}{dt^\beta} \right) = s^\beta y_n^k(s) - \tag{26}$$

$$\sum_{j=0}^{m-1} s^{\beta-j-1} (y_n^k)^j(0), \text{ for } m-1 < \beta \leq m.$$

The Laplace transforms of Eqs. (24) and (25), assuming homogeneous initial conditions, can be written as:

$$y_n(s) = \sum_{k=0}^{\infty} y_n^k(s), \tag{27a}$$

$$Z_i(s) = \sum_{k=0}^{\infty} Z_i^k(s), \tag{27b}$$

where:

$$y_n^0(s) = \frac{P_0 \Omega_n \eta_1}{(s^2 + \omega_n^2)(s^2 + \Omega_n^2)}, \tag{28a}$$

$$Z_i^0(s) = \sum_{r=1}^{\infty} \sin(\Omega_r d_i / v) \left(\frac{\hat{\omega}_i^2 + 2\hat{\omega}_i \hat{\zeta}_i s^\gamma}{s^2} \right) y_r^0(s) \tag{28b}$$

$$y_n^{k+1}(s) = \frac{-2\omega_n \zeta_n s^\beta}{s^2 + \omega_n^2} y_n^k(s) - \tag{28c}$$

$$\eta_1 \sum_{i=1}^N \sin(\Omega_n d_i / v) \frac{\hat{M}_i s^2}{s^2 + \omega_n^2} Z_i^k(s)$$

$$Z_i^{k+1}(s) = \frac{-2\hat{\omega}_i \hat{\zeta}_i s^\gamma}{(s^2 + \hat{\omega}_i^2)} Z_i^k(s) + \tag{28d}$$

$$\sum_{r=1}^{\infty} \sin(\Omega_r d_i / v) \left(\frac{\hat{\omega}_i^2 + 2\hat{\omega}_i \hat{\zeta}_i s^\gamma}{(s^2 + \hat{\omega}_i^2)} \right) y_r^{k+1}(s)$$

for $k \geq 0$ and $(i = 1, 2, \dots, N)$ where N is the number of the SDOF fractionally-damped oscillators attached to the beam, and $\ell(\cdot)$ designates the Laplace transform of (\cdot) . Hence, $\ell(\hat{z}_i(t)) = Z_i(s)$ and $\ell(Y_n(t)) = y_n(s)$

Performing the Laplace inverse term-by-term of Eqs. (28) produces the first two sets of equations in the time-domain as:

$$Y_n^0(t) = \frac{\eta_2 \eta_5 [\omega_n \sin(\Omega_n t) - \Omega_n \sin(\omega_n t)]}{\omega_n \Omega_n} \tag{29a}$$

$$\hat{z}_i^0(t) = \sum_{r=1}^{\infty} \eta_2 \eta_3 \left\{ \begin{aligned} & \left[\frac{\hat{\omega}_i^2 t}{\Omega_r^2 \omega_r^2} + \frac{\hat{\omega}_i^2 \eta_6 \sin(\omega_r t)}{\omega_r^3} - \right. \\ & \left. \frac{\hat{\omega}_i^2 \eta_6 \sin(\Omega_r t)}{\Omega_r^3} + \right. \\ & \left. \frac{2\hat{\omega}_i \eta_6 \hat{\zeta}_i t^{(3-\gamma)}}{(3-\gamma)\Gamma(3-\gamma)} \mathcal{G}_1(\gamma, \omega_r) - \right. \\ & \left. \frac{2\hat{\omega}_i \eta_6 \hat{\zeta}_i t^{(3-\gamma)}}{(3-\gamma)\Gamma(3-\gamma)} \mathcal{G}_1(\gamma, \Omega_r) \right] \end{aligned} \right\} \tag{29b}$$

$$Y_n^1(t) = 2\omega_n \zeta_n \eta_2 \eta_5 \left\{ \begin{aligned} & \left[\frac{\eta_5 t^{1-\beta}}{(1-\beta)\Gamma(1-\beta)} \right. \\ & \left. \mathcal{G}_1(\beta, \omega_n) \right] + \left. \frac{t^{3-\beta}}{\Gamma(4-\beta)} \mathcal{G}_2(\beta, \omega_n) \right] \end{aligned} \right\} -$$

$$\eta_1 \sum_{i=1}^N \eta_4 \sum_{r=1}^{\infty} \eta_2 \eta_3 \eta_7 \left\{ \begin{aligned} & \left[\frac{\eta_6 \hat{K}_i \sin(\omega_n t)}{\omega_n} + \right. \\ & \left. \frac{\hat{K}_i \sin(\omega_r t)}{\omega_r} + \right. \\ & \left. \frac{\eta_6 \hat{K}_i \sin(\Omega_r t)}{\Omega_r} + \right. \\ & \left. \frac{\eta_6 \hat{C}_i t^{1-\gamma}}{\Gamma(2-\gamma)} \mathcal{G}_1(\gamma, \omega_n) + \right. \\ & \left. \frac{\hat{C}_i t^{1-\gamma}}{\Gamma(2-\gamma)} \mathcal{G}_1(\gamma, \omega_r) + \right. \\ & \left. \frac{\eta_6 \hat{C}_i t^{1-\gamma}}{\Gamma(2-\gamma)} \mathcal{G}_1(\gamma, \Omega_r) \right] \end{aligned} \right\} \tag{29c}$$

$$\hat{z}_i^1(t) = \sum_{r=1}^{\infty} \left[\begin{aligned} & \{ \Psi_1 - \Psi_2 \} + \\ & \left[\sum_{i=1}^N \sum_{r=1}^{\infty} \{ \Psi_3 + \Psi_4 \} + \sum_{r=1}^{\infty} \{ \Psi_5 + \Psi_6 \} \right] \end{aligned} \right] \tag{29d}$$

where:

$$\eta_2 = P_0 \Omega_n \frac{2}{\mu L}, \tag{30a}$$

$$\eta_3 = \sin(\Omega_r d_i / v), \tag{30b}$$

$$\eta_4 = \sin(\Omega_n d_i / v), \tag{30c}$$

$$\eta_5 = \frac{1}{(\omega_n^2 - \Omega_n^2)}, \tag{30d}$$

$$\eta_6 = \frac{1}{(\omega_r^2 - \Omega_r^2)}, \tag{30e}$$

$$\eta_7 = \frac{1}{(\omega_n^2 - \Omega_r^2)}, \tag{30f}$$

$$\mathcal{G}_1(\gamma, \zeta) = \text{hypergeom} \left(\begin{matrix} [1], \left[\frac{3-\gamma}{2}, \frac{2-\gamma}{2} \right] \\ -(\zeta t)^2 \\ 4 \end{matrix} \right), \tag{30g}$$

$$\mathcal{G}_2(\beta, \zeta) = \text{hypergeom} \left(\begin{matrix} [2], \left[\frac{4-\beta}{2}, \frac{5-\beta}{2} \right] \\ -(\zeta t)^2 \\ 4 \end{matrix} \right), \tag{30h}$$

$$\mathcal{G}_3(\beta, \zeta) = \text{hypergeom} \left(\begin{matrix} [2], \left[2-\beta, \frac{5-2\beta}{2} \right] \\ -(\zeta t)^2 \\ 4 \end{matrix} \right), \tag{30i}$$

$$\mathcal{G}_4(\gamma, \zeta) = \text{hypergeom} \left(\begin{matrix} [1], \left[\frac{3-2\gamma}{2}, 1-\gamma \right] \\ -(\zeta t)^2 \\ 4 \end{matrix} \right), \tag{30j}$$

$$\Psi_1 = \frac{2\eta_1\eta_2\eta_3\eta_6^2\zeta_r\hat{K}_i t^{1-\beta}}{\hat{M}_i(1-\beta)\Gamma(1-\beta)} \left\{ \frac{\omega_r t^{1-\beta}\mathcal{G}_1(\beta, \Omega_r)}{\Omega_r^2} - \frac{2\mathcal{G}_1(\beta, \omega_r)}{\omega_r} + \frac{\Omega_r^2 t^{1-\beta}\mathcal{G}_1(\beta, \omega_r)}{\omega_r^3} \right\}, \tag{30k}$$

$$\begin{aligned} \Psi_2 = & \frac{-2\eta_1\eta_2\eta_3\zeta_r\hat{C}_i t^{1-\beta-\gamma}}{\hat{M}_i\Omega_r^2\omega_r^3(1-\beta-\gamma)\Gamma(1-\beta-\gamma)} + \frac{2\eta_1\eta_2\eta_3\eta_6^2\hat{C}_i\omega_r\zeta_r t^{1-\gamma-\beta}\mathcal{G}_1(\gamma+\beta, \Omega_r)}{\hat{M}_i\Omega_r^2(1-\gamma-\beta)\Gamma(1-\gamma-\beta)} - \\ & \frac{2\eta_1\eta_2\eta_3\zeta_r\hat{K}_i t^{1-\beta}}{\hat{M}_i\omega_r^3\Omega_r^2(1-\beta)\Gamma(1-\beta)} - \frac{2\eta_1\eta_2\eta_3\eta_6\hat{C}_i\zeta_r t^{3-\gamma-\beta}\mathcal{G}_2(\gamma+\beta, \omega_r)}{\hat{M}_i\omega_r\Gamma(4-\gamma-\beta)} - \\ & \frac{2\eta_1\eta_2\eta_3\eta_6\hat{K}_i\zeta_r t^{1-\beta}\mathcal{G}_1(\beta, \omega_r)}{\hat{M}_i\omega_r(1-\beta)\Gamma(1-\beta)} + \frac{2\eta_1\eta_2\eta_3\eta_6^2\hat{C}_i\zeta_r\Omega_r^2 t^{1-\gamma-\beta}\mathcal{G}_1(\gamma+\beta, \omega_r)}{\hat{M}_i\omega_r^3(1-\gamma-\beta)\Gamma(1-\gamma-\beta)} - \\ & \frac{4\eta_1\eta_2\eta_3\eta_6^2\hat{C}_i\zeta_r t^{1-\gamma-\beta}\mathcal{G}_1(\gamma+\beta, \Omega_r)}{\hat{M}_i\omega_r(1-\gamma-\beta)\Gamma(1-\gamma-\beta)} \end{aligned} \tag{30l}$$

$$\begin{aligned} \Psi_3 = & -\frac{2\eta_1^2\eta_2\eta_3^2\eta_4\hat{K}_i t}{\hat{M}_i\omega_r^4\Omega_r} + \frac{2\eta_1^2\eta_2\eta_3^2\eta_4\eta_6^2\hat{K}_i\hat{C}_i\Omega_r^2 t^{1-\gamma}\mathcal{G}_1(\gamma, \omega_r)}{\hat{M}_i\omega_r^4(\gamma^2-\gamma)\Gamma(-\gamma)} + \\ & \frac{2\eta_1^2\eta_2\eta_3^2\eta_4\eta_6^2\hat{K}_i\hat{C}_i\Omega_r^2 t^{1-\gamma}\mathcal{G}_1(\gamma, \Omega_r)}{\hat{M}_i\Omega_r^2\gamma\Gamma(-\gamma)(\gamma-1)} + \frac{2\eta_1^2\eta_2\eta_3^2\eta_4\eta_6\hat{K}_i\hat{C}_i t^{3-\gamma}\mathcal{G}_2(\gamma, \omega_r)}{\hat{M}_i\omega_r^2\gamma\Gamma(-\gamma)(\gamma-1)(\gamma-2)(\gamma-3)} - \\ & \frac{\eta_1^2\eta_2\eta_3^2\eta_4\hat{C}_i t^{1-2\gamma}}{2\hat{M}_i\Omega_r^2\omega_r^4\gamma\Gamma(-2\gamma)(2\gamma-1)} - \frac{2\eta_1^2\eta_2\eta_3^2\eta_4\eta_6^2\hat{K}_i\hat{C}_i t^{1-\gamma}\mathcal{G}_1(\gamma, \omega_r)}{\hat{M}_i\omega_r^2\gamma\Gamma(-\gamma)(\gamma-1)} - \\ & \frac{2\eta_1^2\eta_2\eta_3^2\eta_4\hat{K}_i\hat{C}_i t^{1-\gamma}}{\hat{M}_i\omega_r^4\Omega_r^2\gamma\Gamma(-\gamma)(\gamma-1)} - \frac{\eta_1^2\eta_2\eta_3^2\eta_4\eta_6\hat{C}_i^2 t^{3-2\gamma}\mathcal{G}_3(\gamma, \omega_r)}{4\hat{M}_i\omega_r^2\gamma\Gamma(-2\gamma)(\gamma-1)(2\gamma-1)(2\gamma-3)}, \end{aligned} \tag{30m}$$

$$\Psi_4 = \frac{\eta_1^2 \eta_2 \eta_3^2 \eta_4 \eta_6^2 \hat{C}_i^2 t^{1-2\gamma} \mathcal{G}_4(\gamma, \Omega_r)}{2\hat{M}_i \Omega_r^2 \gamma \Gamma(-2\gamma) (2\gamma - 1)} + \frac{\eta_1^2 \eta_2 \eta_3^2 \eta_4 \eta_6^2 \hat{C}_i^2 \Omega_r^2 t^{1-2\gamma} \mathcal{G}_4(\gamma, \omega_r)}{2\hat{M}_i \omega_r^4 \gamma \Gamma(-2\gamma) (2\gamma - 1)} - \frac{\eta_1^2 \eta_2 \eta_3^2 \eta_4 \eta_6^2 \hat{C}_i^2 t^{1-2\gamma} \mathcal{G}_4(\gamma, \omega_r)}{\hat{M}_i \omega_r^2 \gamma \Gamma(-2\gamma) (2\gamma - 1)} + \frac{\eta_1^2 \eta_2 \eta_3^2 \eta_4 \eta_6^2 \Omega_r^2 \hat{K}_i^2 \sin(\omega_r t)}{\hat{M}_i \omega_r^5} - \frac{\eta_1^2 \eta_2 \eta_3^2 \eta_4 \eta_6 \hat{K}_i^2 \sin(\omega_r t)}{2\hat{M}_i \omega_r^5} + \frac{\eta_1^2 \eta_2 \eta_3^2 \eta_4 \eta_6 \hat{K}_i^2 \cos(\omega_r t)}{2\hat{M}_i \omega_r^4} + \frac{\eta_1^2 \eta_2 \eta_3^2 \eta_4 \eta_6^2 \hat{K}_i^2 \sin(\Omega_r t)}{\hat{M}_i \Omega_r^3} - \frac{2\eta_1^2 \eta_2 \eta_3^2 \eta_4 \eta_6^2 \hat{K}_i^2 \sin(\omega_r t)}{\hat{M}_i \omega_r^3}, \tag{30n}$$

$$\Psi_5 = \frac{\eta_1^2 \eta_2 \eta_3 \hat{C}_i^2 t^{1-2\gamma}}{\hat{M}_i^2 \Omega_r^4 \omega_r^2 \Gamma(2-2\gamma)} - \frac{\eta_1^2 \eta_2 \eta_3 \hat{C}_i^2 t^{1-2\gamma}}{\hat{M}_i^2 \Omega_r^2 \omega_r^4 \Gamma(2-2\gamma)} - \frac{\eta_1^2 \eta_2 \eta_3 \hat{C}_i^2 t^{3-2\gamma}}{\hat{M}_i^2 \Omega_r^2 \omega_r^2 \Gamma(4-2\gamma)} + \frac{\eta_1^2 \eta_2 \eta_3 \eta_6 \hat{C}_i^2 t^{1-2\gamma} \mathcal{G}_4(\gamma, \omega_r)}{\hat{M}_i \omega_r^4 \Gamma(2-2\gamma)} - \frac{\eta_1^2 \eta_2 \eta_3 \eta_6^2 \hat{C}_i^2 t^{1-2\gamma} \mathcal{G}_4(\gamma, \Omega_r)}{\hat{M}_i \Omega_r^4 \Gamma(2-2\gamma)} + \frac{2\eta_1^2 \eta_2 \eta_3 \hat{C}_i \hat{K}_i t^{1-\gamma}}{\hat{M}_i^2 \Omega_r^4 \omega_r^2 \gamma(\gamma-1)\Gamma(-\gamma)} + \frac{2\eta_1^2 \eta_2 \eta_3 \hat{C}_i \hat{K}_i t^{1-\gamma}}{\hat{M}_i^2 \Omega_r^2 \omega_r^4 \gamma(\gamma-1)\Gamma(-\gamma)}, \tag{30o}$$

$$\Psi_6 = -\frac{2\eta_1^2 \eta_2 \eta_3 \hat{C}_i \hat{K}_i t^{3-\gamma}}{\hat{M}_i^2 \Omega_r^2 \omega_r^2 \gamma(\gamma-1)(2\gamma-1)(2\gamma-3)\Gamma(-\gamma)} + \frac{2\eta_1^2 \eta_2 \eta_3 \eta_6 \hat{C}_i \hat{K}_i t^{1-\gamma} \mathcal{G}_1(\gamma, \omega_r)}{\hat{M}_i^2 \Omega_r^4 \gamma(\gamma-1)\Gamma(-\gamma)} - \frac{2\eta_1^2 \eta_2 \eta_3 \eta_6 \hat{C}_i \hat{K}_i t^{1-\gamma} \mathcal{G}_1(\gamma, \Omega_r)}{\hat{M}_i^2 \Omega_r^4 \gamma(\gamma-1)\Gamma(-\gamma)} + \frac{\eta_1^2 \eta_2 \eta_3 \hat{K}_i^2 t}{\hat{M}_i^2 \Omega_r^4 \omega_r^2} + \frac{\eta_1^2 \eta_2 \eta_3 \hat{K}_i^2 t^3}{6\hat{M}_i^2 \Omega_r^2 \omega_r^2} + \frac{\eta_1^2 \eta_2 \eta_3 \eta_6 \hat{K}_i^2 \sin(\omega_r t)}{\hat{M}_i^2 \omega_r^5} - \frac{\eta_1^2 \eta_2 \eta_3 \eta_6 \hat{K}_i^2 \sin(\Omega_r t)}{\hat{M}_i^2 \Omega_r^5}. \tag{30p}$$

Therefore, substituting Eqs. (29) into Eqs. (24), the general dynamic response of both the beam and the oscillators can be found. Hence, the analytical solution for the handled problem can be found using term-by-term inversion of the series presented in Eqs. (28), based on the general expansion theorem for the Laplace transform [66]:

$$\ell^{-1} \left(\frac{s^{\lambda-\mu}}{(s^\lambda \mp a)^{k+1}} \right) = \frac{t^{\lambda k + \mu - 1} E_{\lambda, \mu}(\pm at)}{k!}, \Re(s) > |a|^{1/\lambda}, \tag{31}$$

where $k! = \Gamma(k+1)$, and $E_{\lambda, \mu}(y)$ is the Mittag-Leffler function in two parameters, defined as [66, 77]:

$$E_{\lambda, \mu}^{(k)}(y) \equiv \frac{d^k}{dy^k} E_{\lambda, \mu}(y) = \sum_{j=0}^{\infty} \frac{(j+k)! y^j}{j! \Gamma(\lambda j + \lambda k + \mu)}, (k = 0, 1, 2, \dots) \tag{32}$$

In Eq. (30), $hypergeom(\cdot)$ is the generalized hypergeometric function defined as [55]:

$$hypergeom([n_1], [d_1, d_2], z) = \sum_{k=0}^{\infty} \frac{z^k \left(\frac{\Gamma(n_1 + k)}{\Gamma(n_1)} \right)}{k! \left(\prod_{j=1}^2 \frac{\Gamma(d_j + k)}{\Gamma(d_j)} \right)} \tag{33}$$

In the aforementioned formulation and by introducing the Mittag-Leffler function in two parameters, the method yielded an infinite series solution. A new direct operational inversion method is introduced for solving coupled linear systems of ordinary fractional differential equations, where the obtained solutions are expressed explicitly in terms of multivariate Mittag-Leffler functions [53].

The higher terms of the solution presented in Eq. (24), i.e., $\{Y_n^1(t) + Y_n^2(t) + \dots, \hat{z}_i^1(t) + \hat{z}_i^2(t) + \dots\}$ become smaller and smaller. These higher order terms go to zero as the generalized damping ratios (ζ_n) and ($\hat{\zeta}_i$) go to zero. However, the remaining non-zero series terms fit exactly the following analytical solution for the free undamped beam:

$$Y_n(t) = \frac{\eta_2 \eta_5 [\omega_n \sin(\Omega_n t) - \Omega_n \sin(\omega_n t)]}{\omega_n \Omega_n}. \tag{34}$$

This precisely fits the well-known exact solution obtained by the Duhamel integral [30].

3. Results and Discussion

In this Section, one example is given to verify the validity of the technique proposed in this paper. Furthermore, two more important case studies are introduced to show the affect of fractional-damping behaviors for both of the beam and oscillators as well as the effect of the number of oscillators (N). In all of the following case studies, the dynamic response of the beam are mainly governed by the fundamental mode ($n = 1$) of the beam. Hence, this mode has the highest influential weight upon the beam dynamic response.

3.1. Verification problem

This example is given to verify the validity of the technique proposed in this paper, data from [72, 83] are used for this purpose (see Table 1). In this problem, the response of an initially stationary beam subjected to a moving load with a constant velocity is considered. The beam is assumed to be free or appendaged to one, two or three oscillators ($N = 0, 1, 2, 3$) and ($i = 1, \dots, N$) at different locations of the beam (see Figure 2), where ($N = 0$) refers to a beam without any appendages, i.e., all properties of oscillator are null. The case for ($N = 1$) was studied in [83] as a two DOF system, while in [72] it was analyzed using

the Euler-Bernoulli theory. In [72], the Galerkin-Bubnov variation method is used to solve the beam problem with only one absorber attached at the mid-span of the beam. The order of the fractional derivative for both the beam and the oscillator is assumed to be unity, i.e., $\beta = \gamma = 1$. Figures 3-5, show the maximum response of the beam at the mid-span versus the velocity of the moving load for three different values of the damping ratio of the beam, i.e., $\zeta = 0$, $\zeta = 0.075$ and $\zeta = 0.15$, respectively. The upper two curves in Figure 3 agree with published results in [72, 83].

The curve for ($N = 0$) in Figure 3 fits exactly the well-known exact solution which is obtained by the Duhamel integral [30]. Furthermore, we note from Figs. 3-5 that as both the number of absorbers attached to the beam and as the damping beam-ratio increases the dynamic response decreases. This is clearly seen from the lowest curve in Figure 5 where $N=3$ and $\zeta = 0.15$. Moreover, from Figure 3 the critical velocity of the moving load at which the maximum displacement occurs is $v = 22$ m/s. It can be noticed that, at this velocity the second load frequency ($n=2$) approaches the first natural frequency of the beam. However, this value can be verified theoretically by computing the load frequency Ω_n , Eq. (23), and compare it with the first natural frequency ω_1 , Eq. 14, for the given data of Table 1.

Table 1. Material and geometrical properties of beam and oscillators

Problem	Properties of Beam and Oscillators
Verification Problem in Sec. 3.1	$\beta = 1, \gamma = 1, \hat{\zeta}_i = 0.1846356 (i = 1, 2, \dots, N), N = 1: \{d_1 = L/2(m)\},$ $N = 2: \left\{ \begin{array}{l} d_1 = (L/2 - \delta)m \\ d_2 = (L/2 + \delta)m \end{array} \right\}, N = 3: \left\{ \begin{array}{l} d_1 = (L/2 - \delta)m \\ d_2 = (L/2)m \\ d_3 = (L/2 + \delta)m \end{array} \right\}, \delta = 0.02 \text{ m}.$
Problems in Sec. 3.2	$N = 1, d_1 = (L/2)m, v = 22 \text{ m/s}.$
Problems in Sec. 3.3	$\beta = 1.2, \gamma = 1.05, v = 22, \hat{\zeta}_i = 0.3693712 (i = 1, 2, \dots, N), \delta = 0.02 \text{ m},$ $N = 1: \{d_1 = L/2(m)\}, N = 2: \left\{ \begin{array}{l} d_1 = (L/2 - \delta)m \\ d_2 = (L/2 + \delta)m \end{array} \right\}, N = 3: \left\{ \begin{array}{l} d_1 = (L/2 - \delta)m \\ d_2 = (L/2)m \\ d_3 = (L/2 + \delta)m \end{array} \right\}.$
For all Problems	$L = 4 \text{ m}, E = 206.8 \text{ GPa}, \rho = 7820 \text{ kg/m}^3, P_0 = 9.8 \text{ N}, A = 0.03 \times 0.03 \text{ m}^2,$ $\hat{M}_i = 1.4076 \text{ kg}, \hat{K}_i = 877.767 \text{ N/m}, \text{ for } i = 1, 2, \dots, N$

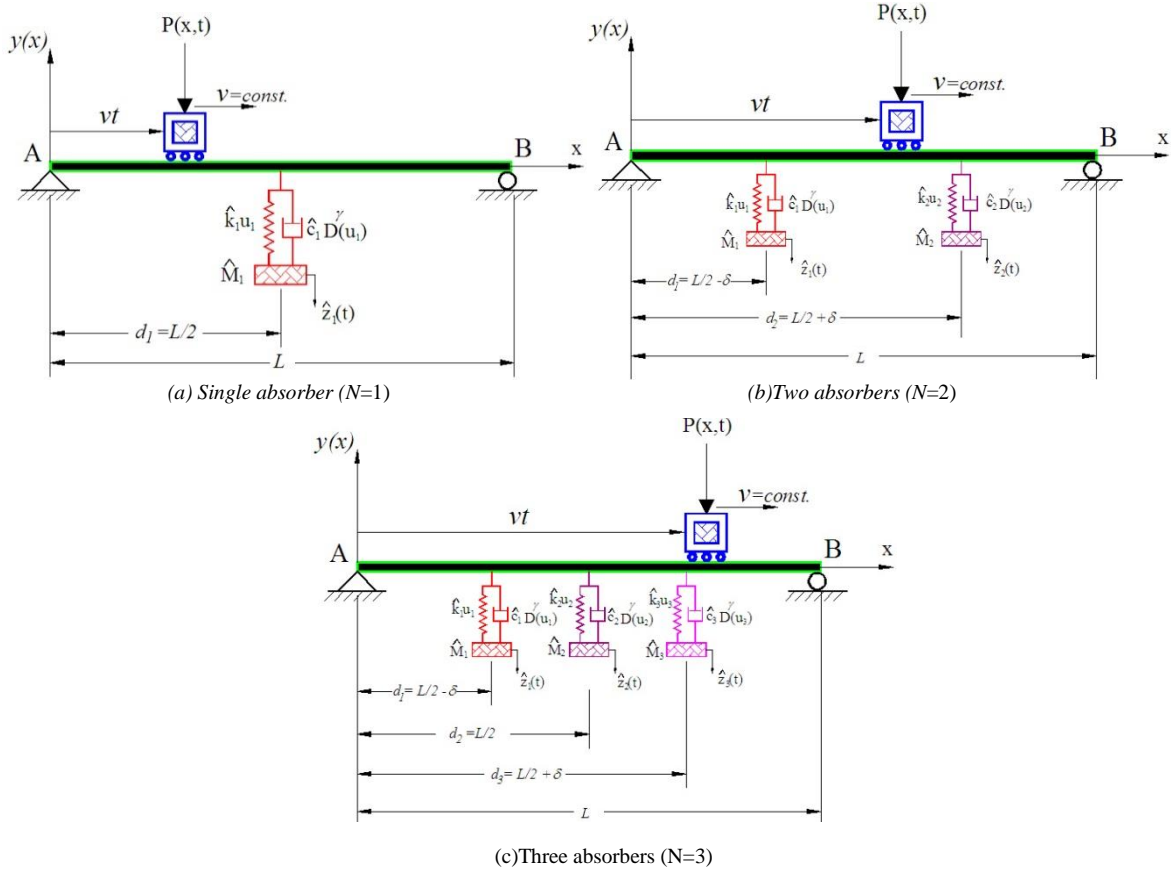


Figure 2. Case studies for simply-supported beam with multi-absorbers: (a) $N=1$, (b) $N=2$, and (c) $N=3$.

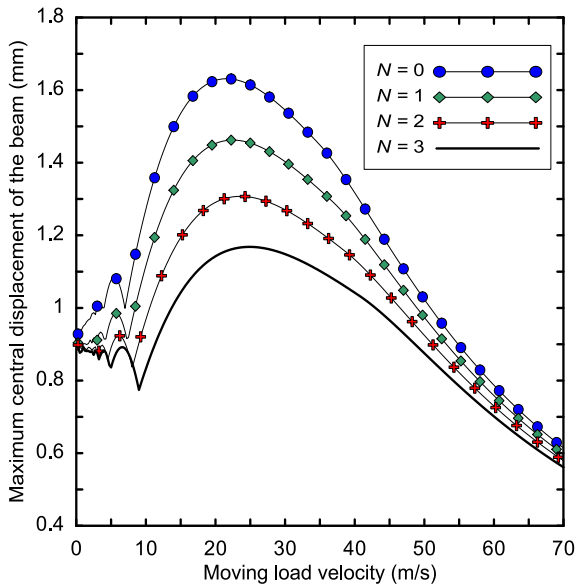


Figure 3. The maximum displacement of the beam at mid-span versus the velocity of the moving load for $\zeta = 0$.

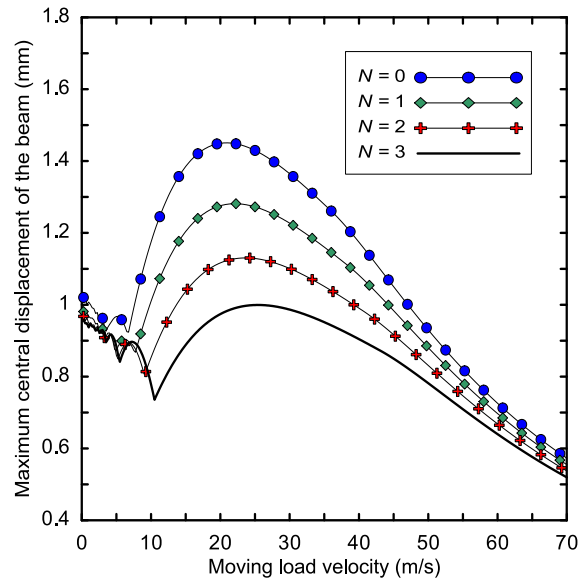


Figure 4. The maximum displacement of the beam at mid-span versus the velocity of the moving load for $\zeta = 0.075$.

3.2. Optimization of the Fractional Derivative

In this Section, two examples are analyzed to show the effect of the order of fractional derivatives for both of the beam and absorbers. In the first example, we assume that ($N=1, \gamma=1, \hat{\zeta}_1=0.1846356, 0 < \beta < 2$) while in the second example we assume that ($N=1, \beta=1, \zeta_1=0.15, 0 < \gamma < 2$). For both examples, one SDOF absorber is appendaged at the mid-span of the beam ($N=1$). Moreover, the critical mean velocity of the moving load at which the maximum displacement occurs (c.f. Figs. 3-5), is almost $v=22$ m/s. This velocity is the mean value for ($N=1$) with ($\zeta_1=0, \zeta_1=0.075$, and $\zeta_1=0.15$). This velocity ($v=22$ m/s) is further used in performing the upcoming numerical examples. The curves shown in Figure 6 (for the data given in Table 1) represent the variation of maximum central deflection of the beam mid-span (where the absorber is attached) with the beam fractional derivative β . On the other hand, Figure 7 shows the variation of maximum central deflection of the beam at mid-span with the oscillator fractional derivative γ .

The obtained curves in Figs. 6-7 lead to a very interesting critical values of β and γ ; these values are ($\beta=1.2$ when $\zeta=0.15$, $\beta=1.35$ when $\zeta=0.075$, $\gamma=1.05$ when $\hat{\zeta}_1=0.3692712$, $\gamma=1.175$ when $\hat{\zeta}_1=0.1846356$) at which the beam has minimum deflections.

3.3. Effect of the Number of Oscillators on Central Deflection

In this Section, the optimal values obtained in Secs. 3.1-3.2 ($\beta=1.2, \gamma=1.05, v=22$ m/s) for $\hat{\zeta}_1=0.3692712$ and $\zeta=0.15$ of the beam and oscillator are used to determine the dynamic response of the beam attached to many oscillators. The other parameters considered in this example are shown in Table 1. Figures 8-10 show the dynamic response of the beam for various values of beam damping ratio ($\zeta=0, \zeta=0.075, \zeta=0.15$), respectively. The effects of the beam damping ratio and the number of oscillators clearly observed from the corresponding curves in Figs. 8-10. The effect of the previously obtained optimal values is seen clearly when Figure 5 is compared with Figure 10. The percent relative error reduction in the central deflection of the beam is computed for ($N=0, N=1, N=2, N=3$) as (14.52%, 25.22%, 37.88%, 48.03%), respectively. This reduction in beam displacement is due to the effect of the optimal values of the fractional order derivatives, beam damping ratio, oscillators damping ratios, and the number of the attached oscillators.

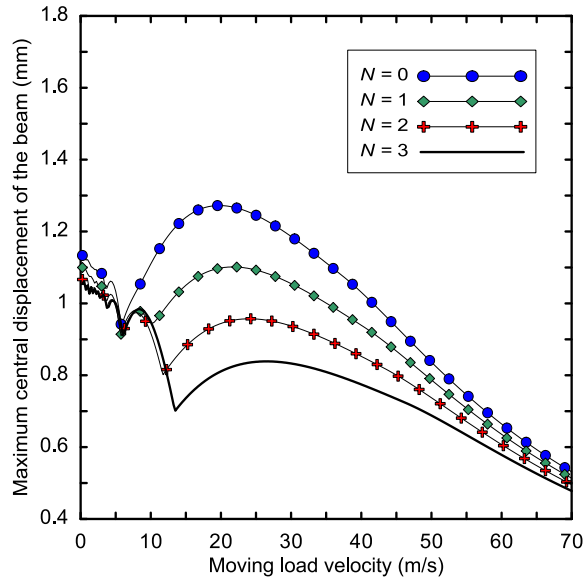


Figure 5. The maximum displacement of the beam at mid-span versus the velocity of the moving load for $\zeta = 0.15$.

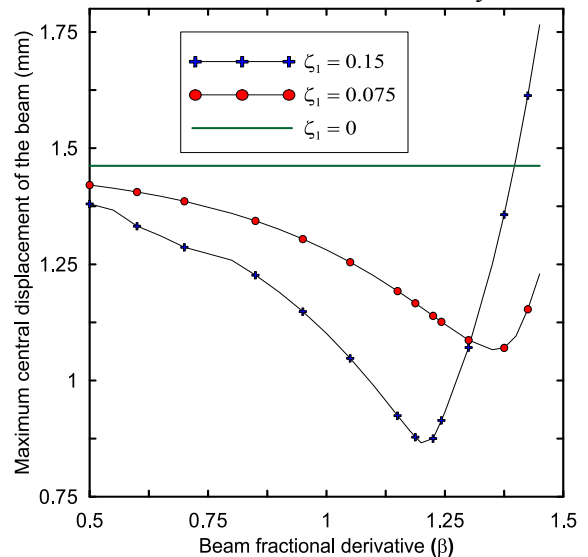


Figure 6. The maximum central deflection of the beam against the order of the beam's fractional derivative (β).

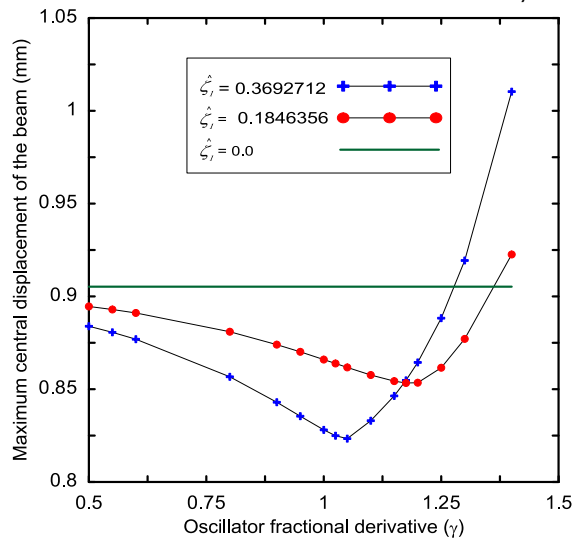


Figure 7. The maximum central deflection of the beam against the order of the oscillator's fractional derivative (γ).

4. Conclusions and Future Work

An analytical model is presented to solve the transverse vibration of Bernoulli-Euler beam attached to SDOF N -oscillators with damping characteristics that are described in terms of fractional derivatives. Furthermore, the damping characteristics of the absorbers are assumed to be fractional. The method employed is the Laplace transform with the decomposition method to find the solution. Although the method used has the ability to get the analytical solution directly by introducing the Mittag-Leffler function, this solution may be written in a closed form for some special cases; otherwise, it may be truncated and fulfilled easily by using mathematical software such as Maple.

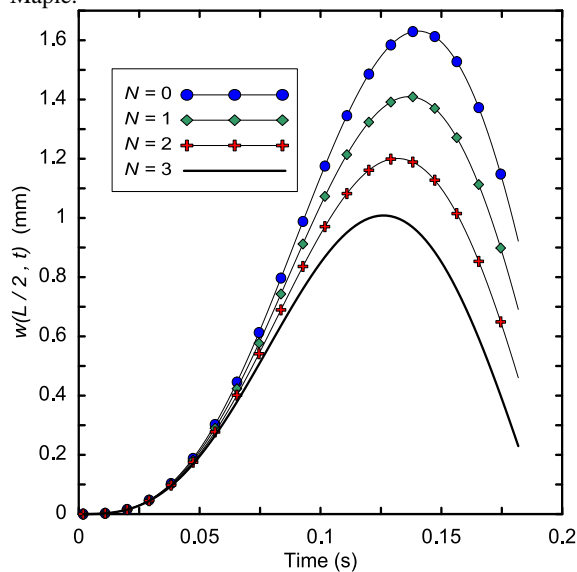


Figure 8. The dynamic response ($w(L/2, t)$) for the beam attached to many absorbers with $\zeta = 0$.

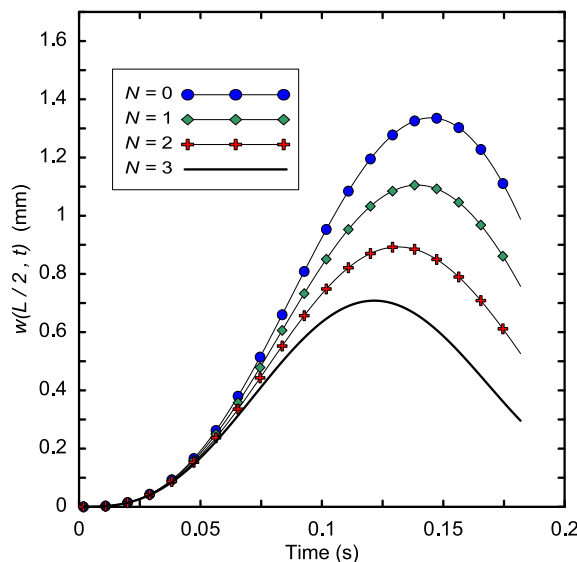


Figure 9. The dynamic response ($w(L/2, t)$) for the beam attached to many absorbers with $\zeta = 0.075$.

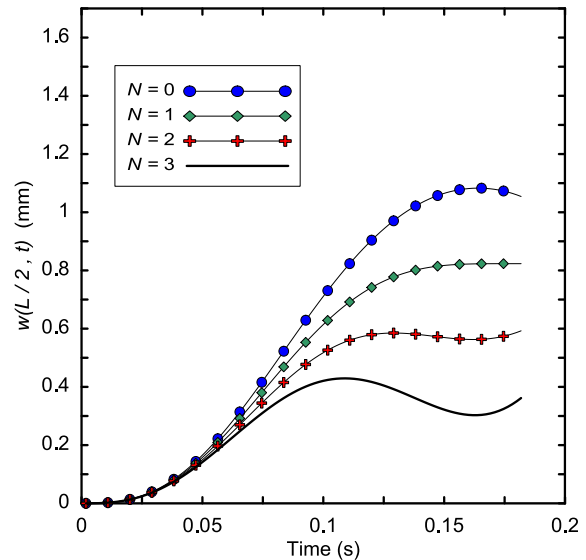


Figure 10. The dynamic response ($w(L/2, t)$) for the beam attached to many absorbers with $\zeta = 0.15$.

The numerical results obtained in this paper, show that: (1) the dynamic response decreases as the number of absorbers attached to the beam increases, (2) as both the damping-ratios of absorbers and beam increase the dynamic response decreases, and (3) there are some critical values of β and γ ($\beta > 1$, $\gamma > 1$) at which the beam has less deflection than that obtained from the full-order derivative models (i.e., $\beta = 1$ and $\gamma = 1$).

Finally, even though the fractional derivative provides better damping models of fractionally damped structures and materials, limited number of papers have been presented in this field. This is probably due to the fact that the underlying mathematics of the fractional derivative models is not well-developed. Hence, recent development in this field will lead to the development of fractional derivative models in many engineering problems. The approach of the fractional derivative damping may allow researchers to choose suitable mathematical models that fit precisely experimental models. In general, there is no clear industrial application where the empirical formulas describing viscoelastic or elastic materials fit exactly the experimental data. So, what the researchers are trying to do is to study a proper model that governs the internal or external damping behavior of even simple realistic models that use complex industrial materials.

Future work will involve the following items for the application of the fractional calculus-based approach that is used in this paper within: (1) quantum computing circuits and systems [7-9], (2) fractal-based formulations to the micro-quasistatic thermo-viscoelastic creep for rough surfaces in contact [3], and (3) other beam configurations for various boundary conditions and moving loads and oscillators.

References

- [1] M. Abu-Hilal, H. Zibdeh, "Vibration Analysis of Beams with General Boundary Conditions Traversed by a Moving Force". *Journal of Sound and Vibration*, Vol. 229 (2000) No. 2, 377-388.
- [2] R. Abu-Mallouh, I. Abu-Alshaiikh, H. S. Zibdeh, Khalid Ramadan, "Response of Fractionally Damped Beams with General Boundary Conditions Subjected to Moving Loads". *Shock and Vibration*, Vol. 19 (2012) No. 3, 333-347.
- [3] O. M. Abuzeid, A. N. Al-Rabadi, H. S. Alkhalidi, "Recent Advancements in Fractal Geometric-Based Nonlinear Time Series Solutions to the Micro-Quasistatic Thermo viscoelastic Creep for Rough Surfaces in Contact". *Mathematical Problems in Engineering (MPE)*, U.S.A., Vol. 2011 (2011), Article ID 691270, 29 pages, doi:10.1155/2011/691270.
- [4] S. Adhikari, "Qualitative Dynamic Characteristics of a Non-Viscously Damped Oscillator". *Proceedings of the Royal Society of London, Series-A*, 461(2059), p. 2269-2288, 2005.
- [5] G. Adomian, "A New Approach to Nonlinear Partial Differential Equations". *Journal of Mathematical Analysis and Applications*, Vol. 102 (1984), 420-434.
- [6] G. Adomian, "Solving Frontier Problems of Physics: The Decomposition Method". *Fundamental Theories of Physics*, Kluwer Academic Publication, 1994.
- [7] A. N. Al-Rabadi, *Reversible Logic Synthesis: From Fundamentals to Quantum Computing*, Springer-Verlag, First Edition, New York, 2004.
- [8] A. N. Al-Rabadi, "Soft Computation Using Artificial Neural Estimation and Linear Matrix Inequality Transmutation for Controlling Singularly-Perturbed Closed Time-Independent Quantum Computation Systems, Part A: Basics and Approach". *Intelligent Automation and Soft Computing (IASC)*, AutoSoft, TSI Press, U.S.A., Vol. 18 (2012) No. 1, 75-95.
- [9] A. N. Al-Rabadi, "Soft Computation Using Artificial Neural Estimation and Linear Matrix Inequality Transmutation for Controlling Singularly-Perturbed Closed Time-Independent Quantum Computation Systems, Part B: Hierarchical Regulation Implementation". *Intelligent Automation and Soft Computing (IASC)*, AutoSoft, TSI Press, U.S.A., Vol. 18 (2012) No. 1, 97-115.
- [10] K. Alsaif, M. Foda, "Vibration Suppression of a Beam Structure by Intermediate Masses and Springs". *Journal of Sound and Vibration*, Vol. 256 (2002) No. 4, 629-645.
- [11] L. Andrews, *Special Functions of Mathematics for Engineers*, SPIE Publications, 2nd Edition, 1997.
- [12] O. Agrawal, "Analytical Solution for Stochastic Response of a Fractionally Damped Beam". *Journal of Vibration and Acoustics*, Vol. 126 (2004), 561-566.
- [13] A. Argento, H. Morano, R. Scott, "Accelerating Load on a Rotating Rayleigh Beam". *Journal of Vibration and Acoustics*, Vol. 116 (1994), 397-403.
- [14] A. Argento, R. Scott, "Dynamic Response of a Rotating Beam Subjected to an Accelerating Distributed Surface Force". *Journal of Sound and Vibration*, Vol. 157 (1992) No. 2, 221-231.
- [15] K. Avramov, O. Gendelman, "On Interaction of Vibrating Beam with Essentially Nonlinear Absorber". *Meccanica*, Vol. 45 (2009) No. 3, 355-365.
- [16] R. Bagley, P. Torvik, "On the Appearance of the Fractional Derivative in the Behavior of Real Materials". *Journal of Applied Mechanics*, Vol. 51 (1984) No. 2, 294-298.
- [17] R. Bagley and P. Torvik, "On the Fractional Calculus Model of Viscoelastic Behavior". *Journal of Rheology*, Vol. 30 (1986) No. 1, 133-135.
- [18] R. Bogacz, C. Bajer, "Active Control of Beams Under a Moving Load". *Journal of Theoretical and Applied Mechanics*, Vol. 38 (2000) No. 3, 523-530.
- [19] P. Cha, "A General Approach to Formulating the Frequency Equation for a Beam Carrying Miscellaneous Attachments". *Journal of Sound and Vibration*, Vol. 286 (2005) No. 4-5, 921-939.
- [20] A. Chatterjee, "Statistical Origins of Fractional Derivatives in Viscoelasticity". *Journal of Sound and Vibration*, Vol. 284 (2005) No. 5, 1239-1245.
- [21] Y. Chen, D. Chen, "Timoshenko Beam with Tuned Mass Dampers to Moving Loads". *ASCE Journal of Bridge Engineering*, Vol. 9 (2004) No. 2, 167-177.
- [22] G. Cottone, M. Di-Paola, S. Butera, "Stochastic Dynamics of Nonlinear Systems with a Fractional Power-Law Nonlinear Term: The Fractional Calculus Approach". *Probabilistic Engineering Mechanics*, Vol. 26 (2011), 101-108.
- [23] J. Cresson, P. Inizan, "About Fractional Hamiltonian Systems". *Physica Scripta*, T136, Vol. 2009, doi:10.1088/0031-8949/2008/T136/014007, 6 pages, 2009.
- [24] J. Donga, M. Xu, "Some Solutions to the Space Fractional Schrödinger Equation Using Momentum Representation Method". *Journal of Mathematical Physics*, Vol. 48 (2007), 072105.
- [25] R. Eid, S. Muslih, D. Baleanu, E. Rabei, "Fractional Dimensional Harmonic Oscillator". *Romanian Journal of Physics*, Vol. 56 (2011) No. 3-4.
- [26] J. Espindola, G. Cruz, E. Lopes and C. Bavastrri, "Design of Optimum Viscoelastic Vibration Absorbers Based on the Fractional Calculus Model". *Proceedings of the XI DINAME, Ouro Preto-MG-Brazil*, 2005.
- [27] K. Fa, "A Falling Body Problem Through the Air in View of the Fractional Derivative Approach". *Physica A: Statistical Mechanics and its Applications*, Vol. 350 (2005) No. 2-4, 199-206.
- [28] M. Foda and Z. Abduljabbar, "A Dynamic Green Function Formulation for the Response of a Beam Structure to a Moving Mass". *Journal of Sound and Vibration*, Vol. 210 (1998) No. 3, 295-306.
- [29] M. Friswell, S. Adhikari, Y. Lei, "Non-Local Finite Element Analysis of Damped Beams". *International Journal of Solids and Structures*, Vol. 44 (2007) No. 22-23, 7564-7576.
- [30] L. Fryba, "Vibration of Solids and Structures under Moving Loads". *Noordhoff International Publishing, Groningen, The Netherlands*, 1972.
- [31] L. Fryba, "Non-Stationary Response of a Beam to a Moving Random Force". *Journal of Sound and Vibration*, Vol. 46 (1976), 323-338.
- [32] F. Georgiades, A. Vakakis, "Dynamics of a Linear Beam with an Attached Local Nonlinear Energy Sink". *Communications in Nonlinear Science and Numerical Simulation*, Vol. 12 (2007), 643-651.
- [33] E. Goldfain, "Fractional Dynamics and Standard Model for Particle Physics". *Communications in Nonlinear Science and Numerical Simulation*, Vol. 13 (2008), 1397-1404.
- [34] M. Gurgoze, "A Note on the Vibrations of Restrained Beams and Rods with Point Masses". *Journal of Sound and Vibration*, Vol. 96 (1984) No. 4, 461-468.
- [35] R. Gutiérrez, J. Rosário, J. Machado, "Fractional Order Calculus: Basic Concepts and Engineering Applications". *Mathematical Problems in Engineering*, Vol. 2010, Article ID 375858, 19 pages, 2010.
- [36] R. Hibbeler, *Mechanics of Materials*, Prentice-Hall, 8th Edition, 2011.
- [37] Z. Huang, X. Jin, "Response and Stability of a SDOF Strongly Nonlinear Stochastic System with High Damping Modeled by a Fractional Derivative". *Journal of Sound and Vibration*, Vol. 319 (2009), 1121-1135.
- [38] A. Jimenez, J. Santiago, A. Garcia, J. Gonzalez, "Relaxation Modulus in PMMA and PTFE Fitting by Fractional Maxwell Model". *Polymer Testing*, Vol. 21 (2002) 325-331.
- [39] R. Katz, C. Lee, A. Ulsoy, R. Scott, "The Dynamic Response of a Rotating Shaft Subject to a Moving Load". *Journal of Sound and Vibration*, Vol. 122 (1988) No. 1, 131-148.
- [40] R. Keltie, C. Cheng, "Vibration Reduction of a Mass-Loaded Beam". *Journal of Sound and Vibration*, Vol. 187 (1995) No. 2, 213-228.
- [41] C. Koh, J. Kelly, "Application of Fractional Derivatives to Seismic Analysis of Base-Isolated Models". *Earthquake*

- Engineering and Structural Dynamics, Vol. 19 (1990), 229–241.
- [42] K. M. Kolwankar, *Studies of Fractal Structures and Processes Using Methods of the Fractional Calculus*, Ph.D. Dissertation, University of Pune, 1998.
- [43] H. Kwon, M. Kim, I. Lee, “Vibration Control of Bridges under Moving Loads”. *Computers and Structures*, Vol. 66 (1998) No. 4, 473-480.
- [44] M. Li, “Fractal Time Series- A Tutorial Review”. *Mathematical Problems in Engineering*, Vol. 2010, Article ID 157264, 26 pages, doi:10.1155/2010/157264, 2010.
- [45] M. Li, “Approximating Ideal Filters by Systems of Fractional Order”. *Computational and Mathematical Methods in Medicine*, Vol. 2012, Article ID 365054, 6 pages, doi: 10.1155/2012/365054, 2012.
- [46] M. Li, C. Cattani, SY Chen, “Viewing Sea Level by a One-Dimensional Random Function with Long Memory”. *Mathematical Problems in Engineering*, Vol. 2011, Article ID 654284, 13 pages, doi:10.1155/2011/654284, 2011.
- [47] M. Li, S. C. Lim, C. Cattani, M. Scalia, “Characteristic Roots of a Class of Fractional Oscillators”. *Advances in High Energy Physics*, Vol. 2013, Article ID 853925, 7 pages, 2013.
- [48] M. Li, S. C. Lim, SY Chen, “Exact Solution of Impulse Response to a Class of Fractional Oscillators and its Stability”. *Mathematical Problems in Engineering*, Vol. 2011, Article ID 657839, 9 pages, doi:10.1155/2011/657839, 2011.
- [49] M. Li, W. Zhao, “Representation of a Stochastic Traffic Bound”. *IEEE Transactions on Parallel and Distributed Systems*, Vol. 21 (2010) No.9, 1368-1372.
- [50] M. Li, W. Zhao, “Visiting Power Laws in Cyber-Physical Networking Systems”. *Mathematical Problems in Engineering*, Vol. 2012, Article ID 302786, 13 pages, doi:10.1155/2012/302786, 2012.
- [51] M. Li, W. Zhao, C. Cattani, “Delay Bound: Fractal Traffic Passes through Servers”. *Mathematical Problems in Engineering*, Vol. 2013, Article ID 157636, 15 pages, 2013.
- [52] Z. Liang, X. Tang, “Analytical Solution of Fractionally Damped Beam by Adomian Decomposition Method”. *Applied Mathematics and Mechanics*, Vol. 28 (2007) No. 2, 219-228.
- [53] S. C. Lim, C. H. Eab, K. H. Mak, M. Li, SY Chen, “Solving Linear Coupled Fractional Differential Equations and their Applications”. *Mathematical Problems in Engineering*, Vol. 2012, Article ID 653939, 28 pages, doi:10.1155/2012/653939, 2012.
- [54] S. C. Lim, M. Li, L. P. Teo, “Langevin Equation with Two Fractional Orders”. *Physics Letters A*, Vol. 372 (2008) No.42, 6309-6320.
- [55] Y. L. Luke, *The Special Functions and their Approximations*, Academic Press, New York, 1969.
- [56] N. Makris, M. Constantinou, “Fractional Derivative Maxwell Model for Viscous Damper”. *Journal of Structural Engineering*, ASCE, Vol. 117 (1991) No. 9, 2708–2724.
- [57] A. Mallik, S. Chandra, A. Singh, “Steady State Response of an Elastically Supported Infinite Beam to a Moving Load”. *Journal of Sound and Vibration*, Vol. 291 (2006) No. 3-5, 1148-1169.
- [58] G. Michaltsos, D. Sophianopoulos, A. Kounadis, “The Effect of a Moving Mass and Other Parameters on the Dynamic Response of a Simply Supported Beam”. *Journal of Sound and Vibration*, Vol. 191 (1996) No. 3, 357-362.
- [59] R. Matušů, “Application of Fractional Order Calculus to Control Theory”. *International Journal of Mathematical Models and Methods in Applied Sciences*, Vol. 5 (2011) No. 7, 1162-1169.
- [60] S. Momani, R. Ibrahim, “Analytical Solutions of a Fractional Oscillator by the Decomposition Method”. *International Journal of Pure and Applied Mathematics*, Vol. 37 (2007) No. 1, 119-131.
- [61] J. Nicholson, L. Bergman, “Free Vibration of Combined Dynamical Systems”. *ASCE Journal of Engineering Mechanics*, Vol. 112 (1986) No. 1, 1-13.
- [62] H. Ouyang, “Moving-Load Dynamic Problems: A Tutorial (With a Brief Overview)”. *Mechanical Systems and Signal Processing*, Vol. 25 (2011), 2039–2060.
- [63] A. Palfalvi, “Efficient Solution of a Vibration Equation Involving Fractional Derivatives”. *International Journal of Non-Linear Mechanics*, Vol. 45 (2010), 169–175.
- [64] M. Di Paola, A. Pirrotta, A. Valenza “Visco-elastic behavior through fractional calculus: An easier method for best fitting experimental results”. *Mechanics of Materials*, Vol. 43 (2011), 799-806.
- [65] A. Pesterev, L. Bergman, “An Improved Series Expansion of the Solution to the Moving Oscillator Problem”. *ASME Journal of Vibration and Acoustics*, Vol. 122 (2000) No. 1, 54-61.
- [66] I. Podlubny, *Fractional Differential Equations*, Academic Press, San Diego, 1999.
- [67] T. Pritz, “Five-Parameter Fractional Derivative Model for Polymeric Damping Materials”. *Journal of Sound and Vibration*, Vol. 265 (2003) No. 5, 935-952.
- [68] H. Qi, M. Xu, “Unsteady Flow of Viscoelastic Fluid with Fractional Maxwell Model in a Channel”. *Mechanics Research Communications*, Vol. 34 (2007) No. 2, 210-212.
- [69] R. Rao, *Mechanical Vibrations*, Addison-Wesley, 3rd Edition, 1995.
- [70] S. Ray, B. Poddar, R. Bera, “Analytical Solution of a Dynamic System Containing Fractional Derivative of Order One-Half by Adomian Decomposition Method”. *Journal of Applied Mechanics*, Vol. 72 (2005), 290-295.
- [71] P. Rozmej, B. Bandrowski, “On Fractional Schrödinger Equation”. *Computational Methods in Science and Technology*, Vol. 16 (2010) No. 2, 191-194.
- [72] F. Samani, F. Pellicano, “Vibration Reduction on Beams Subjected to Moving Loads Using Linear and Nonlinear Dynamic Absorbers”. *Journal of Sound and Vibration*, Vol. 325 (2009), 742-754.
- [73] F. Samani, F. Pellicano, “Vibration Reduction of Beams Under Successive Traveling Loads by Means of Linear and Nonlinear Dynamic Absorbers”. *Journal of Sound and Vibration*, Vol. 331 (2012) No. 10, 2272-2290.
- [74] E. Savin, “Dynamic Amplification Factor and Response Spectrum for the Evaluation of Vibrations of Beams under Successive Moving Loads”. *Journal of Sound and Vibration*, Vol. 248 (2001) No. 2, 267-288.
- [75] A. Shahin, E. Ahmed, Y. Omar, “On Fractional Order Quantum Mechanics”. *International Journal of Nonlinear Science*, Vol. 8 (2009) No. 4, 469-472.
- [76] N. Shimizu, W. Zhang, “Fractional Calculus Approach to Dynamic Problems of Viscoelastic Materials”. *JSME International Journal, Series C*, Vol. 42 (1999) No. 4, 825–837.
- [77] H. Sheng, Y.-Q. Chen, and T.-S. Qiu, *Fractional Processes and Fractional Order Signal Processing*, Springer, 2012.
- [78] D. Sierociuk, A. Dzielinski, “Fractional Kalman Filter Algorithm for the States, Parameters and Order of Fractional System Estimation”. *International Journal of Applied Mathematics and Computer Science*, Vol. 16 (2006) No. 1, 129-140.
- [79] P. Sniady, “Dynamic Response of Linear Structures to a Random Stream of Pulses”. *Journal of Sound and Vibration*, Vol. 131 (1989) No. 1, 91-102.
- [80] R. Soares, Z. Prado, P. Gonçalves, “On the Vibration Control of Beams Using a Moving Absorber and Subjected to Moving Loads”. *Asociación Argentina de Mecánica Computacional*, Vol. XXIX, 1829-1840, 2010.
- [81] Y. Starosvetsky, O. Gendelman, “Attractors of Harmonically Forced Linear Oscillator With Attached Nonlinear Energy Sink II: Optimization of a Nonlinear Vibration Absorber”. *Nonlinear Dynamics*, Vol. 51 (2008), 47-57.
- [82] D. Thambiratnam, Y. Zhuge, “Dynamic Analysis of Beams on an Elastic Foundation Subjected to Moving Point Loads”. *Journal of Sound and Vibration*, Vol. 198 (1996) No. 2, 149-169.

- [83] J. Wu, "Study on the Inertia Effect of Helical Spring of the Absorber on Suppressing the Dynamic Responses of a Beam Subjected to a Moving Load". *Journal of Sound and Vibration*, Vol. 297 (2006), 981-999.
- [84] B. Yang, C. Tan, L. Bergman, "Direct Numerical Procedure for Solution of Moving Oscillator Problems". *ASCE Journal of Engineering Mechanics*, Vol. 126 (2000) No. 6, 462-469.
- [85] Y. Yang, C. Lin, "Vehicle-Bridge Interaction Dynamics and Potential Applications". *Journal of Sound and Vibration*, Vol. 284 (2005) No. 1-2, 205-226.
- [86] W. ZaiHua, H. Yan, "Stability of a Linear Oscillator with Damping Force of the Fractional-Order Derivative". *Science China Physics, Mechanics & Astronomy*, Vol. 53 (2010) No. 2, 345-352.
- [87] H. Zibdeh, "Stochastic Vibration of an Elastic Beam Due to Random Moving Loads and Deterministic Axial Forces". *Engineering Structures*, Vol. 17 (1995) No. 7, 530-535.
- [88] H. Zibdeh, R. Rackwitz, "Moving Loads on Beams with General Boundary Conditions". *Journal of Sound and Vibration*, Vol. 195 (1996) No. 1, 85-102.
- [89] H. Zibdeh, H. Juma, "Dynamic Response of a Rotating Beam Subjected to a Random Moving Load". *Journal of Sound and Vibration*, Vol. 223 (1999) No. 18, 741-758.
- [90] H. Zibdeh, I. Abu-Alshaikh, "Vibration Response of a Beam with Different Appendages Subjected to a Moving System". *International Journal of Vehicle Noise and Vibration*, Vol. 4 (2008), 93-106.

Nonlinear Dynamic Modeling of Double Helical Gear System

Chang Qinglin, Hou Li ^{*}, Sun Zhijun, Wang Wei, You Yunxia

School of Manufacturing Science and Engineering, Sichuan University, No.24 South Section 1, Yihuan Road, 610065 Chengdu, China.

Received 3 April 2014

Accepted 3 Sep 2014

Abstract

Double helical gear transmission is a very important transmission component. A lot of dynamic models of spur and helical gears for studying dynamic characteristics have been put forward, but the studies on double helical gears are scarce. To study the nonlinear dynamic characteristics of the double helical gear system, the nonlinear dynamic model of double helical gear system was established. Then the dimensionless dynamic model was summarized. Through numerical computation, the nonlinear dynamic characteristic was revealed in some aspect. The vibration amplitude of gear is smaller than the vibration amplitude of pinion at the same direction and the vibration amplitude of the same component at direction is larger than the amplitude of gear at direction. Through the numerical method, we find that there is a plenty of nonlinear dynamic characteristics in the double helical gear system, and thus more research is needed.

© 2014 Jordan Journal of Mechanical and Industrial Engineering. All rights reserved

Keywords: : *Time-Varying Meshing Stiffness; Meshing Damping; Double Helical Gear; Nonlinear Characteristics.*

1. Introduction

Gear transmission is the most common transmission system and is widely used in the production of national industries. It is also a particularly important key component. It has three basic forms: spur, helical and double helical. Because of alternate meshing of single and double spur gear teeth in the transmission, the meshing stiffness changed with large amplitude when the coincidence degree is not an integer, motivating large vibration and noise [1-3]. There is not alternate meshing of single and double gear teeth in the helical gear system and the stiffness mutation, so it's meshing smoother. But there are some shortcomings in the helical gear system, for example: the dynamic axial load, time-varying mesh wire length, time-varying frictional force and time-varying frictional torque [4-9]. The dynamic axial load of double helical gear was eliminated though the time-varying frictional force and time-varying frictional torque exist. Because of its high carrying capacity, smooth transmission, and no axial load, the double helical gear has been widely used. As we all known, many nonlinear factors such as time-varying mesh stiffness, time-varying mesh damping, meshing impact, backlash, time-varying frictional force and friction torque in double helical gear system will generate complex nonlinear vibration. However, studies on system dynamics of double helical gear is seldom, the research on double helical gear system dynamics is very necessary.

Wesley Blankenship G. and Singh R. [10] studied the dynamic meshing force, stiffness and transfer matrix in

helical gear system, and researched backlash nonlinear characteristics under different modal parameters. IMAMURA.Y and SATO.S [11] studied the distribution of dynamic stress in gear systems. Walha L. [12] and his partners studied the nonlinear dynamic response of helical gear system with mass eccentricity. Wei [13-14] studied the friction nonlinear characteristics in-depth in the spur gear system. Ma Hui [15] analyzed the influence of eccentric load in helical gear system in detail and studied the dynamic characteristic in eccentric helical gear system by the method of modal analysis and coupling analysis. Wang Qing [16] established the coupling dynamic model and system differential equations of cylindrical helical gear transmission considering time-varying mesh stiffness, backlash and transmission error. N. Leiba [17] studied the vibro-impact phenomenon by experimental and numerical method. Song Xiaoguang [18] studied the nonlinear characteristics of the flexible shaft helical gear system considering backlash, bearing radial clearance and gear unbalanced force. Tang Jinyuan and Chen Siyu [19-20] proposed an improved nonlinear dynamics model of the spur gear. On the basis of the model, the gap nonlinear characteristics were analyzed. Wang Feng and Wang Cheng [21-23] established a dynamic model of herringbone gears, then the herringbone gears' dynamic characteristics were analyzed, but the calculation and analysis of time-varying parameters and nonlinear factors were not concerned. Li Wenliang [24] analyzed the friction force in helical gear and the bending effect. Wei Jing [25] discussed the backlash nonlinear characteristic in helical gear system. Guo Jiashun [26] analyzed dynamic profile modification with herringbone gear tooth based on

^{*} Corresponding author. e-mail: chang_qinglin@126.com.

analytical solutions. Bu Zhonghong [27-28] studied the inherent characteristic and free vibration characteristics of herringbone planetary gear set. Feng Zhigang [29] studied the meshing static-dynamic vibration characteristics of herringbone gear. Yang Xiaofang [30] analyzed the distribution of power flow of the three branches of herringbone gear drive system by simulation. Ma Shangjun [31] analyzed the steady-state response of plate convergence herringbone gears. Wu Xinyue [32, 33] established a simplified kinetic model of herringbone gear and got preliminary solution. Xie Zuiwei [34] analyzed the stress on herringbone gear tooth surface by using the contact stress finite element method. Ahmad Al-Shhyab and Ahmet Kahraman [35] developed a non-linear time-varying dynamic model to study torsional dynamic behavior for a multi-mesh gear system.

Referring to the modeling process of helical gear system and combining its own characteristics, bending-torsion-axis coupled nonlinear vibration model with 16 degrees of freedom was established. Nonlinear factors considered in the process of modeling include time-varying mesh stiffness, meshing impact and backlash. Dimensionless operation was adopted to process the system dynamics equations. To solve the dimensionless differential equations, the 4-5 Runge-Kutta method was used. Then the nonlinear characteristic of time history diagram, phase diagrams, Lyapunov exponent, Lyapunov dimension, Poincare map and global bifurcation graphs in the double helical gear system was studied.

2. Nonlinear Dynamic Model of the Double Helical Gear System

2.1. The Nonlinear Dynamic Model

The double helical gear is widely used in industry, such as truck, train and other overload machines. A pair of double helical gear is shown in the Figure.1. From the Figure1, we find that the double helical gear could regard as two helical gear with opposite helical angle. Then the 12 degrees bend-twist-axis coupling vibration model of double helical gear pair is established just as Figure2 shown.



Figure 1. A pair of double helical gear

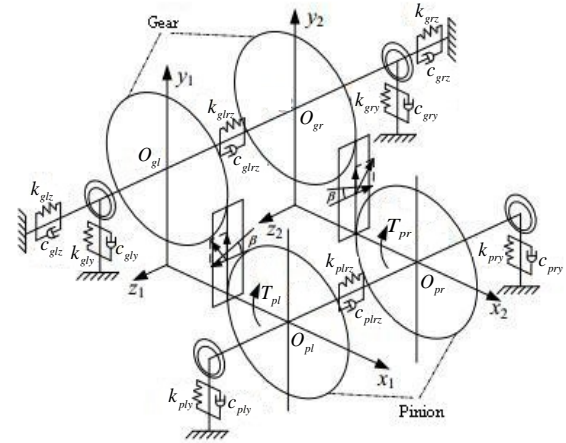


Figure 2. 12 degrees bend-twist-axis coupling vibration model of double helical gear pair

As shown in Figure 2, to establish the nonlinear dynamic model of double-helical gear system of 12 degrees, the tooth surface friction and the friction torque are not considered and the generalized displacement matrix of 12 degrees can be expressed as:

$$\delta = (y_{pl}, z_{pl}, \theta_{pl}; y_{pr}, z_{pr}, \theta_{pr}; y_{gl}, z_{gl}, \theta_{gl}; y_{gr}, z_{gr}, \theta_{gr})^T \quad (1)$$

Where, $y_{ij}, z_{ij}, \theta_{ij}$ ($i = p, g; j = l, r$) is the translational and rotational vibration displacement of center of pinion and gear O_{ij} ($i = p, g; j = l, r$) at y, z direction, respectively.

Vibration displacement of meshing point P_l, P_r and G_l, G_r can be expressed as:

$$\bar{y}_{pi} = y_{pi} + \theta_{pi} r \quad (2a)$$

$$\bar{z}_{pi} = z_{pi} - \bar{y}_{pi} \tan \beta = z_{pi} - (y_{pi} + \theta_{pi} r) \tan \beta \quad (2b)$$

$$\bar{y}_{gi} = y_{gi} - \theta_{gi} R \quad (2c)$$

$$\bar{z}_{gi} = z_{gi} - \bar{y}_{gi} \tan \beta = z_{gi} - (y_{gi} - \theta_{gi} R) \tan \beta \quad (2d)$$

Where, $i = l, r$.

Taking the double helical gear, seen as two helical gears with opposite helical gears direction, and assuming the two helical gears have the same parameters except the helix angle, normal meshing stiffness of unilateral can be expressed as:

$$K_{mn}(t) = K_{mn} + \sum_{\xi=1}^{\infty} \{a_{n1} \cos[\xi \omega_h(t)t] + b_{n1} \sin[\xi \omega_h(t)t]\} \quad (3a)$$

$$= K_{mn} + K_{mna} \cos(\omega_h t)$$

Where: K_m is the normal average mesh stiffness of double helical gear pair; $\omega_h(t)$ is the meshing frequency of double helical gear pair; a_n and b_n are the Fourier coefficients in Eq. (3a).

Mesh stiffness at the tangential and axial directions can be expressed as:

$$K_{mry}(t) = K_{mly}(t) = K_{mn}(t) \cos \beta \quad (3b)$$

$$K_{mrz}(t) = K_{mlz}(t) = K_{mn}(t) \sin \beta \quad (3c)$$

Where, $i = l, r$.

The normal damping is expressed as:

$$C_{mn}(t) = 2\zeta_v \sqrt{K_{mn}(t)m_e} \quad (4a)$$

Where: m_e is the equivalent mass of double helical gear

pair, $m_e = \frac{J_p J_g}{J_g R_b^2 + J_p r_b^2}$; ζ_v is the relative damping of

double helical gear pair, and $\zeta_v = 0.070$.

Mesh damping at the tangential and axial can be expressed as:

$$C_{mry}(t) = C_{mly}(t) = C_{mn}(t) \cos \beta \quad (4b)$$

$$C_{mrz}(t) = C_{mlz}(t) = C_{mn}(t) \sin \beta \quad (4c)$$

Where, $i = l, r$.

The tangential and axial dynamic meshing force at left and right ends of double helical gear pair can be expressed as:

$$F_{yl}(t) = K_{mly}(t) f(\bar{y}_{pl} - \bar{y}_{gl} - e_{ly}) + C_{mly}(t) (\dot{\bar{y}}_{pl} - \dot{\bar{y}}_{gl} - \dot{e}_{ly}) \quad (5a)$$

$$F_{zl}(t) = K_{mlz}(t) f(\bar{z}_{pl} - \bar{z}_{gl} - e_{lz}) + C_{mlz}(t) (\dot{\bar{z}}_{pl} - \dot{\bar{z}}_{gl} - \dot{e}_{lz}) \quad (5b)$$

$$F_{yr}(t) = K_{mry}(t) f(\bar{y}_{pr} - \bar{y}_{gr} - e_{ry}) + C_{mry}(t) (\dot{\bar{y}}_{pr} - \dot{\bar{y}}_{gr} - \dot{e}_{ry}) \quad (5c)$$

$$F_{zr}(t) = K_{mrz}(t) f(\bar{z}_{pr} - \bar{z}_{gr} - e_{rz}) + C_{mrz}(t) (\dot{\bar{z}}_{pr} - \dot{\bar{z}}_{gr} - \dot{e}_{rz}) \quad (5d)$$

Where: $e_{ij}(t)$ ($i = l, r; j = y, z$) are the tangential and axial meshing error at left and right ends of double helical gear pair, respectively; they can be then expressed in sine function forms

as: $e_{ij}(t) = \tilde{e}_{ij} + e_{aj} \sin[\omega_h(t)t + \phi_{eij}]$ ($i = l, r; j = y, z$).

From Eq. (5a) to Eq. (5d), $f(j_i)(i = l, r; j = y, z)$ is the backlash nonlinear function, and also the tangential and axial relative displacement at left and right ends of double helical gear pair, respectively. Assume that the backlash at left and right ends of double helical gear pair is equal, and the normal backlash is $2b_n$, then the tangential and axial backlash is $2b_t = 2b_n \cos \beta$ and $2b_a = 2b_n \sin \beta$, respectively, where β is the helical angle of the double helical gear system.

$$f(y_i) = \begin{cases} y_i - b_t & (y_i > b_t) \\ 0 & (|y_i| \leq b_t) \\ y_i + b_t & (y_i < -b_t) \end{cases} \quad (6a)$$

$$f(z_i) = \begin{cases} z_i - b_a & (z_i > b_a) \\ 0 & (|z_i| \leq b_a) \\ z_i + b_a & (z_i < -b_a) \end{cases} \quad (6b)$$

Where, $i = l, r$.

Through the Newton's second law and considering the dynamic meshing force and backlash in double helical gear pair shown in Figures 1 and 2, the kinetic equation of gear system shown in Figure 2 can be established as:

$$\begin{cases} m_{pl} \ddot{y}_{pl} + c_{ply} \dot{y}_{pl} + k_{ply} y_{pl} = -F_{yl}(t) + m_{pl} g \\ m_{pl} \ddot{z}_{pl} + c_{plr} (\dot{z}_{pl} - \dot{z}_{pr}) + k_{plr} (z_{pl} - z_{pr}) = -F_{zl}(t) \\ J_{pl} \ddot{\theta}_{pl} = -F_{yl}(t)r + T_{pl} \end{cases} \quad (7a)$$

$$\begin{cases} m_{pr} \ddot{y}_{pr} + c_{pry} \dot{y}_{pr} + k_{pry} y_{pr} = -F_{yr}(t) + m_{pr} g \\ m_{pr} \ddot{z}_{pr} - c_{plr} (\dot{z}_{pl} - \dot{z}_{pr}) - k_{plr} (z_{pl} - z_{pr}) = -F_{zr}(t) \\ J_{pr} \ddot{\theta}_{pr} = -F_{yr}(t)r + T_{pr} \end{cases} \quad (7b)$$

$$\begin{cases} m_{gl} \ddot{y}_{gl} + c_{gly} \dot{y}_{gl} + k_{gly} y_{gl} = F_{yl}(t) + m_{gl} g \\ m_{gl} \ddot{z}_{gl} + c_{glz} \dot{z}_{gl} + k_{glz} z_{gl} + c_{glrz} (\dot{z}_{gl} - \dot{z}_{gr}) + k_{glrz} (z_{gl} - z_{gr}) = F_{zl}(t) \\ J_{gl} \ddot{\theta}_{gl} = F_{yl}(t)R - T_{gl} \end{cases} \quad (7c)$$

$$\begin{cases} m_{gr} \ddot{y}_{gr} + c_{gry} \dot{y}_{gr} + k_{gry} y_{gr} = F_{yr}(t) + m_{gr} g \\ m_{gr} \ddot{z}_{gr} + c_{grz} \dot{z}_{gr} + k_{grz} z_{gr} - c_{glrz} (\dot{z}_{gl} - \dot{z}_{gr}) - k_{glrz} (z_{gl} - z_{gr}) = F_{zr}(t) \\ J_{gr} \ddot{\theta}_{gr} = F_{yr}(t)R - T_{gr} \end{cases} \quad (7d)$$

Where, m_{ij} ($i = p, g; j = l, r$) are the mass at left and right ends of pinion and gear, respectively; J_{ij} ($i = p, g; j = l, r$) are the moment of inertia at left and right ends of pinion and gear respectively; r, R are reference radius of pinion and gear, respectively.

2.2. Dimensionless of Kinetic Equations

In order to obtain these kinetic equations dimensionless, define the system dimensionless time and dimensionless excitation frequency, respectively as:

$$\tau = t \cdot \omega_n \quad (8a)$$

$$\omega = \omega_h / \omega_n \quad (8b)$$

Where: ω_n is the natural frequency of the system, and $\omega_n = \sqrt{K_{mn} / m_e}$; m_e is the equivalent mass of gear pair; K_{mn} is the normal average mesh stiffness of gear pair.

Take b_n as the nominal dimension to take the Eq. (7) dimensionless. The dimensionless displacement of double helical gear system can be expressed as:

$$\begin{aligned}
 p_1 &= y_{pl} / b_n, p_2 = z_{pl} / b_n, p_3 = r\theta_{pl} / b_n \\
 p_4 &= y_{pr} / b_n, p_5 = z_{pr} / b_n, p_6 = r\theta_{pr} / b_n \\
 p_7 &= y_{gl} / b_n, p_8 = z_{gl} / b_n, p_9 = R\theta_{gl} / b_n \\
 p_{10} &= y_{gr} / b_n, p_{11} = z_{gr} / b_n, p_{12} = R\theta_{gr} / b_n \\
 p_{1,1} &= y_l / b_n, p_{1,2} = z_l / b_n \\
 p_{2,1} &= y_r / b_n, p_{2,2} = z_r / b_n
 \end{aligned} \tag{9}$$

Then the dimensionless kinetic equation of gear system can be expressed as:

$$\begin{cases}
 \ddot{p}_1 + 2\xi_{ply} \dot{p}_1 + \eta_{ply} p_1 + \eta_{mlyp}(\tau) f(p_{1,1}) \\
 + 2\xi_{mlyp}(\tau) \dot{p}_{1,1} = \tilde{F}_1 \\
 \ddot{p}_2 + 2\xi_{plrz} (\dot{p}_2 - \dot{p}_5) + \eta_{plrz} (p_2 - p_5) \\
 + \eta_{mlzp}(\tau) f(p_{1,2}) + 2\xi_{mlzp}(\tau) \dot{p}_{1,2} = \tilde{F}_2 \\
 \ddot{p}_3 + 2[\eta_{mlyp}(\tau) f(p_{1,1}) + 2\xi_{mlyp}(\tau) \dot{p}_{1,1}] = \tilde{F}_3
 \end{cases} \tag{10a}$$

$$\begin{cases}
 \ddot{p}_4 + 2\xi_{pry} \dot{p}_4 + \eta_{pry} p_4 + \eta_{mryp}(\tau) f(p_{2,1}) \\
 + 2\xi_{mryp}(\tau) \dot{p}_{2,1} = \tilde{F}_4 \\
 \ddot{p}_5 - 2\xi_{plrz} (\dot{p}_2 - \dot{p}_5) - \eta_{plrz} (p_2 - p_5) \\
 + \eta_{mrzp}(\tau) f(p_{2,2}) + 2\xi_{mrzp}(\tau) \dot{p}_{2,2} = \tilde{F}_5 \\
 \ddot{p}_6 + 2[\eta_{mryp}(\tau) f(p_{2,1}) + 2\xi_{mryp}(\tau) \dot{p}_{2,1}] = \tilde{F}_6
 \end{cases} \tag{10b}$$

$$\begin{cases}
 \ddot{p}_7 + 2\xi_{gly} \dot{p}_7 + \eta_{gly} p_7 - \eta_{mlyg}(\tau) f(p_{1,1}) \\
 - 2\xi_{mlyg}(\tau) \dot{p}_{1,1} = \tilde{F}_7 \\
 \ddot{p}_8 + 2\xi_{glz} \dot{p}_8 + \eta_{glz} p_8 + 2\xi_{glrz} (\dot{p}_8 - \dot{p}_{11}) + \eta_{glrz} (p_8 \\
 - p_{11}) - \eta_{mlzg}(\tau) f(p_{1,2}) - 2\xi_{mlzg}(\tau) \dot{p}_{1,2} = \tilde{F}_8 \\
 \ddot{p}_9 - 2[\eta_{mlyg}(\tau) f(p_{1,1}) + 2\xi_{mlyg}(\tau) \dot{p}_{1,1}] = \tilde{F}_9
 \end{cases} \tag{10c}$$

$$\begin{cases}
 \ddot{p}_{10} + 2\xi_{gry} \dot{p}_{10} + \eta_{gry} p_{10} - \eta_{mryg}(\tau) f(p_{2,1}) \\
 - 2\xi_{mryg}(\tau) \dot{p}_{2,1} = \tilde{F}_{10} \\
 \ddot{p}_{11} + 2\xi_{grz} \dot{p}_{11} + \eta_{grz} p_{11} - 2\xi_{grlz} (\dot{p}_8 - \dot{p}_{11}) - \eta_{grlz} (p_8 \\
 - p_{11}) - \eta_{mrzg}(\tau) f(p_{2,2}) - 2\xi_{mrzg}(\tau) \dot{p}_{2,2} = \tilde{F}_{11} \\
 \ddot{p}_{12} - 2[\eta_{mryg}(\tau) f(p_{2,1}) + 2\xi_{mryg}(\tau) \dot{p}_{2,1}] = \tilde{F}_{12}
 \end{cases} \tag{10d}$$

Where:

ξ_{ijk} ($i = p, g; j = l, r; k = y, z$) is the dimensionless support damping at bearing at left and right ends of pinion and gear at Y, Z direction, respectively;

η_{ijk} ($i = p, g; j = l, r; k = y, z$) is the dimensionless support stiffness at bearing at left and right ends of pinion and gear at Y, Z direction, respectively;

$\xi_{mij}(\tau)$ ($i = l, r; j = y, z$) is the dimensionless meshing damping at left and right ends of gear at Y, Z direction, respectively;

$\eta_{mij}(\tau)$ ($i = l, r; j = y, z$) is the dimensionless meshing stiffness at left and right ends of gear at Y, Z direction, respectively;

ξ_{ilrj} and η_{ilrj} ($i = p, g; j = y, z$) are dimensionless internal damping and internal stiffness at left and right ends of pinion and gear, respectively;

\tilde{F}_i ($i = 1, 12$) is the dimensionless external excitation.

The expressions of dimensionless parameter in Eq. (10a) to Eq. (10d) are:

$$\begin{aligned}
 \xi_{ply} &= \frac{c_{ply}}{2m_{pl}\omega_n}, \eta_{ply} = \frac{k_{ply}}{m_{pl}\omega_n^2}, \eta_{mlyp}(\tau) = \frac{K_{mly}(\tau)}{m_{pl}\omega_n^2} \\
 \xi_{mlyp}(\tau) &= \frac{C_{mly}(\tau)}{2m_{pl}\omega_n}, \xi_{plrz} = \frac{c_{plrz}}{2m_{pl}\omega_n}, \eta_{plrz} = \frac{k_{plrz}}{m_{pl}\omega_n^2} \\
 \eta_{mlzp}(\tau) &= \frac{K_{mlz}(\tau)}{m_{pl}\omega_n^2}, \xi_{mlzp}(\tau) = \frac{C_{mlz}(\tau)}{2m_{pl}\omega_n}, \xi_{pry} = \frac{c_{pry}}{2m_{pr}\omega_n} \\
 \eta_{pry} &= \frac{k_{pry}}{m_{pr}\omega_n^2}, \eta_{mryp}(\tau) = \frac{K_{mry}(\tau)}{m_{pr}\omega_n^2}, \xi_{mryp}(\tau) = \frac{C_{mry}(\tau)}{2m_{pr}\omega_n} \\
 \eta_{mrzp}(\tau) &= \frac{K_{mrz}(\tau)}{m_{pr}\omega_n^2}, \xi_{mrzp}(\tau) = \frac{C_{mrz}(\tau)}{2m_{pr}\omega_n}, \xi_{gly} = \frac{c_{gly}}{2m_{gl}\omega_n} \\
 \eta_{gly} &= \frac{k_{gly}}{m_{gl}\omega_n^2}, \xi_{glz} = \frac{c_{glz}}{2m_{gl}\omega_n}, \eta_{glz} = \frac{k_{glz}}{m_{gl}\omega_n^2} \\
 \xi_{mlzg}(\tau) &= \frac{C_{mlz}(\tau)}{2m_{gl}\omega_n}, \eta_{mryg}(\tau) = \frac{K_{mry}(\tau)}{m_{gr}\omega_n^2}, \xi_{mryg}(\tau) = \frac{C_{mry}(\tau)}{2m_{gr}\omega_n} \\
 \eta_{mrzg}(\tau) &= \frac{K_{mrz}(\tau)}{m_{gr}\omega_n^2}, \xi_{mrzg}(\tau) = \frac{C_{mrz}(\tau)}{2m_{gr}\omega_n}, \tilde{F}_3 = \frac{2T_{pl}}{b_n m_{pl} \omega_n^2} \\
 \tilde{F}_1 = \tilde{F}_4 = \tilde{F}_7 = \tilde{F}_{10} &= \frac{g}{b_n \omega_n^2}, \tilde{F}_2 = \tilde{F}_5 = \tilde{F}_8 = \tilde{F}_{11} = 0, \\
 \tilde{F}_6 &= \frac{2T_{pr}}{b_n m_{pr} \omega_n^2}, \tilde{F}_9 = -\frac{2T_{gl}}{b_n m_{gl} \omega_n^2}, \tilde{F}_{12} = -\frac{2T_{gr}}{b_n m_{gr} \omega_n^2}
 \end{aligned}$$

The dimensionless backlash nonlinear function can be expressed as:

$$f(p_{i,j}) = \begin{cases} p_{i,j} - \frac{b_k}{b_n} & (p_{i,j} > \frac{b_k}{b_n}) \\ 0 & (|p_{i,j}| \leq \frac{b_k}{b_n}) \\ p_{i,j} + \frac{b_k}{b_n} & (p_{i,j} < -\frac{b_k}{b_n}) \end{cases} \tag{11}$$

Where, $i = 1, 2; j = 1, 2, k = t, a$

The dimensionless transmission error can be expressed as:

$$e_{ij}(\tau) = \frac{e_{ij}}{b_n} + \frac{e_{aij}}{b_n} \sin(\omega\tau + \phi_{eij}) \quad (i = l, r; j = y, z) \tag{12}$$

3. Numerical Results and Discussion

Take the basic parameters as:
 $z_p = 30$, $z_g = 90$, $m = 3$, $\alpha = 20^\circ$, $\beta = 10^\circ$,
 $g = 9.8 N / kg$, $b_n = 0.1 mm$, $B = 60 mm$,
 $T_p = 300 N \cdot m$, $T_g = 900 N \cdot m$, $f = 5000 r / min$,
 $m_p = 5 kg$, $m_g = 45 kg$, $K_{ma} = 2 \times 10^8 N / m$,
 $K_{mn} = 6 \times 10^8 N / m$, $\xi_{plr_z} = \xi_{glr_z} = 0.1$,

$$k_{ply} = k_{pry} = k_{gby} = k_{gry} = 6.15 \times 10^9 N / m .,$$

$$\xi_{glz} = \xi_{grz} = 0.008, k_{glz} = k_{grz} = 3.03 \times 10^6 N / m ,$$

$$\xi_{ply} = \xi_{pry} = \xi_{gby} = \xi_{gry} = 0.008 ,$$

$$k_{plr_z} = k_{glr_z} = 6.02 \times 10^{10} N / m , e_{ij}(\tau) = 0 .$$

Then Figure 3 to Figure 5 can be obtained by 4-5 Runge-Kutta method, in which the nonlinear characteristics of double helical gear system can be revealed.

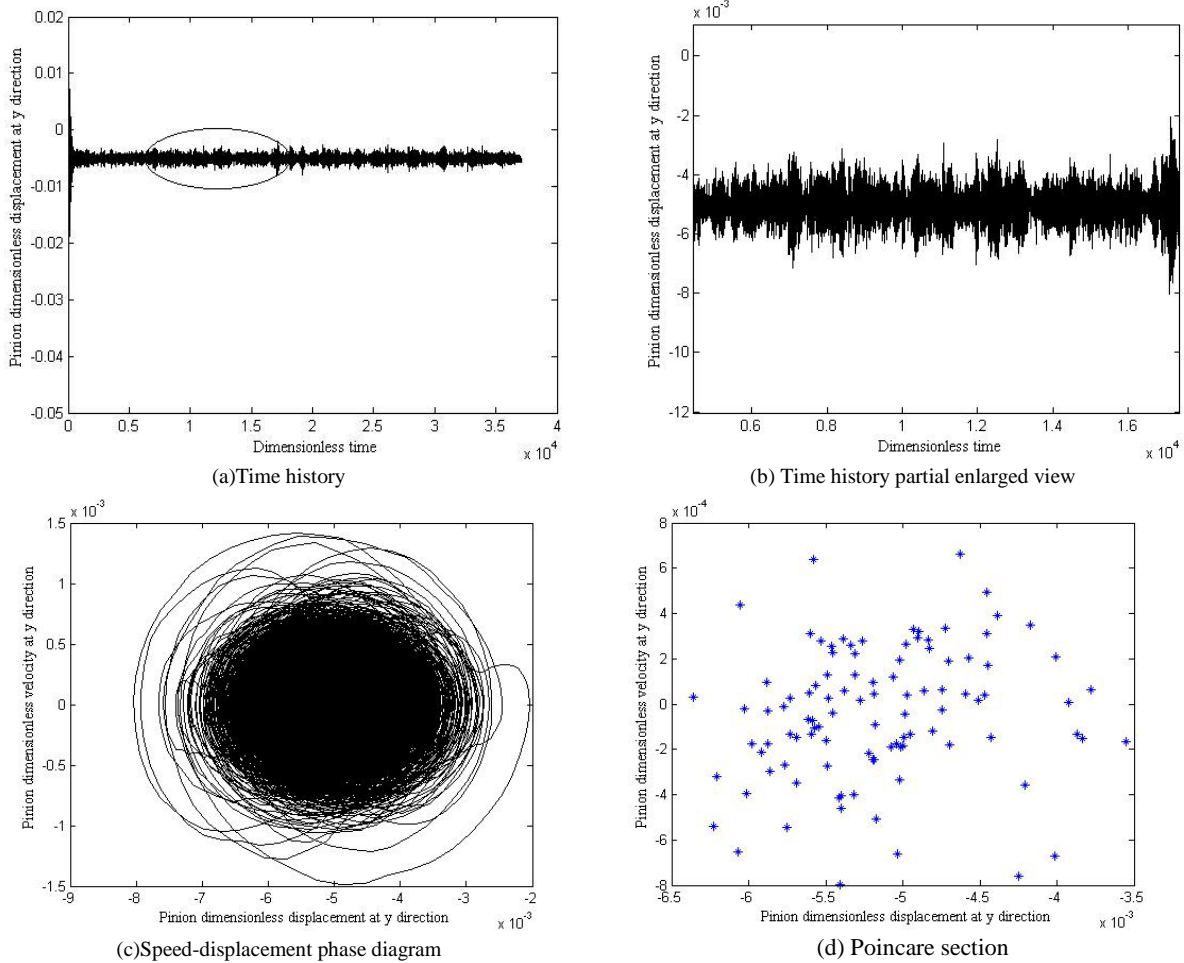


Figure 3. The numerical result of pinion at y direction

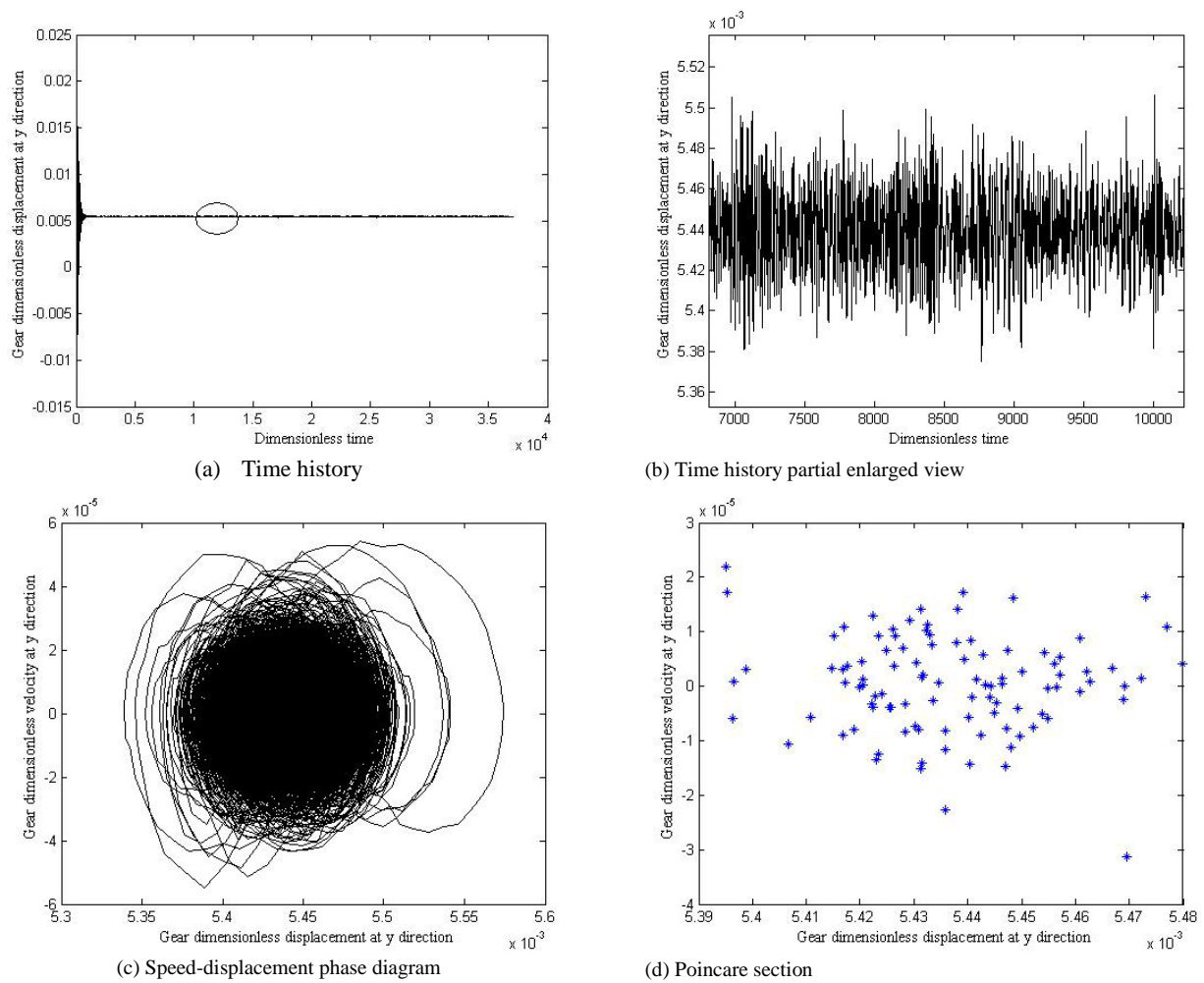


Figure 4. The numerical result of gear at y direction

In Figures 3 to 5, some nonlinear characteristics are revealed. From Figure (3a), Figure (4a) and Figure (5a), we get that the vibration is in the double helical gear system. From Figure (3a), Figure (4a), Figure (3b) and Figure (4b), we find that the amplitude of gear at y direction is smaller than the amplitude of pinion at direction. From Figure (4a), Figure (5a), Figure (4b) and Figure (5b), we find that the amplitude of gear at z direction is larger than the amplitude of gear at y direction. To a certain extent, we could obtain that the vibration amplitude of gear is smaller than the vibration

amplitude of pinion at the same direction and the vibration amplitude of the same component at z direction is larger than the amplitude of gear at y direction.

From Figures 3 to 5, we find that there are abundant nonlinear characteristics existing in the double helical gear system. According to their nonlinear characteristics, we should take the dynamic performance into consideration when designing the double helical gear system. At the same time, we could use the vibration signal to monitor the operation of double helical gear system.

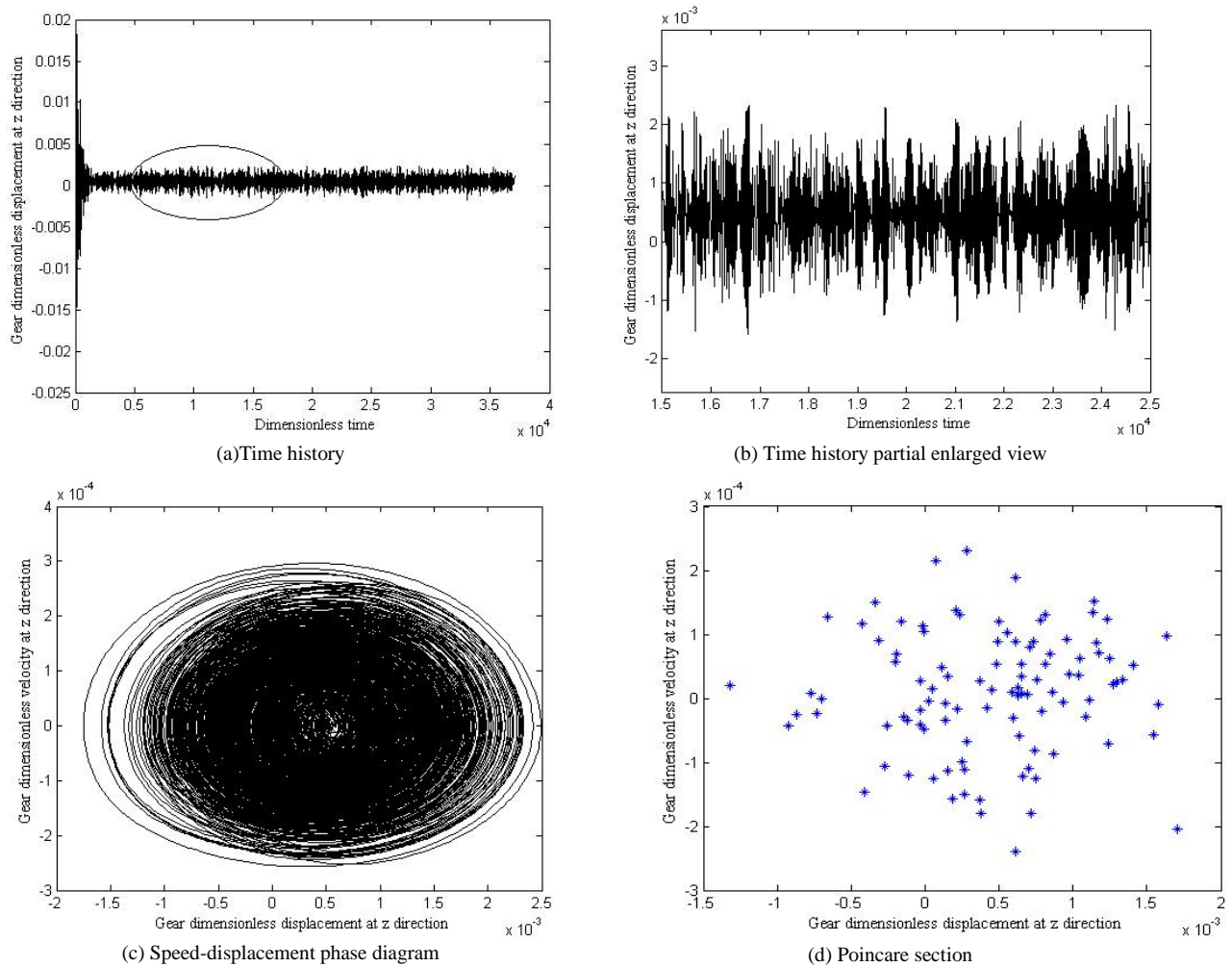


Figure 5. The numerical result of gear at z direction

4. Conclusions

In this paper, we obtained the nonlinear dynamic vibration model of the double helical gear system by taking the time-varying nonlinear factors into consideration. The time-varying nonlinear factors in this model include time-varying mesh stiffness, time-varying meshing damping, backlash, time-varying transmission error and time-varying meshing force.

Based on the nonlinear dynamic vibration model, the dimensionless nonlinear dynamic vibration model had been formed. Then take the Runge-Kutta method to solve the differential equations.

Through the numerical result, we find that there are a lot of nonlinear vibration characteristics in the double helical gear system. The vibration amplitude of gear is smaller than the vibration amplitude of pinion at the same direction and the vibration amplitude of the same component at z direction is larger than the amplitude of gear at y direction. From the study of nonlinear characteristics and performance of double helical gear system, the double helical gear can be optimistic designed. What is more, there are many unknown nonlinear vibration characteristics that need to be researched further.

Acknowledgments

We would like to thank the reviewers for their encouraging comments and constructive suggestions that brought the present paper to its current form.

References

- [1] Li Runfang, Wang Jianjun, Gear system dynamics: vibration, impact, noise. Beijing: Science Press, 1997.
- [2] Chinmaya Kar, A.R. Mohanty, "An algorithm for determination of time-varying frictional force and torque in a helical gear system". Mechanism and Machine Theory, Vol. 42 (2007), 482–496.
- [3] Chinmaya Kar, A.R. Mohanty, "Determination of time-varying contact length, friction force, torque and forces at the bearings in a helical gear system". Journal of Sound and Vibration, Vol. 309 (2008), 307–319.
- [4] Song He, Sungmin Cho, Rajendra Singh, "Prediction of dynamic friction forces in spur gears using alternate sliding friction formulations". Journal of Sound and Vibration, Vol. 309 (2008), 843–851.
- [5] P. Velex, M. Ajmi, "Dynamic tooth loads and quasi-static transmission errors in helical gears—Approximate dynamic factor formulae". Mechanism and Machine Theory, Vol. 42 (2007), 1512–1526.

- [6] J. Borner, D.R. Houser, "Friction and bending moments as gear noise excitations". SAE Transaction, Vol. 105 (1996) No. 6, 1669-1676, No.961816.
- [7] A. Parey, N. Tondon, "Spur gear dynamic models including defects: a review". The Shock and Vibration Digest, Vol. 35 (2003) No.6, 465-478.
- [8] Tugan Eritenel, Robert G. Parker, "Three-dimensional nonlinear vibration of gear pairs". Journal of Sound and Vibration, Vol. 331 (2012) 3628-3648
- [9] Mohamed Taoufik Khabou, Taissir Hentati, Mohamed Slim Abbas, Fakher Chaari, Mohamed Hadda, "Nonlinear modeling and simulation of spur gear with defected bearings". Nonlinear Modeling and Simulation, (2011) 197-212.
- [10] G. WESLEY BLANKENSHIP, RAJENDRA SINGH, "Dynamic force transmissibility in helical gear pairs". Mechanism and Machine Theory, Vol. 30 (1995) No.3, 323-339.
- [11] Yi Guoa, Robert G. Parker, "Dynamic modeling and analysis of a spur planetary gear involving tooth wedging and bearing clearance nonlinearity". European Journal of Mechanics-A/Solids, Vol. 29 (2010) 1022-1033.
- [12] Lassâad Walha, Yassine Driss, Mohamed Taoufik Khabou, Tahar Fakhfakh, Mohamed Haddar, "Effects of eccentricity defect on the nonlinear dynamic behavior of the mechanism clutch-helical two stage gear". Mechanism and Machine Theory, Vol. 46 (2011) 986-997.
- [13] Wei Yiduo, Liu Kai, Cui Yahui, Yuan Yuan, Zhang Wu, "Study on Nonlinear Response of Gear System with Double Periodic Parametrically under Friction Effect". China Mechanical Engineering, Vol. 23 (2012) No. 4, 389-442.
- [14] Wei Yiduo, Liu Kai, Ma Chaofeng, Zhao Changqing, Yuan Yuan, "Effect of Friction on the Nonlinear Vibration and Stability of Gear System". Mechanical Science and Technology for Aerospace Engineering, Vol. 31 (2012) No. 5, 760-765.
- [15] MA Hui, ZHU Lisha, WANG Qibin, Zhang Yimin, "Modal Coupling Characteristic Analysis of a Helical Gear Rotor System With Parallel Shafts". Proceedings of the CSEE, Vol. 32 (2012) No. 29, 131-136.
- [16] WANG Qing, ZHANG Yidu, "Coupled analysis based dynamic response of two-stage helical gear transmission system". Journal of Vibration and Shock, Vol. 31 (2012) No.10, 87-91.
- [17] N. Leiba,b, S. Nacivet B, F. Thouverez, "Experimental and numerical study of a vibro-impact phenomenon in a gear shift cable". Journal of Sound and Vibration, Vol. 329 (2010) 289-301.
- [18] Song Xiaoguang, Cui Li, Zheng Jianrong, "Nonlinear Dynamics Analysis of Flexible Rotor Bearing System with Helical-gear". China Mechanical Engineering, Vol. 24 (2013) No.11, 1484-1493.
- [19] TANG Jinyuan, CHEN Siyu, ZHONG Jue, "A Improved Nonlinear Model for a Spur Gear Pair System". Engineering Mechanics, Vol. 25 (2008) No.1, 217-223.
- [20] CHEN Siyu, TANG Jinyuan, "Effect of Backlash on Dynamics of Spur Gear Pair System with Friction and Time-varying Stiffness". Journal of Mechanical Engineering, Vol. 45 (2009) No.6, 119-123.
- [21] WANG Cheng, GAO Chang-qing, CUI Huanyong, "Dynamic modeling and analysis of double helical gears based on meshing characters". Journal of Central South University (Science and Technology), Vol. 43 (2012) No.8, 3019-3024.
- [22] WANG Feng, FANG Zongde, LI Shengjin, "Dynamic characteristics of a double helical gear under multi-load". Journal of Vibration and Shock, Vol. 32 (2013) No.1 49-52.
- [23] WANG Feng, FANG Zongde, LI Shengjin, "Research and Analysis on Power Transmission Processing of Herringbone Gear Trains System with Rolling Bearing Support". Journal of Mechanical Engineering (2013).
- [24] LI Wenliang, WANG Liqin, CHANG Shan, DAI Guanghao, "Tooth friction bending effect of helical gear on gear dynamics". Journal of Ship Mechanics, Vol.17 (2013) No.8, 937-947.
- [25] WEI Jing, SUN Wei, CHU Yanshun, ZENG Jing, "Bifurcation and chaos characteristics of helical gear system and parameters influences". Journal of Harbin Engineering University, Vol.34 (2013) No.10, 1-8.
- [26] GUO Jiashun, WANG Sanmin, Wang Ying, "Dynamic analysis of tooth profile modification to herringbone gears based on analytical solution". Journal of Aerospace power, Vol.28 (2013) No.3, 613-620.
- [27] BU Zhonghong, LIU Geng, WU Liyan, "Natural Characteristics Analysis on Herringbone Planetary Gear Trains with Slide Bearing Support". JOURNAL OF MECHANICAL ENGINEERING, Vol.47 (2011) No.1, 80-88.
- [28] Bu Zhonghong, Liu Geng, Wu Liyan, Ma Shangjun, "Free Vibration Characterization Analysis of Encased Differential Herringbone Gear Train". China Mechanical Engineering, Vol.20 (2009) No.20, 2420-2424.
- [29] FENG Zhigang, WU Xingyue. "Analysis on static and dynamic characteristics of herringbone gear in meshing". SHIP & OCEAN ENGINEERING, Vol.36 (2007) No.5, 72-76.
- [30] YANG Xiaofang, FANG Zongde, WANG Baobin, DONG Hao, "Analysis of power-split for herringbone gears power three-branching transmission system by simulation algorithm". Journal of Yanshan University, Vol.36 (2012) No.2, 131-135.
- [31] Ma Shangjun, Liu Geng, Zhou Jianxing, Zhao Yangdong. "Characteristics of Steady-state Structural Response of a Herringbone Gear with Web". Mechanical Science and Technology for Aerospace Engineering, Vol.29 (2010) No.2, 229-233.
- [32] WU Xinyue, ZHU Shijian, "Theoretical vibration pattern of herringbone gearing". JOURNAL OF NAVAL UNIVERSITY OF ENGINEERING, Vol.13 (2001) No.5, 13-19.
- [33] WU Xinyue, DENG Fushun, "Solving methods of herringbone gear's vibration pattern". JOURNAL OF NAVAL UNIVERSITY OF ENGINEERING, Vol.13 (2001) No.6, 32-36.
- [34] XIE Zuiwei, WU Xinyue, CHEN Yanfeng, "Contacting element of tooth surface stress of herringbone gears". JOURNAL OF MACHINE DESIGN, Vol.24 (2007) No.10, 25-28.

Automobile Longitudinal Axis Detection Method Based on Image Segmentation and Preliminary Results

Peijiang Chen^{a,b} and Yongjun Min^{*,a}

^a College of Mechanical and Electronic Engineering, Nanjing Forestry University, Jiangsu, China

^b School of Automobile, Linyi University, Shandong, China

Received 27 Feb 2014

Accepted 10 Oct 2014

Abstract

With the growing number and high usage frequency, it was important for automobiles to test the performance. In order to detect automobiles effectively, the technologies of automobile contour detection and longitudinal axis extraction, based on digital image processing, were studied. The basic concepts of automobile testing technology were introduced, and several commonly used image segmentation methods were analyzed. Before image segmentation, the automobile image was preprocessed, including gray scale transformation, gray scale stretching and median filtering. According to the monotonicity of interclass variances to both sides of threshold, the rapid realization method of image segmentation based on OTSU was proposed. The extraction of automobile longitudinal axis was realized by using approximation method. The software running showed that it could effectively detect automobile contour and extract longitudinal axis, which laid foundation for subsequent automobile image analysis and feature extraction, and it had certain practical value.

© 2014 Jordan Journal of Mechanical and Industrial Engineering. All rights reserved

Keywords: : Automobile Contour; Longitudinal Axis; Image Segmentation; OTSU; Approximation Method.

1. Introduction

Automobiles play important roles in our daily life and have greatly changed lifestyle. With the rapid progress of automobile technology and fast development of automobile industry, the automobile performance has been improved significantly [1]. At the same time, the automobile structure becomes more complex. With the increase of automobile travelling mileage, it is inevitable for some performance changes to take place, such as power declination, economic deterioration, reduction of safety and reliability, etc. [2]. These changes affect the normal operation and use of automobiles seriously, and they may even pose a threat to people's lives. In order to protect the safety of automobiles and people, the automobiles' technical states and usage performance should be known. Therefore, it is vital and necessary to identify and eliminate the faults in advance by detecting the vehicle performance.

The technologies of automobile detection are mainly concerned with the operation performance, which can identify the technical conditions without disassembling and providing a reliable basis for the fault detection and maintenance. With the advances of science and technology, especially the technologies of computer and communication, the traditional detection methods cannot

meet the needs of modern automobile testing [3]. A variety of advanced equipment is used to make the automobile detecting process safer, faster and more accurate [4].

Automobile longitudinal axis, the center line or symmetrical line, is one of the basic characteristics of automobiles. In general, when an automobile moves along the road, the body sides are parallel with the road direction, and then the automobile's longitudinal axis is parallel with the road surface [5].

The extraction of automobile longitudinal axis is significant in automobile detection. For example, in the automobile headlamp detection, the longitudinal axis should be vertical with the pathway of headlamp tester, or the detection results may have errors. There are two general methods to resolve the measurement errors: a) using automobile adjusting device to alien the automobile, and b) using a certain technology to correct the detection results. For the first method, the instrument has a fixed length for the platforms of the front axle and the rear axle, which cannot adapt to the automobiles with different wheelbases; the adjusting time is long and the detection efficiency is low; due to this, then this method cannot meet the need of fast automatic detection in automobile testing stations. For the second method, a computer is used to process an automobile image; the first step is to extract the automobile contour and longitudinal axis, then to analyze the offset between the actual position and the ideal

* Corresponding author. e-mail: yjmin@njfu.edu.cn.

position of the automobile, and finally to correct the headlamp testing results according to the positional deviation. The second method is low-cost, and can obtain accurate measurement results. The correction of headlamp detection results can indirectly decrease the accidents caused by headlamp faults [6].

The detection of automobile longitudinal axis has mainly two methods: 1) a method based on machine vision, and 2) a method based on digital image processing. Lin [7] used the stereo vision technology to detect the longitudinal axis of an automobile which was parked on the automobile straightening apparatus. The two images of the automobile body were captured and the boundary lines, within certain slopes and lengths, were extracted, and, finally, their centerlines were gotten. This method has a good accuracy, but it needs a special straightening apparatus and two cameras; the system is very costing.

The image is the main source of information acquisition and exchange [8]. In recent years, the methods of image acquisition, processing, and non-contact measurement are widely used in many fields, such as traffic monitoring, automobile headlamp detection, automatic identification of automobile license, shape measurements of the automobile body, smart identification of automobile type, etc. [9]. In the process of automobile detection based on image processing technology, there are other objects and background besides the vehicles in the image. In order to further extract, analyze and process the automobile characteristics, the key step is to separate the automobile from the complex scene of the original image and obtain the automobile contour.

Based on image processing, the technologies of image segmentation and contour detection of automobiles are discussed and the longitudinal axis of automobile is extracted in this study. Since the method uses one camera only, it can reduce the system cost. Besides, it is a noncontact measurement method; the system is suited for online application in vehicle detection station.

The remainder parts of this paper are as follows: the second section analyzes the commonly used methods of image segmentation; the third part gives the system design of automobile longitudinal axis detection based on image segmentation; section four analyzes the main idea of image segmentation based on maximum interclass variance, puts forward the quick achievement process of OTSU, and discusses the realization process of automobile longitudinal axis extraction; section five concludes the paper to show that the automobile longitudinal axis extraction method based on image processing has practical value in automobile detection.

2. Image Segmentation Methods

Image segmentation is a key technology in digital image processing, which occupies important position in the image engineering. On the one hand, image segmentation is the basis of target expression and it has an important impact on the characteristic measurement. On the other hand, image segmentation and segmentation-based technologies including target expression, feature extraction and parameter measurement convert the original image into more abstract and compact form, and then the

higher level of image analyzing and understanding become possible [10].

Simply, image segmentation refers to the fact that different regions, with special meanings in an image, are distinguished, and each region meets the consistency of a specific area. Image segmentation can also extract interesting targets, including gray scale of pixel, color, texture, etc. [11]. There are many ways to segment images, the most classic methods include threshold-based segmentation [12], edge detection, region extraction, and so on.

2.1. Threshold Segmentation Method

The threshold-based method is the most common way to segment images [13]. This method can directly process gray scale information in a binary or a multi-valued way. Firstly, one or several thresholds are selected. Then, the gray scale value of each pixel in the image is compared with the threshold to classify the corresponding pixels according to the comparison results and classify the pixels within the same gray scale interval as the same area. It is obvious that the threshold determination is a key factor that has a direct impact on the segmentation result.

This segmentation method has a simple process, low cost and strong practicality. However, when the difference of image gray scales is not obvious, or the most of gray scales are overlapped, it is often difficult to get an accurate segmentation result and many over-segmentation or under-segmentation errors occur [14]. The basic threshold segmentation methods include histogram twin peaks method, iterative method, OSTU method, etc.

2.2. Edge Detection Method

Edge detection is an important way to achieve image segmentation by detecting the place where the gray scale or structure has mutation, which indicates the end of an area and the start of another area. At the edge of an image, the gray scales are not continuous which can be detected by derivative operation [15]. The position of step edge corresponds to the extreme points of the first order derivative and the zero crossing points of the second derivative. Therefore, the basic image edge detection technologies are mostly realized based on a differential operation. The edge detection operator can extract image boundary by checking the neighborhood of each pixel and quantify the changes of gray scales. Because edge and noise are not consecutive points, it is difficult to overcome the effects of noise for using direct differential operation. In general, the images are smoothed by filters before edge detection.

The commonly used first-order differential operators include Roberts, Prewitt and Sobel. The second-order differential operators have Laplace, Log and Canny. In practice, the variety of differential operators are usually expressed by small region templates. Each operator is best suited to a certain application field. This feature has superiority in application because it can help accomplish specific edge detection. But it is limited due to the fact that the predefined edge detection method may not achieve the best results for other application or unknown circumstances.

2.3. Region Segmentation Method

The essence of image segmentation method based on region is to connect the pixels of the same nature together to constitute the final divided regions. It utilizes local space information of the image and can effectively overcome some shortcomings of other ways. The method is characterized by dividing the segmentation process into several sequential steps, in which the subsequent steps should be judged according to the results of the previous steps.

There are two major implementation ways: a) region growing, and b) region splitting and merging. The basic idea of the region growing method is to aggregate the pixels or sub-regions of a similar nature to form a larger area. The key point of this method is to select a suitable growth or similar criteria. The growth guidelines can be generally divided into three kinds: 1) rule based on regional gray difference, 2) rule based on gray scale distribution statistical properties, and 3) rule based on region shape [16]. The method of splitting and merging is to divide the image into many small regions with strong consistency, to combine them into a large region, and finally the image segmentation is achieved [17].

2.4. Segmentation Method Combined with Specific Theory

In recent years, with the appearance of many new theories and methods, there have been many segmentation techniques combining with certain theories, including mathematical morphology [18], genetic algorithm, wavelet transformation, neural network, etc.

3. Design of Automobile Longitudinal Axis Detection System

When detecting automobile headlamps in vehicle testing stations, and because of the misalignment between the tested automobile and headlamp tester, there may be errors in detecting results. The errors can be corrected by analyzing the deviation of automobile parking location [19]. In this application, the extraction of automobile longitudinal axis is a critical step.

In order to reduce the system cost, a single camera is applied to capture the automobile images. Firstly, the automobile is parked in predetermined position in the vehicle testing station. The camera is set just above the automobile [20], and the image plane is aligned with the testing field by camera calibration. Then, the automobile overlooking image is captured, and it is processed by the computer to obtain the automobile outline by image segmentation technology. Finally, the longitudinal axis of the automobile can be extracted.

The process of system implementation of automobile longitudinal axis detection is shown in Figure 1.

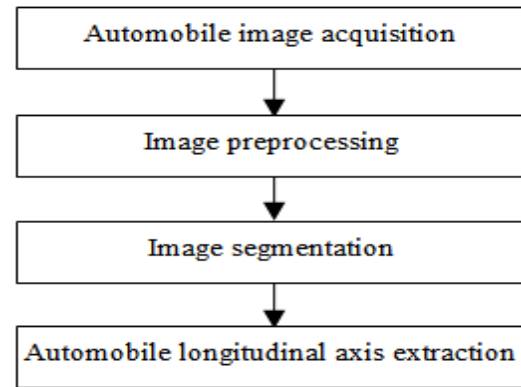


Figure 1. Implementation process of automobile longitudinal axis detection system

4. Realization of Automobile Longitudinal Axis Extraction

In order to test the effectiveness of this algorithm preliminary, a longitudinal axis detection system of automobile is designed. Due to the limitations of the experimental conditions, only two images of different types of automobiles are used to test the algorithm.

4.1. Preprocessing of Automobile Image

After acquiring the automobile image, the preprocessing is necessary, including gray scale conversion, gray scale stretching and image smoothing.

In the case of low light condition, the clarity of the gray scale image is greater than that of the color image. In order to adapt to different lighting conditions, the color automobile images are converted to gray scale images. Moreover, the process can reduce the complexity of information computation.

The gray scale stretching method is used to manipulate the image to enhance the variation range of image gray scale, rich gray scale levels and enhance contrast and resolution of the image. The commonly used gray scale stretching function is given, as shown in Eq. 1:

$$f(x) = \begin{cases} \frac{y_1}{x_1}x & x < x_1 \\ \frac{y_2 - y_1}{x_2 - x_1}(x - x_1) + y_1 & x_1 \leq x < x_2 \\ \frac{255 - y_2}{255 - x_2}(x - x_2) + y_2 & x_2 \leq x \end{cases} \quad (1)$$

Where, x_1, x_2 are gray scale values of turning points of the original image; y_1, y_2 are gray scale values used for the transformed image.

In the application of automobile longitudinal axis detection, the image is smoothed to reduce noise. The median filter is used to realize this function in this study. The gray scale images of the tested automobiles after preprocessing are shown in Figure 2:



(a) Automobile 1



(b) Automobile 2

Figure 2. The gray scale images of the tested automobiles

4.2. Image Segmentation Based on Maximum Interclass Variance

A maximum interclass variance, a dynamic threshold method, was brought out by Nobuyuki Otsu [21], which is simply called OTSU. The basic idea is to find a threshold value through a gray histogram of the image. The value makes the interclass variance get the maximum and divides the image into two parts: target and background [22].

Supposing that the number of image pixels is N , the gray scale range is $[0, K-1]$, the number of pixels corresponding to the gray level i is n_i , the probability is

$$p_i = n_i / N, \text{ and } \sum_{i=0}^{K-1} p_i = 1.$$

According to gray scales, a certain threshold T divides the image pixels into two categories: C_0 and C_1 . The former contains the pixels which gray scale belongs to $[0, T]$; the latter includes the pixels which gray scale range is $[T+1, K-1]$.

The means of C_0 and C_1 are given respectively, as shown in Eq. 2:

$$u_0 = \sum_{i=0}^T iP_i / w_0, \quad u_1 = \sum_{i=T+1}^{K-1} iP_i / w_1 \tag{2}$$

Where, $w_0 = \sum_{i=0}^T p_i, w_1 = \sum_{i=T+1}^{K-1} p_i = 1 - w_0$.

The mean of the total image is gotten, as shown in Eq. 3:

$$u_T = \sum_{i=0}^{K-1} iP_i = w_0u_0 + w_1u_1 \tag{3}$$

The interclass variance is defined, as shown in Eq. 4:

$$\begin{aligned} \sigma^2 &= w_0(u_0 - u_T)^2 + w_1(u_1 - u_T)^2 \\ &= w_0w_1(u_0 - u_1)^2 \end{aligned} \tag{4}$$

The largest value of T can be gotten when the interclass variance gets the maximum. The value is the best segmentation threshold for OTSU segmentation method.

4.3. Quick Achievement of Automobile Image Segmentation Algorithm

The basic idea of the OTSU algorithm is to select a certain gray scale as the threshold value which divides the image into two groups and calculates the interclass variance of the two groups. When the interclass variance is maximal, the threshold is used to segment the image.

It is obvious that the main calculation amount of this algorithm lies in computing the interclass variance. The method is simple in idea, but the computation amount is large, which hinders the rapid implementation of image segmentation. As for the standard 256 level grayscale image, in general, it needs 256 calculations to get the maximum variance [23]. In order to improve the operating speed, a rapid implementation method of OTSU is proposed in this study.

In order to find out how to segment the automobile gray scale image quickly, the interclass variance for each gray scale value of the automobile image, shown in Figure 2 (a), is given, as shown in Figure 3.

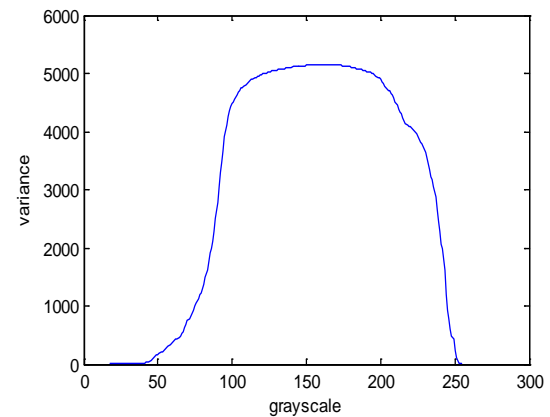


Figure 3. Interclass variances of image pixels

It can be seen that the maximum of interclass variance corresponds to the best segmentation threshold value. The interclass variance monotonically decreases when the gray scale is less than the threshold and the interclass variance monotonically increases when the gray scale is greater than the value. This feature can provide convenience to quickly calculate the optimal segmentation threshold value. The rapid calculation process is given, as shown in Figure 4.

For the given automobile image, shown in Figure 2 (a), the gray scale threshold value, using conventional OTSU algorithm, is 159, and the value with the rapid method is 160. The difference is very small, but the analyzing speed is greatly enhanced. In this case, the threshold can be obtained by 40 calculations in the rapid method, which is much smaller compared with the 256 calculations in the conventional method.

4.4. Implementation of Automobile Longitudinal Axis Extraction

According to the symmetrical characteristics of the outline of automobile overlooking image, the approximation method is used to detect the automobile longitudinal axis after getting the automobile outline [24]. The analyzing method of automobile longitudinal axis extraction is shown in Figure 5.

The extraction process of automobile longitudinal axis, based on approximation method, is as follows:

1. Set the error threshold ε according to the measurement accuracy requirement and camera resolution.
2. Select the starting positions by drawing two lines, get four points a_1, b_1, c_1, d_1 , and then obtain two midpoints m_1 and n_1 according to the lines a_1b_1 and c_1d_1 , respectively.
3. Analyze the angle between the two lines a_1b_1 and m_1n_1 , as shown in Eq. 5:

$$\theta_1 = \arctan\left(-\frac{1}{k_1}\right) \tag{5}$$

where, $k_1 = \frac{(y_{a_1} + y_{b_1}) - (y_{c_1} + y_{d_1})}{2(x_{a_1} - x_{c_1})}$

If $|\theta_1 - 90| \geq \varepsilon$, draw the vertical line of m_1n_1 , and obtain the edge points a_2, b_2, c_2, d_2 .

4. Analyze the angle between the two lines a_2b_2 and m_2n_2 , as shown in Eq. 6:

$$\theta_2 = \arctan\left(-\frac{1+k_1k_2}{k_1-k_2}\right) \tag{6}$$

The process is repeated until $|\theta_2 - 90| < \varepsilon$, finally the automobile longitudinal axis is acquired. The extraction results of longitudinal axis for the tested automobiles are shown in Figure 6:

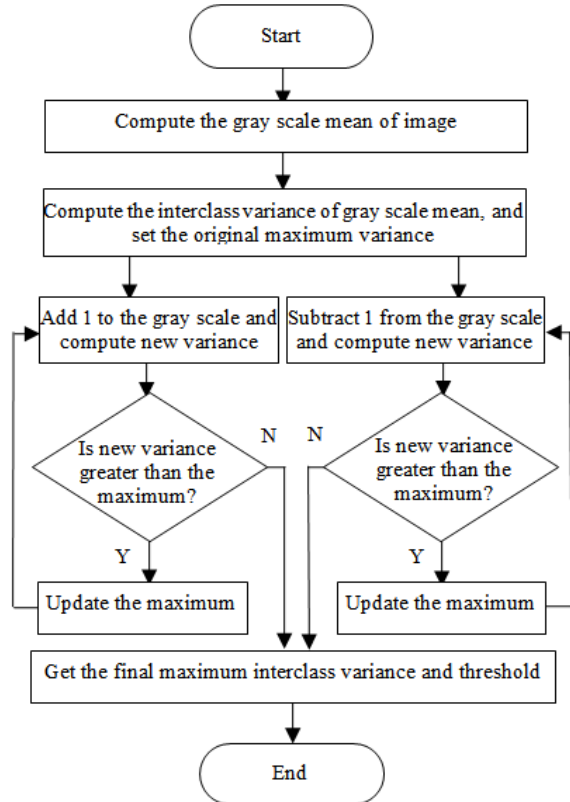


Figure 4. Rapid calculation process of OTSU

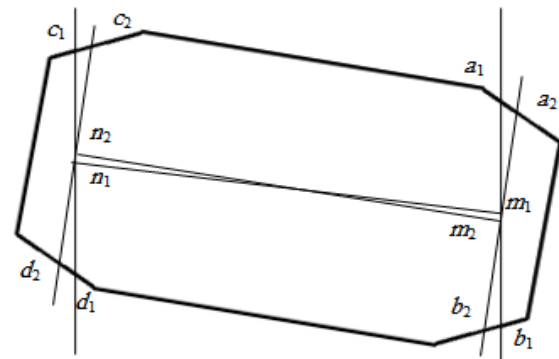
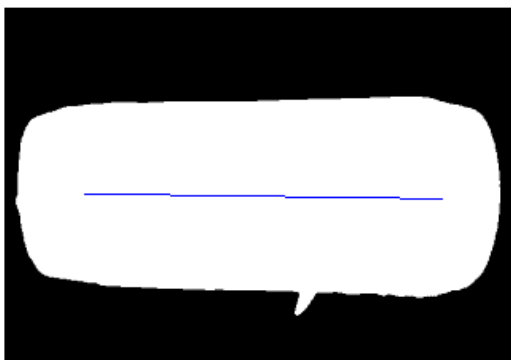
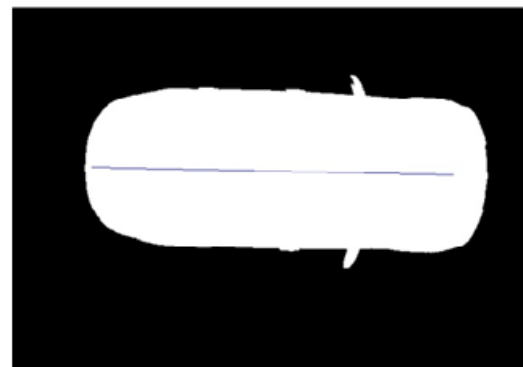


Figure 5. Analyzing method of detecting automobile longitudinal axis based on approximation method



(a) Automobile 1



(b) Automobile 2

Figure 6. Detection results of the automobile longitudinal axis

As can be seen from Figure 6, the algorithm proposed in this study can effectively extract the longitudinal axes of the two tested automobiles in different backgrounds. And from the extraction process, the angle between the longitudinal axis and the horizontal axis of the image coordinate system can be obtained. After camera calibration, the image plane is aligned with the testing field, then the parking deviation angle of the automobile is obtained, which can be used to correct the measurement data of the headlamp tester and improve the measurement accuracy in automobile headlamp testing. In addition, the measurement precision of automobile longitudinal axis is affected by the color difference between the automobile body and background, camera resolution, field lighting, etc.

5. Conclusions

On the basis of analyzing several commonly used image segmentation methods, the system of automobile contour detection and longitudinal axis extraction is designed and implemented. The experiment results show that the quick realization of image segmentation, based on OTSU, can effectively detect the outline of the automobile image and can greatly improve the detection speed. The automobile longitudinal axis can be extracted through approximation method. Compared with other methods, it has low cost and real time. It can lay a good foundation for the subsequent analysis and feature extraction of the automobile image, and the automobile longitudinal axis method has a certain application value.

It is important to note that this method needs a high demand for image segmentation; then a more accurate image segmentation method should be developed to achieve a better extraction result of the automobile longitudinal axis in future research. Furthermore, due to the limitations of the experimental conditions of this study, only two automobiles are selected to detect longitudinal axes, more experiments need to be carried out to test the algorithm. In addition, considering that the method is mainly used in a vehicle test station, only cars are selected for the test. In order to widen the application scope, the method should be improved to test other type of vehicles in our future studies.

Acknowledgements

This study is supported by the Graduate Student Research and Innovation Program of Jiangsu Province (No. CXLX13_513) and the Science and Technology Development Planning Project of Shandong Province (No. 2013YD05004), P. R. China.

References

- [1] N. S. Asad, Y. S. Ge, H. Zhao, "Aldehyde and BTX Emissions from a Light Duty Vehicle Fueled on Gasoline and Ethanol-Gasoline Blend, Operating with a Three-Way

- Catalytic Converter". *Jordan Journal of Mechanical and Industrial Engineering*, Vol. 4 (2010) No. 3, 340-345.
- [2] P. Wu, "Study on Correction Method of Parking Error in Automobile Headlamp Testing". Master Thesis, Changchun, China: Jilin University; 2009.
- [3] J. Wei, "Development of Automobile Detection Technology". *Technology and Life*, (2011) No. 9, 217-217.
- [4] L. Liu, C. Deng, S. Wang, "Overview on Development of Vehicle Detecting Technology". *Special Purpose Vehicle*, (2008) No. 7, 46-49.
- [5] J. Peng, "Research on Measurement of Vehicle Size Based on Digital Image Processing". Master Thesis, Hefei, China: Hefei University of Technology; 2008.
- [6] H. Zhu, "Research on the Image Processing Technology for Automobile Headlamp Testing". Master Thesis, Nanjing, China: Nanjing Forestry University; 2007.
- [7] H. Lin, "Study on Testing System of the Position Deviation of Vehicle-body and Axle Based on Stereo Vision". Master Thesis, Changchun, China: Jilin University; 2008.
- [8] X. Zhao, C. Lin, L. Huang, Y. Yang, "Vehicle Detection and Recognition of MATLAB-Based Image Processing Method". *Journal of Data Acquisition & Processing*, Vol. 24 (2009) No. 5, 141-143.
- [9] Y. Lu, C. Yang, T. Zhang, X. Yan, "Application of Image processing technology in motor vehicle testing industry". *China Measurement Technology*, (2003) No. 6, 36-37.
- [10] F. Li, "Research and Implementation of Image Segmentation Algorithm in Vehicle Detection System". Master Thesis, Shenyang, China: Northeastern University; 2005.
- [11] X. Luo, J. Tian, Y. Zhu, J. Wang, R. Dai, "A Survey on Image Segmentation Methods", *Pattern Recognition and Artificial Intelligence*. Vol. 12 (1999) No. 3, 301-312.
- [12] A. B. Adnan, A. N. Bassam, "A Fusion Technique Based on Image-Statistical Analysis for Detection of Throat Cancer Types". *Jordan Journal of Mechanical and Industrial Engineering*, Vol. 4 (2010) No. 6, 677-684.
- [13] H. Hou, M. Wang, S. Ren, "An Improved Ray Casting Algorithm Based on 2D Maximum Entropy Threshold Segmentation". *Journal of Convergence Information Technology*, Vol. 7 (2012) No. 17, 243-250.
- [14] R. Xu, "An Overview of Image Segmentation Technique and Performance Evaluation". *Journal of Ningbo University of Technology*, Vol. 23 (2011) No. 3, 76-79.
- [15] G. Zhang, "Machine Vision". Beijing, China: Science Press; 2005.
- [16] S. Le, H. Wu, Y. Fu, "Research and Prospect on Image Segmental Methods". *Journal of Nanchang College of Water Conservancy and Hydroelectric Power*, Vol. 23 (2004) No. 2, 15-20.
- [17] W. Yang, Z. Li, Y. Wang, P. Lv, "Survey of Image Segmentation Method Based on Region". *Journal of Electronic Measurement and Instrument*, (2007) No. 5, 278-281.
- [18] P. Chen, "Study on Medical Image Processing Technologies Based on DICOM", *Journal of Computers*, Vol. 7 (2012) No. 10, 2354-2361.
- [19] Y. Min, Y. Zhai, "Direction Detection for Automobile Headlamp Beam Based on Digital Computer Image Processing". *Journal of Southeast University (Natural Science Edition)*, Vol. 31 (2001) No. 6, 1-4.
- [20] L. Zhu, "Research on the Test Technology of Automobile Headlamp based On Image Processing". Master Thesis, Nanjing, China: Nanjing Forestry University; 2005.

- [21] N. Otsu, "A threshold selection method from gray-level histograms". IEEE Transactions on Systems, Man, and Cybernetics, Vol. 9 (1979) No. 1, 62-66.
- [22] D. Zhang, Detailed Notes to MATLAB Digital Image Processing, Beijing, China: Publishing House of Electronics Industry; 2010.
- [23] S. Zhou, P. Yang, W. Xie, "Infrared image segmentation based on Otsu and genetic algorithm". International Conference on Multimedia Technology, Hangzhou, China, 2011.
- [24] Y. Min, L. Zhu, H. Zhu, Z. Xu, "Design and implementation of correction system for measuring error of automobile headlamp beam". Journal of Nanjing Forestry University (Natural Science Edition), Vol. 34 (2010) No. 2, 107-110.

Performance Comparison of Adaptive Neural Networks and Adaptive Neuro-Fuzzy Inference System in Brain Cancer Classification

Bassam Al-Naami^{a*}, Mohammed Abu Mallouh^b, Eman Abdel Hafez^c

^aDepartment of Biomedical Engineering, Hashemite University, P.O. Box 150459, Zarqa 13115, Jordan

^bDepartment of Mechatronics Engineering, Hashemite University, P.O. Box 150459, Zarqa 13115, Jordan

^cDepartment of Mechanical engineering, Al-Zaytoonah University of Jordan, P.O.Box 130, Amman 11733, Jordan

Received 13 Jul 2014

Accepted 15 Sep 2014

Abstract

Brain tumors are amongst the top death-leading health conditions worldwide. Biopsy is the most accurate procedure that determines the brain tumor type whether it is malignant or benign. However, biopsy may not be applicable for some patients with brain cancer (BCa) and could be life-threatening. In this paper, an intelligent diagnostic image-based systems are implemented to assist physicians in making diagnostic decisions about the BCa type without biopsy procedures. A combined method of artificial intelligent systems and MRI image segmentation is proposed as a tumor classification tool. This study employs image filtration and segmentation on a region of interest (ROI) of an MRI image. Then, extract accurate statistical features are fed into four artificial intelligent (AI) systems: Adaptive neuro-fuzzy inference system (ANFIS), Elman Neural Network (Elman NN), Nonlinear AutoRegressive with exogenous neural networks (NARXNN), and feedforward NN. The four AI classifiers are investigated and tested on 107 patients with brain tumors. The data base of the brain tumor images used in this study contains both malignant and benign cancers. The performance of the four intelligent tumor classifiers is evaluated. It is found that the NARX NN shows best performance with a classification accuracy of 99.1%. The achieved accuracy level is superior and could be very helpful in clinical purposes.

© 2014 Jordan Journal of Mechanical and Industrial Engineering. All rights reserved

Keywords: : Adaptive Neuro-Fuzzy Inference Systems (ANFIS); Neural Networks; Brain Cancer; Image Segmentation; Nonlinear Auto Regressive; Region of Interest (ROI).

1. Introduction

Brain tumors are the most complicated cancer diseases that are globally recognized by different organizations of cancer registry. It has been shown that brain tumors are fatal especially for children and they are listed among the highest causes of cancer among young adults [1]. In Jordan, 154 cases of malignant brain tumor were reported in 2008. The Age Specific Incidence Rates of brain tumors for males and females were reported in [2] as 8.1 and 4.8 per 100,000 populations for the age group (0-20 years), respectively, 5.1 and 10.3 per 100,000 populations for the age group (20-40 years), and 33.9 and 19.1 per 100,000 populations for the age group (40-60 years).

There are varieties of cancer treatment techniques, such as: chemotherapy, radiotherapy, surgery, and amalgamation. However, the early determination the type of brain tumor is one of the most important factors for curing [1]. Therefore, tumor type and nature must be diagnosed before starting the treatment procedures.

Advanced medical imaging modalities followed by a histological test known as biopsy are usually used in diagnosing. However, biopsy is still not applicable for some patients with brain cancer and could be life-threatening, and can cause a significant damage to the healthy brain tissues.

Thus, the objective of the proposed adaptive neural fuzzy system was to give primary information about the cancer existence in form of Classification Accuracy (CA) and the higher classification accuracy percentage, the greater the options for treatment. For under these circumstances, artificial intelligence, like fuzzy logic, neural networks and hybrid fuzzy logic and neural networks are implemented in image-based diagnostic systems. Such system serves to assist physicians in making diagnostic decisions based on database analysis and pattern recognition and without any risk. Also such system will be helpful in monitoring patients with low cancer risk without resorting to the frequent painful biopsy procedures. In [3], the fuzzy logic has been successfully implemented in breast cancer classification. Hybrid

* Corresponding author. e-mail: b.naami@hu.edu.jo.

particle swarm optimized fuzzy logic system was used in the modeling and design of a hypoglycemia monitor for patients with diabetes [4]. A complementary learning fuzzy neural network was proposed in [5] for Ovarian cancer diagnosis. In [6], a modified fuzzy cellular neural network was proposed to effectively segment CT liver images, which will help in early diagnosis of liver cancer. Adaptive Neuro-Fuzzy Inference System (ANFIS) is one of the intelligent systems that showed a promising performance in different aspects of our life, and more widely in medical applications. ANFIS has been implemented in many medical diagnoses such as: human action recognition [7] and epilepsy seizure [8-9]. Content-based image retrieval system, as a tool for discrimination between the normal and abnormal medical images, was developed in [10], heart valve diseases [11], rheumatoid arthritis [12], prostate cancer [13], and breast cancer [14]. ANFIS showed an overall accuracy in detecting glaucoma of 90.0% as reported in [15]. ANFIS illustrated a better performance in detecting four types of brain tumor when compared with the performance of probabilistic neural network classifiers [16].

Another promising intelligent cancer classification tool is based on Artificial Neural Networks (ANN). Karabatak in [17] presented an automatic diagnosis system for detecting breast cancer based on Association Rules (AR) and Neural Network (NN). The proposed AR with NN classifier showed an accuracy of 95.6%. In [18], a classification system was developed to detect tumor blocks or lesions, where the classification step was determined by ANN to discriminate between normal and abnormal MRIs for different patients with Astrocytoma type of brain tumors. An ANN automated diagnosis system was proposed for prostate cancer detection in [19]. Data taken by biopsy for 121 patients were used to train and tests the ANN classifier. The system showed an accuracy of 94.11%. In [19], An ANN discrete wavelet transformation hybrid technique was presented for brain cancer classification. A very adequate performance was obtained via a modified Probabilistic Neural Network (PNN) brain tumors classifier that was proposed in [20]. Their approach incorporated a non-linear Least Squares Features Transformation (LSFT) into the PNN classifier. The achieved classification accuracy was 95.24%.

In this study, a simple MRI tumor segmentation technique combined with artificial intelligent system to assist physicians in determining the brain tumor type is proposed. This proposed brain cancer classification approach will help in minimizing the examination time, cost and avoiding the unnecessary biopsy procedure. The key steps of the proposed method, technically, are illustrated in Figure (1). Step 1 of the approach is to obtain MRI investigated cases; step 2 is a preprocessing step, all images are filtered using the smoothing spatial low pass filter (averaging filter) and enhanced by the equalizing histogram. In step 3, the ROI is performed to segment the tumor part using threshold transformation function. Then the technique of feature extraction from each ROI is implemented to convert the original data set into minimum output features. This process is accomplished by measuring certain properties of the image, or features, that distinguish one input pattern from another pattern. In this Step, three textural features based on ROI of each gray

level for each MRI tumor type are extracted; as: the mean, maximum, and standard deviation of pixel values for both. In Step 4, the extracted features are fed into ANFIS and three ANN systems that classify the tumor type into Malignant or Benign. Three types of ANN are investigated: Elman Network, NARX Network, and Feedforward Network.

This paper is organized as follows: In section 2, a detailed description of image preprocessing and extraction parameters from the ROI, and data collection are presented. Also, ANFIS theory and brief description about Elman NN, NARXNN, and Feedforward NN are reviewed. Section 3 addresses the obtained experimental results and discusses the performance of each classifier (ANFIS, Elman NN, NARXNN, and Feedforward NN) in BCa detection. Finally, section 4 is devoted for the conclusion of the presented work with relevance to BCa classification.

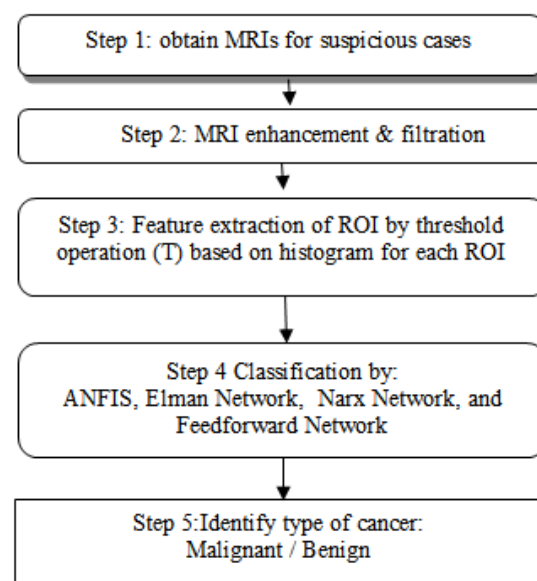


Figure 1. Flow chart of the proposed method

2. Materials and methods

2.1. Image Database

A total of 107 real brain MRIs that contain tumors were used in this study. The MRI data set contains (41) benign and (66) malignant MRIs that were collected from Jordanian hospitals. The MRIs were taken for different patients with several transverse slices. It is important to mention that all used MRIs were diagnosed and classified as benign or malignant by experts in the field. It was noticed that the tumors locations were in the middle, the right, and in the left half of the brain.

2.2. Enhancement and Segmentation

After converting all images to the gray scale, the histogram equalization was applied to improve the MRI quality. In this work, enhancement can be performed using the transformation function $(T(r))$, where r represents the gray levels of the MR image. This image was already normalized to the interval [0, 1], with $r=0$ representing black and $r=1$ representing white [21]. The

transformations ($T(r)$) produces a level s for every pixel value r in the original MRI as shown Eq. 1:

$$s = T(r) \quad 0 \leq r \leq 1 \quad (1)$$

On the other hand, the probability of occurrence of gray level r_k in an image is calculated by Eq. 2:

$$P_r(r_k) = \frac{n_k}{n} \quad k = 0, 1, 2, \dots, L - 1 \quad (2)$$

where n was the total number of pixels in the image, n_k was the number of pixels that have a gray level, and L is the total number of possible gray levels in the image [21]. Therefore, the histogram equalization was calculated by Eq. 3:

$$s_k = T(r_k) = \sum_{j=0}^k P_r(r_j) = \sum_{j=0}^k \frac{n_j}{n} \quad (3)$$

$$k = 0, 1, 2, \dots, L - 1.$$

Thus, the processed tumor image was obtained by mapping each pixel with level r_k in the input image into a corresponding pixel with level s_k in the output image via Eq. 3.

The BCa MRI was filtered using the smoothing spatial low pass filter (averaging filter) as a preprocessing step to remove insignificant details from a brain image before the object of tumor was extracted by the ROI histogram for the segmented region. Averaging filter was chosen with 3×3 pixels containing equal weights of value "1" is applied to the original image (R_i), where $i \in 1$ to 3×3 . In this case, the small objects with low intensity variations was blinded into the background, while leaving the objects of interest relatively (tumor) unchanged. The average filter is calculated by Eq. 4 [22] as follows:

$$X = \frac{1}{m \times n} \sum_{i=1}^{m \times n} R_i \quad (4)$$

Where $m=3$ and $n=3$. Resultant image X after applying the average filter in Eq. 4 is shown in Figures 2 and 3. As seen in both figures, each original image passes through an averaging filter (Figures 2(b) and 3(b)), where the majority of low intensity is eliminated by merging it within the background, while the last high intensity was appeared within tumor's region. In order to find ROI (region growing), threshold transformation function was applied to get the tumor segmented. To produce the ROI, it has to start with a set of "seed" points. Then from these points, the regions grow by appending to each seed those neighboring pixels that have properties similar to the seed [21]. A threshold value (T) is chosen by trial and error to produce a binary image which cut off the bright parts from the background [22]. Implementing the threshold results in two groups of pixels, $G_1(x, y)$ and $G_2(x, y)$ as illustrated in Eq. 5:

$$G(x, y) = \begin{cases} 1 & \text{if } G_1(x, y) \geq T \\ 0 & \text{if } G_1(x, y) < T \end{cases} \quad (5)$$

Figures 2(c) and 3(c) show the MRI after implementing the threshold. At the end of segmentation, the histogram for brain tumor was drawn as shown in Figures 2(d) and 3(d).

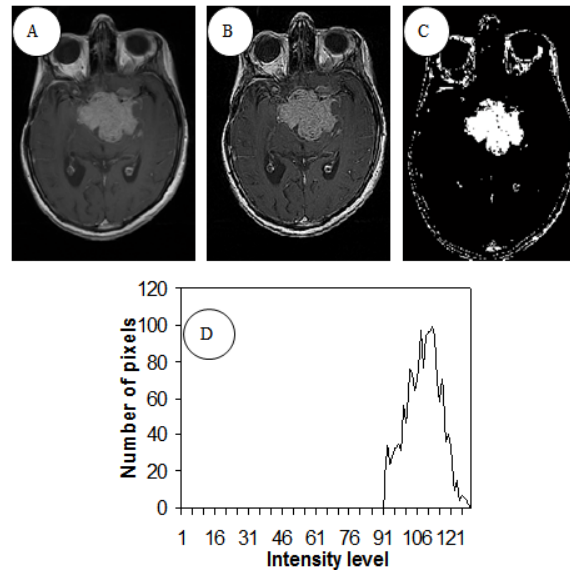


Figure 2. Original image of benign tumor (a), the result of averaging filter (b), segmented image by threshold operator (c), and the histogram for the tumor-ROI (d)

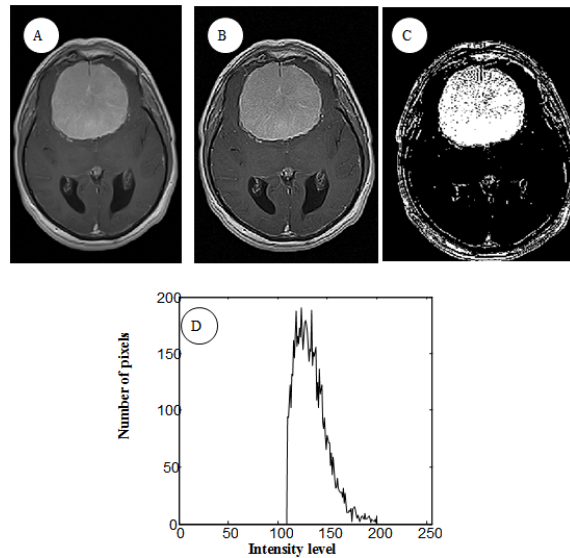


Figure 3. Original image of malignant tumor (a), the result of averaging filter (b), segmented image by threshold operator (c), and the histogram for the tumor-ROI (d)

2.3. Feature Extraction

To select an adequate set of features, we focused on the images characteristics of segmented ROI that physicians use to visually distinguish cancerous tumor from normal tissue. Hence, three features were extracted from the ROI for each of the 107 images, namely: (1) mean of the gray level values, (2) maximum gray level values, and (3) standard deviation of the gray level values. Table 1 shows the range of values for the three extracted features from the 107 MRI. The extracted features will be used as inputs to the intelligent systems tumor classifier as will be explained in next section.

Table 1. Range of extracted features values from all investigated MRI

Tumor Type	Extracted features from the segmented tumor by ROI in Pixels		
	Maximum value	Mean value	Standard deviation
Benign	163.11 ± 38.15	58.41 ± 28.12	22.12 ± 12.34
Malignant	214.96 ± 28.18	78.92 ± 30.36	31.26 ± 10.14

2.4. Adaptive Neuro Fuzzy Inference System

ANFIS is a novel architecture, initially proposed by Jang in 1993, in which a Sugeno fuzzy logic (FL) system is embedded in the framework of NN[23]. This combination of FL and NN produces an intelligent system that can learn and act similar to humans. Figure 4(a) shows a typical FL system. It is well known that constructing the rules and membership functions of a FL are the most difficult parts in designing and building a FL system. Rules and membership function are usually set by experts in the field. However, this drawback in FL design was solved in the ANFIS architecture shown in Figure 4(b). In addition, ANFIS does not need experts to set the rules and

tune its membership functions, but it only needs pairs of input and output data similar to NN. Thus, ANFIS has the ability to tune the membership functions of inputs and outputs in simpler way. As shown in Figure 4(b), ANFIS has five layers Feedforward neural network in which each node performs a particular function on the inputs, for example a bell shape function with maximum equal to 1 and minimum equal to 0, represented as:

$$\sigma_i^1(x) = \frac{1}{1 + [(\frac{x - c_i}{a_i})^2]^{o_i}} \tag{6}$$

where $\{a_i, o_i, c_i\}$ is the parameter set S_1 . Parameters in this layer are referred to as premise parameters. This layer corresponds to the fuzzification step of the FL system, for more details on ANFIS structure refer to [23-25]. A hybrid learning algorithm that combines a gradient descent and least squares are used to identify the adaptive network's premise parameters (S_1) and consequent parameters (S_2). A back propagation method is used in the backward pass and the least squares method is used in the forward pass.

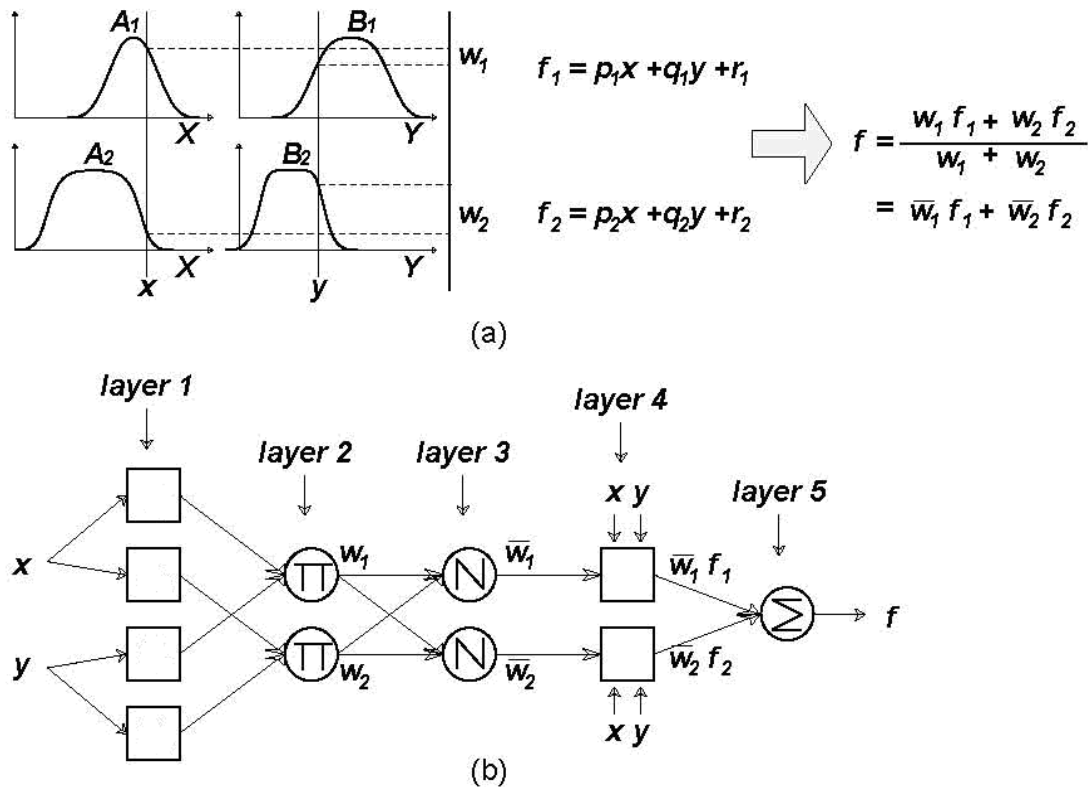


Figure 4. (a) Sugeno's FL system and (b) equivalent ANFIS [23]

2.5. Neural Networks System

2.5.1. Elman Network

The Elman neural network, which was introduced in 1990, is a recurrent one [26]. As indicated in Figure 5, the main components of this network are input, hidden and output layers. In addition to these three layers, this NN also has an additional layer called context, which receives the output from the hidden layer without being weighted and then send them again to the hidden layer using trainable weighted connection. This enables the network to remember these values and used them as inputs to the network for the next run which helps in sequence prediction.

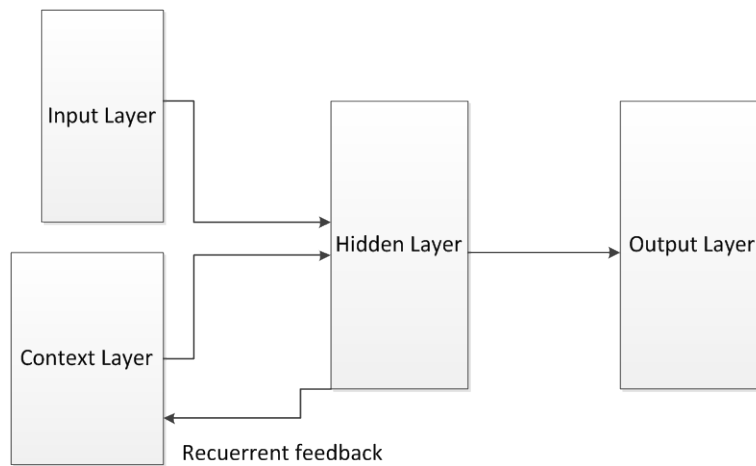


Figure 5. Elman Network

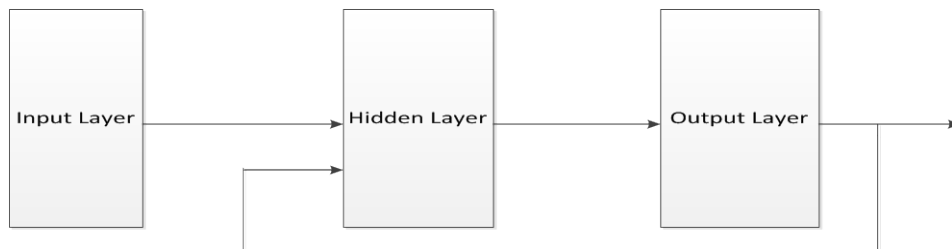


Figure 6. A typical neural network auto-regressive with exogenous inputs

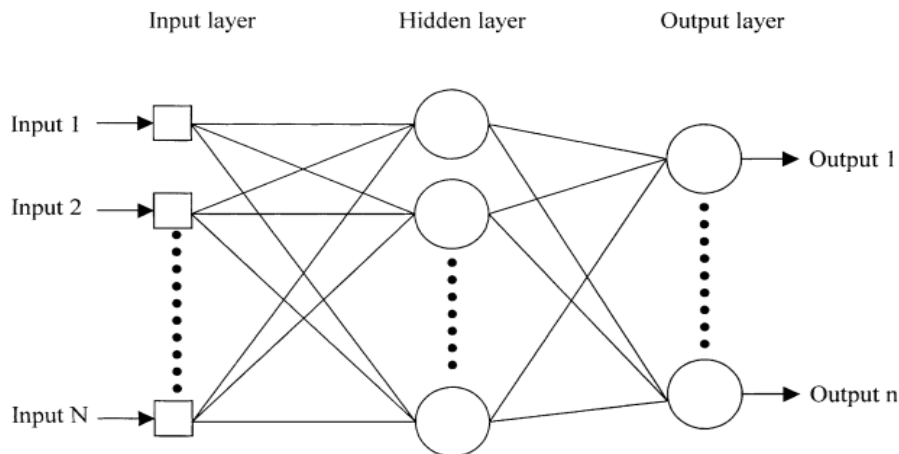


Figure 7. Multilayer feed forward network [29]

2.5.2. NARX Network

The Nonlinear AutoRegressive with Exogenous (NARX) NN is shown in Figure 6. It has exogenous input, which represents the feedback of the network output. This network is usually used to model nonlinear systems and time series [27, 28].

2.5.3. Feedforward Network

This network consists of an input layer of source neurons, at least one hidden layer of computational neurons, and an output layer of computational neurons. As shown in Figure 7, the input signals are propagated in a forward direction on a layer-by-layer basis.

3. Results and Discussion

3.1. ANFIS Tumor classifier

An ANFIS brain tumor classifier is designed with the ANFIS library function available in the Matlab fuzzy logic toolbox. The tuning parameters of ANFIS are number and type of inputs, number and type of membership functions. As shown in Figure 8, the ANFIS tumor classifier has two inputs and one output. The two inputs to the ANFIS are the maximum and mean values and the output is the type of tumor (0 for benign and 1 for malignant).

These two inputs were found to be the most effective in determining the tumor type, where the third input (standard deviation) was excluded due to its similarity for the majority of MR images from statistical aspect. Different types of membership functions were tested, such as triangular, trapezoidal, Gaussian, sigmoidal and bell-shape function; the best results were obtained with bell shape function. In order to achieve good generalization capability of the ANFIS, it is important to have the number of training data set to be larger than the number of the modified parameters. Two bell shape node functions were selected for each input. As shown in Eq. 6, each node function has 3 parameters to be tuned. Thus, the total number premise parameters (S_1) is 12.

The ANFIS classifier has 4 rules and a total of 12 consequent parameters (S_2). Thus, the total tuning parameters are 24. The 107 data were divided randomly into three sets: 70% (75 data points) of the data were used for training, 15% of the data (16 data points) used for checking, and 15% of the data (16 data points) used for testing. The training data are actually used to update the ANFIS parameters, the checking and testing data were not used in updating the ANFIS parameters. The checking data are used to determine when to stop the training process while the testing data are used to test the performance of the ANFIS on data that have not been used in training.

The ratio of number of data to number of ANFIS modifiable parameters is 75/24. The training, checking and testing data consist of both benign and malignant tumor data, where zero output is assigned for benign and one for malignant. The training method used is a combination of traditional back propagation and a least squares technique. The training is done offline, usually once and before

delivering the classifier to real clinic for application. After the training stage the ANFIS classifier was tested using the testing data, which were not used in the training stage.

3.2. NN Tumor Classifiers

The neural network library function available in the Matlab neural network toolbox is used to design the three NN *Tumor classifiers* (Elman, NARX and feedforward). The NN tumor classifiers have two inputs and one output. Ten neurons in the hidden layer are used. The selection of number of hidden neurons is made based on a trial-and-error procedure. Similar to the ANFIS, the two inputs to the NN are the maximum and mean values and the output is the type of tumor (0 for benign and 1 for malignant). The same data used in building the ANFIS are used in building the three NN. The 107 data were divided randomly into three sets. 70% (75 data points) of the data were used for training, 15% of the data (16 data points) used for checking and 15% of the data (16 data points) used for testing. Figures 9, 10 and 11 show the after-training performance responses for Elman, NARX and Feedforward networks, respectively.

Table 2 lists the performance of the ANFIS, Elman, NARX and Feedforward tumor classifiers in terms of sensitivity, specificity and classification accuracy. Sensitivity (Se), Specificity (Sp), and Classification accuracy (Ca) are important measures to validate the performance of the proposed method and calculated using Eqs. 7, 8 and 9, respectively [30].

$$\text{Sensitivity (\%)} = \frac{TP}{TP + FN} \times 100 \quad (7)$$

$$\text{Specificity (\%)} = \frac{TN}{FP + TN} \times 100 \quad (8)$$

$$\text{Classification accuracy (\%)} = \frac{TP + TN}{TP + FP + FN + TN} \times 100 \quad (9)$$

where TP, TN, FP, and FN denotes true positives, true negatives, false positives, and false negatives, respectively.

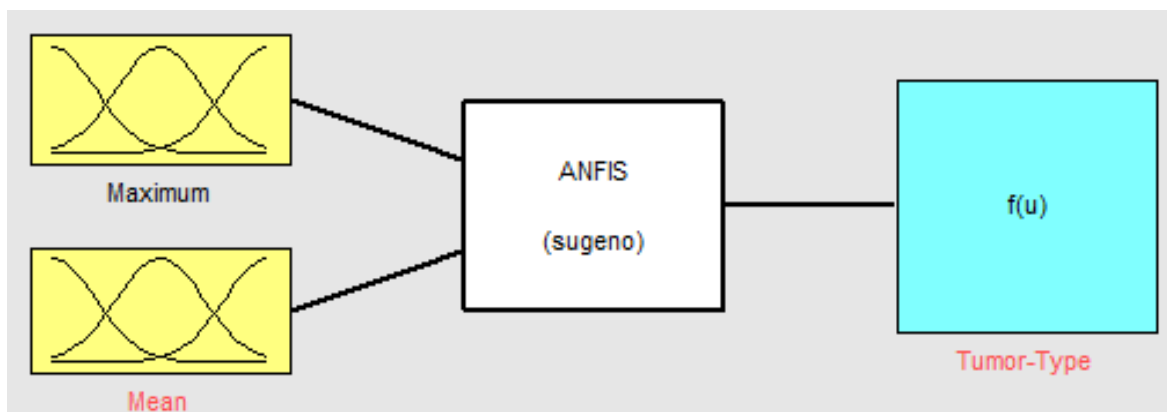


Figure 8. The designed ANFIS tumor classifier

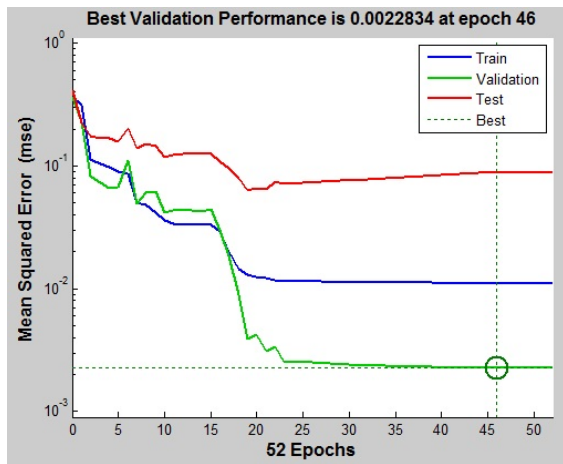


Figure 9. Performance responses for Elman NN

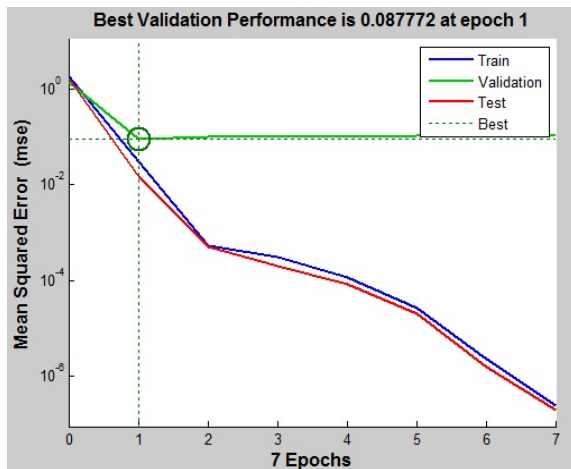


Figure 10. Performance responses for NARX NN

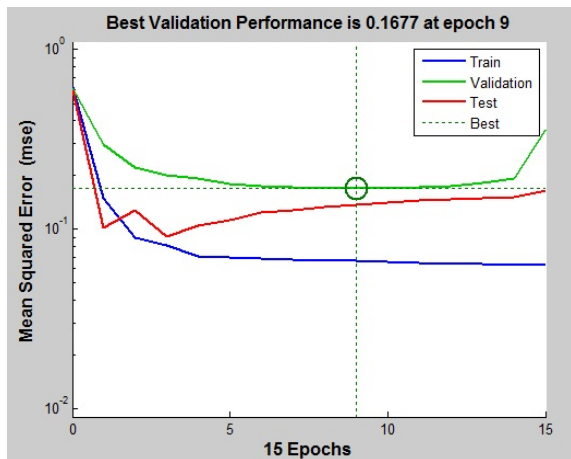


Figure 11. Performance responses for Feedforward NN

Table 2. Performance results of ANFIS with other neural networks.

Model	TP	FN	TN	FP	Se %	Sp %	Ca %
ANFIS	65	3	31	8	95.6	79.5	89.7
Elman	66	0	38	2	100	95	98.1
NARX	67	0	38	1	100	97.4	99.1
FeedForward	60	6	33	8	90.9	80.5	86.9

ANFIS classifier performance in terms of sensitivity, specificity and accuracy are 95.6%, 79.5% and 89.7%, respectively. The performance of Elman classifier shows better results than those of the ANFIS, where sensitivity, specificity and accuracy values are 100%, 95% and 98.1%, respectively. The best performance is achieved by NARX classifier with values of 100%, 97.4% and 99.1% for sensitivity, specificity and accuracy, respectively. Feedforward classifier has the worst performance in terms of sensitivity and accuracy with values of 90.9% and 86.9%, respectively, while the specificity is 80.5%.

4. Conclusion

In this study, four artificial intelligent MRI image-based systems were developed for brain tumor classification. The developed systems consist of three stages. The first stage includes image filtration and enhancement. In the second stage, the ROI is employed for features extraction and the histogram is constructed for each case. In the third stage, the extracted features (mean and maximum values of ROI pixels) are fed into an artificial intelligent brain tumor classifier. Four artificial intelligent systems are investigated: ANFIS, Elman NN, NARX NN and feedforward NN. The best performance, in terms of classification accuracy, was obtained with the NARX NN with a value of 99.1% that is better than ANFIS, Elman and feedforward classifiers by 89.7%, 98.1%, and 86.9%, respectively.

The classification results show that the proposed method is effective in detecting BCa and it could be considered as an alternative approach for the previous approach in [31]. Moreover, development of this diagnostic approach will provide assistance to physicians in determining the tumor type without the need of performing biopsy or any other invasive procedures.

References

- [1] O.C.Andronesi, K.D.Blekas, D.Mintzopoulos, L.Astrakas, P.M. Black, A.A.Tzika, "Molecular Classification of Brain Tumor Biopsies using Solid-State Magic Angle Spinning Proton Magnetic Resonance Spectroscopy and Robust Classifiers". International Journal of Oncology, Vol. 33 (2008) 1017–1025.
- [2] M. Tarawneh, O. Nimri, K. Arqoub, M. Zaghafal, "Cancer Incidence in Jordan". 2009. Available at: <http://www.moh.gov.jo>.
- [3] D. Soriaa, J.M. Garibaldi, A.R. Green, D.G. Powe, C.C. Nolan, C. Lemetre, G.R. Ball and I.O. Ellis, "A quantifier-based fuzzy classification system for breast cancer patients". Artificial Intelligence in Medicine, Vol. 58 (2013) 175–184.
- [4] S.H. Ling and H.T. Nguyen, "Natural occurrence of nocturnal hypoglycemia detection using hybrid particleswarm optimized fuzzy reasoning model". Artificial Intelligence in Medicine, Vol.55 (2012) 177–184.
- [5] T.Z. Tan, C. Queka, G.S. Ng, and K. Razvi, "Ovarian cancer diagnosis with complementary learning fuzzy neural network". Artificial Intelligence in Medicine, Vol. 43 (2008) 207–222.
- [6] W. Shitong, F. Duan, X. Min, and H. Dewen, "Advanced fuzzy cellular neural network: Application to CT liver images". Artificial Intelligence in Medicine, Vol. 39 (2007) 65–77.

- [7] K. Subramanian and S. Suresh, "Human action recognition using meta-cognitive neuro-fuzzy inference system". *International Journal of Neural Systems*, Vol. 22 (2012) 21-35.
- [8] U.R. Acharya, R. Yanti, J.W. Zheng, M.R. Krishnan, J.H. Tan, R.J. Martis, and C.M. Lim, "Automated diagnosis of epilepsy using cwt, hos and texture parameters". *International Journal of Neural Systems*, Vol. 23 (2013) DOI: 10.1142/S0129065713500093.
- [9] Subasi, "Application of adaptive neuro-fuzzy inference system for epileptic seizure detection using wavelet feature extraction". *Computers in Biology and Medicine*, Vol. 37 (2007) 227-44.
- [10] M. Tarjoman, E. Fatemizadeh, and K. Badie, "An interactive cbir system based on anfis learning scheme for human brain magnetic resonance images retrieval". *Biomedical Engineering: Applications, Basis and Communications*, Vol. 24 (2012) 27-36.
- [11] E. Avci, I. Turkoglu, "An intelligent diagnosis system based on principle component analysis and ANFIS for the heart valve diseases". *Expert Systems with Applications*, Vol. 36 (2009) 2873-8.
- [12] O. Özkan, S. Kara, A. Salli, M. E. Sakarya, S. Güneş, "Medical diagnosis of rheumatoid arthritis disease from right and left hand Ulnar artery Doppler signals using adaptive network based fuzzy inference system (ANFIS) and MUSIC method". *Advances in Engineering Software*, Vol. 41(2010), 1295-301.
- [13] Keles, S. Hasiloglu, A. Keles, and Y. Aksoy, "Neuro-fuzzy Classification of Prostate Cancer using NEFCLASS". *Journal of Computers in Biology and Medicine*, Vol. 37 (2007) 1617-1628.
- [14] E. D. Übeyli, "Adaptive neuro-fuzzy inference systems for automatic detection of breast cancer". *Journal of Medical Systems*, Vol. 33 (2009) 353-358.
- [15] M. L. Huang, H. Y. Chen, J. J. Huang, "Glaucoma detection using adaptive neuro-fuzzy inference system". *Expert Systems with Applications*, Vol. 32 (2007) 458-68.
- [16] D. J. Hemanth, C. K. Vijila, J. Anitha, "Application of Neuro-Fuzzy Model for MR Brain tumor image classification". *International Journal of Biomedical Imaging*, Vol. 16 (2009) 95-102.
- [17] M. Karabatak, M. C. Ince, "An expert system for detection of breast cancer based on association rules and neural network". *Expert Systems with Applications*, Vol. 36 (2009) 3465-3469.
- [18] D. M. Joshi, N. K. Rana, and V. M. Misra, "Classification of Brain Cancer Using Artificial Neural Network". *IEEE-International Conference on Electronic Computer Technology (ICECT)*, Kuala Lumpur, 2010.
- [19] Saritas, I. A. Ozkan, and I. U. Sert, "Prognosis of prostate cancer by artificial neural networks". *Expert Systems with Applications*, Vol. 37 (2010) 6646-6650.
- [20] P. Georgiadis, D. Cavouras, I. Kalatzis, A. Daskalakis, G. C. Kagadis, K. Sifaki, M. Malamas, G. Nikiforidis, and E. Solomou, "Improving brain tumor characterization on MRI by probabilistic neural networks and non-linear transformation of textural features". *Computer methods and programs in biomedicine*, Vol. 89 (2008) 24-32.
- [21] R. C. Gonzalez, R. E. Woods, S.L Eddins, "Digital Image Processing," 2nd Ed., New Jersey. Prentice Hall; 2004.
- [22] Reza, C. Swaran, and S. Hati, "Automatic Tracing of Optic Disc and Exudates from Color Fundus Images using Fixed and Variable Thresholds". *Journal of Medical System*, Vol. 33 (2009) 73-80.
- [23] R. Jang, "ANFIS: Adaptive-network-based fuzzy inference system". *IEEE Transactions on System, Man and Cybernetics*, Vol. 23 (1993) 181-198.
- [24] Al-Naami, M. Abu mallouh, and A.A. Khesman, "Automated intelligent diagnostic of Alzheimer disease based on neuro-fuzzy system and discrete wavelet transform". *Biomedical Engineering: Applications, Basis and Communications*, Vol. 26 (2014) No. 3, 1450035.
- [25] M. Samhoury, A. Al-Ghandoor, S. Alhaj Ali, I. Hinti, W. Massad, "An Intelligent Machine Condition Monitoring System Using Time-Based Analysis: Neuro-Fuzzy Versus Neural Network". *Jordan Journal of Mechanical and Industrial Engineering*, Vol. 3 (2009) 294 - 305.
- [26] J. Elman, "Finding structure in time". *Cognitive Science*, Vol. 14 (1990) 179-211.
- [27] M.I.P. Hidayat, P.S.M.M. Yusoff, and W. Berata, "Neural networks with NARX structure for material lifetime assessment application". *IEEE Symposium on Computers & Informatics*, Kuala Lumpur, 2011.
- [28] L. B. Mohammed, M.A. Hamdan, E. A. Abdelhafez And W. Shaheen. "Hourly Solar Radiation Prediction Based on Nonlinear Autoregressive Exogenous (Narx) Neural Network". *Jordan Journal of Mechanical and Industrial Engineering* Vol. 7 (2013) 11 - 18.
- [29] Dorvlo, J. Jervase, and A. Al-Lawati, "Solar radiation estimation using artificial neural networks", *Applied Energy*, Vol. 71 (2002) 307-319.
- [30] B. Al-Naami, J. Al-Nabulsi, H. Amasha, and J. Torry, "Utilizing wavelet transform and support vector machine for detection of the paradoxical splitting in the second heart sound". *Medical & Biological Engineering & Computing*, Vol. 48 (2010) 177-184.
- [31] B. Al-Naami, A. Bashir, H. Amasha, J. Al-Nabulsi, and A. Almalty, "Statistical Approach for Brain Cancer Classification Using a Region Growing Threshold". *Journal of Medical Systems*, Vol. 35 (2011) No. 4, 463-471.

Fabrication and Characterization of Copper-Red Mud Particulate Composites Prepared by Powder Metallurgy Technique

N. Vijaya Sai *

Dept. of Mechanical Engineering, V. R. Siddhartha Engineering. College, Vijayawada - 520 007, India

Received 17 Jul 2014

Accepted 10 Sep 2014

Abstract

Copper-red mud powder mixtures containing 0-14 wt% red mud with 75, 53 and 38 μm particle sizes were prepared. Small cylindrical specimens of 9 mm diameter and 10.5 mm length were fabricated at 300 MPa, using single action die compaction at ambient temperature. These compacts were sintered in argon atmosphere at 8500C. The physical, mechanical and electrical properties of green and sintered compacts were determined as a function of particle size of red mud and its weight percent. It was observed that the ejection pressure, green density, and strength decreased, while spring back, green porosity and hardness increased with increasing the weight percent of red mud. It was also observed that ejection pressure, green density, green hardness and strength increased, while spring back and green porosity decreased with decreasing particle size of red mud. Sintering resulted in a decrease in volume and an increase in the density of green compacts. It was found that the sintered density of the compacts decreases with increasing weight percent of red mud. It was also observed that the addition of red mud results in an increase in hardness and a decrease in compressive yield strength and electrical conductivity of sintered compacts under the present experimental conditions. It was further observed that with the decrease in particle size of red mud, the density, hardness, compressive yield strength and electrical conductivity of sintered compacts gradually increase.

© 2014 Jordan Journal of Mechanical and Industrial Engineering. All rights reserved

Keywords: : Ejection Pressure, Spring Back, Density, Porosity, Hardness, Strength, Electrical Conductivity.

1. Introduction

Management of waste materials has become very much important for protecting the environment. One way to achieve this objective is to reuse/recycle the waste materials for the development of new materials. The alumina manufacturing industry produces voluminous quantity of red mud as a waste product. It is estimated that an amount of 90 million tons of red mud is produced annually in various parts of the world. Its disposal causes significant economic and environmental problems [1-3]. As a result, exploring new avenues to utilize red mud is highly essential. To solve the disposal problem, considerable research and development work have been carried out, and efforts are made to use red mud as a cheap adsorbent for removal of toxic metals such as nickel [4], arsenic [5], lead and chromium [6] from aqueous solutions, for preparation of building materials, namely iron rich cement and ceramic tiles [7, 8], and as a filler material in metal and polymer matrix composites [9-13].

Copper matrix composites with particulate ceramic reinforcements such as SiC and Cu_2O are potential candidate materials for electrical and electronic applications [14-18]. These copper composites combine the superior ductility, toughness and thermal conductivity

of copper and high strength, improved wear resistance and low coefficient of thermal expansion of these ceramic reinforcements. However, the high cost of these ceramic reinforcements remains a major barrier in their wide spread use. Hence, there has been an increasing interest in composites containing low density and low cost reinforcements such as fly ash [19] and red mud.

Red mud mainly consists of silica and oxides of aluminum, iron, and titanium, along with other minor constituents. Red mud particles have been used as filler in aluminum and as well as polymer matrices. It is reported that the addition of red mud to aluminum matrix increased the hardness and wear resistance and decreased the coefficient of friction [9, 10]. The addition of red mud to polymer matrices has increased tensile strength, impact and flexural strengths considerably [11-13]. Hence, this low cost and low density particulate reinforcement is added to copper matrix to study the effect of red mud content and its particle size on the physical, mechanical and electrical properties of the copper-red mud composites for possible electrical and electronic applications.

Several processing techniques are used for the production of the metal matrix composites, which can be grouped into two main routes depending on the state of the matrix during the fabrication process, either liquid or solid routes. Copper-red mud composites by casting are likely to

* Corresponding author. e-mail: nvs64@yahoo.com.

exhibit segregation and non-uniform distribution of particles because of the differences in density between the red mud particles and the matrix. So, powder metallurgy is used to prepare copper-red mud composites in the present work. With this aim, the present experimental investigations are carried out on fabrication and characterization of copper-red mud particulate composites prepared by powder metallurgy technique.

2. Experimental Procedure

Copper powder (99.5% pure) was procured from M/s Loba Chemie Pvt. Ltd., Mumbai and the red mud material was obtained from the aluminum refinery of NALCO located at Damanjodi, Orissa, India. The average size of copper powder is 44 μm . The chemical analysis of the red mud was carried out by M/s Natural Resource Development Cooperative Society Ltd., Hyderabad, India. The chemical composition of red mud is shown in Table 1.

The coarse particles of red mud, obtained from the aluminium refinery, were pulverized into finer particles manually. In order to study the effect of red mud particle size on the properties of copper-red mud composites, three different sizes of red mud powders, namely 75, 53 and 38 μm were prepared using sieve analysis. The densities of these red mud powders were measured using Archimedes principle and are represented in Table 2. Mixtures of copper-red mud powders containing 0-14 wt % red mud with 75, 53 and 38 μm particle sizes were prepared. In order to obtain uniform distribution of copper and red mud powders, they were mixed mechanically using a rotating rectangular container for a period of one hour. Cylindrical compacts were obtained at 300 MPa using single action die compaction at ambient temperature. The specimens were compacted at a uniform load rate of 5 kN/min for a period of 3.8 min. Silicone spray was used as the die wall lubricant. The compact dimensions were 9 mm diameter and 10.5 mm length. The above compacts were sealed in transparent silica tube under argon atmosphere and sintered at 850 $^{\circ}\text{C}$ in a tubular furnace for a period of 45 min.

Scanning electron micrographs were used to study the structural details of the particles. Metallographic examination of green and sintered compacts was carried out using optical microscopy. The green properties, namely spring back, ejection pressure, green density, green porosity, green hardness and green strength were evaluated as a function of particle size of red mud and its weight percent. Density, porosity, hardness, compressive yield strength and electrical conductivity of the sintered compacts were also determined as a function of particle size of red mud and its weight percent. The spring back of the cylindrical green specimen is determined using the following equation:

$$\% \text{ Spring back} = (D_g - D_d) \times 100 / D_d,$$

where

D_g = Diameter of the green specimen

D_d = Diameter of the die bore (9 mm)

Table 1. Chemical composition of red mud (wt%)

Constituents	Al ₂ O ₃	SiO ₂	Fe ₂ O ₃	TiO ₂	CaO	Na ₂ O	P ₂ O ₅	V ₂ O ₅	ZnO	MgO	MnO	K ₂ O
Wt%	14.14	11.53	48.5	5.42	3.96	7.5	0.3	0.12	0.03	0.05	0.17	0.06

Green and sintered densities were determined by physical measurements. The porosity of the green and sintered compacts was determined by taking theoretical density of the specimen into consideration. Vickers hardness measurements were obtained using TIME TH130 Integrated Micro Hardness Tester. Compression testing was conducted using an electronic UTM at a crosshead speed of 0.2 mm/min. The electrical conductivity was measured in % IACS using a digital electrical conductivity meter.

Table 2. Density of red mud

Particle size of Red mud	Density (kN/m ³)
0-75 microns	29.23
0-53 microns	29.42
0-38 microns	30.35

3. Results and Discussion

3.1. Powder Characteristics

The scanning electron micrographs of copper and red mud particles as shown in Figures 1 & 2 indicate their size, shape, size distribution and structure. Figure 1 indicates the flaky and dendritic structure of copper powder, whereas Figure 2 reveals the presence of partially round, angular and elongated shapes of red mud particles.

3.2. Green Properties

The variation of spring back with increasing red mud weight percent and its particle size is shown in Table 3 as well as Figure 3. They show that spring back increases with the increase in red mud content. It is known that spring back increases with increasing plastic strain and yield stress and decreasing modulus of elasticity of the particles. The relative increase in spring back with the addition of red mud is due to the deformation of red mud particles under elastic mode during compaction. It also shows that spring back decreases with decrease in particle size of red mud. This may be attributed to the red mud particle size distribution.

The variation of ejection pressure with increasing red mud content and its particle size is presented in Table 3 as well as Figure 4. They indicate that the ejection pressure decreases with the increase in red mud content. The high ejection pressure in the case of pure copper compacts is due to the high frictional characteristics of flaky and dendritic copper powder. The gradual decrease in ejection pressure with increasing red mud weight percent may be attributed to the low frictional properties of partially rounded red mud particles in the composite. The increase in ejection pressure with decrease in particle size of red mud may be due to increase in real area of contact between the die wall and the green compact. The optical microstructure of copper-red mud green compact is shown in Figure 5. The figure shows the deformation and uniform distribution of 6 wt% of 38 μm red mud powder in copper matrix at 300 MPa compaction pressure.

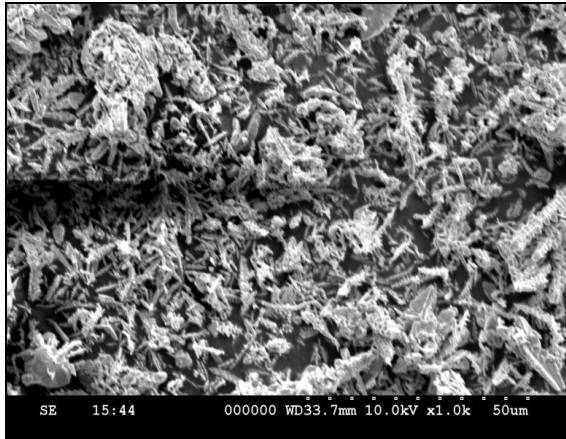


Figure 1. SEM of copper particles

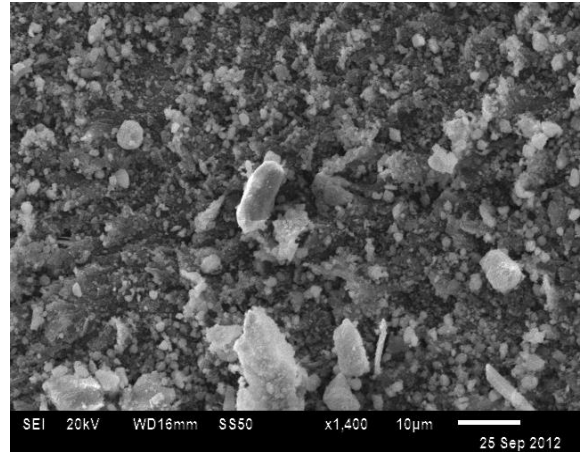


Figure 2. SEM of red mud particles (38 μm)

Table 3. Effect of red mud content and particle size on spring back & ejection pressure

Composition	Spring back (%)			Ejection Pressure (MPa)		
	Size of Red mud particles			Size of Red mud Particles		
	75 μm	53 μm	38 μm	75 μm	53 μm	38 μm
Copper	0.446			32		
Copper + 2% Red mud	0.505	0.498	0.459	18.46	22.46	29
Copper + 4% Red mud	0.522	0.502	0.476	16.8	21.04	26.93
Copper + 6% Red mud	0.537	0.516	0.503	16.01	19.83	26.23
Copper + 8% Red mud	0.544	0.525	0.519	15.89	18.05	23.56
Copper + 10% Red mud	0.551	0.539	0.53	14.05	17.56	21.31
Copper + 12% Red mud	0.631	0.572	0.56	12.83	15.62	18.54
Copper + 14% Red mud	0.637	0.625	0.602	11.7	13.71	17.71

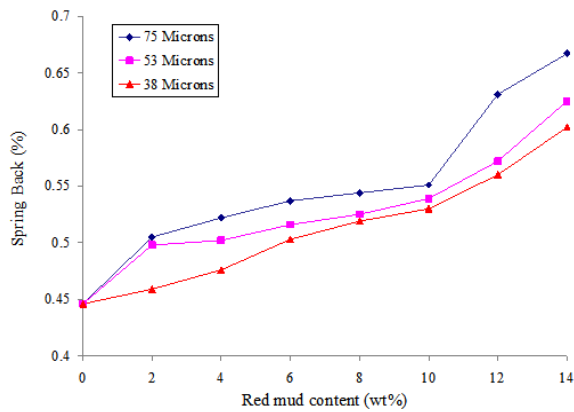


Figure 3. Effect of red mud content on spring back

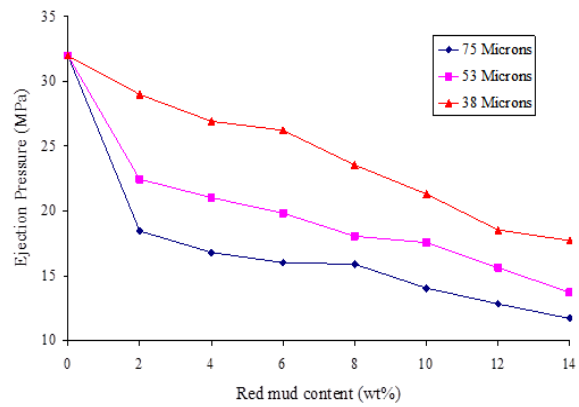


Figure 4. Effect of red mud content on ejection pressure

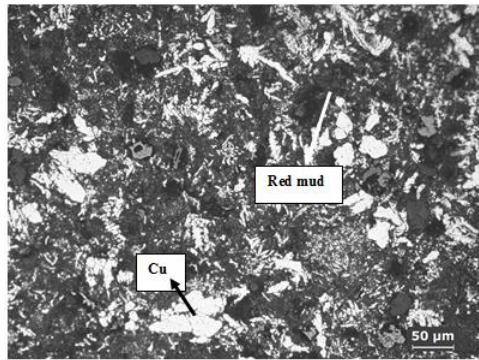


Figure 5. Microstructure of Cu-6% Red mud (38 μm) green compact

The effect of red mud weight percent and its particle size on green density and porosity are shown in Tables 4 & 5 and Figures 6 & 7, respectively. They show that green density decreases, whereas porosity increases with increase in red mud weight percent. The decrease in green density with addition of red mud to copper matrix is due to the relative density differences of red mud and copper powder mixtures. The increase in porosity with the addition of red mud can be attributed to the partially round shape of red mud particles. It also shows that green density increases while green porosity decreases with decrease in particle size of red mud. Finer particles of red mud result in more particle to particle contacts and plastic deformation leading to cold welding of particles. This results in more density and less porosity of the green compacts. Larger particles of red mud may lead to the partial welding of particles and voids resulting in less density and more porosity of the green compacts.

Table 4. Effect of red mud content and particle size on density

Composition	Green Density (kN/m^3)			Sintered Density (kN/m^3)		
	Size of Red mud particles			Size of Red mud Particles		
	75 μm	53 μm	38 μm	75 μm	53 μm	38 μm
Copper	68.26			77.97		
Copper + 2% Red mud	58.83	62.02	66.68	69.02	70.4	72.05
Copper + 4% Red mud	54.35	60.69	63.91	63.57	67.71	70.71
Copper + 6% Red mud	54.2	57.98	61.18	62.96	64.03	66.02
Copper + 8% Red mud	54.05	56.59	59.99	60.09	60.07	63.78
Copper + 10% Red mud	53.6	54.87	57.58	58.18	58.58	60.32
Copper + 12% Red mud	47.23	51.1	54.03	50.43	55.36	56.33
Copper + 14% Red mud	45.48	51.12	53.26	48.46	53.22	54.69

Table 5. Effect of red mud content and particle size on porosity

Composition	Green Porosity (%)			Sintered Porosity (%)		
	Size of Red mud particles			Size of Red mud Particles		
	75 μm	53 μm	38 μm	75 μm	53 μm	38 μm
Copper	18			12.01		
Copper + 2% Red mud	26.25	22.59	21.25	18.3	16.56	15.02
Copper + 4% Red mud	30.32	26.31	21.73	20.34	16.66	15.98
Copper + 6% Red mud	30.88	27.45	22.35	20.87	18.24	16.31
Copper + 8% Red mud	31.02	27.23	21.8	21.16	19.87	16.38
Copper + 10% Red mud	33.16	27.68	22.37	22.15	20.85	18.41
Copper + 12% Red mud	33.99	28	24.48	28.84	21.76	21.25
Copper + 14% Red mud	34.08	28.63	24.92	29.41	22.33	21.37

Table 6. Effect of red mud content and particle size on hardness

Composition	Green Hardness (HV)			Sintered Hardness (HV)		
	Size of Red mud particles			Size of Red mud Particles		
	75 μm	53 μm	38 μm	75 μm	53 μm	38 μm
Copper	30			24.6		
Copper + 2% Red mud	30.9	31.7	32.4	25.14	26.6	27.08
Copper + 4% Red mud	33.7	35.5	38.2	27.75	29.61	31.73
Copper + 6% Red mud	35.2	36.6	42.1	32.58	34.4	35.16
Copper + 8% Red mud	37.3	38.6	42.9	36.33	37.93	38.38
Copper + 10% Red mud	39.2	40.6	43.8	38.39	39.94	42.03
Copper + 12% Red mud	43.2	45.8	50.1	41.48	43.01	48.66
Copper + 14% Red mud	46.4	47.3	51.2	44.39	45.08	49.13

Table 7.Effect of red mud content and particle size on strength

Composition	Green Strength (MPa)			Sintered Compressive Yield Strength (MPa)		
	Size of Red mud particles			Size of Red mud Particles		
	75 μm	53 μm	38 μm	75 μm	53 μm	38 μm
Copper	152			56.6		
Copper + 2% Red mud	116.29	125.09	136.68	49.4	51.74	53.83
Copper + 4% Red mud	105.63	115.83	125.4	42.7	44.23	48.57
Copper + 6% Red mud	95.13	106.71	120.31	36.5	38.33	43.06
Copper + 8% Red mud	81.7	97.45	106.87	31.87	34.38	38.91
Copper + 10% Red mud	73.36	82.47	101.93	28.32	33.29	35.04
Copper + 12% Red mud	61.31	71.97	89.26	26.38	29.18	33.36
Copper + 14% Red mud	52.97	55.59	65.32	24.08	27.56	31.08

Tables 6 & 7 and Figures 8 & 9 represent the red mud content's effects and its particle size on green hardness and strength. They show that the green hardness increases, while the green strength decreases with increasing red mud content. The increase in green hardness with increase in red mud content is due to the presence of silica and oxides of aluminium, iron and titanium present in the red mud. The decrease in green

strength with increasing red mud content may be attributed to the poor mechanical bonding between the red mud and the copper powder mixture. This may be because of the round surface and lack of plasticity of red mud particles as compared to that of copper. These figures also show that the green hardness and strength increase with the decrease in the particle size of red mud.

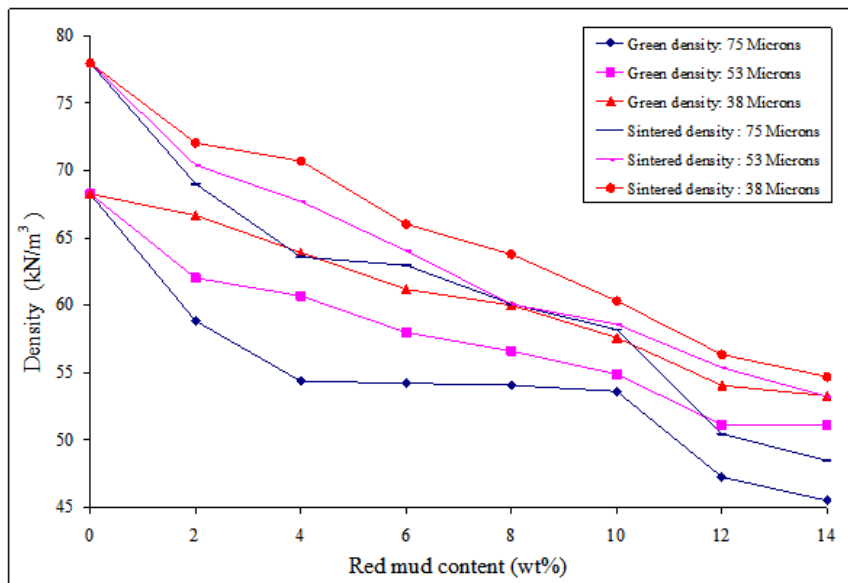


Figure 6. Effect of red mud content on density

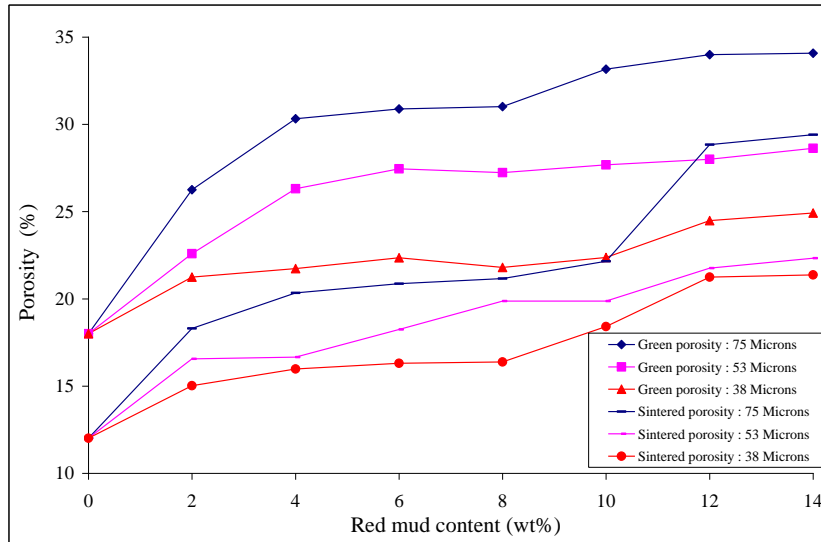


Figure 7. Effect of red mud content on porosity

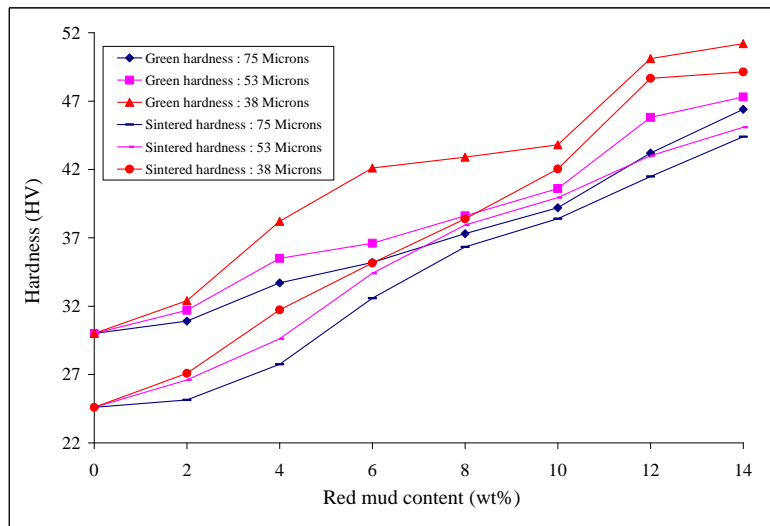


Figure 8. Effect of red mud content on hardness

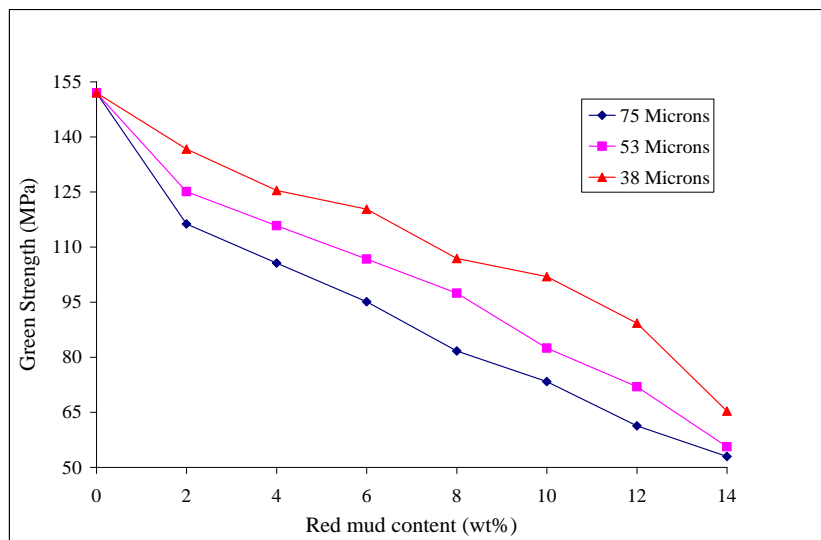


Figure 9. Effect of red mud content on green strength

4. Sintered Characteristics

Dimensional changes (volume changes) always occur during sintering of a green compact due to solid state diffusion processes or liquid phase sintering in a multi-component system with widely different melting points of constituents. Since the sintering temperature employed in the present investigation (850°C) is less than the melting point of copper (1083°C) and red mud (1300°C)[3], the composites undergo solid state sintering.

Tables 4 & 5 and Figures 6 & 7 also indicate the red mud content's effect and its particle size on sintered density and porosity. Comparing the sintered densities with those of the corresponding green densities for respective compositions, it can be clearly noticed that the density after sintering is always more than the corresponding green density due to negative growth in volume on sintering. Sintered density decreases with increasing red mud content. Sintered porosity increases with increasing red mud content. The addition of 38 µm red mud powder to copper increased the sintered porosity of pure copper compacts from 12% to 21.3%. Since the density of red mud is very low, for a given weight percentage, significant volume of matrix phase is replaced. With increase in red mud content, the proportion of direct red mud-red mud contacts increases. The direct red mud-red mud contacts degrades the quality of sintering at the processing temperature, because the red mud has a melting point (1300°C) higher than the sintering temperature. This aids in the reduction of volume change and sintered density with a corresponding increase in sintered porosity of the composites. Figures 6 & 7 also show that the sintered density increases with the corresponding reduction in sintered porosity with decrease in particle size of red mud. The microstructure of copper-6% red mud (38 µm) sintered compact depicted in Figure 10 shows a uniform dispersion of red mud in the copper matrix.

Tables 6 & 7 and Figures 8 & 11 represent the variation of sintered hardness and compressive yield strength of the copper-red mud composites as a function of red mud weight percent and its particle size. The figures show that sintered hardness increases, while sintered compressive yield strength decreases with increase in red mud content. These figures also show that with decrease in particle size, sintered hardness and yield strength increases. The sintered compressive yield strength is particularly low for composites containing more than 10 wt% red mud. It indicates that the useful range of red mud that can be added to copper matrix lies below 10%. The decrease in

strength is due to the high porosity and ineffective sintering between red mud particles and the copper matrix in sintered red mud composites.

The red mud's effect and its particle size on electrical conductivity is shown in Table 8 and Figure 12. Electrical conductivity gradually decreases with the increase in red mud content. This may be due to the poor conductivity of the constituents of red mud apart from the low density and high porosity of the sintered red mud compacts. The electrical conductivity of the sintered red mud compacts gradually increases with decrease in particle size of red mud. This can be attributed to the increased density of compacts with decrease in particle size.

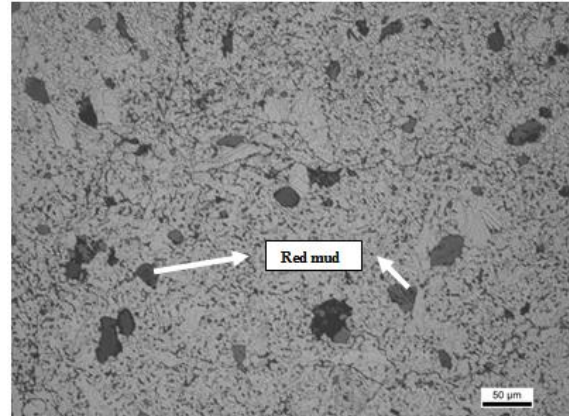


Figure 10. Microstructure of Cu-6% red mud (38 µm) sintered compact

Table 8. Effect of red mud content and particle size on electrical conductivity

Composition	Electrical Conductivity (% IACS)		
	Size of Red mud particles		
	75 µm	53 µm	38 µm
Copper	44.2		
Copper + 2% Red mud	41.7	42.6	43.5
Copper + 4% Red mud	39.3	40.8	42.3
Copper + 6% Red mud	34.6	38.8	41.2
Copper + 8% Red mud	32.5	33.2	33.6
Copper + 10% Red mud	25.2	28.5	29.8
Copper + 12% Red mud	23.7	25.8	27.6
Copper + 14% Red mud	20.9	22.4	24.1

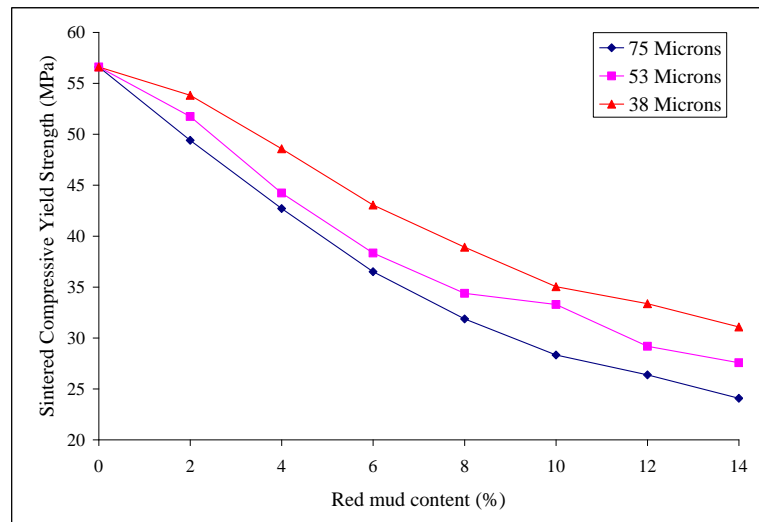


Figure 11. Effect of red mud content on sintered compressive yield strength

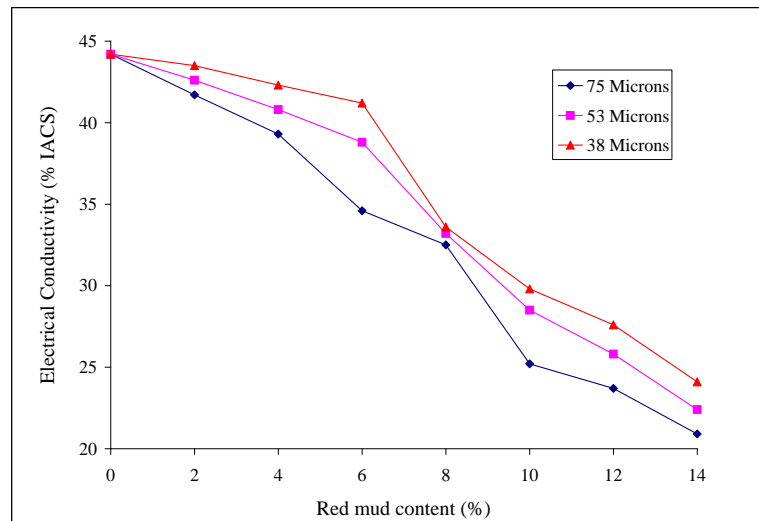


Figure 12. Effect of red mud content on electrical conductivity

Conclusions

From this investigation, the following conclusions are obtained:

The copper-red mud composites with uniform dispersion of red mud can be obtained by powder metallurgy processing route. Incorporation of red mud particles modified the physical, mechanical and electrical conductivity properties of the pure copper compacts. Ejection pressure, green density and strength decreased with increase in red mud content. Spring back, green porosity and hardness increased with increase in red mud content. Ejection pressure, green density, green hardness and strength increased with decrease in particle size of red mud. Spring back and green porosity decreased with decrease in particle size of red mud.

Sintering of copper-red mud compacts resulted in an increase in density of the green compacts and sintered

density decreased with increasing red mud content. Sintered porosity and hardness increased with increasing red mud weight percent. Compressive yield strength of sintered copper-red mud composites decreased with increasing red mud weight percent. The electrical conductivity of the sintered copper compacts decreased with addition of red mud.

Sintered density, sintered hardness, sintered compressive yield strength and electrical conductivity gradually increased with decrease in particle size of red mud. Sintered porosity decreased with decrease in particle size of red mud. These results suggest that the useful range of red mud that can be added to copper lies below 10% and finer particles of red mud result in improved physical, mechanical and electrical conductivity properties of the copper-red mud composites.

References

- [1] Sneha Samal, A.K. Ray, Amitava Bandopadhyay, "Proposal for resources, utilization and processes of red mud in India-A review", *International Journal of Mineral Processing*, Vol. 118, 2013, 43-55.
- [2] R.S. Thakur, S.N. Das, "International series on environment in red mud – analysis and utilization", edited by S. Sivakamasundari (PID and Wiley Eastern Ltd., New Delhi, India) 1994.
- [3] S.N. Meher., "Thermal Analysis of Nalco Red Mud, *International Journal of Chemical Studies*", Vol.1, No.5, 2014, 1-9.
- [4] A.I. Zouboulis., & K.A. Kydros, "Use of red mud for toxic metals removal: The case of Nickel", *Journal of Chemical Technology and Biotechnology*, Vol. 58, Issue 1, 1993, 95–101.
- [5] H.S. Altundogan, S. Altundogan, F. Tumen, M. Bildik, "Arsenic adsorption from aqueous solutions by activated red mud", *Waste Management*, Vol. 22, 2002, 357-363
- [6] V.K.Gupta, M.Gupta, S. Sharma, "Process development for the removal of lead and chromium from aqueous solutions using red mud-an aluminium industry waste", *Water Research*, Vol.35, Issue 5, 2001, 1125-1134.
- [7] S.S. Amritphale, M. Patel, "Utilisation of red mud, fly ash for manufacturing bricks with pyrophyllite", *Silicates Industriels*, Vol. 2, No. 3, 1987, 31-35.
- [8] M.S. Vincenzo, C. Renz, M. Stefano, C. Giovanni, "Bauxite red mud in the ceramic industry. Part 2: production of clay based ceramics", *Journal of European Ceramic Society*, 2000; 20(3):245-252.
- [9] Naresh Prasad., Harekrishna Sutar., Subash Chandra Mishra., Santosh Kumar Sahu., & Samir Kumar Acharya, "Dry sliding wear behaviour of Aluminium Matrix composite using red mud an industrial waste", *Industrial Research Journal of Pure & Applied Chemistry*, Vol.3, Issue1, 2013, 59-74.
- [10] Hemalata Jena, A.K. Satapathy, "Fabrication, Mechanical Characterization and Wear Response of Hybrid Composites Filled with Red Mud: an Alumina Plant Waste", *AMAE International Journal on Manufacturing and Material Science*, Vol. 2, No.1, 2012, 27-31.
- [11] Y. Zhang, A. Zhang, Z. Zhen, F. Lv, P.K. Chu, J. Ji, "Red mud/polypropylene composite with mechanical and thermal properties", Vol. 45, No.6, 2011, 2811-2816.
- [12] A.H. Bhat, A.K. Banthia, "Preparation and characterization of poly(vinyl alcohol)-modified red mud composite materials", Vol.103, Issue 1, 238-243.
- [13] B. Singh, M. Gupta, "Surface treatment of red mud and its influence on the properties of particulate-filled polyester composites", *Bulletin of Material Science*, Vol.18, Issue 5, 1995, 603-621.
- [14] P. Yih, D.D.L. Chung, "Copper-Matrix Molybdenum Particle Composites made from Copper Coated Molybdenum Powder", *Journal of Electronica Materials*, Vol.24, 1994, 841-842.
- [15] Y. -F. Lee, S.-L. Lee, C. -L. Chuang, J.C. Lin, "Effects of SiCp Reinforcement by Electroless Copper Plating on Properties of Cu/SiCp Composites", *Powder Metallurgy*, Vol.42, 1999, 147-152.
- [16] S.F. Moustafa, Z. Abdel-Hamid, A.M. Abd-Elhay, "Copper Matrix SiC and Al₂O₃ Particulate Composites by Powder Metallurgy Technique", *Materials Letters*, Vol. 53, 2002, 244-249.
- [17] Y. Zhan, G. Zhang, "The Effect of Interfacial Modifying on the Mechanical and Wear Properties of SiCp/Cu Composites", *Materials Letters*, Vol. 57, 2003, 4583-4591.
- [18] Tong Chingping, Yasuyuki Igo, Yasuo Kondo, "Development of Low Expansion Copper Based Composite Materials (L-COP)". *Hitachi Cable Review*, Vol. 22, 2003, 62-65.
- [19] N.Vijaya Sai, M.Komaraiah, A.V.Sita Rama Raju, "Brass-matrix fly ash particulate composites by powder metallurgy", *International Journal of Material Science*, Vol.3 (2008), No.2, 113-123.

Multi-Objective Optimization of Process Parameters for Electrochemical Machining of 6061Al/ 10% Wt Al₂O₃/ 5% Wt SiC Composite using Hybrid Fuzzy-Artificial Bee Colony Algorithm

Ayyappan Solaiyappan^{a*}, Kalaimathi Mani^b, Venkatachalam Gopalan^b

^a Department of Mechanical Engineering, Government College of Engineering, Salem-636011, Tamilnadu, India.

^b School of mechanical and building sciences, VIT University, Vellore-632014, Tamilnadu, India.

Received 22 April 2014

Accepted 7 Sep 2014

Abstract

A new hybrid fuzzy-Artificial Bee Colony algorithm (Fuzzy-ABC) for the optimization of electrochemical machining (ECM) process parameters is presented in this paper. The 6061Al/10%wt Al₂O₃/5%wt SiC composite is taken as a test specimen and its machining characteristics on ECM process are studied. Maximizing the material removal rate (MRR), minimizing the surface roughness (R_a) and minimizing the over-cut (OC) are the main indicators of quality of an ECM process and thus are considered as objectives. The main process parameters governing the ECM process are current, applied voltage, flow rate, tool feed rate, inter-electrode gap and electrolyte concentration. The central composite design of response surface methodology was employed in order to identify the effective machining parameters on the above objectives. Fuzzy Logic (FL) concepts provide a fairly accurate prediction, when sufficient information is not available. The artificial bee colony (ABC) algorithm is a new evolutionary computational technique provides better results to that of other algorithms. Hence, in this paper, fuzzy logic was integrated with artificial bee colony algorithm, thus making a new hybrid Fuzzy-ABC algorithm. The optimized values for ECM were obtained through the hybrid Fuzzy-ABC algorithm. Confirmatory experiments reveal that the experimental values are fairly close with optimized values.

© 2014 Jordan Journal of Mechanical and Industrial Engineering. All rights reserved

Keywords: : Electrochemical Machining (ECM), Artificial Bee Colony Algorithm (ABC), Fuzzy Inference System (FIS), Hybrid Fuzzy-ABC Algorithm, Metal Matrix Composite (MMC).

1. Introduction

Electrochemical machining (ECM) is a controlled anodic dissolution process at atomic level of the work piece that is electrically conductive by a shaped tool through an electrolyte. In ECM, work piece is the anode and the tool is the cathode and the electrolyte is pumped through the gap between tool and work piece, while direct current is passed through the cell, to dissolve metal from the work piece. ECM is widely used in aerospace, auto, mould and dies, roller and gear industries. Electrochemical machining of metal matrix composites (MMCs) has not been explored to a great extent. Senthilkumar *et al.* [1] analyzed the electrochemical machining characteristics of Al/SiC_p composites using response surface methodology. Machining suitability of Al/B₄C composites were also studied with ECM [2, 3]. Product parameter such as percentage of reinforcement of SiC particles in aluminum matrix along with some ECM process parameters were

optimized [4]. Since the investment cost on this machine is really high, it becomes very much important to find out the optimal process parameters to achieve enhanced machining performance. Noorul Haq *et al.* [5] studied the machinability issues in drilling of Al/SiC particle reinforced composites. Grey relational analysis in the Taguchi method is used to optimize the process parameters. Patil Nilesh *et al.* [6] conducted the experiment on electro discharge machining to study the machinability of alumina particle reinforced aluminium composites. Muthukrishnan *et al.* [7] discussed in detail the machinability issues of silicon carbide reinforced aluminium composites particularly in turning operation. Taweel [8] analyzed the machining characteristics of Al/Al₂O₃ composite using electrochemical turning with magnetic abrasive finishing. The abrasive nature of ceramic particles reinforced in the metallic matrix will erode the tool there by reducing the life of the tool. Since ECM is the electrochemical dissolution process, tool is not affected by wear. Thus ECM becomes a standard process

* Corresponding author. e-mail: ayyappansola@gmail.com.

for machining the hard materials, super alloys, ceramics, MMCs etc. It is evident that ECM process for metal matrix composites has not been explored to a great extent. In this globally competitive world, the process modeling and multi-objective optimization are very important for utilizing the full potential of the manufacturing processes in order to meet the demands on surface quality, tolerances, production rate and costs. Hybrid ECM process such as electrochemical honing (ECH) performance was studied and optimized by Dubey [9]. Ayyappan *et al.* [10, 11] investigated the electrochemical machining characteristics of 20MnCr5 alloy steel and optimized the process parameters using genetic algorithm (GA)-desirability function (DF). Kalaimathi *et al.* [12, 13] investigated the electrochemical machining characteristics of Monel 400 alloys and optimized the process parameters using response surface methodology. Artificial Bee Colony (ABC) algorithm is a new optimization algorithm outperforms other optimization tools for finding out the global best solution [14-16]. Fuzzy logic has rapidly become one of the most successful tools of today's technologies for developing sophisticated control systems [17-21]. Fuzzy logic addresses such applications perfectly as it resembles human decision making with an ability to generate precise solutions from certain or approximate information. Thus, in this work, a new novel hybrid Fuzzy-ABC algorithm is proposed by integrating fuzzy logic with ABC algorithm for optimizing ECM process parameters for 6061Al/10%wt Al₂O₃/5%wt SiC composite.

2. Experimentation

Figure 1 shows an experimental set-up of the ECM system used in this work. It comprises of a power supply, electrolyte supply and filtering system, tool and tool feed mechanism, work holding and position system, control panel and frame and housing. A 5-30V DC potential with current adjustable up to 300A is applied across the inter-electrode gap (IEG) between a copper tool and an anode work piece. Tool is fed against the work piece which is firmly fixed on to the vice. Copper tool with hexagonal end is used. Aqueous sodium chloride (NaCl₂) solution was used as electrolyte. Current(C), voltage (V) and feed rate (F) settings were controlled in control panel. Digital

flow meter and pressure gauge is fixed across the electrolyte flow pipe to control electrolyte flow rate (U) and pressure. The work piece material is a 6061 aluminium alloy reinforced with aluminium oxide (Al₂O₃) ceramic particles with 10 percent weight fractions and silicon carbide (SiC) particles with 5 percent weight fractions. The samples were fabricated through liquid metallurgy technique stir casting. Properties of the work piece material are density 2844.5 kg/m³, electrical conductivity 0.224287 x 10⁶ mho/cm and average porosity 0. The experiment is based on central composite design (CCD) of response surface methodology (RSM). Fifty-four tests were carried out with different parameter combinations. Machining time of each test considered was 300 seconds. The parameter ranges considered in this work are as shown below in table 1.

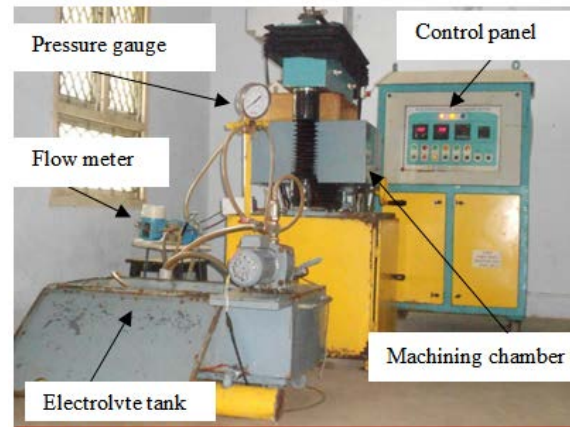


Figure 1. Electrochemical machining set-up

The experimental values are displayed in Table 2. In this work, MRR is measured based on weight loss during machining time with weighing machine:

$$MRR = \frac{LW}{MT} \quad (1)$$

Where, LW- Loss of weight (grams)

MT-Manufacturing time (minutes).

Weights are measured from weighing machine with least count of 1 mg and maximum weight up to 1 kg.

Table 1. Process Parameters and their values at different levels

Symbol	Process parameter	Level				
		-2	-1	0	+1	+2
U	Electrolyte flow rate (L/min)	7	9	11	13	15
F	Feed rate (mm/min)	0.2	0.4	0.6	0.8	1
V	Voltage (volts)	10	14	18	22	26
C	Current(Amps)	205	220	235	250	265
IEG	Inter-electrode gap(mm)	0.1	0.2	0.3	0.4	0.5
EC	Electrolyte concentration(g/L)	100	130	160	190	220

Table 2. Experimental values

Trial Order	C Amps	V volts	U L/min	IEG mm	F mm/min	EC g/L	MRR g/min	R _a µm	OC mm
1	-1	1	1	1	1	-1	0.733	3.16	0.267
2	0	0	0	0	0	0	0.203	7.81	0.233
3	0	0	0	0	0	0	0.490	4.82	0.200
4	1	-1	-1	-1	1	-1	0.436	3.90	0.356
5	0	0	0	0	0	0	0.607	1.58	0.133
6	1	-1	1	-1	-1	-1	0.391	2.74	0.323
7	-1	1	1	-1	-1	-1	0.354	1.94	0.253
8	1	1	-1	1	-1	1	0.409	3.38	0.218
9	1	1	-1	-1	1	1	0.899	4.88	0.353
10	-1	-1	1	1	1	1	0.362	3.39	0.083
11	-1	-1	-1	-1	1	1	0.432	6.89	0.683
12	0	0	0	0	0	0	0.580	5.73	0.168
13	1	-1	-1	1	-1	-1	0.244	6.34	0.328
14	1	1	1	-1	-1	1	0.341	4.22	0.613
15	-1	-1	-1	1	-1	1	0.152	2.12	0.228
16	-1	1	-1	-1	1	-1	0.741	2.54	0.418
17	-1	-1	1	-1	-1	1	0.356	1.94	0.333
18	1	-1	1	1	1	-1	0.382	3.55	0.468
19	-1	1	-1	1	-1	-1	0.323	3.90	0.478
20	1	1	1	1	1	1	0.691	2.48	0.011
21	1	-1	-1	-1	-1	1	0.360	6.09	0.523
22	-1	-1	1	1	-1	-1	0.264	3.47	0.163
23	1	-1	1	-1	1	1	0.521	2.22	0.208
24	1	-1	-1	1	1	1	0.217	3.22	0.013
25	1	1	-1	-1	-1	-1	0.336	4.56	0.733
26	0	0	0	0	0	0	0.457	4.40	0.277
27	1	1	-1	1	1	-1	0.572	4.07	0.015
28	-1	-1	1	-1	1	-1	0.373	8.75	0.773
29	-1	1	-1	1	1	1	0.663	3.24	0.185
30	1	1	1	-1	1	-1	0.671	4.27	0.265
31	-1	-1	-1	-1	-1	-1	0.270	5.68	0.313
32	-1	1	1	1	-1	1	0.299	1.67	0.483
33	0	0	0	0	0	0	0.623	1.92	0.378
34	1	1	1	1	-1	-1	0.328	2.85	0.078
35	-1	1	1	-1	1	1	0.755	2.31	0.383
36	-1	1	-1	-1	-1	1	0.421	1.53	0.448
37	1	-1	1	1	-1	1	0.365	3.45	0.108
38	-1	-1	-1	1	1	-1	0.194	1.84	0.223
39	0	0	0	0	0	0	0.613	2.90	0.403
40	0	0	0	0	0	0	0.656	1.86	0.088
41	0	0	0	0	2	0	0.431	3.81	0.578
42	0	0	0	0	0	-2	0.442	1.48	0.248
43	-2	0	0	0	0	0	0.456	5.66	0.268
44	0	2	0	0	0	0	0.641	6.56	0.358
45	0	0	2	0	0	0	0.492	4.18	0.323
46	0	0	0	-2	0	0	0.759	4.44	0.463
47	0	0	0	0	0	2	0.488	3.28	0.093
48	2	0	0	0	0	0	0.516	3.66	0.488
49	0	0	-2	0	0	0	0.686	4.09	0.093
50	0	0	0	0	0	0	0.647	3.57	0.718
51	0	0	0	0	-2	0	0.515	2.63	0.408
52	0	0	0	2	0	0	0.451	5.61	0.658
53	0	-2	0	0	0	0	0.654	2.94	0.488
54	0	0	0	0	0	0	0.426	1.14	0.618

The overcut (OC) was calculated using the equation (2):

$$OC = \frac{D_2 - D_1}{2} \quad (2)$$

Where, D_1 -Diagonal distance between the two opposite corners of the tool(mm)

D_2 -Diagonal distance between the two opposite corners of the machined profile (mm)

The diagonal distances (D_2) of machined surface as shown in Figure 2 were measured with the help of profile projector. The machined surface roughness was measured using a mitutoyo surface roughness tester with sampling length of 10mm. The results are the average of three measurements in different positions.

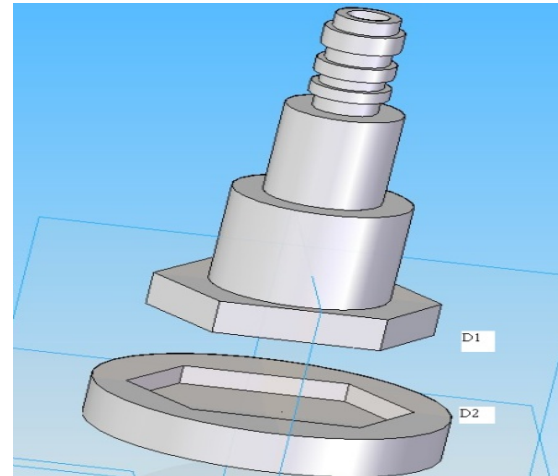


Figure 2. 3D modeling of tool and work piece interaction

2.1. Main Effects due to Parameters

The main effects are assessed by level average response analysis of the raw data. This analysis was done by averaging the raw data at each level of each parameter and plotting the values in graphical form. The level average responses from the raw data help in the analysis of the trend of the performance characteristic with respect to the variation in the factor under study. Figures 3 to 5 show the main effects due to all the six parameters.

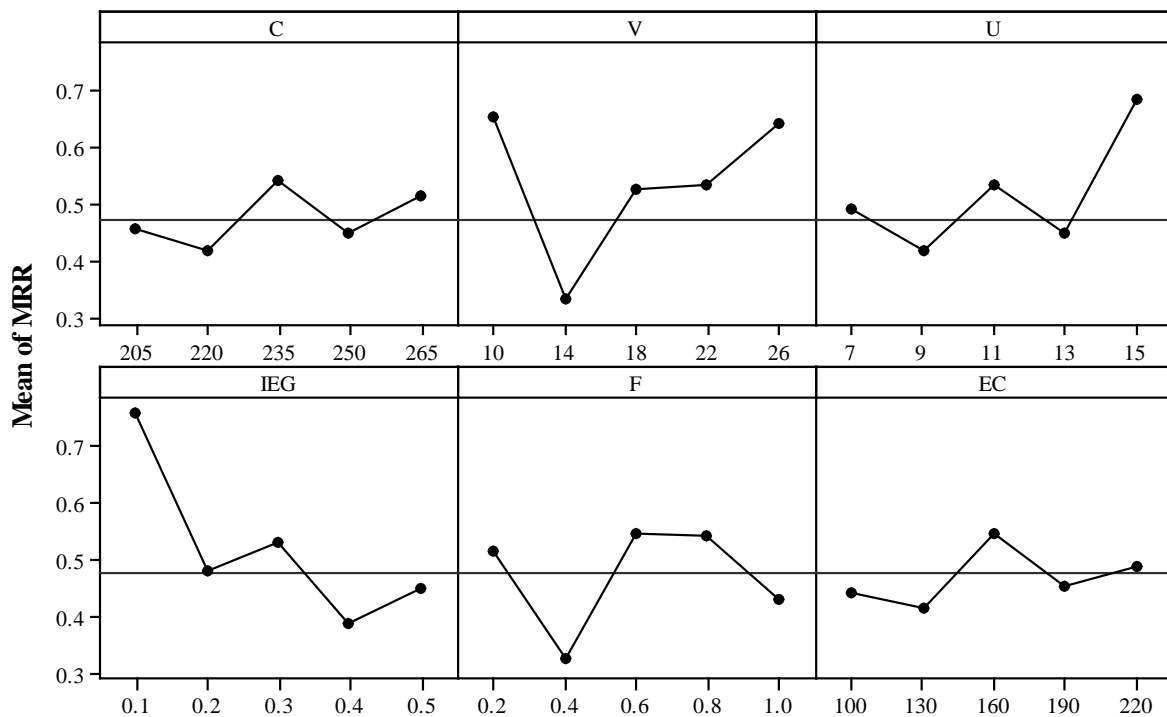


Figure 3. Data mean of MRR (g/min) against parameters

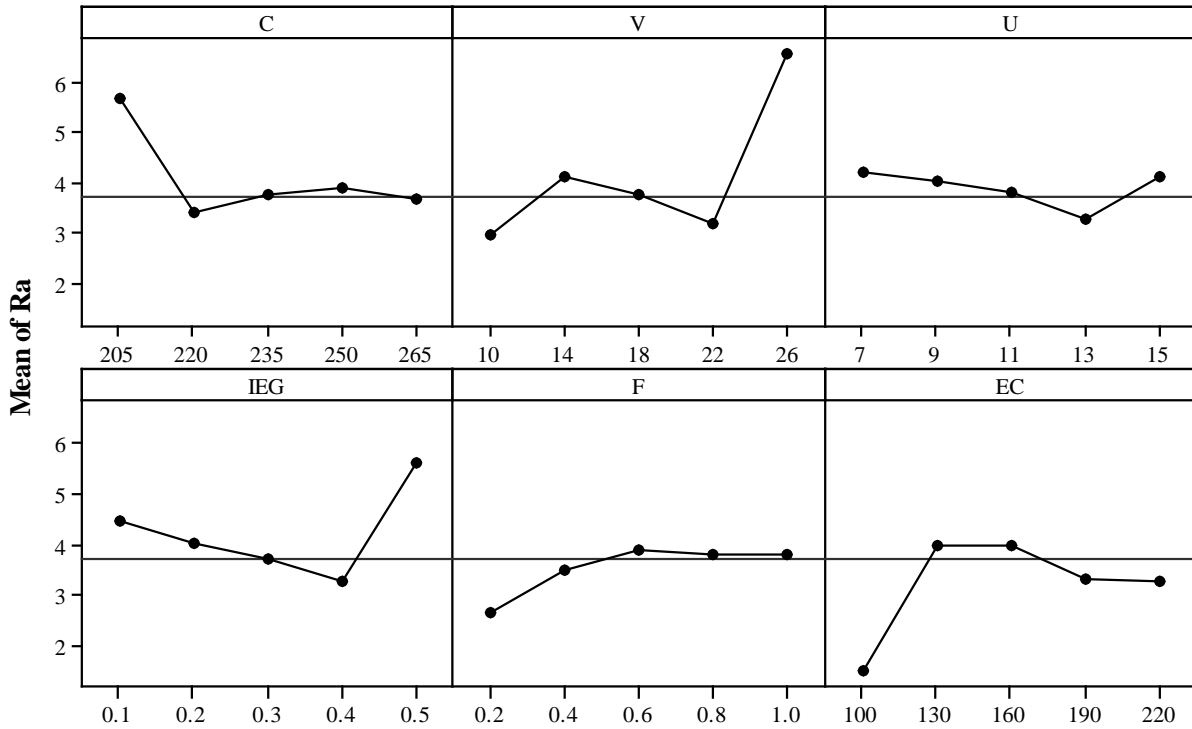


Figure 4. Data mean of Surface roughness (R_a) μm against parameters

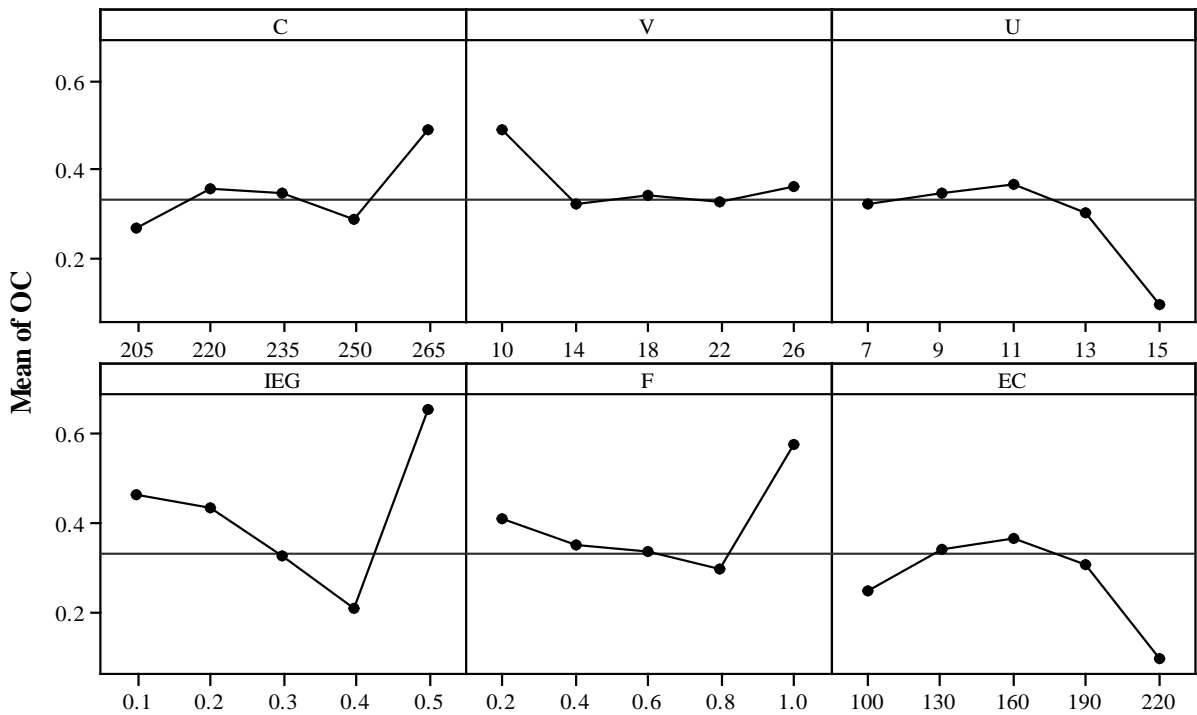
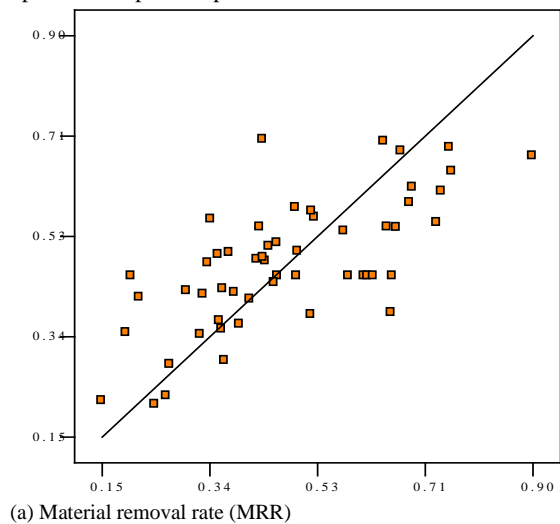


Figure 5. Data mean of Overcut (OC) mm against parameters

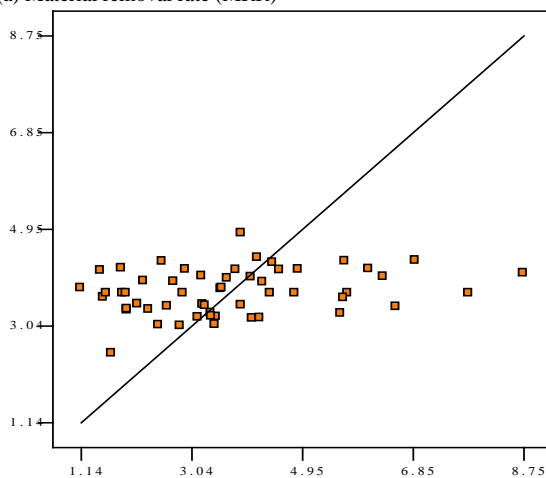
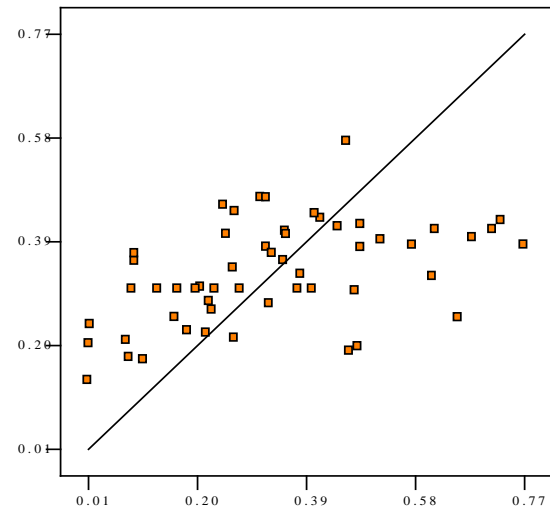
As shown in the Figures above, at low current 205 amps, surface roughness (R_a) is high as 5.66 μm , while MRR is low. But over-cut shows good performance. As current increases, MRR and over-cut also increases while surface roughness decreases. This is due to the high current density in the inter-electrode gap which increases the MRR. At a current of 235 amps, all the performance measures show good result. At a lower flow rate of 13 L/min, all the output parameters shows very good result.

At higher voltage of 26 volts, MRR reaches the maximum value. But surface roughness is very high which is not desirable. Over-cut is also very good at this voltage. At the low voltage of 10 volts, the MRR and surface roughness shows good performance. But over-cut shows poor performance. Optimal voltage for these conflicting objectives is 22 volts. As IEG value decreases, MRR increases whereas surface roughness decreases and then increases. Over-cut shows good value at lower IEG. The

best value of IEG for all objectives is just about 0.1 mm. When feed rate increases, MRR increases while surface roughness decreases and over-cut increases. The best feed rate value for all output parameters is 0.8 mm/min approximately. NaCl concentration in water affects the ECM performances largely. NaCl concentration of 100 grams per liter of water produces a good surface roughness and over-cut. But MRR is low at this value. This is because of molar conductance which is not sufficient for complete ionization process, which in turn produces poor material removal. Since material removal is low, surface roughness and overcut values are very well. Attempt was made to fit the regression equation for the above data. However, the co-efficient of determination (R^2) values of the regression equations of MRR, surface roughness and over-cut were very low. Linear fit of above data is reasonably good but with very low R^2 values. Graphs between predicted and actual values of linear equation of all responses are shown in Figure 6. Therefore, the regression equation doesn't represent the exact relationship between input and output parameters. This situation leads to fitting the experimental characteristics with fuzzy logic concepts. In this work, a new novel hybrid Fuzzy-ABC algorithm is proposed to optimize the process parameters.



(a) Material removal rate (MRR)

(b) Surface roughness (R_a)

(c) Over-cu

Figure 6. Prediction versus actual values of objectives

X label: Actual value
Y label: Predicted value

3. Objective Function Modeling using Fuzzy Inference System (FIS)

Fuzzy Inference System (FIS) used to model the responses (MRR, R_a and OC). The variables of this manufacturing process are electrolyte flow rate (U), feed rate (F), voltage (V), current (C), inter-electrode gap (IEG), electrolyte concentration (EC), which can have any continuous value subject to the limits available. The FIS system develops the relationship between the machining parameters and the objectives. Mamdani's fuzzy inference method is used in this work. FIS structure maps parameters through input (parameter) membership functions and then through output (objective) membership functions to outputs (objectives). It excellently approximates the non-linear functions. FIS modeling process starts by:

- Dividing the input and output parameters by equally spacing five membership functions.
- Strength (0, 1) is calculated for each membership functions.
- Fuzzy rules are defined for the output with the given input.

4. Artificial Bee Colony (ABC) Algorithm

Karaboga [15, 16] described the Artificial Bee Colony (ABC) algorithm based on the foraging behavior of honey bees for numerical optimization. In nature, the bees crawl along a straight line, and turns left, moving and swinging their belly. Such a dance is called waggle dance, and the angle between the gravity direction and the center axis of the dance is equal to the angle between the sun and the food source. Waggle dance of the bees can also deliver more detailed information about the food sources such as distance and direction. Then each bee in the hive selects food source for nectar or researches new food sources around the bee hive, according to the information delivered by other bee's waggle dance. Through this kind of information exchanging and learning, whole colony would always find relatively prominent nectar source. This

process leads to the emergence of collective intelligence of honey bee swarms. This was implemented to some nontraditional machining methods for the parameter optimization and was proved very effective [14].

5. Process Optimization using Hybrid Fuzzy-ABC Algorithm

Implementation of the proposed Hybrid Fuzzy-ABC algorithm in ECM process comprises the following steps:

1. Use the response surface methodology (RSM) to design and conduct the experiments.
2. Use the FIS mamdani architecture to model the input and output parameters and simulate.
3. Initialize the population of solutions (food sources) $x_i = C, V, U, IEG, F, EC, i=1, 2, \dots, N_e$
With the variable bounds
 $205 \leq C \leq 265$ (amps)
 $10 \leq V \leq 26$ (volts)
 $7 \leq U \leq 15$ (L/min)
 $0.1 \leq IEG \leq 0.5$ (mm)
 $0.2 \leq F \leq 1$ (mm/min)
 $100 \leq EC \leq 220$ (g/L)
Total number of bees (N_s)=100
Colony size of the employed bees (N_e)=50
Size of the unemployed bees (N_u)=50
 $N_s = N_e + N_u$
 $N_e = N_u$
4. Calculate the fitness value (nectar amount) $f(x_i) = (MRR \text{ or } R_a \text{ or } OC)$ of each solution vector using Fuzzy Inference System(FIS) model.
5. Iteration $T=1$
6. Produce new solutions (food source positions) $v_i = C, V, U, IEG, F, EC$ in the neighborhood of x_i for the employed bees using the formula $v_i = x_i + \Phi(x_i - x_k)$ evaluate its profitability (fitness) using FIS model.
 x_k - is a randomly selected food source,
 $k \in \{1, 2, \dots, N_e\}, k \neq i$
 Φ is a random number $[0, 1]$
7. Apply the greedy selection process to choose the better position between v_i and x_i as follows
If $f(v_i) \geq f(x_i)$
New position is v_i
Else
New position is x_i
8. Calculate the probability values P_i for the solutions x_i by means of their fitness values using the equation

$$P_i = \frac{fit_i}{\sum_{n=1}^{N_e} fit_n} \quad (3)$$
 Normalize P_i values into $[0, 1]$
9. Produce the new solutions (new positions) v_i for the onlookers from the solutions x_i , selected depending on P_i , and evaluate (MRR or R_a or OC or Combined normalized objective) using FIS model.
10. Apply the greedy selection process for the onlookers between x_i and v_i .
11. Determine the abandoned solution (source), if exists, and replace it with a new randomly produced solution x_i for the scout using the following equation.

$$x_{(i,j)} = [\min]_j + \text{rand}(0,1) * ([\max]_j - [\min]_j) \quad (4)$$

$$j = U, F, V, C, IEG, EC$$

12. Memorize the best food source position (solution) achieved so far
13. Iteration $T = \text{Iteration } T + 1$
14. Until Iteration = T_{\max} (Maximum number of iterations).

Figure 7 shows the scheme of proposed Hybrid Fuzzy-ABC algorithm in this work.

5.1. Hybrid Fuzzy-ABC Algorithm for Multiple Objectives

Optimization problems that have more than one objective function, the objectives to be optimized are normally in conflict with respect to each other, which means that there is no single solution for these problems. Thus it is required to find best possible compromises among the objectives. In this work, multiple objectives are normalized and its sum of normalized values faces a minimization objective. In each iteration, positions are updated with the normalized objective. The combined normalized objective (Z) is formulated by considering equal weightages to all the objectives and is given by the following equation according to Rao et al. [22] work and the same was also used by Suman et al. [14].

$$\text{Min } Z = w_1 * R_{a, \min} / R_{a, \min} + w_2 * OC / [OC]_{\min} - w_3 * MRR / [MRR]_{\max} \quad (5)$$

$R_{a, \min}$ -Minimum value of surface roughness obtained when the single-objective optimization problem considering only surface roughness as an objective.

OC_{\min} - Minimum value of over-cut obtained when the single-objective optimization problem considering only over-cut as an objective.

MRR_{\max} - Maximum value of MRR obtained when the single-objective optimization problem considering only MRR as an objective.

$$\text{Weights } W_1, W_2, W_3 = 0.33; W_1 + W_2 + W_3 = 1.$$

Results of single objective optimization with hybrid Fuzzy-ABC algorithm are as follows:

$$\begin{aligned} MRR_{\max} &= 0.8314 \text{ g/min} \\ \text{Surface Roughness } (R_a) &= 1.4 \mu\text{m} \\ \text{Over-cut} &= 0.1 \text{ mm} \end{aligned}$$

Combined normalized objective function is obtained by substituting weights and objective function values in equation (5):

$$\text{Min } Z = 0.33 * R_a / 1.4 + 0.33 * OC / 0.1 - 0.33 * MRR / 0.8314 \quad (6)$$

This function is treated as a fitness function for Hybrid Fuzzy-ABC algorithm.

The optimization results are as follows:

Process parameters:

Feed rate	= 0.89 mm/min
Flow rate	= 9.64 L/min
Voltage	= 24.88 volts
Current	= 259 Amps
Inter-electrode gap	= 0.1760 mm
Electrolyte concentration	= 204 g/L

Output parameters:

MRR_{\max}	= 0.813 g/min
Surface Roughness (R_a)	= 1.23 μm
Over-cut	= 0.142 mm

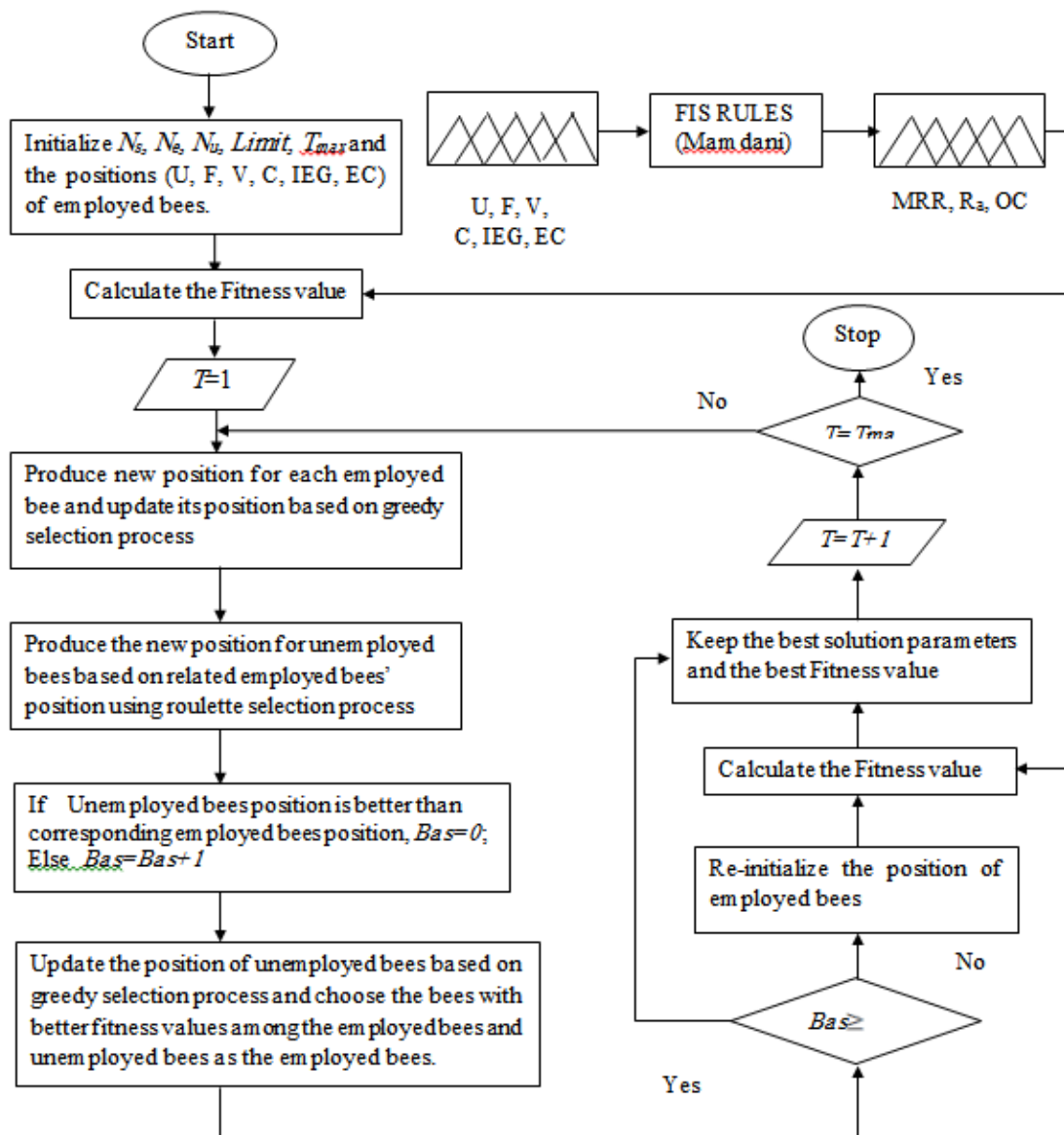


Figure 7. Scheme of Proposed Hybrid Fuzzy-ABC algorithm

6. Confirmatory Experiment

A confirmation test is used to validate the conclusions drawn with new proposed Hybrid Fuzzy-ABC algorithm. Optimized parameters of multi-objective optimization were set in the electrochemical machining and machining was conducted. Performance parameters were measured and its variance with optimized values is as follows:

	Predicted performance values	Experimental performance values	% of error values
MRR(g/min)	0.813	0.841	3.544
R _a (µm)	1.23	1.28	4.065
Over-cut(mm)	0.142	0.148	4.225

Percentage of error between predicted and experimental performance values are very acceptable around 4%. Hence the proposed algorithm is very efficient to implement with electrochemical machining process.

7. Conclusion

A novel new Hybrid Fuzzy-Artificial Bee Colony (ABC) algorithm has been developed for multi-objective optimization of process parameters in electrochemical machining (ECM). The predicted values for the best performance is feed rate 0.89 mm/min, flow rate 9.64 L/min, voltage 24.88 volts, current 259 Amps, inter-electrode gap 0.176 mm, electrolyte concentration 204 g/L. Confirmation test results proved that the determined optimum combination of machining parameters satisfy the real requirements of electrochemical machining of 6061Al/10% wt Al₂O₃/5% wt SiC composite. The optimal results depend upon the modeling accuracy of Fuzzy

Inference System (FIS) as well as the consistency of artificial bee colony (ABC) algorithm convergence. Hybrid Fuzzy-Artificial Bee Colony (ABC) algorithm is quite advantageous than other optimization techniques in terms of computational efficiency and simplicity to work. Algorithm parameters are easy to understand and implement. Integration of the proposed algorithm with an intelligent manufacturing system will lead to reduction in production cost, reduction in production time and greater gain in flexibility of machining parameter selection.

Acknowledgement

The authors would like to appreciatively acknowledge the TEQIP scheme of World Bank for funding electrochemical machining at Govt. College of Engineering, Salem-636011, Tamilnadu, India.

References

- [1] C.Senthilkumar, G.Ganesan, R.Karthikeyan, "Study of electrochemical machining characteristics of Al/SiC_p Composites". *International Journal of Advanced Manufacturing Technology*, Vol.43 (2009), 256-263.
- [2] S.Rama Rao, G.Padmanabhan, "Effect of process variables on metal removal rate in electrochemical machining of Al-B4C composites". *Archives of Applied Science Research*, Vol.4 (2012) No.4, 1844-1849.
- [3] S.Rama Rao, G. Padmanabhan, "Linear Modeling of the Electrochemical Machining Process Using Full Factorial Design of Experiments". *Journal of Advanced Mechanical Engineering*, Vol.1 (2013), 13-23.
- [4] K.L.SenthilKumar,R.Sivasubramanian, K.Kalaiselvan, "Selection of Optimum Parameters in Non Conventional Machining of Metal Matrix Composite". *Portugaliae Electrochimica Acta*, Vol.27 (2009) No.4,477-486
- [5] A.Noorul Haq, P.Marimuthu, R.Jeyapaul, "Multi response optimization of machining parameters of drilling Al/SiC metal matrix composite using grey relational analysis in the Taguchi method". *International Journal of Advanced Manufacturing Technology*, Vol.37 (2008), 250-255.
- [6] G.Patil Nilesh, P. K.Brahmankar, "Some studies into wire electro-discharge machining of alumina particulate-reinforced aluminum matrix composites". *International Journal of Advanced Manufacturing Technology*, Vol.48 (2010), Issue 5-8, 537-555.
- [7] N.Muthukrishnan, M.Murugan, K.Prahlada Rao, "Machinability issues in turning of Al-SiC (10p) metal matrix composites". *International Journal of Advanced Manufacturing Technology*, Vol.39 (2008), 211-218.
- [8] T. A. El-Taweel, "Modeling and analysis of hybrid electrochemical turning magnetic abrasive finishing of 6061 Al/Al₂O₃ composite". *International Journal of Advanced Manufacturing Technology* Vol.37 (2008), 705-714.
- [9] A.K.Dubey, "A hybrid approach for multi-performance optimization of the electro-chemical honing process". *International Journal of Advanced Manufacturing Technology*, (2008), DOI 10.1007/s00170-008-1422-8.
- [10] S.Ayyappan, K.Sivakumar, "Investigation of electrochemical machining characteristics of 20MnCr5 alloy steel using potassium dichromate mixed aqueous NaCl electrolyte and optimization of process parameters". *Proceedings of Institution of Mechanical Engineers Part B: J Engineering Manufacture*,(2014),1-13.
- [11] S.Ayyappan, K.Sivakumar, "Experimental investigation on the performance improvement of electrochemical machining process using oxygen-enriched electrolyte". *International Journal of Advanced Manufacturing Technology*, Vol.75 (2014), Issue 1-4, 479-487.
- [12] M.Kalaimathi, G.Venkatachalam, Neil Makhijani, Ankit Agrawal, "Investigations on Machining of Monel 400 alloys using Electrochemical Machining with Sodium Nitrate as Electrolyte". *Applied Machanics and Materials*, Vols.592-594(2014), 467-472, Trans Tech Publications, Switzerland.
- [13] M.Kalaimathi, G.Venkatachalam, M.Sivakumar, "Experimental Investigations on the Electrochemical Machining Characteristics of Monel 400 Alloys and Optimization of Process Parameters". *Jordan Journal of Mechanical and Industrial Engineering*, Vol.8 (2014), No.3, 143-151.
- [14] Suman Samanta, Shankar Chakraborty, "Parametric optimization of some non-traditional machining processes using artificial bee colony algorithm". *Engineering Applications of Artificial Intelligence*, Vol.24 (2011), 946-957.
- [15] B.Basturk, D.Karaboga, "An artificial bee colony (ABC) algorithm for numeric function optimization". *Proceedings of the IEEE Swarm Intelligence Symposium*, Indianapolis, IN, USA, 2006.
- [16] D.Karaboga, B.Basturk, "Artificial Bee Colony (ABC) Optimization Algorithm for Solving Constrained Optimization Problems". *Foundations of Fuzzy Logic and Soft Computing*, Lecture Notes in Computer Science, Vol.4529 (2007), 789-798.
- [17] Chin-Teng Lin, I-Fang Chung, Shih-Yu Huang, "Improvement of machining accuracy by fuzzy logic at corner parts for wire – EDM". *Fuzzy sets and systems*, Vol.122 (2001), No.3, 499-511.
- [18] M.A.El.Baradie, "A Fuzzy logic model for machining data selection". *International Journal of Machine Tools & Manufacture*, Vol.37 (1995), No.9, 1353-1372.
- [19] Oguzhan Yilmaz, Omer Eyercioglu, Nabil N.Z. Gindy, "A user-friendly fuzzy based system for the selection of electro discharge machining process parameters". *Journal of Materials Processing Technology*, Vol.172 (2006), 363-371.
- [20] Mohanad Alata, Wael Masarweh, Said Kamal, "A Fuzzy Monitoring System for an Extrusion Line". *Jordan Journal of Mechanical and Industrial Engineering*, Vol.1 (2007), No.1, 17-21.
- [21] Kasim M.Daws, Zouhair I, AL-Dawood, Sadiq H.AL-Kabi, "Selection of Metal Casting Processes: A Fuzzy Approach". *Jordan Journal of Mechanical and Industrial Engineering*, Vol.2 (2008), No.1, 45-52.
- [22] R.V.Rao, P.J.Pawar, Ravi Shankar, "Multi-objective optimization of electrochemical machining process parameters using a particle Swarm optimization algorithm". *Proceedings of Institution of Mechanical Engineers Part B: J Engineering Manufacture*, Vol. 222(2008), 949-958.

PSO-Based Neural Network Prediction and its Utilization in GMAW Process

Pathiyasseril Sreeraj ^{a*}, Thangavel Kannan ^b, Subhasis Maji ^c

^a Department of Mechanical Engineering, Valia Koonambakulathamma College of Engineering Technology, Kerala, 692574 India

^b Principal, SVS College of Engineering, Coimbatore, Tamilnadu, 642109 India.

^c Professor, Department of Mechanical Engineering IGNOU, Delhi, 110068, India

Received 31 Jan 2013

Accepted 25 Sep 2014

Abstract

This paper presents a Particle Swarm Optimization (PSO) technique in training an Artificial Neural Network (ANN) which is used for predicting Gas Metal Arc Welding (GMAW) process parameters for a given input set of welding parameters. Experiments were conducted according to central composite rotatable design with full replication technique and results are used to develop a multiple regression model. Multiple set of data from multiple regression are utilised to train the intelligent network. The trained network is used to predict the weld bead geometry. The welding parameters welding current, welding speed, contact tip to distance, welding gun angle and pinch are predicted with consideration of performance of bead width, penetration, reinforcement and dilution. Instead of training with conventional back propagation algorithm a new concept of training with PSO algorithm is used in this paper. The proposed ANN-PSO model developed using MATLAB function is found to be flexible, speedy and accurate than conventional ANN system.

© 2014 Jordan Journal of Mechanical and Industrial Engineering. All rights reserved

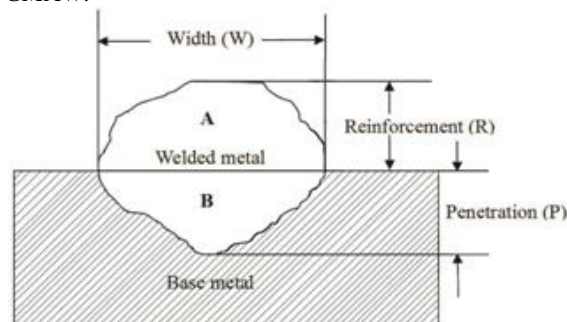
Keywords: : GMAW, Weld Bead Geometry, Multiple Regression, ANN, PSO.

1. Introduction

Prediction of bead geometry in welding plays an important role in improving the quality of weld. The quality of a weld depends on mechanical properties of the weld metal which in turn depends on metallurgical characteristics and chemical composition of the weld. The mechanical and metallurgical feature of weld depends on bead geometry which is directly related to welding process parameters. In other words quality of weld depends on in process parameters [1, 2]. GMA welding is a multi-objective and multifactor metal fabrication technique. The process parameters have a direct influence on bead geometry. Much effort has been done for predicting the bead geometry using artificial neural network. Due to their excellent ability in mapping, generalisation, self-organisation and self-learning ANN became a powerful tool. Particle Swarm Optimization (PSO) is an evolutionary computational technique originated from the behaviour of bird flocking and fish schooling. In this paper a new method of training, instead of Back Propagation (BP) training, for ANN with PSO training is used.

Figure 1 shows the clad bead geometry. Mechanical strength of clad metal is highly influenced by the

composition of metal but also by clad bead shape [2, 3]. This is an indication of bead geometry. It mainly depends on wire feed rate, welding speed, arc voltage etc. Therefore, it is necessary to study the relationship between in-process parameters and bead parameters to study clad bead geometry in which A and B represents area of reinforcement and area of penetration respectively. This paper highlights the study carried out to develop mathematical, ANN and ANN-PSO models to predict clad bead geometry in stainless steel cladding deposited by GMAW.



$$\text{Percentage dilution (D)} = [B / (A+B)] \times 100$$

Figure 1. Clad bead geometry

* Corresponding author. e-mail: pathiyasseril@yahoo.com.

2. Experimentation

The following machines and consumables were used for the purpose of conducting experiment:

1. A constant current gas metal arc welding machine (Invrtee V 350 – PRO advanced processor with 5 – 425 amps output range)
2. Welding manipulator
3. Wire feeder (LF – 74 Model)
4. Filler material Stainless Steel wire of 1.2mm diameter (ER – 308 L).
5. Gas cylinder containing a mixture of 98% argon and 2% of oxygen.
6. Mild steel plate (grade IS – 2062)

Test plates of size 300 x 200 x 20mm were cut from mild steel plate of grade IS – 2062 and one of the surfaces is cleaned to remove oxide and dirt before cladding. ER-308 L stainless steel wire of 1.2mm diameter was used for depositing the clad beads through the feeder. Argon gas at a constant flow rate of 16 litres per minute was used for shielding. The properties of base metal and filler wire are shown in Table 1. The important and most difficult parameter found from trial run is wire feed rate. The wire feed rate is proportional to current. Wire feed rate must be greater than critical wire feed rate to achieve pulsed metal transfer. The relationship found from trial run is shown in equation (1). The formula derived is shown in Figure 2:

$$\text{Wire feed rate} = 0.96742857 * \text{current} + 79.1 \quad (1)$$

The selection of the welding electrode wire based on the matching the mechanical properties and physical characteristics of the base metal, weld size and existing electrode inventory [4]. A candidate material for cladding which has excellent corrosion resistance and weld ability is stainless steel. These have chloride stress corrosion cracking resistance and strength significantly greater than other materials. These have good surface appearance, good radiographic standard quality and minimum electrode wastage.

Table 1. Chemical Composition of Base Metal and Filler Wire

Materials	Elements, Weight %								
	C	SI	Mn	P	S	Al	Cr	Mo	Ni
IS 2062	0.150	0.160	0.870	0.015	0.016	0.031	-	-	-
ER308L	0.03	0.57	1.76	0.021	1.008	-	19.52	0.75	10.02

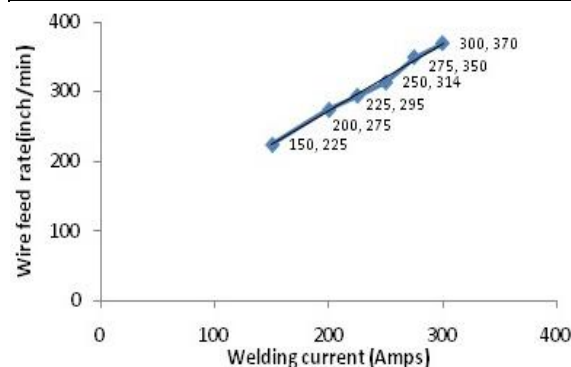


Figure 2. Relationship between Current and Wire Feed Rate

3. Plan of Investigation

The research work is carried out in the following steps [5,6]. Identification of factors, finding the limit of process variables, development of design matrix, conducting experiments as per design matrix, recording responses, development of mathematical models, checking adequacy of developed models, and predicting the parameters using ANN, and using ANN-PSO parameters predicted.

3.1. Identification of Factors and Responses

The basic difference between welding and cladding is the percentage of dilution. The properties of cladding are significantly influenced by the dilution obtained. Hence, the control of the dilution is important in cladding where a low dilution is highly desirable. When dilution is quite low, the final deposit composition will be closer to that of the filler material and, hence, the corrosion resistant properties of cladding will be greatly improved. The chosen factors have been selected on the basis of getting minimal dilution and optimal clad bead geometry [1]. These are: wire feed rate (W), welding speed (S), and welding gun angle (T), contact tip. The following independently controllable process parameters were found to be affecting output parameters distance (N) and pinch (Ac). The responses chosen were clad bead width (W), height of reinforcement (R), Depth of Penetration (P), and percentage of dilution (D). The responses were chosen based on the impact of parameters on the final composite model.

3.2. Finding the Limits of Process Variables

Working ranges of all the selected factors are fixed by conducting a trial run. This was carried out by varying one of factors while keeping the rest as constant values. The working range of each process parameters was decided upon by inspecting the bead for smooth appearance without any visible defects. The upper limit of the given factor was coded as -2. The coded values of intermediate values were calculated using the equation (2):

$$X_i = \frac{2[2X - (X_{\max} + X_{\min})]}{(X_{\max} - X_{\min})} \quad (2)$$

Where X_i is the required coded value of parameter X is any value of parameter from X_{\min} – X_{\max} . X_{\min} is the lower limit of parameters and X_{\max} is the upper limit parameters [7].

The chosen level of the parameters with their units and notation are given in Table 2:

3.3. Development of Design Matrix

The design matrix chosen to conduct the experiments was a central composite rotatable design. The design matrix comprises full replication of $2^5 (= 32)$, and factorial designs. All welding parameters in the intermediate levels (o) constitute the central points and a combination of each welding parameter at either highest value (+2) or lowest (-2) with other parameters of intermediate levels (0) that constitute star points. 32 experimental trails were conducted, making the estimation of linear quadratic and two way interactive effects of process parameters on clad geometry [8,9].

3.4. Conducting Experiments as per Design Matrix

In this work, 32 experimental runs were allowed for the estimation of linear quadratic and two-way interactive effects corresponding to each treatment combination of parameters on bead geometry at random as shown Table 3. At each run, settings for all parameters were disturbed and reset for the next deposit. Figure 3 shows the GMAW circuit diagram. This is very essential for introducing variability caused by errors in the experimental set up. The experiments were conducted at SVS College of Engineering, Coimbatore, 642109, India.

3.5. Recording of Responses

For measuring the clad bead geometry, the transverse section of each weld overlays was cut using a band saw of mid length. Position of the weld and end faces were machined and grinded. The specimen and faces were polished and etched using a 5% nital solution to display bead dimensions. The clad bead profiles were traced using a reflective type optical profile projector at a magnification of X10, in M/s Roots Industries Ltd. Coimbatore. Then, the bead dimensions, such as depth of penetration height of reinforcement and clad bead width, were measured [10, 11]. The profiles traced using AUTO CAD software. This is shown in Figure 4. This represents the profile of the specimen (front side). The cladded specimen is shown in Figure 5. The measured clad bead dimensions and percentage of dilution are shown in Table 4.

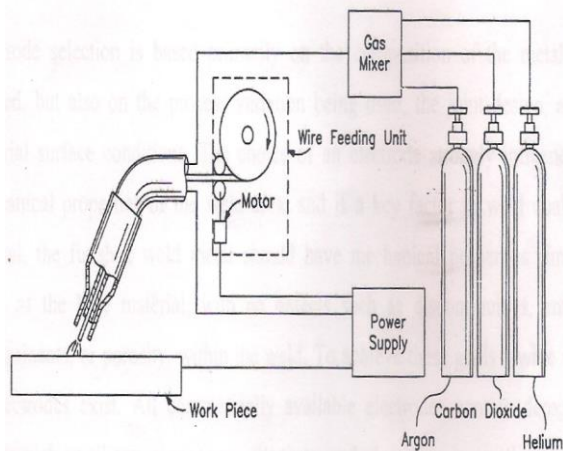


Figure 3. GMAW Circuit Diagram

Table 2. Welding Parameters and their Levels

Parameters	Factor Levels						
	Unit	Notation	-2	-1	0	1	2
Welding Current	A	I	200	225	250	275	300
Welding Speed	mm/min	S	150	158	166	174	182
Contact tip to work distance	mm	N	10	14	18	22	26
Welding gun Angle	Degree	T	70	80	90	100	110
Pinch	-	Ac	-10	-5	0	5	10

Table 3. Design Matrix

Trial Number	Design Matrix				
	I	S	N	T	Ac
1	-1	-1	-1	-1	1
2	1	-1	-1	-1	-1
3	-1	1	-1	-1	-1
4	1	1	-1	-1	1
5	-1	-1	1	-1	-1
6	1	-1	1	-1	1
7	-1	1	1	-1	1
8	1	1	1	-1	-1
9	-1	-1	-1	1	-1
10	1	-1	-1	1	1
11	-1	1	-1	1	1
12	1	1	-1	1	-1
13	-1	-1	1	1	1
14	1	-1	1	1	-1
15	-1	1	1	1	-1
16	1	1	1	1	1
17	-2	0	0	0	0
18	2	0	0	0	0
19	0	-2	0	0	0
20	0	2	0	0	0
21	0	0	-2	0	0
22	0	0	2	0	0
23	0	0	0	-2	0
24	0	0	0	2	0
25	0	0	0	0	-2
26	0	0	0	0	2
27	0	0	0	0	0
28	0	0	0	0	0
29	0	0	0	0	0
30	0	0	0	0	0
31	0	0	0	0	0
32	0	0	0	0	0

I - Welding current; S - Welding speed; N - Contact tip to work distance; T - Welding gun angle; Ac - Pinch

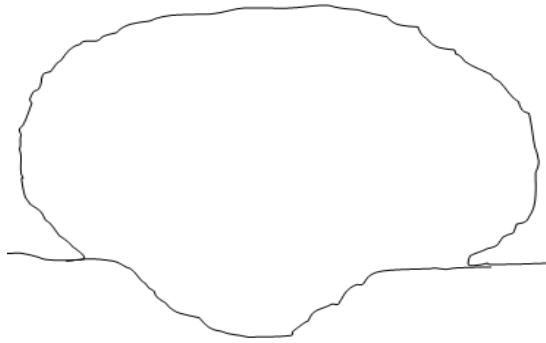


Figure 4. Traced Profile of bead geometry

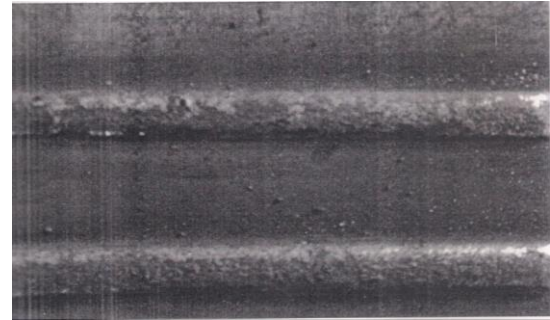


Figure 5. clad specimen

Table 4. Design Matrix and Observed Values of Clad Bead Geometry

Trial No.	Design Matrix					Bead Parameters			
	I	S	N	T	Ac	W (mm)	P (mm)	R (mm)	D (%)
1	-1	-1	-1	-1	1	6.9743	1.67345	6.0262	10.72091
2	1	-1	-1	-1	-1	7.6549	1.9715	5.88735	12.16746
3	-1	1	-1	-1	-1	6.3456	1.6986	5.4519	12.74552
4	1	1	-1	-1	1	7.7635	1.739615	6.0684	10.61078
5	-1	-1	1	-1	-1	7.2683	2.443	5.72055	16.67303
6	1	-1	1	-1	1	9.4383	2.4905	5.9169	15.96692
7	-1	1	1	-1	-1	6.0823	2.4672	5.49205	16.5894
8	1	1	1	-1	-1	8.4666	2.07365	5.9467	14.98494
9	-1	-1	-1	1	-1	6.3029	1.5809	5.9059	10.2749
10	1	-1	-1	1	1	7.0136	1.5662	5.9833	9.707297
11	-1	1	-1	1	1	6.2956	1.58605	5.5105	11.11693
12	1	1	-1	1	-1	7.741	1.8466	5.8752	11.4273
13	-1	-1	1	1	1	7.3231	2.16475	5.72095	15.29097
14	1	-1	1	1	-1	9.6171	2.69495	6.37445	18.54077
15	-1	1	1	1	-1	6.6335	2.3089	5.554	17.23138
16	1	1	1	1	1	10.514	2.7298	5.4645	20.8755
17	-2	0	0	0	0	6.5557	1.99045	5.80585	13.65762
18	2	0	0	0	0	7.4772	2.5737	6.65505	15.74121
19	0	-2	0	0	0	7.5886	2.50455	6.4069	15.77816
20	0	2	0	0	0	7.5014	2.1842	5.6782	16.82349
21	0	0	-2	0	0	6.1421	1.3752	6.0976	8.941799
22	0	0	2	0	0	8.5647	3.18536	5.63655	22.94721
23	0	0	0	-2	0	7.9575	2.2018	5.8281	15.74941
24	0	0	0	2	0	7.7085	1.85885	6.07515	13.27285
25	0	0	0	0	-2	7.8365	2.3577	5.74915	16.63287
26	0	0	0	0	2	8.2082	2.3658	5.99005	16.38043
27	0	0	0	0	0	7.9371	2.1362	6.0153	15.18374
28	0	0	0	0	0	8.4371	2.17145	5.69895	14.82758
29	0	0	0	0	0	9.323	3.1425	5.57595	22.8432
30	0	0	0	0	0	9.2205	3.2872	5.61485	23.6334
31	0	0	0	0	0	10.059	2.86605	5.62095	21.55264
32	0	0	0	0	0	8.9953	2.72068	5.7052	19.60811

W-Width; R - Reinforcement W - Width; P - Penetration; D - Dilution %

3.6. Development of Mathematical Models

The response function representing any of the clad bead geometry can be expressed as [12, 13]:

$$Y = f(A, B, C, D, E) \tag{3}$$

Where,

Y = Response variable

A = Welding current (I) in amps

B = Welding speed (S) in mm/min

C = Contact tip to Work distance (N) in mm

D = Welding gun angle (T) in degrees

E = Pinch (Ac)

The second order surface response model equals can be expressed as below:

$$Y = \beta_0 + \sum_{i=0}^5 \beta_i X_i + \sum_{i=0}^5 \beta_{ii} X_i^2 + \sum_{i=0}^5 \sum_{j=0}^5 \beta_{ij} X_i X_j \tag{4}$$

$$Y = \beta_0 + \beta_1 A + \beta_2 B + \beta_3 C + \beta_4 D + \beta_5 E + \beta_{11} A^2 + \beta_{22} B^2 + \beta_{33} C^2 + \beta_{44} D^2 + \beta_{55} E^2 + \beta_{12} AB + \beta_{13} AC + \beta_{14} AD + \beta_{15} AE + \beta_{23} BC + \beta_{24} BD + \beta_{25} BE + \beta_{34} CD + \beta_{35} CE + \beta_{45} DE$$

Where, β_0 is the free term of the regression equation, the coefficient $\beta_1, \beta_2, \beta_3, \beta_4$ and β_5 is linear terms, the coefficients $\beta_{11}, \beta_{22}, \beta_{33}, \beta_{44}$ and β_{55} quadratic terms, and the coefficients $\beta_{12}, \beta_{13}, \beta_{14}, \beta_{15}$, etc are the interaction terms. The coefficients were calculated by using Quality America six sigma software (DOE – PC IV). After determining the coefficients, the mathematical models were developed. The developed mathematical models are given as follows:

$$\beta_0 = 0.166338(\sum X_0 Y) + 0.05679(\sum \sum X_{ii} Y) \tag{5}$$

$$\beta_i = 0.166338(\sum X_i Y) \tag{6}$$

$$\beta_{ii} = 0.0625((\sum X_{ii} Y) + 0.06889(\sum \sum X_{ii} Y) - 0.056791(\sum \sum X_0 Y)) \tag{7}$$

$$\beta_{ij} = 0.125(\sum X_{ij} Y) \tag{8}$$

$$\begin{aligned} \text{Clad Bead Width (W), mm} = & 8.923 + 0.701A + 0.388B + \\ & 0.587C + 0.040D + 0.088E - 0.423A^2 - 0.291B^2 - \\ & 0.338C^2 - 0.219D^2 - 0.171E^2 + 0.205AB + 0.405AC + \\ & 0.105AD + 0.070AE - 0.134BC + 0.225BD + 0.098BE + \\ & 0.26CD + 0.086CE + 0.012DE \end{aligned} \tag{9}$$

$$\begin{aligned} \text{Depth of Penetration (P), mm} = & 2.735 + 0.098A - \\ & 0.032B + 0.389C - 0.032D - 0.008E - 0.124A^2 - 0.109B^2 - \\ & 0.125C^2 - 0.187D^2 - 0.104E^2 - 0.33AB + 0.001 AC + \\ & 0.075AD + 0.005 AE - 0.018BC + 0.066BD + 0.087BE + \\ & 0.058CD + 0.054CE - 0.036DE \end{aligned} \tag{10}$$

$$\begin{aligned} \text{Height of Reinforcement (R), mm} = & 5.752 + 0.160A - \\ & 0.151B - 0.060C + 0.016D - 0.002E + 0.084A^2 + 0.037B^2 - \\ & 0.0006C^2 + 0.015D^2 - 0.006E^2 + 0.035AB + 0.018AC - \\ & 0.008AD - 0.048AE - 0.024BC - 0.062BD - 0.003BE + \\ & 0.012CD - 0.092CE - 0.095DE \end{aligned} \tag{11}$$

$$\begin{aligned} \text{Percentage Dilution (D), \%} = & 19.705 + 0.325A + 0.347B + \\ & 3.141C - 0.039D - 0.153E - 1.324A^2 - 0.923B^2 - \\ & 1.012C^2 - 1.371D^2 - 0.872E^2 - 0.200AB + 0.346 AC + \\ & 0.602 AD + 0.203AE + 0.011BC + 0.465BD + 0.548BE + \\ & 0.715CD + 0.360CE + 0.137DE \end{aligned} \tag{12}$$

Co-efficient of the above polynomial equation were calculated by regression as given by equations (5) to (8)

3.7. Checking the Adequacy of the Developed Models

Analysis of variance (ANOVA) technique was used to test the adequacy of the model. As per this technique, if the F – ratio values of the developed models do not exceed the standard tabulated values for a desired level of confidence (95%) and the calculated R – ratio values of the developed model exceed the standard values for a desired level of confidence (95%) then the models are said to be adequate within the confidence limit [14]. These conditions were satisfied for the developed models. The values are shown in Table 5:

Table 5. Analysis of variance for Testing Adequacy of the Model

Parameter	1 st Order terms		2 nd order terms		Lack of fit		Error terms		F-ratio	R-ratio	Whether model is adequate	
	SS	DF	SS	DF	SS	DF	SS	DF				
W	36.889	20	6.233	11	3.51	3	6	2.721	5	1.076	3.390	Adequate
P	7.810	20	0.404	11	0.142	6	6	0.261	5	0.454	7.472	Adequate
R	1.921	20	0.572	11	0.444	6	6	0.128	5	2.885	3.747	Adequate
D	506.074	20	21.739	11	6.289	6	6	15.45	5	0.339	8.189	Adequate

SS - Sum of squares; DF - Degree of freedom; F Ratio (6, 5, 0.5) = 3.40451; R Ratio (20, 5, 0.05) = 3.20665

4. Artificial Neural Network

Artificial neural network models are generally comprised of three independent layers: input, hidden, and output. Each layer consists of several processing neurons. Each neuron in a layer operates in logical similarity. Information is transmitted from one layer to others in serial operations. The neurons in the input layer include the input values. Each neuron in the hidden layer processes the inputs into the neuron outputs. The pattern of hidden layers to be applied in the modelling can be either multiple layers or a single layer. The most widely used training algorithm for neural networks is the back-propagation algorithm [15, 16].

The MLP is one of artificial neural networks that are extensively used to solve a number of different problems, including pattern recognition and interpolation. Each layer is composed of neurons which are interconnected with each other in a previous layer by weights. In each neuron, a specific mathematical function called the activation function accepts a weighed sum of the outputs from a previous layer as the function's input, and generates the function's output. In the experiment, the hyperbolic tangent sigmoid transfer function [17] is used as the activation function. It is defined by:

$$f(s) = \frac{1 - e^{-2s}}{1 + e^{-2s}} \tag{13}$$

Where $S = \sum_{i=0}^n wixi + b$ in which w_i are weights, x_i are inputs of neuron, b is bias and n is the number of variables.

The MLP is trained by using the Levenberg-Marquardt technique. This technique is more powerful than the conventional gradient descent technique.

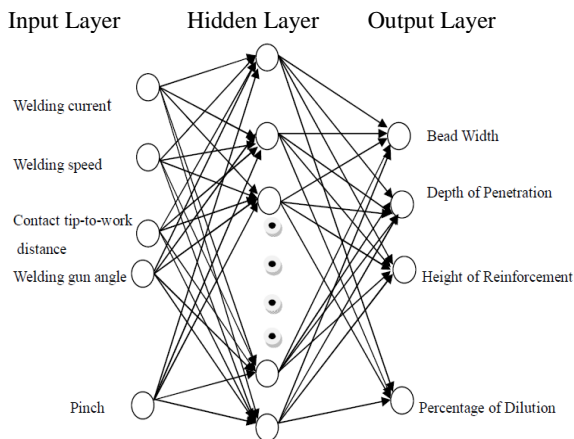


Figure 6. Neural Network Architecture

MAT LAB 7 was used for training the network for the prediction of clad bead geometry. Statistical mathematical model was used compare results produced by the work. For normalizing the data the goal is to examine the statistical distribution of values of each net input and outputs are roughly uniform in addition the value should scaled to match range of input neurons [18]. This is basically range 0 to 1 in practice it is found to between 01 and 9. In this paper, data bases are normalized using the Equation (9):

$$X_{norm} = 0.1 + \frac{(X - X_{min})}{1.25(X_{max} - (X_{min}))} \tag{14}$$

- X_{norm} = Normalized value between 0 and 1
- X = Value to be normalized
- X_{min} = Minimum value in the data set range the particular data set rage which is to be normalized.
- X_{max} = Maximum value in the particular data set range which is to be normalized.

The accuracy of prediction may be decreased with the increase in the number of neurons in the hidden layer in other words increase in number of neurons could not directly improve the capability of function approximation of network. In this study, five welding process parameters were employed as input to the network. The Levenberg-Marquardt approximation algorithm was found to be the best fit for application because it can reduce the MSE to a significantly small value and can provide better accuracy of prediction. So, neural network model with feed forward back propagation algorithm and Levenberg-Marquardt approximation algorithm was trained with data collected for the experiment. Error was calculated using equation (10):

$$\text{Error} = \frac{(\text{Actual value} - \text{Predicted value}) \times 100}{\text{Predicted value}} \tag{15}$$

The difficulty using the regression equation is the possibility of over fitting the data. To avoid this the experimental data is divided in to two sets, one training set and other test data set .The ANN model is created using only training data the other test data is used to check the behaviour the ANN model created. All variables are normalized using the equation (9).The data was randomized and portioned in to two one training and other test data.

$$y = \sum_i w_{ij} h_i + \theta \tag{16}$$

$$h_i = \tan h(\sum_j w_{ij} x_j + \theta_i) \tag{17}$$

The Neural Network general form can be defined as a model shown above y representing the output variables and x_j the set of inputs, shown in equations [19, 20]. The subscript i represents the hidden units shown in Figure 6 and θ represents the bias and w_j represents the weights. The equation above defines the function giving output as a function of input.

In this work, the number of input neurons is five and output neurons are four. It is necessary to find the number of hidden layers and number of neurons in the hidden layer. From Figure 7, it is found that twelve neurons give minimum error. So, a structure of 5-12-4 is created for the prediction of data. The data for prediction are taken from Table 4. First eleven data are used for testing and the next seventeen data are used for training. This is shown in Tables 7 and 8.

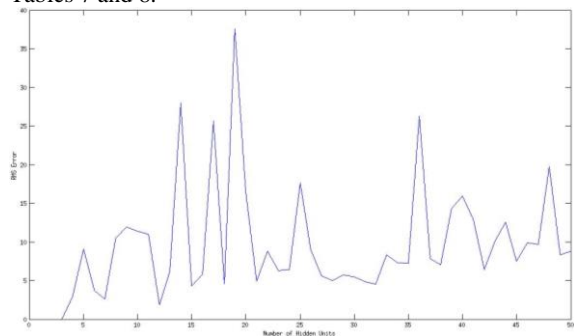


Figure7. comparisons between number of hidden units and Error

Table 6. Comparison of actual and predicted values of the clad bead parameters using neural network data (training)

Trial NO	Actual Bead Parameters				Predicted Bead Parameters				Error			
	W	P	R	D	W	P	R	D	W	P	R	D
	(mm)	(mm)	(mm)	(%)	(mm)	(mm)	(mm)	(%)	(mm)	(mm)	(mm)	(%)
1	7.741	1.8466	5.8752	11.4273	7.335	2.0986	6.0792	10.8222	0.406	-0.252	-0.204	0.6051
2	7.3231	2.16475	5.72095	15.29097	6.8214	2.0617	5.6946	14.9379	0.5017	0.10305	0.02635	0.35307
3	9.6171	2.69495	6.37445	18.54077	9.3713	2.8982	6.4084	17.4578	0.2458	0.20325	-0.0339	1.08297
4	6.6335	2.3089	5.554	17.23138	7.4306	2.2927	5.6232	15.7908	-0.7971	0.0162	-0.0692	1.44058
5	10.514	2.7298	5.4645	20.8755	7.8991	2.5154	5.8078	18.0664	2.6149	0.2144	-0.3433	2.8091
6	6.5557	1.99045	5.80585	13.65762	6.5761	1.9158	5.7867	14.2039	-0.0204	0.07465	0.01915	-0.5462
7	7.4772	2.5737	6.65505	15.74121	7.393	2.7191	6.7112	14.7525	0.0842	-0.1454	-0.0561	0.98871
8	7.5886	2.50455	6.4069	15.77816	7.5943	2.4317	6.3834	15.9881	-0.0057	0.07285	0.0235	-0.2099
9	7.5014	2.1842	5.6782	16.82349	7.4652	2.2814	5.7674	16.5744	0.0362	-0.0972	-0.0892	0.24909
10	6.1421	1.3752	6.0976	8.941799	5.6583	1.44	6.2054	9.3753	0.4838	-0.0648	-0.1078	-0.4335
11	8.5647	3.18536	5.63655	22.94721	9.9724	2.962	5.5227	18.9566	-1.4077	0.22336	0.11385	3.99061
12	7.9575	2.2018	5.8281	15.74941	9.0693	2.6919	6.2337	17.5548	-1.1118	-0.4901	-0.4056	-1.8053
13	7.7085	1.85885	6.07515	13.27285	6.7699	1.7807	6.109	12.8584	0.9386	0.07815	-0.0338	0.41445
14	7.8365	2.3577	5.74915	16.63287	8.5364	2.9431	6.6735	15.9653	-0.6999	-0.5854	-0.9243	0.66757
15	8.2082	2.3658	5.99005	16.38043	8.0083	2.371	6.0186	16.3701	0.1999	-0.0052	-0.0285	0.01033
16	7.9371	2.1362	6.0153	15.18374	7.9441	2.1197	6.01	15.3735	-0.007	0.0165	0.0053	-0.1897
17	8.4731	2.17145	5.69895	14.82758	8.6735	2.5165	5.4985	15.2875	-0.2001	-0.3450	0.2031	-0.4599

Table 7. Comparison of actual and predicted values of the clad bead parameters using neural network data (test)

Trial No	Actual Bead Parameters				Predicted Bead Parameters				Error			
	W	P	R	D	W	P	R	D	W	P	R	D
	(mm)	(mm)	(mm)	(%)	(mm)	(mm)	(mm)	(%)	(mm)	(mm)	(mm)	(%)
1	6.9743	1.6735	6.0262	10.721	6.1945	1.85	5.9611	12.367	0.7798	-0.177	0.0651	-1.646
2	7.6549	1.9715	5.8873	12.167	7.1815	2.1507	6.5553	10.268	0.4734	-0.179	-0.668	1.899
3	6.3456	1.6986	5.4519	12.746	7.4954	1.5339	5.4923	9.3808	-1.15	0.1647	-0.04	3.3652
4	7.7635	1.7396	6.0684	10.611	6.4936	1.854	6.5573	9.4799	1.2699	-0.114	-0.489	1.1311
5	7.2683	2.443	5.7206	16.673	7.3354	2.6576	5.5657	19.104	-0.067	-0.215	0.1549	-2.431
6	9.4383	2.4905	5.9169	15.967	7.6066	2.1045	6.4342	18.49	1.8317	0.386	-0.517	-2.523
7	6.0823	2.4672	5.492	16.589	8.0417	2.1722	5.5126	16.874	-1.959	0.295	-0.021	-0.285
8	8.4666	2.0737	5.9467	14.985	8.3236	2.2349	5.9031	16.972	0.143	-0.161	0.0436	-1.987
9	6.3029	1.5809	5.9059	10.275	8.2381	1.7955	5.6022	11.219	-1.935	-0.215	0.3037	-0.944
10	7.0136	1.5662	5.9833	9.7073	7.5899	2.4579	6.542	13.415	-0.576	-0.892	-0.559	-3.708
11	6.2956	1.586	5.5105	11.117	7.7318	1.7647	5.8676	10.71	-1.436	-0.179	-0.357	0.407

5. PSO algorithm

The particle swarm optimization algorithm gives a solution much similar to problems such as genetic algorithms. In PSO, a point in the problem space is called a particle, which is initialized with a random position and search velocity [21, 22]. Each particle flies through the problem space and keeps track of its positions and its fitness. Where the latter means the best solution achieved. Its position and velocity are adjusted by its fitness to the environment. Given that a swarm consists of m particles in a D -dimensional problem space, the position and velocity of the i th particle is presented as:

$$S_i = (S_{i1}, S_{i2}, \dots, S_{iD}), i=1, 2, \dots, m,$$

$$v_i = (v_{i1}, v_{i2}, \dots, v_{iD})$$

The best position of a particle is denoted by P_{best} , $pi = (pi_1, pi_2, \dots, pi_3)$. Treating the swarm population as a

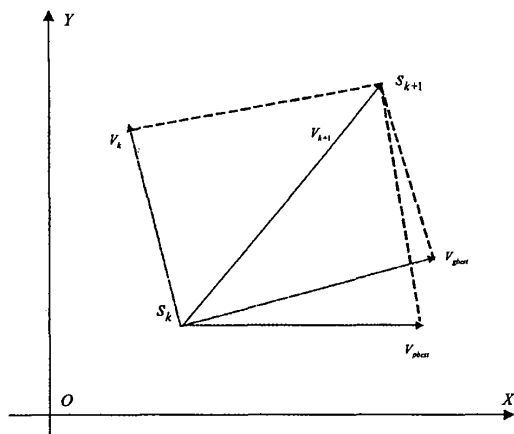


Figure 8. The illustration of searching in a two – dimensional space.

Whole, the best position of the best positions of all particles is denoted by G_{best} in which $p_g = (p_{g1}, p_{g2}, \dots, p_{g3})$.

The PSO algorithm is formulated as [12]:

$$v_{id}^{k+1} = w_{id}^k + c_1 \text{ran} d_1 (Pbest - s_{id}^k) + c_2 \text{ran} d_2 (g_{best} - s_{id}^k) \quad (18)$$

$$S_{id}^{k+1} = s_{id}^k + v_{id}^{k+1}, i = 1, 2, \dots, m, d = 1, 2, \dots, D \quad (19)$$

where, v_{id}^k is the velocity of the i th particle at the k th iteration, w the inertia weight, c_j the accelerating factor, and the random in a range [0, 1] and S_{id}^k is the current position of the i th particle.

Figure 8 illustrates the search process of a particle in a two-dimensional space, where S^k is the current position, S^{k+1} the search position next to the current position, v^k the velocity at the current position, v^{k+1} the velocity at the next position, P_{best} the best velocity based on the v_{best} and u_p is the velocity based on G_{best}

To ensure the convergence of the search, a constriction factor is introduced into the standard PSO algorithm. Eq. (18) is converted into:

From Eq. (20), k is constricted by c_1 and c_2 . Due to k , there is no need of the maximum search velocity V_{max} and the search convergence is ensured mathematically. In other words, the vibration amplitude of the particle decreases when it is near to the best position. Obviously, the constriction factor in the PSO algorithm can produce the solution better than that of the standard PSO [21, 22].

6. Neural Network Training with PSO and Comparison

Instead of back propagation algorithm (BP) ANN is trained with PSO. The predicted results are shown in Table 8. Figure 9 shows convergence comparison.

$$v_{id}^{k+1} = k[v_{id}^k + c_1 \text{ran} d_1 (Pbest - s_{id}^k) + c_2 \text{ran} d_2 (g_{best} - s_{id}^k)] \quad (20)$$

$$k = \frac{2}{|2 - \varphi - \sqrt{\varphi^2 - 4\varphi}|} \quad \text{Where } \varphi = c_1 + c_2\varphi > 4\varphi. \quad (21)$$

Table 8. Comparison of actual and predicted data using ANN-PSO (Test)

Trial No	Actual Bead Parameters				Predicted Bead Parameters				Error			
	W (mm)	P (mm)	R (mm)	D (%)	W (mm)	P (mm)	R (mm)	D (%)	W (mm)	P (mm)	R (mm)	D (%)
1	6.9743	1.6735	6.0262	10.721	6.7317	1.5807	6.5376	10.192	0.2426	0.0928	-0.4114	0.5290
2	7.6549	1.9715	5.8873	12.167	7.7314	1.5231	4.5848	12.628	-0.0765	0.4484	1.3025	-0.461
3	6.3456	1.6986	5.4519	12.746	6.7698	1.9721	5.6432	12.588	-0.4242	-0.2735	-0.0913	0.158
4	7.7635	1.7396	6.0684	10.611	7.2224	1.7116	6.8496	11.665	0.3482	0.0820	-0.7812	1.044
5	7.2683	2.443	5.7206	16.673	7.6165	2.8299	5.5489	16.052	-0.3482	-0.3799	0.1717	0.621
6	9.4383	2.4905	5.9169	15.967	9.4902	2.4324	5.4616	15.729	-0.0512	0.0581	0.4545	0.2382
7	6.0823	2.4672	5.492	16.589	6.9565	2.4565	5.9655	15.654	-0.8742	0.0101	0.4730	0.9390
8	8.4666	2.0737	5.9467	14.985	8.4301	2.0245	5.3226	15.666	0.0366	0.0492	0.6241	-0.6811
9	6.3029	1.5809	5.9059	10.275	4.6652	1.8028	5.1061	10.997	1.6377	-0.2219	0.7998	-0.7218
10	7.0136	1.5662	5.9833	9.7073	6.4065	1.4028	5.6872	9.4375	0.6071	0.1634	0.1871	0.2698
11	6.2956	1.586	5.5105	11.117	5.9413	1.7973	5.0204	11.570	0.3543	-0.2219	0.4901	-0.453

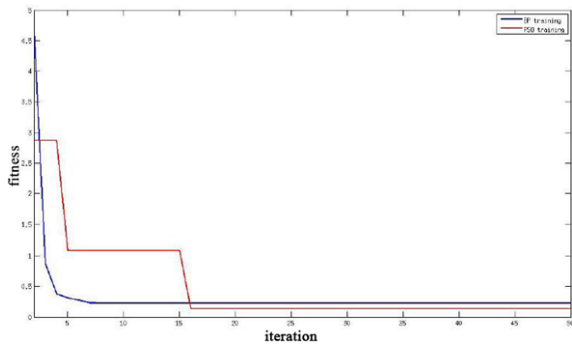


Figure 9. Convergence velocity comparison of the PSO and BP

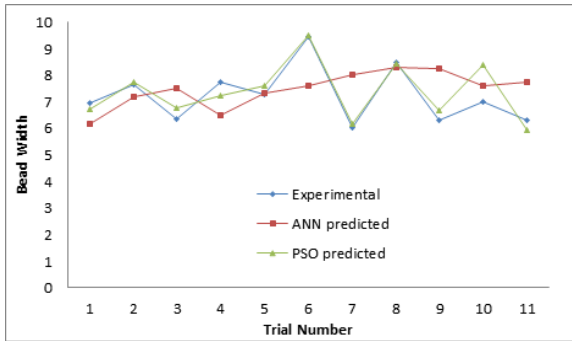


Figure 10. Comparison of ANN and ANN-PSO prediction in Bead Width

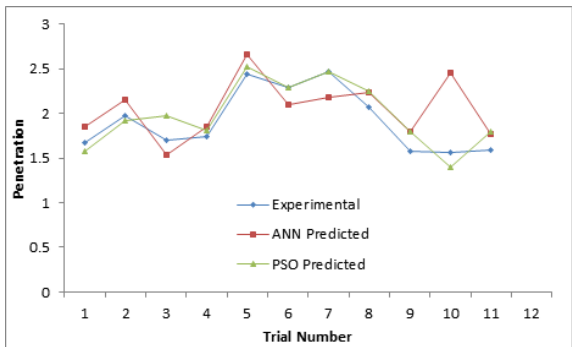


Figure 11. Comparison of ANN and ANN-PSO prediction in Penetration

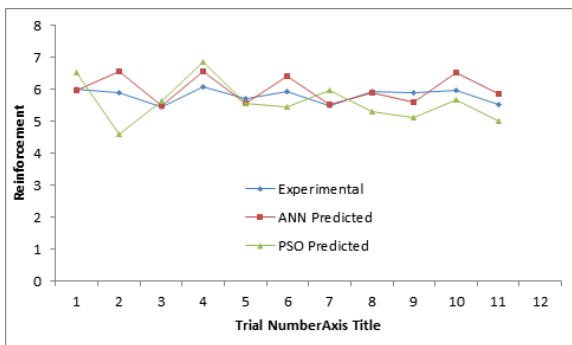


Figure 12. Comparison of ANN and ANN-PSO prediction in Reinforcement

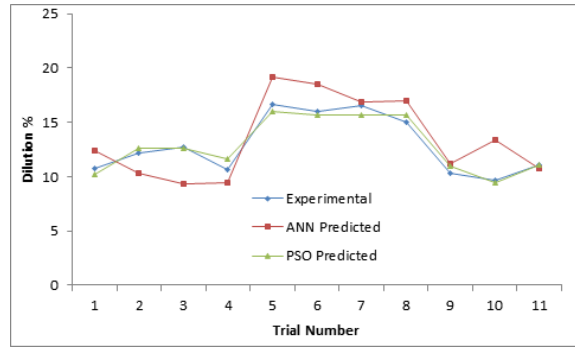


Figure 13. Comparison of ANN and ANN-PSO prediction in Percentage of Dilution

7. Results and Discussions

1. A five-level five-factor full factorial design matrix based on central composite rotatable design technique was used for the mathematical development of model to predict the clad bead geometry of austenitic stainless steel deposited by GMAW.
2. ANN tool, available in MATLAB 7 software, was efficiently employed for prediction of clad bead geometry.
3. In cladding by a welding process, clad bead geometry is very important for economising the material. This study effectively used ANN and ANN-PSO models to predict weld bead geometry.
4. In this study, two models Artificial Neural Network (ANN) and ANN-PSO system for prediction of bead geometry in GMAW welding process are studied and compared. It is proved that ANN-PSO model prediction is more efficient than neural network model. The comparison of prediction between ANN and ANN-PSO is shown through Figures 10-13.
5. The paper presents the adoption of a particle swarm optimization technique to train perceptrons in predicting the outcome of clad bead geometry. A key contribution of the presented work is the adoption of PSO-based training of prediction of bead geometry. The performance of the PSO-based multilayer ANN is bench marked with conventional BP base neural network. It is noted that the testing case of the PSO based network is able to give a successful prediction rate with less error. Moreover, the PSO-based perceptron exhibits much better and faster convergence performance in the training process as well as a better ability in the validation process than the conventional BP-based perceptron. It can be observed from Figure 9 that the PSO-based training is better than the conventional BP-based training. It can be concluded that the PSO-based perceptron performs better than the conventional BP-based perceptron.

8. Conclusions

Based on the above study, it can be observed that the developed model can be used to predict clad bead geometry within the applied limits of process parameters. In this study, ANN-PSO and ANN were used for predicting clad bead geometry. In the case of any cladding process, bead geometry plays an important role in determining the properties of the surface exposed to hostile environments and reducing cost of manufacturing. It is proved that PSO is faster and more accurate than ANN.

Instead of conventional back propagation algorithm used in the conventional artificial neural network training, a new method of PSO-based training of ANN is used in this study. It can be shown that error is less in PSO-based training and, thus, PSO-based training is more accurate, speedy and precise. While comparing the convergence of PSO and BP algorithms, PSO is better converged. Comparing reinforcement, penetration, bead width and dilution with conventional BP algorithm and new PSO training, it can be seen that the new method is acceptable and can be used in predicting the bead geometry.

Acknowledgement

The authors sincerely acknowledge the help and facilities extended to them by the department of mechanical engineering SVS college of Engineering, Coimbatore, India.

References

- [1] T.Kannan, N. Murugan, "Effect of flux cored arc welding process parameters on duplex stainless steel clad quality". *Journal of Material Processing Technology*, Vol. 176 (2006) 230-239.
- [2] T.Kannan, N.Murugan, B.N.Sreeharan, "Optimization of Flux cored arc welding process parameter using genetic and memetic algorithms". *Journal of Manufacturing Science and Production*, Vol. 13 (2013) No. 4, 239-250.
- [3] Lijopaul, Somashekher, S. Hiremath, "Response surface modelling of micro holes in electro chemical discharge machining process". *Procedia Engineering*, Vol. 64 (2013), 1335-1404.
- [4] K.Kalaiselvan, N. Murugan, " Optimization of friction stir welding process parameters for the welding of AL-B4C composite plates using generalised reduced gradient method". *Procedia Engineering*, Vol. 38 (2012) 49-55.
- [5] Dawei Zhao, Yuanxun Wang, Suing Sheng, Zongguo Lin, " Multi-objective optimal design of small scale resistance spot welding process with principal component analysis and response surface methodology". *Journal of Intelligent Manufacture*, DOI10.1007/s 10845-013-0733-2, (2013).
- [6] HariOm, Sunil Pandey, "Effect of heat input on dilution and heat affected zone in submerged arc welding process", *Indian Academy of Sciences*, Vol. 36 (2013) 1369-1391.
- [7] Norasiah Muhammad, Yupiter HP Manurung, Mohammead Hafidzi, Sunhaji Kiyai Abas ,GhalibTham, EsaHaruman, "Optimization and modelling of spot welding parameters with simultaneous multiple response consideration using multi objective Taguchi method and RSM", *Journal of Mechanical Science and Technology*, Vol. 26 (2012) No. 8, 2365-2370.
- [8] A.Pradeep, S. Muthumaran ,P.R. Dhanush ,T. Nakkeran , "A study on friction stir welding of low alloy steel by using a tool with conical pin". *International Journal of Mechanical and Materials Engineering*, Vol. 8 (2013) 132 - 137.
- [9] T.Kannan, N. Murugan, "Prediction of ferrite number of duplex stainless steel clad metals using RSM". *Welding Journal*, Vol. 85 (2006) No. 5, 91-99.
- [10] V.Gunaraj, N. Murugan, "Prediction and control of weld bead geometry and shape relationships in submerged arc welding of pipes". *Journal of Material Processing Technology*, Vol. 168 (2005) 478-487.
- [11] I.S.Kim, K.J. Son, Y.SYang, P. K. D.V. Yaragada, (2003). "Sensitivity analysis for process parameters in GMA welding process using factorial design method". *International Journal of Machine Tools and Manufacture*, Vol. 43 (2003) 763-769.
- [12] W.G Cochran, G.M Coxz, *Experimental Design*.3rd ed. New York: John Wiley & Sons :(1987)
- [13] Serdar Karaoglu, Abdullah Secgin, "Sensitivity analysis of submerged arc welding process parameters". *Journal of Material Processing Technology*, Vol. 202 (2008) 500-507.
- [14] P.K.Ghosh, P.C. Gupta, V.K. Goyal, "Stainless steel cladding of structural steel plate using the pulsed current GMAW process". *Welding journal*,Vol. 77 (1998) No. 7, 307-314.
- [15] V.Gunaraj, N. Murugan, " Prediction and comparison of the area of the heat effected zone for the bead on plate and bead on joint in SAW of pipes". *Journal of Material Processing Technology*, Vol. 95 (1999), 246-261.
- [16] T.Kannan, Yoganath,"Effect of process parameters on clad bead geometry and shape relationships of stainless steel cladding deposited by GMAW". *Int. Journal of Manufacturing Technology*, Vol. 47 (2010) 1083-1095.
- [17] S.N.Deepa, S.N Sivanandam, *Introduction to Genetic Algorithms*. Springer, ISBN-978-3-540-73989-4, Spin: 12053230.
- [18] J. Edwin Raja Dhas, S. Kumaanan, "Optimization of process parameters of submerged arc welding using non-conventional techniques". *Applied Soft Computing*, Vol. 11 (2001) 5198-5204.
- [19] P.K.Giridharan, N.Murugan, "Optimization of pulsed GTA welding process parameters for the welding of AISI 304 L stainless steel". *International Journal of Advanced Manufacturing Technology*, Vol. 40 (2009) 478 - 489.
- [20] k.Siva, N.Murugan, R.Logesh, "Optimisation of Weld Bead Geometry in Plasma Transferred Arc Hard faced Austenitic Stainless Steel Plates using Genetic Algorithm". *International Journal of Advanced Manufacturing Technology*, Vol. 4(2009) 24-30.
- [21] Azlan Mohad Zain., Habibullah Haron, Safian Sharif, "Optimization of process parameters in abrasive water jet machining using integrated SA-GA". *Applied Soft Computing*, Vol. 11 (2011) 5350-5359.
- [22] Jialin Zhou, Zhengcheng Duan, Yong Li, Jianchun Deng, Daoyuan Yu, "PSO based neural network optimization and its utilization in boring". *Journal of Material Processing and Technology*, Vol. 178 (2006) 19-23.



الجامعة الهاشمية



المملكة الأردنية الهاشمية

المجلة الأردنية
للمهندسة الميكانيكية والصناعية

JJIMIE

مجلة علمية عالمية محكمة
تصدر بدعم من صندوق البحث العلمي

<http://jjmie.hu.edu.jo/>

ISSN 1995-6665

المجلة الأردنية للهندسة الميكانيكية والصناعية

مجلة علمية عالمية محكمة

المجلة الأردنية للهندسة الميكانيكية والصناعية: مجلة علمية عالمية محكمة تصدر عن الجامعة الهاشمية بالتعاون مع صندوق دعم البحث العلمي في الاردن

هيئة التحرير

رئيس التحرير

الأستاذ الدكتور نبيل عناقرة

قسم الهندسة الميكانيكية و الصناعية، الجامعة الهاشمية، الزرقاء، الأردن.

الأعضاء

الأستاذ الدكتور ناصر الحنيطي	الأستاذ الدكتور محمد أحمد حمدان
الأستاذ الدكتور سهيل كيوان	الأستاذ الدكتور إبراهيم الروابدة
الأستاذ الدكتور محمود زعل ابو زيد	الأستاذ الدكتور امين الربيدي

مساعد رئيس هيئة التحرير

الدكتور خالد الوديان

فريق الدعم

تنفيذ وإخراج

م.مهنا عقدة

المحرر اللغوي

الدكتور قصي الذبيان

ترسل البحوث إلى العنوان التالي

رئيس تحرير المجلة الأردنية للهندسة الميكانيكية والصناعية

الجامعة الهاشمية

كلية الهندسة

قسم الهندسة الميكانيكية

الزرقاء - الأردن

هاتف : 00962 5 3903333 فرعي 4537

Email: jjmie@hu.edu.jo

Website: www.jjmie.hu.edu.jo